Dense Gas and Star Formation in Nearby Galaxies

Dense Gas and Star Formation in Nearby Galaxies

By Ashley R. Bemis
MSc. (University of Bonn, Bonn, Germany)
BSc. (University of Massachusetts, Amherst MA, USA)

A Thesis Submitted to the School of Graduate Studies in the Partial Fulfillment of the Requirements for the Degree Doctor of Philosophy

McMaster University
Doctor of Philosophy (2020)
Hamilton, Ontario (Physics & Astronomy)

TITLE: Dense Gas and Star Formation in Nearby Galaxies
AUTHOR: Ashley R. Bemis (McMaster University)
SUPERVISOR: Dr. Christine Wilson
NUMBER OF PAGES: 1, 183

Abstract

Star formation occurs within the densest regions of molecular clouds. This is confirmed by the tight scaling relations between star formation and dense gas content in galaxies. One of the most common tracers of dense molecular gas is emission from HCN. Recent studies using HCN have found evidence for variations in the star formation efficiency of dense gas at sub-kiloparsec (kpc) scales in nearby galaxies. This may indicate that environment plays a role in regulating the connection between dense gas and star formation in galaxies. Alternatively, HCN emissivity may also depend on environment within galaxies which could also explain the observed trends. In this thesis, I study the relationship between dense gas and star formation in nearby galaxies. Specifically, I explore the origin of these apparent variations in the star formation efficiency of dense gas.

I begin with a case study of the Antennae Galaxies, the nearest major merger. I explore the star formation efficiency of dense gas and dense gas fraction across different regions of the Antennae system, at sub-kpc scales. I find lower star formation efficiencies of dense gas in the two nuclei relative to their dense gas fractions. I conclude that these low efficiencies are either due to temporal variations in star formation or variations in the emissivity of HCN.

I extend this analysis to a sample of nine other galaxies and incorporate analytical models of star formation to provide context to the observational data. Models which include a varying density threshold for star formation are able to best reproduce the observational trends. This is consistent with an environmental dependence of the star formation efficiency of dense gas within galaxies. I validate these findings with numerical modelling of the HCN and CO emissivities using the radiative transfer code RADEX, which can then be compared directly to analytic models of star formation. I specifically consider whether the HCN/CO ratio universally tracks the fraction of gravitationally bound gas within molecular clouds. The modelled emissivities are consistent with observations and suggest that the HCN/CO ratio is not universally tracking the fraction of gravitationally bound gas, in the case that there are varying threshold densities for star formation. However, the HCN/CO ratio is still a useful tracer of the fraction of gas above $10^{4.5}\,\mathrm{cm}^{-3}$.

The results of this thesis imply that there are clear variations of star formation efficiency of dense gas across galaxies. It is important to consider these variations when interpreting observed trends. Furthermore, when estimating dense gas fractions it is important to incorporate a varying HCN conversion factor, as has been done for CO.

Acknowledgements

Thank you, Dr. Christine Wilson, for providing me with your expertise and guidance through this journey to a PhD. It has been an incredible opportunity to work with you and learn from you. Working with you, I have had the chance to explore research that is compelling and challenging. Thank you for your patience and your kindness. Thank you to my supervisory committee, Dr. Laura Parker and Dr. James Wadsley, who have also provided me with guidance over the course of my PhD. It has been a pleasure working with you both. Thank you to the P&A department at McMaster, especially Dr. Alison Sills, Dr. Bill Harris, and Dr. Ralph Pudritz, I have greatly enjoyed studying here. Thank you to those who have supported me throughout my career, Dr. Adam Leroy, Dr. Rachel Friesen, Dr. Violette Imellizzeri, Dr. Gopal Narayanan, Dr. Min Yun, and Dr. Mark Heyer. I certainly would not be here without your past support. Thank you Dr. Alan Chen for being a wonderful person to assist in teaching Arts & Science. Thank you to Rose, Mara, and Tina for helping an international student find their way. Thank you to fellow members of the Wilson Think Tank, especially Kevin, Nathan, Blake, Hao, and Ryan. You made every day brighter, and your support in the end means more than I can really express. To all my friends, especially Ben, Laura S, Jacqueline, Carmen, Sean, Annica, James L, Joey, Kevin, Gwen, Aaron, Sarah C, Sarah M-P, Sarah D, Mel, Matt, Thanassis, Wyatt, Johnson, and Fraser. You are genuinely some of the greatest people that I have met in my life, and you have had more of a positive impact on me than you could possibly know. Thank you. Thank you to my brother, Adam, who told me that Astronomy would be more practical than a career in dance. :) Mom, thanks for putting up with me and my obsession with astronomy. And, of course, thank you, Dr. Ian Roberts. You lifted me up and helped me get through this journey, and you have been so supportive throughout everything. You are an inspiration to me.

Contents

Abstract **iii**

Acknowledgements **v**

Abbreviations **xv**

Co-authorship **xvii**

1 Introduction **1**
1.1 Galaxies 1
1.1.1 A Spiral Galaxy 3
1.1.2 Starbursts and (U)LIRGs 5
1.2 Phases of the ISM 6
1.3 Molecular Clouds 8
1.3.1 Observations of Molecular Clouds 9
1.3.2 Interpreting the Luminosity of Molecular Lines 10
1.3.3 Molecular Cloud Dynamics 13
1.3.4 Molecular Transitions and Mass Conversion Factors 16
1.4 Emissivity & the Gas Density PDF 18
1.5 Molecular Gas and Star Formation 23
1.5.1 Star Formation Rate Indicators 26
1.6 Thesis Layout 28

2 Kiloparsec-Scale Variations in the Star Formation Efficiency of Dense Gas: The Antennae Galaxies (NGC 4038/39) **39**
2.1 Introduction 41
2.2 Data 44
2.2.1 ALMA Data 44
2.2.2 Infrared Data and Total Infrared Luminosities 46
2.3 Aperture Analysis 48
2.4 Results 51

2.5 Discussion . . . 61
2.5.1 General Characteristics of the Dense Gas: Photon Dominated Regions (PDRs) . . . 62
2.5.2 The Nuclei of NGC 4038 and NGC 4039 . . . 64
2.5.3 The Western Arm . . . 69
2.5.4 The Overlap Region . . . 72
2.5.5 Conversion Factors . . . 74
2.5.6 Dense-gas Fractions . . . 76
2.6 Conclusions . . . 77
2.A Appendix: Uncertainties . . . 80
2.A.1 Molecular Luminosities . . . 80
2.A.2 Infrared Measurements and Luminosities . . . 80
2.B Appendix: L_{TIR} Calibrations . . . 81
2.C Appendix: Luminosity Ratios . . . 84

3 Does the HCN/CO ratio trace the star-forming fraction of gas? I. A comparison to analytical models of star formation. 93
3.1 Introduction . . . 95
3.2 Data and Sample . . . 99
3.2.1 Molecular Gas Surface Densities . . . 101
3.2.2 The Radio Continuum SFR . . . 102
3.2.3 Velocity Dispersion . . . 105
3.2.4 Uncertainties From a Multi-scale Sample . . . 106
3.3 Theoretical Predictions of f_{grav} . . . 107
3.3.1 Connecting Observations to Theory . . . 111
3.3.2 Power Law Slope . . . 115
3.3.3 Two Prescriptions for Density Thresholds . . . 116
3.4 Results . . . 118
3.4.1 The Kennicutt-Schmidt Relationship . . . 119
3.4.2 Does HCN/CO trace f_{grav}? . . . 119
3.5 Discussion . . . 127
3.6 Conclusions . . . 127
3.A Appendix: Moment Maps and Uncertainties . . . 130

4 Does the HCN/CO ratio trace the fraction of gravitationally-bound gas? II. A radiative transfer perspective. 135
4.1 Introduction . . . 137
4.2 Model Framework . . . 139
4.2.1 Emissivity . . . 139
4.2.2 The Model Parameter Space . . . 145
4.3 Model Results . . . 147

4.3.1 Excitation and Optical Depth 149
4.3.2 The HCN/CO Ratio and f_{grav} 152
4.4 The Applicability of the HCN/CO Ratio 158
4.4.1 Dense Gas Fraction 158
4.4.2 Conversion Factors 162
4.4.3 Filling Fractions 164
4.5 Conclusions 168
4.A Star Formation Trends with Observational Analogs 171

5 Discussion and Conclusions **177**
5.1 Summary of this Thesis 177
5.2 Future Work and Open Questions 179

List of Figures

1.1 Kennicutt-Schmidt relationship for five galaxies from Wilson et al. (2019). 25

2.1 ALMA observations of the Antennae Galaxies, overlaid on an optical image from the Hubble Space Telescope. 45
2.2 L_{TIR} vs. L_{HCN}, $L_{\mathrm{HCO^+}}$, and L_{HNC} from hexagonal aperture analysis. 52
2.3 L_{TIR} vs. L_{HCN}, $L_{\mathrm{HCO^+}}$, and L_{HNC} from elliptical aperture analysis. . 54
2.4 L_{TIR} vs. L_{HCN} 57
2.5 Σ_{SFR} vs. $\Sigma_{\mathrm{M_{dense}}}$. 58
2.6 Ratio maps of Galametz et al. (2013) calibrations at the 250 μm resolution. 82

3.1 The grid of σ_{v} and Σ_{mol} used as inputs to the analytical models, colored by P_{turb}. 112
3.2 The Kennicutt-Schmidt relationship for our galaxies and the EMPIRE sample, compared to the model predictions. 120
3.3 Gas fraction as a function of turbulent pressure. 121
3.4 Gas fraction as a function of turbulent pressure with model predictions. 121
3.5 Efficiency per free-fall time as a function of P_{turb} and $I_{\mathrm{HCN}}/I_{\mathrm{CO}}$. . . 123
3.6 The efficiency of star formation per free-fall time as a function of P_{turb}, model predictions of f_{grav}, model predictions of f_{dense}. 124
3.7 Depletion time of the total molecular gas content as a function of P_{turb} and $f_{\mathrm{dense}} = 3.2\, I_{\mathrm{HCN}}/I_{\mathrm{CO}}$. 125
3.8 The depletion time of the total molecular gas content as a function of P_{turb}, gas fraction including the model predictions of f_{grav}, and gas fraction including the model predictions of f_{dense}. 126
3.9 Depletion time of the dense molecular gas content as a function of P_{turb} and f_{dense}. 127

3.10 The depletion time of the dense molecular gas content as a function of $P_{\rm turb}$, and gas fraction. 128

4.1 Left: Example gas density PDF, Center: HCN and CO luminosity versus density, Right: Emissivity of HCN and CO. 143
4.2 $\sigma_{\rm v}^2/R$ versus $\Sigma_{\rm mol}$ 147
4.3 n-PDFs weighted by emissivity, optical depth, and excitation temperature. 148
4.4 Correlations between HCN/CO emissivity ratio, HCN and CO excitation temperatures, and HCN and CO optical depths. 150
4.5 The HCN/CO emissivity ratio, kinetic temperature, mean density, velocity dispersion, and the relative HCN-to-CO filling fractions. . . 151
4.6 Optical depths of CO and HCN, kinetic temperature, mean density, and velocity dispersion. 153
4.7 Excitation temperatures of CO and HCN relative to kinetic temperature, mean density, and velocity dispersion 154
4.8 The HCN/CO emissivity ratio, $f_{\rm grav}$, $f_{\rm dense}$, $\epsilon_{\rm ff}$, and $\epsilon_{\rm ff,obs}$. 157
4.9 The HCN/CO emissivity ratio, $f_{\rm grav}$, $t_{\rm dep,grav}$, $f_{\rm dense}$, and $t_{\rm dep,dense}$. . 159
4.10 $n-$PDF Gas fractions as a function of the HCN/CO emissivity ratio. 160
4.11 The fraction of gas above $n \sim 10^{4.5}$ cm^{-3} as a function of $I_{\rm HCN}/I_{\rm CO}$. 163
4.12 The CO conversion factor as a function of CO intensity. 165
4.13 The CO filling fraction as a function of CO intensity. 169
4.14 The HCN/CO emissivity ratio, $t_{\rm dep}$, $t_{\rm ff}$, $\epsilon_{\rm ff}$, and $\Sigma_{\rm SFR}$. 172
4.15 The HCN/CO emissivity ratio, $t_{\rm dep}$, $f_{\rm dense}$, $t_{\rm dep,dense}$, $P_{\rm turb}$, and $\Sigma_{\rm SFR}$. 173

List of Tables

2.1 Elliptical Apertures 48
2.2 Total Infrared and Molecular Luminosities 55
2.3 Comparison of $L_{\mathrm{TIR}}/L_{\mathrm{HCN}}$ Statistics 56
2.4 Physical Properties 60
2.5 Total Infrared Luminosities from Different Calibrations 84
2.6 Luminosity Ratios from Elliptical Apertures 86

3.1 Spatial and spectral resolutions of the data for each galaxy. Distances and redshifts are also listed, which are used to determine the physical scale (in pc) per pixel, and to convert measured flux to luminosities. Redshifts are taken from the NASA/IPAC Extragalactic Database (NED). Inclination angles are taken from the papers listed below the table. Distances are the same as in Wilson et al. (2020), except for NGC 3627. We use the distance for NGC 3627 taken from Jimenez-Donaire et al. (2019) for consistency when comparing with the EMPIRE data. 100
3.2 Relevant characteristics of the galaxies in this sample, including the presence/absence of an AGN, bar, or interaction with another galaxy. These classifications are taken from NED. 104
3.3 Observational quantities (top panel) compared to model inputs and outputs (bottom panel). We fix $T_{\mathrm{kin}} = 45$ K, $b = 0.4$, and $\beta \to \infty$ in this analysis, and we model over the observed ranges of Σ_{mol} and σ_{v}. Quantities with the subscript 'grid' are input from the grid shown in Fig. 3.1. 114

4.1 Observational quantities (top panel) compared to model inputs and outputs (bottom panel). We fix $b = 0.4$, and $\beta \to \infty$ in this analysis, and we model over the observed ranges of Σ_{mol} and σ_{v}. 155

4.2 Fit coefficients and $1-\sigma$ confidence intervals. They are ordered from their appearance in each equation from left to right. 161
4.3 Fit coefficients and $1-\sigma$ confidence intervals.. They are ordered from their appearance in each equation from left to right. 167
4.4 The results of the calibrations applied to the data. Average values are shown for each galaxy. Units of conversion factors are $\mathrm{M_\odot\,(K\,km\,s^{-1}\,pc^2)^{-1}}$ 170

Abbreviations

ALMA	Atacama large millimeter/sub-millimeter array
AGN	Active galactic nucleus (nuclei)
CMZ	Central molecular zone
CNM	Cold neutral medium
FUV	Far ultraviolet
FWHM	Full width at half maximum
GMC	Giant molecular cloud
HIM	Hot Intercloud Medium
IR	Infrared
ISM	Interstellar medium
KS	Kennicutt-Schmidt
LN	Lognormal
LOS	Line of sight
LTE	Local thermodynamic equilibrium
MC	Molecular cloud
MFF	Multi free-fall
n**-PDF**	Volumetric gas density PDF
N**-PDF**	Column gas density PDF
PDF	Probability distribution function
PDR	Photon dominated region
PL	Powerlaw
RC	Radio continuum
SED	Spectral energy distribution
SFE	Star formation efficiency
SFF	Single free-fall
SFR	Star formation rate
SGMC	Super giant molecular complex
TIR	Total infrared
(U)LIRG	(Ultra) luminous infrared galaxy
ULX	Ultraluminous X-ray

UV	Ultraviolet
WIM	Warm ionized medium
WNM	Warm neutral medium
XDR	X-ray dominated region

Co-authorship

Chapters 2, 3, and 4 of this thesis contain original scientific research written by myself, Ashley R. Bemis. Chapter 2 has been published as a peer-reviewed journal article in the Astronomical Journal. The citation for this work is: Bemis A.R., Wilson C.D., 2019, AJ, Volume 157, Issue 3, pp. 131-148. This work was co-authored with my supervisor, Dr. Christine Wilson. Chapter 3 is in preparation and will be submitted to a peer-reviewed journal. The author list for this work is *Bemis A.R., Wilson C.D.*. This work was co-authored with my supervisor, Dr. Christine Wilson. Chapter 4 is in preparation and will be submitted to a peer-reviewed journal. The author list for this work is *Bemis A.R., Wilson C.D.*. This work was co-authored with my supervisor, Dr. Christine Wilson.

1 | Introduction

1.1 Galaxies

Galaxies are the primary sites of star formation in the Universe, and are complex systems comprised of varying amounts of gas, dust, stars, and dark matter. Their morphologies vary, with non-interacting systems spanning the Hubble tuning fork (Hubble, 1926). These galaxies range from early-type elliptical (E) to late-type spiral (S) and barred spiral (SB) systems. The Hubble classification has been extended to the Hubble - de Vaucouleurs Galaxy Morphology Diagram which also includes irregular (Ir) and dwarf spheroidal (dSph) galaxies, and includes a classification of late-type galaxies (SAB) intermediate between barred (SB) and unbarred (SA, formerly S). A diversity of galaxies clearly exists in the Universe, and can exist in diverse environments such as galaxy groups and clusters.

Groups, in particular, are home to some of the most spectacular events in our Universe, galaxy mergers, which occur when two or more systems interact and eventually coalesce into one. A famous early classification of the merger process is the Toomre sequence (Toomre and Toomre, 1972), a sample of interacting disk galaxies with apparent tidal tails. The study by Toomre and Toomre (1972) provided a physical explanation for the bridges and tails seen around some galaxies, and framed them as a result of tidal interactions between multiple systems. This work by Toomre and Toomre gave context to the many interacting galaxies identified in the earlier study by Vorontsov-Velyaminov (1959), which found hundreds of interacting systems. This work was later extended to include galaxies found by Arp in the Palomar Sky Atlas, further increasing the number of identified mergers to ~ 1500. This number continues to grow with citizen science initiatives such as

Galaxy Zoo (Lintott et al., 2008). It is clear this phenomenon is not rare in the Universe, and is an important part of the evolution of galaxies.

Studies have estimated that between $5-15\%$ of galaxies are, or have, merged in the Universe of the last $8-9$ billion years ($z < 1.5$, Lotz et al. 2011). The kind of merger at the focus of the Toomre sequence is a major merger, when two or more galaxies of comparable mass (within a factor of 3 of each other) interact with one another. These mergers are relatively rare (3 times less common, Lotz et al. 2011) compared to minor mergers, which involve galaxies with significant differences in mass. The Toomre sequence also focuses on gas-rich systems which have an abundance of fuel for star formation. These types of mergers are ideal for studying starburst phenomena, and for understanding the role of galaxy environment on the star formation process. They also evolve into (Ultra-) Luminous Infrared Galaxies / (U)LIRGs, galaxies that are incredibly luminous in the infrared due to their abundance of dust, gas, and star formation.

The work in this thesis takes advantage of archival data of a number of galaxy types, including two merging systems that fall into the early and intermediate stages along the Toomre sequence, NGC 4038/9 and NGC 3256. NGC 3256 is a LIRG, while NGC 4038/9 is predicted to evolve into one. Also included for comparison is the 2nd nearest bright ULIRG, IRAS 13120-2422, and the centers of several disk galaxies, some of which include molecular bars (NGC 3627, M82), or circumnuclear disks (Circinus, NGC 3351). The center of NGC 7469, another interacting LIRG, is also included in this study. These systems are complex, gas-rich galaxies that do not fit clearly onto the Hubble sequence, but are home to turbulent environments that are important to our understanding of star formation.

In the following sections I review the major components of spiral galaxies, which are the progenitors of LIRGs and ULIRGs. I describe the phases of the interstellar medium (ISM), with an emphasis on its molecular component since the majority of my work focuses on this specific phase of ISM. I review the basics of excitation, radiative transfer, and mass conversion factors of the CO and HCN $J = 1 \rightarrow 0$ transitions to provide context for interpretation of these transitions. I also review the information we can gather from velocity dispersions of the CO transition, including a discussion on cloud dynamics and the major uncertainties that remain (cf. Heyer and Dame, 2015). Finally, I present gravoturbulent theories that aim to capture the physics that sets the gas density Probability Distribution Functions (Burkhart, 2018; Federrath and Klessen, 2012; Hennebelle and Chabrier, 2011; Krumholz and McKee, 2005; Padoan and Nordlund, 2011) and their connection to star formation and the Kennicutt-Schmidt relationship. Throughout this introduction I will make reference to observational facilities that are relevant for studying these different phases of the ISM.

1.1.1 A Spiral Galaxy

This work focuses on galaxies outside of the Local Group that are still considered nearby ($z < 0.1$), but I turn to our home Galaxy, the Milky Way, as our most detailed example of a spiral galaxy. The Milky Way resides in the Local Group, home to more than 40 galaxies in total (e.g. McConnachie, 2012), most of which are dwarf galaxies. There are currently no major mergers in the Local Group, but the nearby large spiral galaxy, M31, is a system that the Milky Way will eventually merge with in ~ 5 billion years (e.g. Sohn, Anderson, and van der Marel, 2012; van der Marel et al., 2012), and so even our home has a connection with galaxy mergers. I will describe the ISM of the Milky Way in the following paragraphs. The interstellar media of other galaxies contain the same components, although their relative fractions, masses, and physical properties can be different.

The basic structure of spiral galaxies contains several distinct components, including a disk, a bulge, a stellar halo, and a massive dark matter halo. For context, the Milky Way is an Sbc spiral galaxy (Binney and Tremaine, 2008) that contains a total mass of $4.0 - 5.8 \times 10^{11}$ $M_{\odot}$ within a radius of $r = 125$ kpc (Eadie and Harris, 2016). Each galaxy has a dark matter halo that dominates its mass and extends far beyond its luminous matter. It is estimated that the Milky Way's halo has a total mass of $M \sim 10^{12}$ $M_{\odot}$ (e.g. Dehnen, McLaughlin, and Sachania, 2006). These halos are theorized to be ellipsoidal in shape, with entrally concentrated density profiles (Moore et al., 1999; Navarro, Frenk, and White, 1996; Stadel et al., 2009). Within the dark matter halo is a smaller baryonic halo that contain globular clusters, ejected stars, and gas from the Intergalactic Medium (IGM), as well as gas ejected from energetic supernovae explosions. Dwarf galaxies also orbit around the Milky Way within its sphere of influence and dark matter halo.

Also enclosed within the dark matter halo is the Milky Way disk, which is comprised of a thin and thick disk that contain stellar and gas components. The density of stars in the thin and thick disks can be described by flattened elliptical profiles, with distinct characteristic radii and scale heights, given by Binney and Tremaine (2008):

$$\rho(R, z) = \rho(R, 0)e^{-|z|/z_d(R)} \tag{1.1}$$

where $z_d(R)$ is scale height at the characteristic radius, R, and ρ is the stellar density. These disks are roughly divided by stellar age, with the thin disk containing a younger population of stars than the thick disk. The thin disk has a characteristic scale height of $z_d \sim 300$ pc, while the thick disk has $z_d \sim 1$ kpc (Bland-Hawthorn and Gerhard, 2016). A combination of these profiles provides a more-accurate representation of the total stellar density distribution, which has a characteristic radius of $R_d = 2.5$ kpc and a scale height of $R \sim 300$ pc (Kent, Dame, and Fazio, 1991; López-Corredoira et al., 2002; McMillan, 2011; Rix and Bovy, 2013). The actual visible extent of the luminous matter in the disk potentially extends out to ~ 20 kpc. The total mass in the stellar disk is only a fraction of the halo mass, at $M \sim 5 \times 10^{10}$ M$_\odot$ (e.g. Licquia and Newman, 2015). The surface brightness of the Milky Way also likely follows an exponential profile, as observed in other spiral galaxies, which is described by a Sérsic profile with $n = 1$:

$$I(R) = I_e \mathrm{exp}\left\{-b_n\left[\left(\frac{R}{R_e}\right)^{1/n} - 1\right]\right\} \tag{1.2}$$

where I_e is the intensity at the effective radius, R_e, which contains half of the total luminosity, and b_n is a prefactor depending on the index n. R_e in the Milky Way is estimated to be $\sim 2-3$ kpc, with the total mass-to-light ratio of the Milky Way then given by $\Upsilon \sim 2.5$ (Binney and Tremaine, 2008) up to a scale height of ~ 1.1 kpc.

Within the disk is the Interstellar Medium, which itself contains only a fraction of the mass of stars in the disk, $M \sim 10^9 - 10^{10}$ M$_\odot$ (Heyer and Dame, 2015; Kalberla and Kerp, 2009). This is comprised primarily of atomic (HI) and molecular (H_2) hydrogen, which serves as the fuel for star formation. The disk contains several distinct arms, and these spiral patterns contain molecular clouds, the main sites of star formation in the Milky Way. In more disturbed systems such as mergers, these spiral patterns become distorted, and are eventually destroyed completely. Spiral features can be observed in the intermediate stages of merging, but they may be due to tidal interactions rather than relics of their progenitor disks. I defer a more thorough discussion of the ISM to the next section.

The Milky Way also contains a triaxial central bulge (also referred to as a stellar bar) that contains an older population of stars than those in the disk, and is $\lesssim 1 \times 10^{10}$ $M_\odot$ in mass (e.g. Licquia and Newman, 2015). Within the bulge is the Central Molecular Zone (CMZ), the inner 500 pc of the Milky Way, which is fed by a molecular bar or stream of gas that is aligned with the elongated bulge of the Milky Way (e.g. Kruijssen et al., 2014). The CMZ is plentiful in dense molecular gas ($n > 10^4$ cm^{-3}) and contains clouds with low or non-existant levels of star formation compared to their abundance of dense gas (e.g. Kauffmann et al., 2017b; Kruijssen et al., 2014). This makes the CMZ an interesting comparison to other galaxy centers, and perhaps some nuclear regions within mergers (cf. Bemis and Wilson, 2019).

1.1.2 Starbursts and (U)LIRGs

Several of the galaxies studied in this work are Luminous Infrared Galaxies (LIRGs) and will eventually go on to become Ultra-Luminous Infrared Galaxies (ULIRGs). These systems are named after their bright Infrared (IR) luminosities $L_{\rm IR} > 10^{11}$ $L_\odot$, and are the most IR-luminous objects in the nearby Universe ($z < 0.3$, Sanders and Mirabel 1996). (U)LIRGs attain their IR luminosity through powerful starbursts and Active Galactic Nuclei (AGN) activity. This strong activity is a result of the funneling of gas and dust from the progenitor galaxies towards the large gravitational potential of their nuclei. These objects are molecular-gas dominated (Mirabel and Sanders, 1989) and exhibit luminous high-J CO transitions that indicate hotter temperatures ($\sim 60-90$ K) and denser gas ($n_{\rm H_2} \sim 10^{5-7}$ cm^{-3}), (Braine and Combes, 1993; Devereux et al., 1994; Radford, Solomon, and Downes, 1991; Rigopoulou et al., 1996; Sanders et al., 1990). They are also relatively bright in dense gas emission lines such as HCN (cf. Sanders et al., 1990).

Gas-rich mergers are the progenitors of the brightest ULIRGs ($L_{\rm IR} > 10^{12}$ $L_\odot$) associated with coalescence of nuclei of the progenitor galaxies and have centrally-concentrated molecular gas (Sanders and Mirabel, 1996). Below $L_{\rm IR} \sim 10^{12}$ $L_\odot$, LIRGs are primarily gas-rich spirals that are instead bright in the IR primarily due to star formation activity. The majority of merger-based LIRGs occur in groups, and are relatively isolated, gas-rich galaxies. Although LIRGs may be produced in clusters, they appear to be relatively rare.

Mergers and (U)LIRGs are very different from disk galaxies. They appear to have different gas conditions, as well as enhanced star formation activity. (U)LIRGs are also very turbulent systems, and studies of these galaxies will put important constraints on turbulent models of star formation.

1.2 Phases of the ISM

The ISM of our Galaxy and of external galaxies holds key information on the star formation process. It is comprised of multiple phases of gas that each have a role in eventually feeding the stars that form from denser, molecular clumps. Characteristic densities and temperatures of these phases depend on the interchange of energy between different heating and cooling processes, as well as the physics governing its dynamics. I briefly characterize the ionized and neutral phases of the Milky Way's ISM in the following subsections, using it as a template for other disk galaxies. Molecular Clouds and related topics are discussed in a separate section.

Ionized Gas

The most diffuse component of the ISM is the hot gas referred to as the Hot Intercloud Medium (HIM) or coronal gas within the Milky Way. This gas is primarily ionized hydrogen and reaches temperatures $T \sim 10^6$ K and low densities $n \sim 10^{-3}$ cm^{-3} (Tielens, 2005). It has the largest volumetric filling fraction (the fraction of three dimensional space that it inhabits) of the Milky Way ISM, although the exact value is uncertain, but may be $\sim 50\%$ (Tielens, 2005). It reaches a scale height of $z_d \sim 3$ kpc and is continuously heated by stellar winds from hot OB stars and energetic supernova explosions. This gas emits a continuum of bremmstrahlung emission across the X-ray and Ultraviolet range (UV, from $\lambda \sim 1 - 100$ nm), and is superimposed with emission from hot supernova remnants. There are a number of emission lines at these wavelengths from various atomic species that have gone through the process of photodissociation. To study the coronal gas of the Milky

Way, one must then turn to the ultraviolet portion of electromagnetic spectrum. Due to the opacity of the atmosphere at these wavelengths, UV emission and absorption lines must be studied from space, using telescopes with UV capabilities such as the Galaxy Evolution Explorer (GALEX) and the Hubble Space Telescope (HST).

At lower temperatures ($T \gtrsim 10^3$ K), Warm Ionized Medium (WIM) is comprised primarily of ionized hydrogen, and has a density $n \sim 10^{-1}$ cm^{-3} and filling fraction $\sim 20-30\%$ (Tielens, 2005). This is a nearly fully-ionized, diffuse component of gas that contains the majority of the ionized gas mass ($\sim 10^9$ M$_\odot$) and extends to a scale height of ~1 kpc (Tielens, 2005). The WIM can be observed in a number of ways, including UV and optical absorption lines and Hα, which is a recombination line of hydrogen in the visible portion of the electromagnetic spectrum ($n = 3 \rightarrow 2$ at 656.28 nm). While the ionized gas dominates the volume of the ISM, it is too hot to immediately form stars. This gas must therefore go through significant cooling before it becomes available as fuel for star formation. Before it becomes molecular gas, it transitions to the neutral media of our ISM, which we discuss next.

Neutral Gas

The neutral medium is comprised of warm and cold phases, the Warm Neutral Medium (WNM) and the Cold Neutral Medium (CNM), respectively. These phases (cf. Tielens, 2005) are configured separately into warm intercloud gas (WNM) with $T \gtrsim 10^3$ K, $n \sim 10^{-1}$ cm^{-3} and diffuse clouds (CNM) with $T \lesssim 100$ K, $n \sim 10-100$ cm^{-3}. The WNM has a filling fraction similar to the WIM at $\sim 30\%$, but the CNM comprises a much smaller volume in the ISM at $\sim 1\%$ (Tielens, 2005). This neutral gas can only be observed directly using the 21-cm hyperfine line in the microwave regime of the electromagnetic spectrum, produced by the spin flip of a hydrogen atom's electron. This line can be observed from the ground with telescopes such as the Very Large Array (VLA), Arecibo Observatory, and the forthcoming Square Kilometer Array (SKA).

The most important heating mechanism for diffuse atomic clouds in the CNM is photoelectric heating, which occurs when a dust grain absorbs FUV radiation, and an electron or electrons become excited enough to leave the grain (Draine, 2010;

Tielens, 2005). These FUV photons come primarily from early-type stars: hot OB and A stars. The second most important heating mechanism is cosmic-ray heating, followed by CI photoionization, and X-ray ionization (Tielens, 2005). Heating of the warm intercloud gas ($T \gtrsim 1000$ K) is instead dominated by cosmic rays and X-rays at lower gas densities, and the photoelectric effect at high densities. Orders of magnitude below this are turbulent heating and CI photoionization (Tielens, 2005).

Molecular clouds eventually condense out of the atomic gas in the CNM once the atomic gas sufficiently cools. The most important cooling mechanisms of the CNM are fine structure transitions, of which the [CII] 158 μm transition is the most important, and then [OI] 63 μm (Tielens, 2005).

1.3 Molecular Clouds

Embedded within atomic envelopes are molecular clouds (MCs, Hennebelle and Falgarone 2012), which comprise a small volume of the ISM in the Milky Way ($\sim 0.05\%$, Tielens 2005). MCs are colder than the CNM at $T \sim 10$ K, with densities in excess of ($n \sim 10^2$ cm^{-3}), and are comprised primarily of molecular hydrogen (Black and van Dishoeck, 1987; Field, Somerville, and Dressler, 1966; Shull and Beckwith, 1982). Molecular clouds are the main sites of star formation in the Milky Way and other galaxies, and their masses and kinematics contain valuable information on the initial conditions of star formation.

Observations of MCs in the Milky Way reveal a complex, hierarchical structure (Heyer and Dame, 2015; Rosolowsky et al., 2008; Scalo, 1985). Denser ($n > 10^4$ cm^{-3}) associations of gas such as clumps or filaments (André, 2017) are embedded within more diffuse molecular envelopes $n \sim 10^2 - 10^3$ cm^{-3}, and within these clumps are smaller cores that go on to form individual stellar clusters (Goldsmith, Snell, and Lis, 1987; McKee and Ostriker, 2007). MCs can also be further embedded in Giant Molecular Complexes (Heyer and Dame, 2015; Vogel, Kulkarni, and Scoville, 1988). For example, in NGC 4038/9, the famous Overlap region is a highly-molecular gas-rich feature that includes several notable Giant Molecular Complexes (Wilson et al., 2003).

The main heating mechanism of molecular clouds is cosmic rays, which are able to penetrate the denser gas of these objects (Tielens, 2005). This mechanism remains the dominant heating source until higher gas densities ($n \gtrsim 10^{4-5}$ cm^{-3}), where dust-gas heating becomes important, and at even higher densities, gravitational heating may take over (Tielens, 2005). Other heating mechanisms include turbulent heating, and ambipolar diffusion. In some cases, turbulent heating may be more significant than cosmic ray heating if the level of turbulence is high enough (cf. Ao et al., 2013). Cooling in molecular clouds is a combination of dust-gas interactions and molecular line transitions (Tielens, 2005).

1.3.1 Observations of Molecular Clouds

MCs are primarily studied through molecular line emission in the millimeter and submillimeter region of the electromagnetic spectrum. There are numerous facilities around the world that cover this range of wavelengths. The most prominent interferometric facility is the Atacama Large Millimeter/sub-millimeter Array (ALMA[1]), and the data used in this thesis come primarily from the public archive of this facility. ALMA is a state-of-the art interferometric array with sixty-six antennas. Fifty-four of these are 12-meter diameter dishes, and twelve are 7-meter diameter dishes which provides sensitivity to a large range of scales of astrophysical phenomena. ALMA can reach milli-arcsecond resolution in its most extended configuration. ALMA has eight operational receivers that span the high-frequency end of the radio continuum from $\sim 80 - 900$ GHz. Data used in this thesis come primarily from band three, which covers the HCN, HCO^+, HNC $J = 1-0$ transitions at ~ 90 GHz, and the CO $J = 1-0$ transition at 115 GHz. Data span a number of observing cycles which each had different capabilities and various numbers of antennas in use.

Observations of molecular lines are essential for providing information on the ISM of the Milky Way and external galaxies. Their luminosity provides information on the mass that they trace, and their linewidths give insight into the dynamics of the gas. Observations are limited to transitions of molecules heavier than molecular hydrogen due to the high temperatures required to excite H_2. The

[1]https://almascience.eso.org/documents-and-tools/cycle8/alma-technical-handbook

most commonly-used molecular gas tracer is carbon monoxide, ^{12}CO, alongside its isotopologues ^{13}CO and C^{18}O.[2] CO is one of the most abundant molecules relative to H_2, with an abundance of $x_{\rm CO} \sim 10^{-4}$ relative to H_2 in the Milky Way (Heyer and Dame, 2015). Due to its relatively high abundance, it is one of the brightest molecular gas tracers available to astronomers. Its rotational $J = 1 \rightarrow 0$ transition at 115 GHz has therefore become the primary observational tool for estimating the molecular gas mass and gas surface density in external galaxies and is commonly used in the Milky Way. It is used as a tracer of the total molecular gas content in galaxies, under the assumption that its emission extends over the extent of H_2 (e.g. Bolatto, Wolfire, and Leroy, 2013).

Other molecular gas tracers that are important for studies of molecular clouds include those with sensitivity to denser gas. These tracers include molecular transitions from HCN, HCO^+, and HNC, that are used this in work, and that have moderate ($n \sim 10^3$ cm^{-3}) effective excitation densities (Shirley, 2015), although these transitions were historically believed to be primarily tracing denser gas ($n > 10^4$ cm^{-3}). Within the Milky Way, N_2H^+ is better at tracing gas $n > 10^4$ cm^{-3} than the most common extragalactic observable of dense gas, HCN (Kauffmann et al., 2017a). HCN emission extends to moderate densities which leads to overestimates of the dense gas mass, while N_2H^+ is primarily in high-extinction regions (Kauffmann et al., 2017a). However, HCN remains an important observational tool for extraglactic studies due to its brightness relative to other molecular gas tracers. Much of the work in this thesis focuses on comparisons between CO transitions and HCN transitions, which when combined can provide estimates of the fraction of gas in moderate or dense phases.

1.3.2 Interpreting the Luminosity of Molecular Lines

To derive information from molecular lines, we must understand the excitation of the transitions that we are observing *apriori*. Optical depth is another important factor to consider when assessing molecular line observations, and higher optical depths coincide with higher attenuation of emission throughout the molecular medium. And finally, the abundance of a molecule relative to H_2 plays a role in

[2] When we refer to CO on its own, we are referring to ^{12}CO.

setting the optical depth in addition to excitation. All of these factors must be considered when interpreting molecular emission.

Abundance

The abundance of molecules in the ISM of galaxies depends on the balance of their formation rates with their destruction rates, in addition to the overall availability of their individual atoms (characterized by metallicity). There are a number of processes that can lead to the formation of a molecule, that can generally be divided into gas-phase reactions and reactions that occur on the surface of dust grains (Draine, 2010; Tielens, 2005). Gas phase reactions often involve complex chemical networks with multiple paths leading to the same molecule, although there are often bottleneck reactions in these networks that place importance on specific intermediate steps. Observations of Milky Way clouds reveal an average HCN abundance relative to H_2 $x_{\mathrm{HCN}} \sim 10^{-8}$ (Blake et al., 1987; Marr, Wright, and Backer, 1993; Nyman, 1983; Vogel and Welch, 1983).

The formation of molecular hydrogen in the ISM is primarily via dust grain reactions, since gas phase reactions leading to the formation of H_2 are relatively slow (Draine, 2010; Tielens, 2005). H_2 can easily be destroyed through FUV heating, and so H_2 must be sufficiently self-shielded before it can accumulate. Formation itself primarily occurs on dust grains, where Hydrogen atoms become adsorbed (or physisorbed) onto the surface of the grain and migrate around the surface of the grain until they finally meet another H atom. The formation energy of H_2 itself is enough to then eject it back into the gas phase.

The formation of CO depends on complex carbon and oxygen chemical networks. CO is formed in the gas phase, and must also form in regions where molecular gas is well-shielded. CO formation depends on the formation of H_3^+, which initiates the chain of chemical reactions that eventually lead to CO (Tielens, 2005). H_3^+ is formed via cosmic-ray ionization of H_2. H_3^+ then reacts with atomic Oxygen to form OH^+, and finishes via reactions with C^+, CO^+, HCO^+, and finally leads to CO (Glover et al., 2010; Liszt, 2007). We note that there are multiple pathways for these molecules to form.

Different heating sources also play a significant role in setting the abundance of molecules in the ISM. In the turbulent sources that we are interested in, mechanical heating may be of particular importance. As Kazandjian et al. (2012) show, the abundance of CO may be reduced in the presence of mechanical heating. Kazandjian et al. (2012) find that for a starburst with a star formation rate of SFR = 50 $M_\odot$ yr^{-1}, $n \sim 10^4$ cm^{-3}, and an interstellar radiation field with $G_0 \sim 10^3$ in Habing units ($= 1.2 \times 10^{-4}$ erg cm^{-2} s^{-1} sr^{-1}), the mechanical heating rate will be $\Gamma_{\rm mech} \sim 10^{-18}$ erg cm^{-3} s^{-1}, which would reduce the CO abundance by a factor of ~ 2 as CO becomes destroyed through ion-neutral reactions. Contrary to this, the HCN abundance is enhanced with higher $\Gamma_{\rm mech}$ via neutral-neutral reactions by a factor of $\sim 2-3$ (Kazandjian et al., 2012, 2015). In particular, the abundance of HCN is enhanced in the presence of mechanical heating via the exchange reaction (Kazandjian et al., 2012, 2015; Loenen et al., 2008; Meijerink et al., 2011):

$$\mathrm{H + HNC} \Longleftrightarrow \mathrm{H + HCN} \tag{1.3}$$

which becomes unbalanced in the presence of mechanical heating, i.e. more HCN is produced in place of HNC. Variations in abundance will have a direct effect on the relative emissivities of HCN and CO;however abundance continues to be an major uncertainty in studies of molecular gas tracers.

Excitation

The molecular transitions that we observe carry information on gas density, temperature, and optical depth. This makes them valuable tools for determining the conditions within molecular clouds, but this also requires additional information if we want to determine both gas density and gas temperature. The dependence of molecular transitions on the physical conditions of the gas is captured by the excitation temperature, $T_{\rm ex}$, and is defined by the Boltzmann equation. The interdependence of excitation on both density and temperature for a simple, two-level system without radiative trapping is demonstrated via (Tielens, Eq. 2.35 rearranged):

$$T_{\rm ex} = \frac{T_{\rm kin}}{1 + \frac{k\,T_{\rm kin}}{E_{ul}} \ln\left(1 + \frac{n_{\rm crit}}{n}\right)} \tag{1.4}$$

where n is the density, T_{kin} is the kinetic temperature, n_{crit} is the density at which collisional de-excitations equal radiative de-excitations of the transition of interest, and E_{ul} is the energy of the rotational transition from $J = u \rightarrow l$. To determine both T_{kin} and n from molecular transitions alone, multiple transitions then need to be observed with some simplifying assumptions. A common assumption is that T_{ex} is constant across all transitions and equivalent to the kinetic temperature (Local Thermodynamic Equilibrium, LTE), and then it is a simple problem of solving a system of equations. However, this is not the case in general, and T_{ex} decreases (or sometimes increases) towards higher J values.

Optical Depth

Optical depth also plays a significant role in setting the intensity of the transitions we observe, and it also depends on the underlying excitation of the gas, in addition to linewidth (Draine, 2010). Narayanan and Krumholz (2014) find that the optical depth of the CO $J = 1 \rightarrow 0$ line decreases at higher Σ_{SFR} because 1. the low-J CO lines are already in LTE at low Σ_{SFR}, and 2. CO linewidths are higher for larger Σ_{SFR}. The linewidth of HCN is also likely to increase with higher Σ_{SFR}, but it is uncertain is whether this line is truly in LTE at low Σ_{SFR}. Optical depth estimates of HCN are limited to only a few systems and range from $\sim 5-8$ (Jiménez-Donaire et al., 2017), assuming the filling fraction of HCN is twice that of $H^{13}CN$. However, the detections in the sample of Jiménez-Donaire et al. (2017) are primarily in the centers of galaxies with ongoing or recent starburst activity.

1.3.3 Molecular Cloud Dynamics

Spectroscopy has the advantage of providing information on the kinematics of gas through the line profiles of the molecular transitions. Studies of CO velocity dispersions, σ_{v}, resulted in the seminal work by Larson (1981), which shows that there is a correlation between σ_{v} and the size (L) of MCs, such that $\sigma_{\mathrm{v}} \propto L^{0.38}$. The inclusion of mass estimates from CO luminosity allowed Larson (1981) to also estimate the mean densities of these clouds and found that molecular clouds are turbulent, the mass surface density of Milky Way clouds appears relatively constant, and that clouds appear to be close to energy equipartition, such that their kinetic energies (E_{kin}) are comparable to their gravitational potentials (E_{grav}). We now know that clouds exist with a broad range of gas mass surface densities (cf Miville-Deschênes, Murray, and Lee, 2017) in the Milky Way and in other galaxies (cf Sun et al., 2018). Bound gas in molecular clouds (in energy equipartition) can be written in terms of the virial parameter, α_{vir}, which takes on a value of $\alpha_{\mathrm{vir}} = 2$. The virial parameter is then given by[3]:

$$\alpha_{\mathrm{vir}} \equiv \frac{2E_{\mathrm{kin}}}{|E_{\mathrm{grav}}|} \tag{1.5}$$

$$\approx \frac{5\sigma_v^2 R}{G\Sigma} \tag{1.6}$$

where Σ is the gas mass surface density, and $R = L/2$. Earlier studies have found that molecular clouds within the Milky Way appear close to virial equilibrium (Heyer et al., 2009; Solomon et al., 1987), on average, consistent with energy equipartition. Recent studies with larger samples show a distribution of measured α_{vir}, with the peak occuring above $\alpha_{\mathrm{vir}} > 1$ (Miville-Deschênes, Murray, and Lee, 2017). As pointed out in previous works, clouds with apparently high α_{vir} must either by confined by external pressure (Bertoldi and McKee, 1992) or be short-lived (Field, Blackman, and Keto, 2011; Hennebelle and Falgarone, 2012; McKee, Li, and Klein, 2010).

There are only a limited number of cases where this particular form of α_{vir} holds (McKee et al. 1993):

1. The internal pressure must exceed the external pressure, $P_{\mathrm{int}}/P_{\mathrm{ext}} >> 1$. If this is not true, the linewidth is increased by external pressures and Equation 1.6 will lead to an overestimate of mass and density for a fixed cloud size.

2. The cloud cannot be super-critically magnetized, such that the mass supported by magnetic pressure is comparable to the cloud mass. This situation would lead to an underestimate of gas mass and density.

Clouds can still be in virial equilibrium in the presence of an external pressure. Field, Blackman, and Keto (2011) find that clouds in the Milky Way appear to

[3]This is assuming a spherical molecular cloud with a constant density profile.

be systematically offset from the trend of virial equilibrium in the $\sigma_{\rm v}^2/R$ vs. Σ parameter space, and argue that molecular clouds are indeed pressure-bound and also virialized. The work of McKee and Zweibel (1992) shows that the true level of virialization will become smaller than the observed value in the presence of magnetic support. They also show that $\alpha_{\rm vir}$ will appear higher in the presence of external pressures that exceed the internal pressure of a cloud, even if the gas is virialized.

A similar way to frame this is through pressure balance, which is most appropriate for clouds in disk galaxies where hydrostatic equilibrium applies to the gas. In pressure balance, the internal pressure of a molecular cloud, $P_{\rm int}$, and support from magnetic pressure, $P_{\rm B} = B^2/8\pi$, balances the external pressure of the ambient ISM, $P_{\rm ext}$, and the gravitational pressure resulting from the cloud's own mass (P_G, Utomo et al. 2015):

$$P_{\rm int} + P_{\rm B} = P_{\rm ext} + P_G \tag{1.7}$$

As Utomo et al. (2015) show, the dominant source of internal pressure changes depending on the dynamical state of the cloud. The internal motions of all GMCs are dominated by turbulence, such that $P_{\rm int} \approx P_{\rm turb}$, so that $P_{\rm turb}$ is a useful quantity to constrain observationally. For example, gravitationally bound clouds in the absence of external pressure may have $P_{\rm int} \approx P_G$, and observations will show $P_{\rm turb} \approx P_{\rm G}$. In the case that a cloud is bound by external pressure, the internal turbulent pressure will instead scale with the external pressure, $P_{\rm turb} \approx P_{\rm ext}$, and will exceed $P_{\rm G}$. Krumholz, Dekel, and McKee (2012)m propose that clouds like those in the Milky Way and nearby galaxies are confined by their own gravity, such that $P_{\rm turb} \approx P_G$, while clouds in galaxies with denser environments such as starbursts and high$-z$ disks may be dynamically tied to large-scale motions such as the galactic rotation period. More recent work by Sun et al. (2020) shows that clouds in nearby disk galaxies are actually over-pressurized relative to their own gravitational pressure, which instead suggests that these clouds are pressure-confined, and they exist inside clumpy interstellar media. [4]

[4]t is not turbulent pressure that is confining. Instead, observational estimates of turbulent pressure are a measure of the internal pressure of a cloud, which may also reflect a confining, external pressure.

1.3.4 Molecular Transitions and Mass Conversion Factors

One of the most common applications of the CO $J = 1 \rightarrow 0$ transition is to determine the total molecular gas mass in a CO-emitting medium (cf. Bolatto, Wolfire, and Leroy, 2013). Estimates of the mass of the dense component of gas ($n(\mathrm{H_2}) > 10^4$ cm) are measured separately using much weaker emitters, such as HCN, $\mathrm{HCO^+}$, and CS (Gao and Solomon, 2004a,b). CO is found to be optically thick with $\tau \gg 1$, such that its luminosity is mainly tracing the gas surface density of clouds, $\Sigma_{\mathrm{mol}} \approx \alpha_{\mathrm{CO}} I_{\mathrm{CO}}$, and α_{CO} is the typical mass per unit intensity of the CO transition. This is easily seen when adopting the assumption of virial equilibrium, and considering that CO $J = 1 \rightarrow 0$ transition is in the Rayleigh-Jeans regime of the electromagnetic spectrum. The observed intensity of a transition, I_{mol}, is related to the antenna temperature, T_A, measured in our observations. In the Rayleigh-Jeans regime where $h\nu \ll k T_A$, the antenna temperature is approximately the brightness temperature, so that $I_{\mathrm{mol}} \propto T_{\mathrm{B}}$. If a cloud is also in virial equilibrium with $\alpha_{\mathrm{vir}} = 1$, its linewidth will trace the mass of the cloud such that $\Delta \mathrm{v} = \sqrt{G\Sigma_{\mathrm{mol}} R/5}$ (see previous section on dynamics, Draine 2010; Tielens 2005), which provides the needed connection between gas mass surface density and the observed flux.

Furthermore, if the gas is in Local Thermodynamic Equilibrium (LTE), then T_B is equivalent to the gas kinetic temperature, and the molecular conversion factor for an optically-thick transition of a cloud in virial equilibrium in the Rayleigh-Jeans regime can be written as (Tielens, 2005):

$$\alpha_{\mathrm{mol}} \approx \frac{n_{\mathrm{H_2}}^{1/2}}{T_{\mathrm{kin}}} \left(\frac{4\,\mu m_{\mathrm{H}}}{3\pi\, G} \right)^{1/2} \tag{1.8}$$

where m_{H} is the mass of Hydrogen, μ is set by the mean molecular weight of the gas, and G is the gravitational constant. An appropriate density here would be the average density of the gas that the molecular transition of interest is sensitive to, which has historically been characterized by the critical density of a transition, n_{crit}.

A way to estimate this density is to consider a simple, two-level atom, that only undergoes the $J = 1 \rightarrow 0$ transition. The critical density of this transition is given by:

$$n_{\text{crit}} = \frac{\beta A_{jk}}{\gamma_{jk}} \tag{1.9}$$

where A_{jk} is the Einstein A coefficient for spontaneous de-excitation, γ_{jk} is the collisional rate of the transition $j \rightarrow k$, and β is the probability a photon will escape in the optically-thick limit, and depends on the geometry of the gas and the underlying optical depth, τ (Draine, 2010; Tielens, 2005). For CO $J = 1 \rightarrow 0$, we have $\log A_{10} = -7.618$ (from the LAMBDA database, Schöier et al. 2005), and the collisional rate of CO is approximately $\gamma_{10} \approx 6 \times 10^{-11} T^{0.2}$ cm^3 s^{-1} (Flower, 2001; Flower and Launay, 1985). To recover the Milky Way value of $\alpha_{\text{CO}} \approx 4.35$ M$_\odot$ (K km s^{-1} pc^2)$^{-1}$ (which includes He), assuming $T_{\text{kin}} = 20$ K, CO would need to be, on average, sensitive to $n_{\text{crit}} \approx 10^3$ cm^{-3}.

Historically, $\alpha_{\text{HCN}} = 10$ M$_\odot$ (K km s^{-1} pc^2)$^{-1}$ has been used (neglecting He, Gao and Solomon 2004a,b) under the same assumptions applied to CO: that this molecular transition is optically thick, and that the gas it traces is in LTE. Under these assumptions, a virialized cloud core with a mean H_2 density $n_{H_2} \sim 3 \times 10^4$ cm^{-3} and brightness temperature $T_{\text{B}} \sim 35$ K (e.g. Radford, Solomon, and Downes, 1991) then has $\alpha_{\text{HCN}} = 10$ M$_\odot$ (K km s^{-1}pc^2)$^{-1}$ (Gao and Solomon, 2004a,b).

In hotter, denser environments of starbursts and (U)LIRGs, the CO conversion factor is 4-5 times lower than the Milky Way value, as originally argued by Downes, Solomon, and Radford (1993). These conditions can lead to subthermal excitation ($T_{\text{ex}} < T_{\text{kin}}$) of CO, which then means our previous assumption that $T_{\text{B}} \approx T_{\text{kin}}$ is no longer valid. Furthermore, these types of galaxies have larger linewidths which can reduce the optical depth of a transition (Bolatto, Wolfire, and Leroy, 2013). Observations of HCN and its isotopologues show that it is only moderately optically-thick in the centers of disk galaxies (Jiménez-Donaire et al., 2017), and subthermal emission is a possiblity for HCN, as well. Shirley (2015) showed that a substantial amount of subthermal emission can contribute to the total observed line flux, and argued for a different metric for estimating gas density associated with a particular molecular transition, the effective excitation density, n_{eff}. This is instead defined as the density at which the emissivity of a transition produces a total line flux of $I_{\text{mol}} = 1$ K km s^{-1}. This definition requires numerical calculations to be determined.

If I assume for the moment that a molecular conversion factor can be determined using a single characteristic density such as $n_{\rm crit}$, it still will have a nonlinear dependence on $T_{\rm ex}$ and τ. This comes from the dependence of $n_{\rm crit}$ on the collisional rate coefficient, which differs from molecule to molecule. For CO $J = 1 \rightarrow 0$, the simple expression given for γ_{10} above is reliable for a range of temperatures (Draine, 2010; Tielens, 2005). For the HCN $J = 1 \rightarrow 0$ transition, the collisional rate coefficient is more complicated than that of CO, and must be derived numerically for accuracy (cf. Dumouchel, Faure, and Lique 2010). Values for collisional rate coefficients of HCN-H_2 similar to those found by Dumouchel, Faure, and Lique (2010) can be roughly reproduced using (see Draine 2010):

$$\gamma_{10} \approx 1.2 \times 10^{-15} \sqrt{\frac{8kT_{\rm kin}}{\pi\mu}} \frac{E_{10}}{T_{\rm kin}} \exp\left(\frac{E_{10}}{T_{\rm kin}}\right) \tag{1.10}$$

$$\approx 7.54 \times 10^{-11} T_{\rm kin}^{-1/2} \exp\left(\frac{-4.25356\ {\rm K}}{T_{\rm kin}}\right) \tag{1.11}$$

and multiplying by a 1.36 scaling factor to compensate for interactions with He, which returns a critical density of:

$$n_{\rm crit}({\rm HCN}_{1-0}) \approx 3.2 \times 10^5 \frac{\langle\beta_{ul}\rangle}{T_{\rm ex}^{-1/2}} \exp\left(\frac{4.25356\ {\rm K}}{T_{\rm ex}}\right) \tag{1.12}$$

The prefactor $\langle\beta_{ul}\rangle$ accounts for radiative trapping that occurs in the presence of high optical depth and is $\langle\beta_{ul}\rangle \approx 1/(1 + 0.5\tau)$ for a spherical cloud of constant density (Draine, 2010). This is approximately the fraction of gas at the surface layer of the cloud for which we can observe emission.

1.4 Emissivity & the Gas Density PDF

Studies of molecular clouds in the Milky Way have decomposed column density maps of molecular clouds into the two-dimensional column density probability distribution function (N-PDF) (cf. Heyer and Dame, 2015; Kainulainen et al., 2009; Kainulainen and Tan, 2013; Lada et al., 2012; Lada, Lombardi, and Alves, 2010; Schneider et al., 2011, 2015). The shape of the $N-$PDF provides insight into the underlying physics of the ISM. Studies have found that the gas density Probability

Distribution Function ($n-$PDF) of the diffuse ($n < 1$ cm^{-3}) component of gas in the Milky Way and M33 follows a lognormal PDF (cf. Berkhuijsen and Fletcher 2008; Hill et al. 2008; Ostriker, Stone, and Gammie 2001; Passot and Vázquez-Semadeni 1998; Tabatabaei et al. 2008), which is consistent with Kolmogorov turbulence (Kolmogorov, 1962). The seminal analytical work by Vazquez-Semadeni (1994) showed that if the turbulent ISM develops a series of isothermal, interacting supersonic shocks, the gas would naturally follow a lognormal PDF (cf. Nordlund and Padoan 1999; Padoan, Jones, and Nordlund 1997; Scalo et al. 1998; Vazquez-Semadeni 1994). In this picture, the shocks amplify each other via a turbulent cascade of energy, and this multiplicative process results in the gas density PDF taking on a lognormal shape (cf. Nordlund and Padoan 1999; Padoan, Jones, and Nordlund 1997; Scalo et al. 1998; Vazquez-Semadeni 1994):

$$p(\rho) = \frac{1}{\rho\sqrt{2\pi\sigma_\rho^2}}\exp\left(-\frac{\left(\ln(\rho) - \frac{\sigma_\rho^2}{2}\right)^2}{2\sigma_\rho^2}\right) \tag{1.13}$$

where σ_ρ^2 is the linear variance.

At the high density end, the shape of the PDF appears to instead follow a power-law (Chen et al., 2018; Froebrich and Rowles, 2010; Kainulainen et al., 2009; Schneider et al., 2015), with some cloud PDFs being almost entirely power-law (cf. Alves, Lombardi, and Lada, 2017; Froebrich and Rowles, 2010; Kainulainen et al., 2009; Lombardi, Alves, and Lada, 2015; Schneider et al., 2013, 2015, 2016). A power-law is predicted for gravitationally-bound or collapsing gas, and has been observed in simulations that develop self-gravitating gas (cf. Ballesteros-Paredes et al. 2011; Burkhart, Stalpes, and Collins 2017; Collins et al. 2012; Padoan et al. 2017; Schneider et al. 2015). Furthermore, this appears to be the gas that is directly connected to star formation (cf. Burkhart, 2018). This suggests that the gas density PDF in a star-forming molecular cloud is likely a combination of shapes, such as a lognormal and power-law, and that the power-law tail is the result of gas becoming self-gravitating. Arguments have been made for a connection between PDF shape and the evolutionary stage of a gas cloud (Ballesteros-Paredes et al., 2011; Kainulainen et al., 2009), such that earlier stages are purely lognormal and evolve to have a power law as more gas collapses and becomes bound in dense, star-forming clumps.

Observed power law tails have a broad range of slopes (cf. Alves, Lombardi, and Lada, 2017; Froebrich and Rowles, 2010; Kainulainen et al., 2009; Lombardi, Alves, and Lada, 2015; Schneider et al., 2013, 2015, 2016), which may be connected to the evolutionary process of a molecular cloud as suggests by Ballesteros-Paredes et al. (2011). The model of (Burkhart, 2018) predicts that the power-law slope will shallow to values $\alpha \sim 1 - 1.5$ in less than a mean freefall time, which is relatively short compared with GMC lifetimes, $\sim 10 - 50$ Myr (cf. Jeffreson and Kruijssen, 2018; Kruijssen et al., 2018). Thus, this piecewise model provides a natural framework for a time-evolving gas density PDF. Stellar feedback may then steepen the power-law slope again (Federrath and Banerjee, 2015; Grudić et al., 2018; Semenov, Kravtsov, and Gnedin, 2017) shortly after star formation begins in the molecular cloud. For more normal star-forming systems where stellar feedback regulates the SFR, gas may move in and out from the power-law tail, which would provide a natural explanation for observed long depletion times (Burkhart and Mocz, 2019).

The PDF shape is also important for observations because it is ultimately connected to the emissivity of a molecular transition. The total emissivity of a transition is defined as (cf. Leroy et al., 2017):

$$\epsilon_{\rm mol} = \frac{I_{\rm mol}}{N_{\rm H_2}} \tag{1.14}$$

where $I_{\rm mol}$ is the total intensity of that transition, and $N_{\rm H_2}$ is the total column of H_2 traced by that transition. A more explicit definition of total emissivity uses the integral of the density-dependent emissivity over the $n-$PDF, $p(n)$:

$$\epsilon_{\rm mol} \approx \frac{1}{N_{\rm H_2}} \int_{n_{\rm min}}^{n_{\rm max}} I_{\rm mol}(n) p(n) {\rm d}n. \tag{1.15}$$

This expression represents a transition $J = u \rightarrow l$ that emits $I_{\rm mol}(n)$ over a range of densities from $n_{\rm min} \rightarrow n_{\rm max}$. Each parcel of gas represented by $p(n)$ then has its own $\tau(n)$ and $T_{\rm ex}(n)$, which can include a significant fraction of subthermal emission occuring below $n_{\rm crit}$ (Shirley, 2015). Recent works (e.g. Leroy et al., 2017) adopt numerical radiative transfer analyses that attempt to characterize molecular transitions over analytical models of $p(n)$, and I show similar work in this thesis.

Turbulent Driving Mechanisms

The width of the $n-$PDF is likely set by a combination of turbulence and magnetic fields. The dependence of PDF width on these physical properties depends on the equation of state of the gas (Federrath and Banerjee, 2015) and the dependence of magnetic fields on gas density (Molina et al., 2012). The type of turbulence present in the gas (whether it is primarily compressive or solenoidal (or a mixture) also has an impact on the shape of the $n-$PDF (cf. Kainulainen and Federrath, 2017; Molina et al., 2012). For simplicity, we give the width of an $n-$PDF under the assumptions that the gas is isothermal and that the magnetic field within molecular clouds is $B \propto n^{1/2}$ (Molina et al., 2012). The linear density variance is given by:

$$\sigma_\rho^2 = b^2 \mathcal{M}^2 \frac{\beta}{\beta + 1} \tag{1.16}$$

where $\mathcal{M}$ is the sonic mach number of the gas, b is the turbulent forcing parameter that denotes the type of turbulent forcing, and β is the ratio of the magnetic pressure to the thermal pressure of the gas. The forcing parameter is $b \approx 1$ for purely compressive modes and $b \approx 0.3$ for purely solenoidal modes (Federrath and Klessen, 2012; Molina et al., 2012). The exact values of b for different driving mechanisms are still being studied, but there is evidence from numerical simulations that even supernovae will have a significant contribution from solenoidal turbulence (Padoan et al., 2016), and that an intermediate value between $b \sim 0.3 - 1$ is likely more appropriate. The study by Kainulainen and Federrath (2017) puts constraints on these parameter in Milky Way clouds and finds $b^2\beta/(\beta+1) = 0.3 \pm 0.06$.

Different turbulent driving mechanisms will result in different modes of turbulence, which can roughly be divided by the level of gas compression they induce (Federrath and Klessen, 2012; Mac Low and Klessen, 2004). Driving mechanisms that likely contain compressive modes of turbulence include expanding supernovae shells (e.g. Balsara et al., 2004; Padoan et al., 2016), expanding HII regions (e.g. Krumholz, Matzner, and McKee, 2006; McKee, 1989), spiral shocks (Elmegreen, 2009), and gravitational contraction (e.g. Hoyle, 1953; Vázquez-Semadeni, Cantó, and Lizano, 1998), which would act to increase the width of the PDF (Federrath and Klessen, 2012). This is of particular interest to starbursting systems whose SFRs are enhanced, since these systems are likely experiencing a higher incidence of supernovae and expanding HII regions. Alternatively, predominantly solenoidal turbulence may arise via less violent processes such as galactic rotation or magnetorotational instabilities (e.g. Piontek and Ostriker, 2004a,b). The level of compression of the gas is therefore linked to the dominant mode of turbulence.

The strength of turbulence also plays a signficant role in moderating the width of the PDF, since $\sigma_\rho^2 \propto \mathcal{M}^2$. As $\mathcal{M}$ increases, the width of the PDF also increases. An increase in $\mathcal{M}$ tends to have a more significant impact on the width of the PDF than an increase in b, since values for supersonic turbulence have $\mathcal{M} > 1$. Depending on the geometry of the magnetic field with respect to compression from a shock front, the slope of the magnetic field (B) - density (ρ) relationship, $B \propto \rho^k$, can range from $0 \leq k \leq 1$ (Molina et al., 2012). In the limit of $k = 0$, gas flows parallel to the magnetic field lines, and there is no gradient of B with density, and Eq. 1.16 reduces to:

$$\sigma_s^2 = \ln(1 + b^2\mathcal{M}^2), \tag{1.17}$$

which is the same as expected in the purely hydrodynamical, isothermal case with no magnetic contribution (Molina et al., 2012). Alternatively, if $k = 1$, B is oriented perpendicular to gas flow, which results in maximum amplification of B as a result of compression. In this extreme case, the effect of the magnetic field on the PDF dominates over turbulence. Molina et al. (2012) consider the intermediate case where there is a mixture of flow and magnetic field geometries, $k \approx 1/2$. This value is consistent with results found in previous simulations of super-Alfvénic turbulence (e.g. Collins et al. 2011; Li et al. 2004) for isothermal gas. Using Zeeman measurements to infer magnetic field strength in Milky Way clouds, Crutcher et al. (2010) find $k \sim 0.65$ for gas densities $> 3 \times 10^3$ cm^{-3}. Therefore, $k = 1/2$ is likely a reasonable estimate for clouds (Molina et al., 2012).

1.5 Molecular Gas and Star Formation

Numerous studies have shown that the star formation in galaxies is closely connected to the total gas content (atomic and molecular components) spanning > 6 orders of magnitude. The physical origin of this scaling is still being explored, with two, distinct interpretations (cf. Kennicutt, 1998). Both interpretations are consistent with power law scalings between the volumetric density of the star formation rate, $\rho_{\rm SFR}$, and the density of gas, ρ, with a an exponent of n. The first is the bottom-up picture (cf. Kennicutt and Evans, 2012; Krumholz and McKee, 2005), and assumes that star formation is locally-regulated. This picture predicts several, distinct regimes of star formation with different, physical origins, and this work (cf. Krumholz, Dekel, and McKee, 2012) suggests that they are separated by (1) the atomic-to-molecular transition and (2) the threshold for 'efficient' star formation, which is associated with the formation of dense structures in molecular clouds. These transitions both have an underlying dependence on the cooling and heating processes of gas. Within this framework, non-linear scalings between the star formation rate surface density ($\Sigma_{\rm SFR}$) and the gas surface density originate from either changes in the timescale for star formation (Krumholz, Dekel, and McKee, 2012), or an increase in gas mass above a particular gas density threshold.

This picture is consistent with the seminal work by Gao and Solomon (2004a,b) who find a linear scaling between the gas mass traced by HCN and the IR luminosity within galaxies, indicating a close dependence of star formation on dense gas. The linear scaling also implies that the density at which HCN is emitting may be close to a universal, average threshold density associated with star formation. Since this seminal work, follow-up studies have since explored this relationship between HCN emission and IR emission in (U)LIRGs (e.g. Garcıa-Burillo et al., 2012; Graciá-Carpio et al., 2008) and at sub-kpc scales (e.g. Bemis and Wilson, 2019; Chen et al., 2015; Gallagher et al., 2018; Usero et al., 2015), and have found deviations from this linear scaling. At sub-kpc scales, deviations from linearity either support varying local thresholds for star formation, or variations in the emissivity of HCN, or both within individual systems. (U)LIRGs instead either have a superlinear relationship or an offset from the relationship of more-normal type galaxies (Garcıa-Burillo et al., 2012; Graciá-Carpio et al., 2008; Usero et al., 2015). Again, this could indicate either variations in star formation or emissivity of HCN. The centers of disk galaxies also appear to be fundamentally different than their disk counterparts (Gallagher et al., 2018), which have bright HCN emission signalling more dense gas, while also appearing to have longer depletion timescales associated with that dense gas.

The second star formation framework is the top-down picture (Kennicutt and Evans, 2012), and instead argues that star formation is connected to the large-scale dynamics of a galaxy in addition to the density of gas (Krumholz and McKee, 2005; Silk, 1997). Transitions between regimes of star formation are then driven by gravitational instabilities in gas disks, rather than cooling and heating processes, and the underlying dynamical process is fundamentally the same in these different regimes. Wilson et al. (2019) explore the second framework in the context of (U)LIRGs, which are predicted to have a Kennicutt-Schmidt power law scaling with an exponent ~ 1.5 in the case of a constant disk scale height, or ~ 2 if the height is set by self-gravity and the velocity dispersion is relatively constant (Elmegreen, 2018). Wilson et al. (2019) focus on $\Sigma_{\rm SFR}$ and the *molecular* gas surface density, since these galaxies are (U)LIRGs and are molecular-gas dominated.

This (Wilson et al., 2019) to the Kennicutt-Schmidt (KS) relationship in these galaxies yields a slope $\sim 1.7-1.8$, which is indeed higher than the slope ~ 1.4 of the KS relationship for galaxies at lower gas surface densities. This fit is shown in Fig. 1.1 on the right, and on the left is a double power law fit to the data. The slope associated with higher gas surface densities in the double power law fit is consistent with $\sim 1.7 - 1.8$. The slope of the lower surface density fit is ~ 1. Elmegreen (2018) argue that scalings between $\Sigma_{\rm SFR}$ and molecular gas surface density should have a slope of ~ 1, which is a result of their emission being fundamentally tied to a characteristic, mean gas density, and that varying thresholds for star formation are a manifestation of these biases in molecular gas tracers, except in the case where molecular gas is the dominant component of the ISM. The work by Bigiel et al. (2008) is consistent with this picture, who found a linear scaling between the star formation rate surface density and the molecular gas surface density as traced by CO $J = 1 - 0$.

Much of the work in this thesis uses gravoturbulent models of star formation

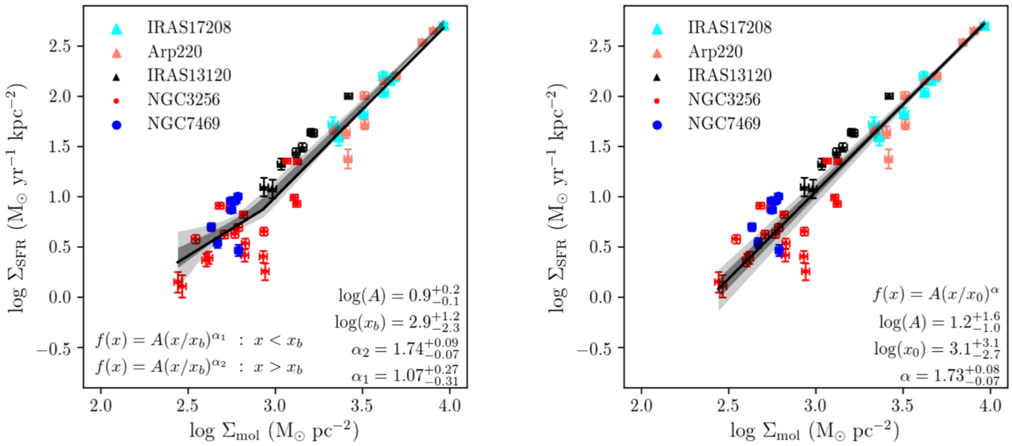

FIGURE 1.1: Figure 1. from Wilson et al. (2019). The Kennicutt-Schmidt relationship is plotted for the five galaxies (color points) and in both panels. *Left:* A double power law fit to the data is shown as the black line with the light and dark gray shaded areas corresponding to the $1-$ and $2-\sigma$ confidence intervals.

(Burkhart, 2018; Federrath and Klessen, 2012; Hennebelle and Falgarone, 2012; Krumholz and McKee, 2005; Padoan and Nordlund, 2011) that are built upon the premise of varying thresholds. These models are successful at reproducing the statistics of column density maps discussed in section 1.4, and are fundamentally tied to the turbulence of the interstellar medium. These models predict the star formation rate per free-fall time, or the efficiency of star formation, $\epsilon_{\rm ff}$, which is the gas mass fraction converted into stars for a free-fall time. This is given via (Burkhart, 2018; Federrath and Klessen, 2012; Hennebelle and Falgarone, 2012; Krumholz and McKee, 2005; Padoan and Nordlund, 2011):

$$\epsilon_{\rm ff} = \epsilon_0 \int_{\rho_{\rm thresh}}^{\infty} \frac{t_{\rm ff}(\rho_0)}{t_{\rm ff}(\rho)} p(\rho) {\rm d}\rho. \tag{1.18}$$

where ϵ_0 is the local efficiency, e.g. due to stellar feedback (Burkhart, 2018), $t_{\rm ff}(\rho_0))$ is the free-fall time at the mean density, ρ_0, and $t_{\rm ff}(\rho))$ is the free-fall time at a general density, ρ. The $\rho-$PDF is represented by $p(\rho)$. These models integrate the gas density PDF above a critical or threshold density associated with star formation, $\rho_{\rm thresh}$, where any gas above $\rho_{\rm thresh}$ is potentially star-forming[5]. Star

[5] We refer to this as the threshold density, rather than critical density, to avoid confusion with the critical density associated with specific molecular transitions discussed earlier.

formation thresholds are described in detail in Chapter 4 of this thesis.

1.5.1 Star Formation Rate Indicators

These dense environments of starbursts and (U)LIRGs are abundant in gas and dust, which enshrouds many regions of star formation. The UV emission from young stars becomes absorbed in the media, making it difficult to use tracers of unobscured star formation to estimate star formation rates (SFRs). Unobscured star formation rate tracers include the UV continuum and Hα emission. This work makes use of two SFR tracers: infrared (IR) and radio continuum (RC) emission. The IR traces obscured star formation through dust emission and the RC is an unobscured tracer that is also unabsorbed by dust due to its long wavelength. Below we briefly outline the basic physics that makes the IR and RC useful tracers of the SFR.

Infrared Emission from Dust

UV emission from regions of star formation can be absorbed and reprocessed by dust in the interstellar medium. This light is re-emitted at longer wavelengths as IR emission, which can then penetrate through regions of dust and gas that UV light cannot. This makes IR emission a useful tracer of the obscured star formation in galaxies, which is more applicable to the galaxies studied in this work (e.g. Kennicutt and Evans, 2012). In this work, we make use of IR emission from the dust Spectral Energy Distribution (SED) in the mid- to far-IR regime, spanning $\lambda \approx 5 - 1000\,\mu$m , to estimate SFRs.

The conversion between the measured luminosity of dust emission and the SFR depends on the stellar population heating the dust, and the timescale over which that population has been heating the dust (cf. Kennicutt and Evans, 2012). Smaller dust grains dominate the emission from $\sim 20 - 60\,\mu$m, which originates in or near young star-forming regions, while emission from larger dust grains dominate at longer wavelengths (Draine, 2003). These larger dust grains are more likely to be in a steady-state of energy balance than their short-wavelength counterparts, indicating that they trace emission of stars existing on longer timescales. Younger populations of stars can have intense radiation fields due to their OB constituents, but these stars are shorter-lived than their lower-luminosity counterparts. As the interstellar radiation field becomes more intense, the peak of the dust SED shifts to shorter wavelengths (Draine, 2010; Siebenmorgen and Krügel, 2007), so that IR emission from longer wavelengths may contribute relatively less to the total SED luminosity in the case of a short-lived starbursts. However, this assumption may not be true in the case of a continuous starburst, and highlights the importance of the star formation history of a galaxy when interpreting SFRs from IR emission at different wavelengths (cf. Kennicutt and Evans, 2012).

The first chapter of this thesis takes advantage of calibrations from Galametz et al. (2013), which aim to capture the connection between SFR and the total IR luminosity spanning $3 - 1100\,\mu$m as predicted by individual IR measurements in various *Herschel* and *Spitzer* bands. Their work applies SED modelling of dust emission to a sample of nearby (< 30 Mpc) galaxies, and from this they produce $L_{\rm IR} - $SFR calibrations using various combinations of *Herschel* and *Spitzer* bands. This then allows observers to compare calibrations combining short- and long-wavelength IR emission across the dust SED to single-wavelength SFR calibrators, such as $24\,\mu$m and $70\,\mu$m, that are at higher resolution and that may perform comparatively well at estimating the SFR. Since we use multiple calibrations from this work we do not list them here.

Radio Continuum

The radio continuum is a composite of thermal (T) free-free emission and non-thermal (NT) synchrotron emission from regions with massive star formation, spanning $\sim 1 - 100$ GHz. The thermal component of the radio continuum is regulated by the rate of ionizing photons, $Q(H^0)$, released from young HII regions (Rubin, 1968), and will come into equilibrium at some electron temperature, $T_{\rm e}$, depending on the cooling rate of the gas, producing a luminosity:

$$\left(\frac{L_\nu^{\rm T}}{\rm erg\ s^{-1}\ Hz^{-1}}\right) = 1.59 \times 10^{-26} \left[\frac{Q(H^0)}{\rm s^{-1}}\right] \times \left(\frac{T_e}{10^4\ \rm K}\right)^{0.45} \left(\frac{\nu}{\rm GHz}\right)^{-0.1} \tag{1.19}$$

A typical value is $T_e \sim 10^4$ K (Murphy et al., 2011). The non-thermal luminosity is a result of decaying synchrotron emission from supernovae, and is proportional to the supernova rate, $\dot{N_{\rm SN}}$ (Murphy et al., 2011):

$$\left(\frac{L_\nu^{\rm NT}}{\rm erg\ s^{-1}\ Hz^{-1}}\right) = 1.3 \times 10^{30} \left(\frac{\dot{N_{\rm SN}}}{\rm yr^{-1}}\right) \left(\frac{\nu}{\rm GHz}\right)^{-\alpha_{\rm NT}} \tag{1.20}$$

For young electron populations producing optically-thin radio emission, the expected value for $\alpha_{\rm NT}$ is ~ 0.8 cf. Murphy et al., 2011. Assuming that the star formation rate estimated by $\dot{N_{\rm SN}}$ should be equal to that estimated by $Q(H^0)$, we get the following relation (Murphy et al., 2011):

$$\left(\frac{\dot{N_{\rm SN}}}{\rm yr^{-1}}\right) = 8.45 \times 10^{-56} \left[\frac{Q(H^0)}{\rm s^{-1}}\right] \tag{1.21}$$

which we use relate Eqs. 1.19 and 1.20 to produce an expression for the thermal to non-thermal luminosity ratio as a function of frequency:

$$\frac{L_\nu^{\rm T}}{L_\nu^{\rm NT}} = 0.14 \left(\frac{T_e}{10^4\ \rm K}\right)^{0.45} \left(\frac{\nu}{\rm GHz}\right)^{-0.1+\alpha_{\rm NT}} \tag{1.22}$$

Assuming $T_e \sim 10^4$ K and $\alpha_{\rm NT} \sim 0.83$, we find that the ratio of thermal to non-thermal emission at 93 GHz is $L_\nu^{\rm T}/L_\nu^{\rm NT} \sim 3.5$. Although the thermal emission dominates at 93 GHz, the NT component can still contribute $\sim 25\%$ to the total luminosity, and more than this if $\alpha_{\rm NT} < 0.83$. We make use of the composite thermal and non-thermal calibration from Murphy et al. (2011), given by:

$$\begin{aligned}\left(\frac{\rm SFR_\nu}{M_\odot\ \rm yr^{-1}}\right) = 10^{-27}\Bigg[2.18 \left(\frac{T_e}{10^4\ \rm K}\right)^{0.45} \left(\frac{\nu}{\rm GHz}\right)^{-0.1} + \\ 15.1 \left(\frac{\nu}{\rm GHz}\right)^{-\alpha^{\rm NT}}\Bigg]^{-1} \times \left(\frac{L_\nu}{\rm erg\ s^{-1}\ Hz^{-1}}\right)\end{aligned} \tag{1.23}$$

1.6 Thesis Layout

The remainder of this thesis is divided into four additional chapters. Chapter 2 focuses on the relationship between dense gas and star formation in the Antennae galaxies (NGC 4038/9) at sub-kpc scales. This work makes use of Cycle 1 archival ALMA data of the HCN, HCO^+, and HNC $J = 1-0$ transitions, OVRO data of the CO $J = 1-0$ transition, in addition to IR data from *Spitzer* and *Herschel*. Chapter 3 transitions into a study of a larger sample of galaxies, which is comprised of ten nearby systems including four (U)LIRGs, the center of five, disk starburst (or post-starburst) galaxies, and the Antennae merger, which is not yet classified as LIRG. This chapter also makes use of ALMA archival data of the HCN, HCO^+, and CO $J = 1-0$ transitions, in addition to the radio continuum at 90 GHz. We compare the star formation properties of these galaxies with the predictions of several gravoturbulent models of star formation. In Chapter 4, we work with the same sample of galaxies and compare measurements of the $I_{\rm HCN}/I_{\rm CO}$ ratio to numerical modelling of this line ratio. This chapter uses the underling $\rho-$PDFs of the gravoturbulent models of star formation, which bridges the analytical estimates of star formation properties and molecular line luminosities. We conclude this thesis with a discussion in Chapter 5.

Bibliography

Alves, João, Marco Lombardi, and Charles J. Lada (2017). *A&A* 606, L2, p. L2.

André, Philippe (2017). *Comptes Rendus Geoscience* 349.5, pp. 187–197.

Ao, Y. et al. (2013). *A&A* 550, A135, A135.

Ballesteros-Paredes, Javier et al. (2011). *MNRAS* 416.2, pp. 1436–1442.

Balsara, Dinshaw S., Jongsoo Kim, Mordecai-Mark Mac Low, and Grant J. Mathews (2004). *ApJ* 617.1, pp. 339–349.

Bemis, Ashley and Christine D. Wilson (2019). *AJ* 157.3, 131, p. 131.

Berkhuijsen, E. M. and A. Fletcher (2008). *MNRAS* 390.1, pp. L19–L23.

Bertoldi, Frank and Christopher F. McKee (1992). *ApJ* 395, p. 140.

Bigiel, F. et al. (2008). *AJ* 136.6, pp. 2846–2871.

Binney, James and Scott Tremaine (2008).

Black, John H. and Ewine F. van Dishoeck (1987). *ApJ* 322, p. 412.

Blake, Geoffrey A., E. C. Sutton, C. R. Masson, and T. G. Phillips (1987). *ApJ* 315, p. 621.

Bland-Hawthorn, Joss and Ortwin Gerhard (2016). *ARA&A* 54, pp. 529–596.

Bolatto, Alberto D., Mark Wolfire, and Adam K. Leroy (2013). *ARAA* 51.1, pp. 207–268.

Braine, J. and F. Combes (1993). *A&A* 269, pp. 7–14.

Burkhart, B. (2018). *ApJ* 863, 118, p. 118.

Burkhart, Blakesley and Philip Mocz (2019). *ApJ* 879.2, 129, p. 129.

Burkhart, Blakesley, Kye Stalpes, and David C. Collins (2017). *ApJl* 834.1, L1, p. L1.

Chen, Hao, Yu Gao, Jonathan Braine, and Qiusheng Gu (2015). *ApJ* 810.2, 140, p. 140.

Chen, Hope How-Huan, Blakesley Burkhart, Alyssa Goodman, and David C. Collins (2018). *ApJ* 859.2, 162, p. 162.

Collins, D. C. et al. (2012). *ApJ* 750, 13, p. 13.

Collins, David C., Paolo Padoan, Michael L. Norman, and Hao Xu (2011). *ApJ* 731.1, 59, p. 59.

Crutcher, Richard M., Benjamin Wandelt, Carl Heiles, Edith Falgarone, and Thomas H. Troland (2010). *ApJ* 725.1, pp. 466–479.

Dehnen, Walter, Dean E. McLaughlin, and Jalpesh Sachania (2006). *MNRAS* 369.4, pp. 1688–1692.

Devereux, Nicholas, Yoshiaki Taniguchi, D. B. Sanders, N. Nakai, and J. S. Young (1994). *AJ* 107, p. 2006.

Downes, D., P. M. Solomon, and S. J. E. Radford (1993). *ApJl* 414, p. L13.

Draine, B. T. (2003). *ARAA* 41, pp. 241–289.

— (2010). Princeton Series in Astrophysics. Princeton University Press.

Dumouchel, F., A. Faure, and F. Lique (2010). *MNRAS* 406.4, pp. 2488–2492.

Eadie, Gwendolyn M. and William E. Harris (2016). *ApJ* 829.2, 108, p. 108.

Elmegreen, Bruce G. (2009). *The Galaxy Disk in Cosmological Context.* Ed. by Johannes Andersen, Nordströara, Birgitta m, and Joss Bland -Hawthorn. Vol. 254. IAU Symposium, pp. 289–300.

— (2018). *ApJ* 854.1, 16, p. 16.

Federrath, C. and R. S. Klessen (2012). *ApJ* 761, 156, p. 156.

Federrath, Christoph and Supratik Banerjee (2015). *MNRAS* 448.4, pp. 3297–3313.

Field, G. B., W. B. Somerville, and K. Dressler (1966). *ARAA* 4, p. 207.

Field, George B., Eric G. Blackman, and Eric R. Keto (2011). *MNRAS* 416.1, pp. 710–714.

Flower, D. R. (2001). *Journal of Physics B Atomic Molecular Physics* 34.13, pp. 2731–2738.

Flower, D. R. and J. M. Launay (1985). *MNRAS* 214, pp. 271–277.

Froebrich, Dirk and Jonathan Rowles (2010). *MNRAS* 406.2, pp. 1350–1357.

Galametz, M. et al. (2013). *MNRAS* 431.2, pp. 1956–1986.

Gallagher, Molly J. et al. (2018). *ApJ* 858.2, 90, p. 90.

Gao, Yu and Philip M. Solomon (2004a). *ApJS* 152.1, pp. 63–80.

— (2004b). *ApJ* 606.1, pp. 271–290.

Garcıa-Burillo, S. et al. (2012). *A&A* 539, A8, A8.

Glover, S. C. O., C. Federrath, M. -M. Mac Low, and R. S. Klessen (2010). *MNRAS* 404.1, pp. 2–29.

Goldsmith, Paul F., Ronald L. Snell, and Dariusz C. Lis (1987). *ApJl* 313, p. L5.

Graciá-Carpio, J., S. Garcá-Burillo, P. Planesas, A. Fuente, and A. Usero (2008). *A&A* 479.3, pp. 703–717.

Grudić, Michael Y. et al. (2018). *MNRAS* 475.3, pp. 3511–3528.

Hennebelle, Patrick and Gilles Chabrier (2011). *ApJl* 743.2, L29, p. L29.

Hennebelle, Patrick and Edith Falgarone (2012). *A&A Rev.* 20, 55, p. 55.

Heyer, Mark and T. M. Dame (2015). *ARAA* 53, pp. 583–629.

Heyer, Mark, Coleman Krawczyk, Julia Duval, and James M. Jackson (2009). *ApJ* 699.2, pp. 1092–1103.

Hill, Alex S. et al. (2008). *ApJ* 686.1, pp. 363–378.

Hoyle, F. (1953). *ApJ* 118, p. 513.

Hubble, E. P. (1926). *ApJ* 64, pp. 321–369.

Jeffreson, Sarah M. R. and J. M. Diederik Kruijssen (2018). *MNRAS* 476.3, pp. 3688–3715.

Jiménez-Donaire, M. J. et al. (2017). *MNRAS* 466.1, pp. 49–62.

Kainulainen, J., H. Beuther, T. Henning, and R. Plume (2009). *A&A* 508.3, pp. L35–L38.

Kainulainen, J. and C. Federrath (2017). *A&A* 608, L3, p. L3.

Kainulainen, J. and J. C. Tan (2013). *A&A* 549, A53, A53.

Kalberla, Peter M. W. and Jürgen Kerp (2009). *ARA&A* 47.1, pp. 27–61.

Kauffmann, Jens et al. (2017a). *A&A* 605, L5, p. L5.

Kauffmann, Jens et al. (2017b). *A&A* 603, A89, A89.

Kazandjian, M. V., R. Meijerink, I. Pelupessy, F. P. Israel, and M. Spaans (2012). *A&A* 542, A65, A65.

— (2015). *A&A* 574, A127, A127.

Kennicutt Robert C., Jr. (1998). *ApJ* 498.2, pp. 541–552.

Kennicutt, Robert C. and Neal J. Evans (2012). *ARAA* 50, pp. 531–608.

Kent, S. M., T. M. Dame, and G. Fazio (1991). *ApJ* 378, p. 131.

Kolmogorov, A. N. (1962). *Journal of Fluid Mechanics* 13, pp. 82–85.

Kruijssen, J. M. Diederik et al. (2014). *MNRAS* 440.4, pp. 3370–3391.

Kruijssen, J. M. Diederik et al. (2018). *MNRAS* 479.2, pp. 1866–1952.

Krumholz, Mark R., Avishai Dekel, and Christopher F. McKee (2012). *ApJ* 745.1, 69, p. 69.

Krumholz, Mark R., Christopher D. Matzner, and Christopher F. McKee (2006). *ApJ* 653.1, pp. 361–382.

Krumholz, Mark R. and Christopher F. McKee (2005). *ApJ* 630.1, pp. 250–268.

Lada, Charles J., Jan Forbrich, Marco Lombardi, and João F. Alves (2012). *ApJ* 745.2, 190, p. 190.

Lada, Charles J., Marco Lombardi, and João F. Alves (2010). *ApJ* 724.1, pp. 687–693.

Larson, R. B. (1981). *MNRAS* 194, pp. 809–826.

Leroy, Adam K. et al. (2017). *ApJ* 846.1, 71, p. 71.

Li, P. S., Michael L. Norman, Mordecai-Mark Mac Low, and Fabian Heitsch (2004). *ApJ* 605.2, pp. 800–818.

Licquia, Timothy C. and Jeffrey A. Newman (2015). *ApJ* 806.1, 96, p. 96.

Lintott, Chris J. et al. (2008). *MNRAS* 389.3, pp. 1179–1189.

Liszt, H. S. (2007). *A&A* 476.1, pp. 291–300.

Loenen, A. F., M. Spaans, W. A. Baan, and R. Meijerink (2008). *A&A* 488.1, pp. L5–L8.

Lombardi, Marco, João Alves, and Charles J. Lada (2015). *A&A* 576, L1, p. L1.

López-Corredoira, M., A. Cabrera-Lavers, F. Garzón, and P. L. Hammersley (2002). *A&A* 394, pp. 883–899.

Lotz, Jennifer M. et al. (2011). *ApJ* 742.2, 103, p. 103.

Mac Low, Mordecai-Mark and Ralf S. Klessen (2004). *Reviews of Modern Physics* 76.1, pp. 125–194.

Marr, J. M., M. C. H. Wright, and D. C. Backer (1993). *ApJ* 411, p. 667.

McConnachie, Alan W. (2012). *AJ* 144.1, 4, p. 4.

McKee, Christopher F. (1989). *ApJ* 345, p. 782.

McKee, Christopher F., Pak Shing Li, and Richard I. Klein (2010). *ApJ* 720.2, pp. 1612–1634.

McKee, Christopher F. and Eve C. Ostriker (2007). *ARAA* 45.1, pp. 565–687.

McKee, Christopher F. and Ellen G. Zweibel (1992). *ApJ* 399, p. 551.

McMillan, Paul J. (2011). *MNRAS* 414.3, pp. 2446–2457.

Meijerink, R., M. Spaans, A. F. Loenen, and P. P. van der Werf (2011). *A&A* 525, A119, A119.

Mirabel, I. F. and D. B. Sanders (1989). *ApJl* 340, p. L53.
Miville-Deschênes, Marc-Antoine, Norman Murray, and Eve J. Lee (2017). *ApJ* 834.1, 57, p. 57.
Molina, F. Z., S. C. O. Glover, C. Federrath, and R. S. Klessen (2012). *MNRAS* 423, pp. 2680–2689.
Moore, Ben et al. (1999). *ApJl* 524.1, pp. L19–L22.
Murphy, E. J. et al. (2011). *ApJ* 737.2, 67, p. 67.
Narayanan, Desika and Mark R. Krumholz (2014). *MNRAS* 442.2, pp. 1411–1428.
Navarro, Julio F., Carlos S. Frenk, and Simon D. M. White (1996). *ApJ* 462, p. 563.
Nordlund, Å. Ke and Paolo Padoan (1999). *Interstellar Turbulence.* Ed. by Jose Franco and Alberto Carraminana, p. 218.
Nyman, L. -A. (1983). *A&A* 120, pp. 307–312.
Ostriker, Eve C., James M. Stone, and Charles F. Gammie (2001). *ApJ* 546.2, pp. 980–1005.
Padoan, Paolo, Troels Haugbølle, Åke Nordlund, and Søren Frimann (2017). *ApJ* 840.1, 48, p. 48.
Padoan, Paolo, Bernard J. T. Jones, and Åke P. Nordlund (1997). *ApJ* 474.2, pp. 730–734.
Padoan, Paolo and Åke Nordlund (2011). *ApJ* 730.1, 40, p. 40.
Padoan, Paolo, Liubin Pan, Troels Haugbølle, and Åke Nordlund (2016). *ApJ* 822.1, 11, p. 11.
Passot, Thierry and Enrique Vázquez-Semadeni (1998). *Phys. Rev. E* 58.4, pp. 4501–4510.
Piontek, Robert A. and Eve C. Ostriker (2004a). *ApJ* 601.2, pp. 905–920.
— (2004b). *ApJ* 601.2, pp. 905–920.
Radford, Simon J. E., P. M. Solomon, and D. Downes (1991). *ApJl* 368, p. L15.
Rigopoulou, D., A. Lawrence, G. J. White, M. Rowan-Robinson, and S. E. Church (1996). *A&A* 305, p. 747.
Rix, Hans-Walter and Jo Bovy (2013). *A&A Rev.* 21, 61, p. 61.
Rosolowsky, E. W., J. E. Pineda, J. Kauffmann, and A. A. Goodman (2008). *ApJ* 679.2, pp. 1338–1351.
Rubin, Robert H. (1968). *ApJ* 153, p. 761.
Sanders, D. B. and I. F. Mirabel (1996). *ARAA* 34, p. 749.

Sanders, D. B., A. I. Sargent, N. Z. Scoville, and T. G. Phillips (1990). *Submillimetre Astronomy*. Ed. by Graeme D. Watt and Adrian S. Webster. Dordrecht: Springer Netherlands, pp. 213–214.

Scalo, J. M. (1985). *Protostars and Planets II*. Ed. by D. C. Black and M. S. Matthews, pp. 201–296.

Scalo, John, Enrique Vázquez-Semadeni, David Chappell, and Thierry Passot (1998). *ApJ* 504.2, pp. 835–853.

Schneider, N. et al. (2011). *A&A* 529, A1, A1.

Schneider, N. et al. (2013). *ApJl* 766.2, L17, p. L17.

Schneider, N. et al. (2015). *A&A* 578, A29, A29.

Schneider, N. et al. (2016). *A&A* 587, A74, A74.

Schöier, F. L., F. F. S. van der Tak, E. F. van Dishoeck, and J. H. Black (2005). *A&A* 432.1, pp. 369–379.

Semenov, Vadim A., Andrey V. Kravtsov, and Nickolay Y. Gnedin (2017). *ApJ* 845.2, 133, p. 133.

Shirley, Yancy L. (2015). *PASP* 127.949, p. 299.

Shull, J. M. and S. Beckwith (1982). *ARAA* 20, pp. 163–190.

Siebenmorgen, R. and E. Krügel (2007). *A&A* 461.2, pp. 445–453.

Silk, Joseph (1997). *ApJ* 481.2, pp. 703–709.

Sohn, Sangmo Tony, Jay Anderson, and Roeland P. van der Marel (2012). *ApJ* 753.1, 7, p. 7.

Solomon, P. M., A. R. Rivolo, J. Barrett, and A. Yahil (1987). *ApJ* 319, p. 730.

Stadel, J. et al. (2009). *MNRAS* 398.1, pp. L21–L25.

Sun, Jiayi et al. (2018). *ApJ* 860.2, 172, p. 172.

Sun, Jiayi et al. (2020). *ApJ* 892.2, 148, p. 148.

Tabatabaei, F. S., M. Krause, A. Fletcher, and R. Beck (2008). *A&A* 490.3, pp. 1005–1017.

Tielens, A. G. G. M. (2005).

Toomre, Alar and Juri Toomre (1972). *ApJ* 178, pp. 623–666.

Usero, Antonio et al. (2015). *AJ* 150.4, 115, p. 115.

Utomo, Dyas et al. (2015). *ApJ* 803.1, 16, p. 16.

van der Marel, Roeland P., Gurtina Besla, T. J. Cox, Sangmo Tony Sohn, and Jay Anderson (2012). *ApJ* 753.1, 9, p. 9.

Vazquez-Semadeni, Enrique (1994). *ApJ* 423, p. 681.

Vázquez-Semadeni, Enrique, Jorge Cantó, and Susana Lizano (1998). *ApJ* 492.2, pp. 596–602.

Vogel, S. N., S. R. Kulkarni, and N. Z. Scoville (1988). *Nature* 334.6181, pp. 402–406.

Vogel, S. N. and W. J. Welch (1983). *ApJ* 269, pp. 568–579.

Vorontsov-Velyaminov, B. A. (1959). *Atlas and Catalog of Interacting Galaxies (1959*, p. 0.

Wilson, Christine D., Bruce G. Elmegreen, Ashley Bemis, and Nathan Brunetti (2019). *ApJ* 882.1, 5, p. 5.

Wilson, Christine D., Nicholas Scoville, Suzanne C. Madden, and Vassilis Charmandaris (2003). *ApJ* 599.2, pp. 1049–1066.

2 | Kiloparsec-Scale Variations in the Star Formation Efficiency of Dense Gas: The Antennae Galaxies (NGC 4038/39)

This chapter represents an unchanged version of the paper, *Kiloparsec-Scale Variations in the Star Formation Efficiency of Dense Gas: The Antennae Galaxies (NGC 4038/39)*, published in the refereed journal, *The Astronomical Journal*. The full reference is given below:

Bemis A., Wilson C.D., 2019, AJ, Volume 157, Issue 3, pp. 131-148

Department of Physics & Astronomy, McMaster University, Hamilton ON L8S 4M1

Abstract

We study the relationship between dense gas and star formation in the Antennae galaxies by comparing Atacama large millimeter/submillimeter array (ALMA) observations of dense-gas tracers (HCN, HCO+, and HNC $J = 1 - 0$) with the total infrared luminosity ($L_{\rm TIR}$) calculated using data from the Herschel Space Observatory and the Spitzer Space Telescope. We compare the luminosities of our star formation rate (SFR) and gas tracers using aperture photometry and employing two methods for defining apertures. We taper the ALMA data set to match the resolution of our $L_{\rm TIR}$ maps and present new detections of dense-gas emission from complexes in the overlap and western arm regions. Using Owens Valley Radio Observatory CO $J = 1 - 0$ data, we compare with the total molecular gas content, $\mathrm{M(H_2)_{tot}}$, and calculate star formation efficiencies and dense-gas mass fractions for these different regions. We derive HCN, HCO+, and HNC upper limits for apertures where emission was not significantly detected, because we expect that emission from dense gas should be present in most star-forming regions. The Antennae extends the linear $L_{\rm TIR} - L_{\rm HCN}$ relationship found in previous studies. The $L_{\rm TIR} - L_{\rm HCN}$ ratio varies by up to a factor of ∼10 across different regions of the Antennae, implying variations in the star formation efficiency of dense gas, with the nuclei, NGC 4038 and NGC 4039, showing the lowest $\mathrm{SFE_{dense}}$ (0.44 and $0.70 \times 10^{-8}\,\mathrm{yr^{-1}}$). The nuclei also exhibit the highest dense-gas fractions (∼9.1% and ∼7.9%).

2.1 Introduction

The Antennae galaxies are the nearest pair of merging galaxies (22 Mpc, Schweizer et al. 2008) and are rich in star formation (e.g. Whitmore et al., 1999), gas (e.g. Wilson et al., 2000, 2003)), and dust (e.g. Klaas et al., 2010). The rarity of wet, major mergers (gas-rich galaxies with a mass ratio ≤ 3) makes the Antennae a particularly unique environment for studying star formation in interactions. Recent simulations suggest that the Antennae is $\sim$40 Myr after its second pass (Karl et al., 2010), placing it at an intermediate stage in the Toomre sequence. Thus, the Antennae contains multiple generations of stars from merger-induced starburst behavior. The two nuclei exhibit post-starburst populations $\sim$65 Myr old (Mengel et al., 2005), and even younger starburst populations ($\sim 3-10$ Myr) are concentrated in the overlap region and western arm (e.g. Mengel et al., 2005; Mengel et al., 2001; Whitmore et al., 2010, 2014). Furthermore, different regions within the Antennae exhibit varying degrees of current (≤ 100 Myr, Brandl et al. 2009) star formation, with the overlap region of the Antennae (see Figure 2.1) experiencing a particularly violent episode (SFR $> 4\,\mathrm{M_\odot\,yr^{-1}}$, Brandl et al. 2009; Klaas et al. 2010; this work).

Major mergers are a testbed for the extreme star formation ongoing at high-z, and show fundamental differences in their star formation properties compared with normal star-forming disk galaxies (e.g. Daddi et al., 2010; Tacconi et al., 2018). Furthermore, star formation occurs primarily in the densest regions within giant molecular clouds (GMCs, $n(H_2) > 10^4\,\mathrm{cm^{-3}}$, Lada, Bally, and Stark 1991; Lada et al. 1991). The HCN $J = 1-0$ transition has a critical density of $n_{\mathrm{crit}} \sim 10^5\,\mathrm{cm^{-3}}$, while the CO $J = 1-0$ has $n_{\mathrm{crit}} \sim 10^2\,\mathrm{cm^{-3}}$. Thus, it is essential to observe molecules such as HCN to constrain the properties of the directly star-forming gas.

Extragalactic studies often use observations of the total infrared luminosity (L_{TIR}) and HCN $J = 1-0$ molecular luminosity (L_{HCN}) in galaxies to study star formation and dense gas. This has largely been motivated by the seminal work of Gao and Solomon (2004a,b), who found a tight and linear relationship between the global values of L_{IR} and L_{HCN} in a sample of 65 galaxies. Their observations were of unresolved systems, thus comparing the total infrared (TIR) and HCN luminosities spanning $L_{\rm IR} \sim 10^9 - 10^{12}\,\mathrm{L}_\odot$. This sample included normal star-forming galaxies as well as more extreme luminous and ultraluminous infrared galaxies (LIRGs/ULIRGs), suggesting a direct scaling between the SFR and dense molecular gas content across galaxy types. Other recent studies show that this linear relationship also extends to the scales of individual, massive clumps in the Milky Way and nearby galaxies (e.g. Bigiel et al., 2015; Chen et al., 2015; Wu et al., 2005), spanning nearly 10 orders of magnitude in luminosity. These observations have motivated density-threshold models of star formation (Lada et al., 2012), which assume that star formation begins once the gas reaches a threshold density ($n(\mathrm{H_2}) = 10^4\,\mathrm{cm^{-3}}$). These models predict a constant star formation efficiency of dense gas ($\mathrm{SFE_{dense}}$) that should span all regimes of star formation.

A number of recent studies target the $L_{\rm TIR} - L_{\rm HCN}$ relationship on a variety of scales, down to several hundred parsecs (Bigiel et al., 2016; Gallagher et al., 2018; Kepley et al., 2014). These studies fit well within the scatter of the original Gao and Solomon (2004a,b) relationship, extending it down to lower luminosities. Some have also revealed variations in the $L_{\rm IR}$ and $L_{\rm HCN}$ relationship at ∼kpc scales (e.g., M51 from Chen et al. 2015; Usero et al. 2015). UUsero et al. (2015) study ∼kpc scales across the disks of normal star-forming galaxies and find a sublinear power-law index (~ 0.5) for their sample of galaxies. Furthermore, evidence exists that (U)LIRGs may turn off the linear portion of the $L_{\rm TIR} - L_{\rm HCN}$ sequence (Graciá-Carpio et al., 2008), suggesting variations at the high luminosity end as well.

A separate class of star formation models that can, to some degree, better explain the variations of the $L_{\rm IR} - L_{\rm HCN}$ relationship are turbulence-regulated density-threshold models (Krumholz and McKee, 2005; Padoan and Nordlund, 2011). These models predict the variation of probability density profiles (PDFs) as a function of turbulence, and show that turbulence acts as a star formation inhibitor and subsequently increases the threshold density of gas required for star formation. Observational evidence of a correlation between stellar mass density and lower $L_{\rm TIR}/L_{\rm HCN}$ in disk galaxies supports the idea that stellar feedback, in the form of turbulence, etc., can inhibit star formation per unit dense-gas mass (Bigiel et al., 2016). Interestingly, there have been observations of increases in the dense-gas fraction (often traced by $L'_{\rm HCN}/L'_{\rm CO}$) in the central regions of disk galaxies, where the star formation efficiency of dense gas (traced by $L_{\rm TIR}/L'_{\rm HCN}$) appears lowest and stellar density appears highest. The central molecular zone (CMZ) of the Milky Way is the closest example of an environment with low $\mathrm{SFE_{dense}}$ and high dense-gas fractions (e.g. Kauffmann et al., 2017b,c) compared with the solar neighborhood. There are a number of possible mechanisms that can explain this, with turbulence being the favored mechanism so far (Federrath and Klessen, 2012; Kruijssen et al., 2014; Rathborne et al., 2014). Federrath and Klessen (2012) compare the expectations of six different star formations with magnetohydrodynamic simulations that vary four fundamental parameters: virial parameter, sonic mach number, turbulent forcing parameter, and Alfvén mach number. They find turbulence is the primary regulator of the SFR, and produce star formation efficiencies of the total gas (SFE) that agree well with observations (1%-10%).

High-resolution ALMA observations have revealed HCN, HCO+, and HNC $J = 1 - 0$ emission throughout star-forming regions in the Antennae (Schirm et al., 2016). Assuming these transitions trace $n(\mathrm{H_2}) > 10^4\,\mathrm{cm^{-3}}$, this suggests there is an abundance of dense gas throughout this system. Furthermore, there are interesting variations in the molecular luminosities of these dense-gas tracers, suggesting differences in dense-gas properties across the system. Schirm et al. (2016) found evidence for variations of the dense-gas fraction across the Antennae, evidenced by higher HCN-to-CO luminosity ratios in the two nuclei when compared with the overlap region (see Figure 2.1). Bigiel et al. (2015) find that the $L_{\mathrm{IR}} - L_{\mathrm{HCN}}$ relationship in the brightest regions of the Antennae galaxies is consistent with the linear relationship revealed by Gao and Solomon (2004a,b), but their sensitivity limits miss a large portion of the star-forming regions in the system (e.g., the western arm and fainter regions in the overlap region). In this paper, we attempt to understand the variations of this relationship in the context of the Antennae galaxies by assessing the variations of the physical properties with $L_{\mathrm{TIR}} - L'_{\mathrm{HCN(1-0)}}$ at subgalactic scales.

In Section 2.2, we present the ALMA, Herschel, and Spitzer data used in our study along with the total infrared luminosity calibrations. In Section 2.3, we describe our aperture photometry analyses. In Section 2.4, we present the luminosity fit results and compare with previous work. In Section 2.5, we discuss the variation we see in $\mathrm{SFE_{dense}}$ across the Antennae and explore potential explanations for these variations. The analysis and results of this study are summarized in Section 2.6.

Molecular and infrared luminosity uncertainties are discussed in more detail in Appendix 2.A. A comparison between total infrared luminosity calibrations from Galametz et al. (2013) is presented in Appendix 2.B.

2.2 Data

We use Herschel, Spitzer, and ALMA data in our study to compare star formation traced by infrared emission to dense gas traced by high critical-density molecular transitions, HCN, HCO+, and HNC $J = 1 - 0$ (see Figure 2.1). We also use CO $J = 1 - 0$ data from the Owens Valley Radio Observatory (OVRO, Wilson et al. 2003) as our bulk molecular gas tracer, and we note that the OVRO data may be missing ~20% of the CO $J = 1 - 0$ flux (Schirm et al., 2016), likely a diffuse component of the gas, due to the limited range of u–v coverage. Our resolution is limited by the Herschel data ($5.5''$ at $70\,\mu$m, and $6.8''$ at $100\,\mu$m), and thus our analysis is performed at these resolutions.

2.2.1 ALMA Data

Details on the observations of the ALMA data are available in Schirm et al. (2016). The original reduction scripts were used to apply calibrations to the raw data using the appropriate common astronomy software applications (CASA) version (CASA 4.2.0, McMullin et al. 2007). The ALMA data were then cleaned and imaged in CASA 4.7.2. We cleaned using a velocity resolution of $\Delta v_{\rm opt} = 5.2\,{\rm km\,s^{-1}}$ at the rest frequency of each transition over an optical velocity range of $1000 - 2000\,{\rm km\,s^{-1}}$. We tapered the data to the full width at half maximum (FWHM) of the Herschel $70,\mu$m point-spread function using a Briggs weighting (Briggs, 1995) of 0.5 while cleaning. The largest angular scale of the ALMA observations is $\sim 17.1''$[1] (~1.8 kpc). The tapered data reach a root mean square (rms) noise level of $\sigma = 1.2\,{\rm mJy\,beam^{-1}}$. When working at the $100\,\mu$m resolution, we further smooth the tapered cube to $6.8''$.

We create moment zero maps of the molecular lines using CASA's IMMOMENTS command. This produces a two-dimensional image of the integrated intensity

[1] ALMA Cycle 1 Proposer's Guide.

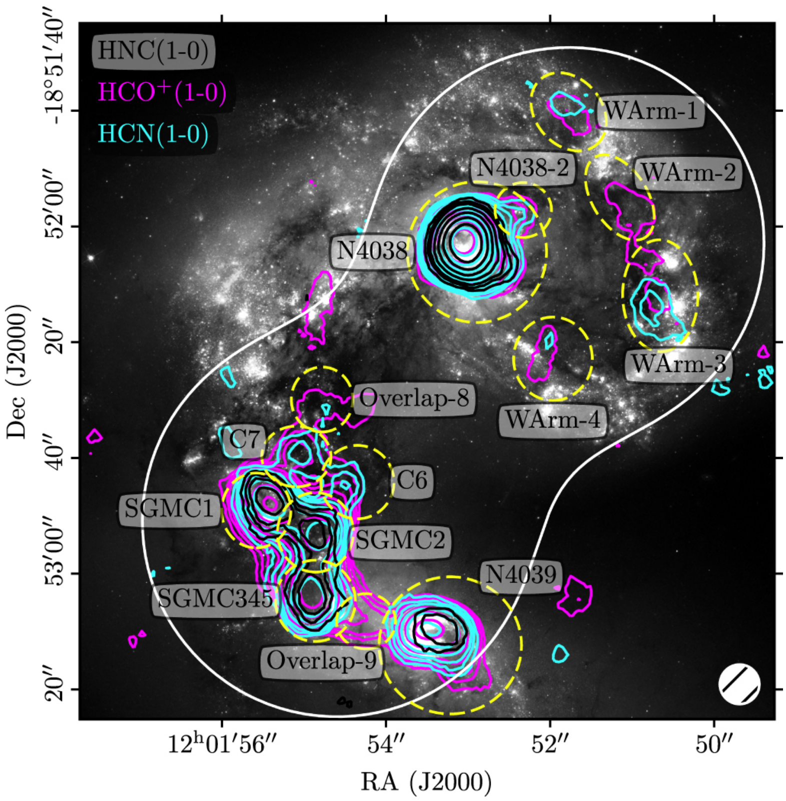

FIGURE 2.1: Magenta, cyan, and black contours (levels = $0.06 \times [4, 6, 8, 12, 17, 24, 34, 49, 70, 100]\,\mathrm{Jy\,beam^{-1}\,km\,s^{-1}}$) of the ALMA HCO+, HCN, and HNC $J = 1-0$ transitions, respectively, overlaid on top of a black and white composite image (435 nm, 550 nm, and 658 nm) from the Hubble Space Telescope (HST). The elliptical apertures are outlined with yellow, dashed curves and labeled according to Tables 2.1 and 2.2; the 50% ALMA primary beam sensitivity is shown as the solid, white curve. The smoothed beam size (6.8″) of the ALMA data is shown in the lower right.

with units of $\mathrm{Jy\,beam^{-1}\,km\,s^{-1}}$. We require that all pixels going into the final moment map be greater than 2σ, where $\sigma = 1.2\,\mathrm{mJy\,beam^{-1}}$ in the $5.5''$ maps and $\sigma = 1.4\,\mathrm{mJy\,beam^{-1}}$ in the smoothed $6.8''$ maps. We then convert to molecular luminosities (L'_{mol}) using the following equation (Wilson et al., 2008):

$$\frac{L'_{\mathrm{mol}}}{\mathrm{K\,km\,s^{-1}\,pc^2}} = 3.2546 \times 10^7 \left(\frac{S_{\mathrm{ap}}}{\mathrm{Jy\,km\,s^{-1}}}\right) \times \left(\frac{D_L}{\mathrm{Mpc}}\right)^2 \left(\frac{\nu_0}{\mathrm{GHz}}\right)^{-2} (1+z)^{-1} \tag{2.1}$$

where S_{ap} is the flux measured in an aperture in $\mathrm{Jy\,km\,s^{-1}}$. This gives molecular luminosity in units of $\mathrm{K\,km\,s^{-1}\,pc^2}$. We use a redshift of $z = 0.005477$. Details on the uncertainty estimates are given in Section 2.3 and Appendix 2.A.1.

2.2.2 Infrared Data and Total Infrared Luminosities

We obtain user-provided data products of the 70, 100, 160, and 250 μm maps from the Herschel (Pilbratt et al., 2010) Science Archive. Details on the observations and reduction of the 70, 100, and 160 μm photodetector array camera and spectrometer (PACS) (Poglitsch et al., 2010) data are available in Klaas et al. (2010) and reach resolutions of $5.5''$, $6.8''$, and $11.3''$, respectively. The spectral and photometric imaging receiver (SPIRE) 250 μm map ($18.1''$ resolution, Griffin et al. 2010) was obtained as part of the Very Nearby Galaxies Survey, and details on the observations and calibrations can be found in Bendo, Galliano, and Madden (2012). We also retrieve user-provided Spitzer (Werner et al., 2004) 24 μm multiband imaging photometer (MIPS) data (Rieke et al. 2004, $6.0''$ resolution) from the Spitzer Heritage Archive. These data were reprocessed by Bendo et al. (2012) to provide ancillary data for the Herschel-SPIRE Local Galaxies Guaranteed Time Programs.

We use several calibrations from Galametz et al. (2013) to estimate L_{TIR}, which is defined in that paper to be:

$$L_{\mathrm{TIR}} \int_{3\,\mathrm{mum}}^{1100\,\mathrm{mum}} L_\nu d\nu.$$

Galametz et al. (2013) derive calibrations of $L_{\rm TIR}$ using a combination of Herschel and Spitzer data from 8 to 250 μm as an alternative to fitting the dust spectral energy distribution (SED). They have provided monochromatic calibrations (e.g., 70 μm), as well as multiband calibrations (e.g., 24 + 70 + 100 μm). We compare several of these calibrations for the Antennae in Appendix 2.B, and show the ratio maps for these calibrations in Figure 2.6 at the 250 μm resolution (18.1″).

In this paper, we use the monochromatic 70 μm (5.5″ ∼590 pc) and the multiband 24 + 70 + 100 μm (6.8″ ∼725 pc) calibrations to estimate $L_{\rm TIR}$ across the Antennae. The 70 μm calibration is the highest-resolution Herschel band and brackets the warm-dust ($30-60\,$K) SED peak (∼100 μm). For multiband calibrations, Galametz et al. (2013) recommend that any $L_{\rm TIR}$ estimate using fewer than 4-5 bands should include the 100 μm flux or a combination of the 70 + 160 bands, which should lead to $L_{\rm TIR}$ predictions reliable within 25% (≤50% for monochromatic calibrations). Additionally, Galametz et al. (2013) note that including the 24 μm flux improves calibrations of $L_{\rm TIR}$ for galaxies with higher 70/100 color, i.e., strongly star-forming environments. The overlap region is known to be vigorously star-forming, which could cause the 70 μm flux to underestimate $L_{\rm TIR}$. Therefore, we include the 24 + 70 + 100 μm calibration as a check for this. Overall, we find our $L_{\rm TIR}(70)$ estimates agree well with the $L_{\rm TIR}(24 + 70 + 100)$ estimates. The $L_{\rm TIR}(70)$ estimate for SGMC345 (the combination of super giant molecular complexes 3, 4, and 5 from Wilson et al. 2000) is only ∼3% lower than the $L_{\rm TIR}(24+70+100)$ estimate and agrees within uncertainties.

To estimate $L_{\rm TIR}$ using multiple IR bands, we converted the Herschel and Spitzer maps to the same units and resolution (i.e., to the FWHM of the beam size of the band with the lowest resolution). The Spitzer MIPS and Herschel SPIRE data were converted to units of $\rm Jy\,pixel^{-1}$ from $\rm MJy\,sr^{-1}$ and $\rm Jy\,beam^{-1}$, respectively (the Herschel PACS data were already in units of $\rm Jy\,pixel^{-1}$). Each data set was then convolved to a common resolution using the Aniano et al. (2011) kernels. The Galametz et al. (2013) calibrations require that infrared measurements be in solar luminosity units ($L_\odot$). We convert the Herschel infrared maps from Jansky units to solar luminosities using the following equation:

$$\frac{\nu L_\nu}{L_\odot} = 3.1256 \times 10^2 \left(\frac{d_L}{\rm Mpc}\right)^2 \left(\frac{\nu}{\rm GHz}\right) \left(\frac{S_\nu}{\rm Jy}\right). \tag{2.2}$$

Table 2.1: Elliptical Apertures

Source	R.A. (J2000)	Decl. (J2000)	EW (″)	NS (″)	Area (kpc^2)
NGC 4038	12:01:52.895	-18:52:04.46	24.1	24.3	5.23
NGC 4039	12:01:53.22	-18:53:12.29	24.6	23.7	5.22
NGC 4038-2	12:01:52.332	-18:51:57.2	9.8	9.5	0.84
WArm-1	12:01:51.779	-18:51:40.27	11.4	14.9	1.52
WArm-2	12:01:51.156	-18:51:55.04	9.5	16.3	1.39
WArm-3	12:01:50.664	-18:52:11.98	13.0	19.3	2.26
WArm-4	12:01:51.97	-18:52:22.86	13.6	14.4	1.76
SGMC1	12:01:55.583	-18:52:49.02	12.0	12.9	1.38
SGMC2	12:01:54.862	-18:52:52.8	13.1	13.7	1.60
SGMC345	12:01:54.862	-18:53:04.6	13.8	14.0	1.73
Schirm-C6	12:01:54.351	-18:52:44.13	12.6	12.7	1.44
Schirm-C7	12:01:55.094	-18:52:39.71	12.0	10.5	1.12
Overlap-8	12:01:54.781	-18:52:29.88	10.6	11.2	1.05
Overlap-9	12:01:54.246	-18:53:08.14	10.2	9.5	0.86

Note. The center coordinates and angular extent of the elliptical apertures. The axes are oriented east-west (EW) and north-south (NS) except for WArm-1, WArm-2, and WArm-3, where the position angles (PA) are 42.2°, 32.3°, and 1.3° east of north.

The background is then estimated and subtracted from each map. Once the data are formatted properly, we apply the corresponding Galametz et al. (2013) calibrations to create $L_{\rm TIR}$ maps. We calculate absolute uncertainties on the $L_{\rm TIR}$ calibrations (see Appendix 2.A.2 for details) and find they are much lower than the calibration uncertainties quoted above (25% uncertainties on the $L_{\rm TIR}(24+70+100)$ measurements and ∼50% uncertainties on the $L_{\rm TIR}(70)$ measurements).

2.3 Aperture Analysis

We compare the emission of our SFR and gas tracers across different regions of the Antennae using aperture photometry. We use two approaches to defining apertures. In our first method, we identify clumps of emission using CPROPS (Rosolowsky and Leroy, 2006) in each of the dense-gas data cubes; we then manually define elliptical apertures (Table 2.1) to encompass infrared and integrated intensity dense-gas emission of individual "clumps" or complexes[2]. We vary the radii and position angles of the apertures to encompass potentially associated emission of the IR and dense-gas tracers. In our second method, we perform a "pixel-by-pixel" analysis by dividing the maps into hexagonal grids that are sampled by the FWHM of the beam (i.e., the incircle diameter of each hexagon is $6.8''$). The hexagons are fixed in size across the map (edge = $3.9''$; inspired by a similar method employed by Leroy et al. 2016). The elliptical aperture method allows us to contrast the behavior of individual regions, while the hexagonal method eliminates selection bias that can be introduced in the manual-aperture method. Therefore, the hexagonal aperture method provides more robust data for trend-fitting, and the emphasis of the elliptical aperture analysis is region-by-region comparisons.

We perform the luminosity-luminosity fits using the Bayesian linear regression code LINMIX (Kelly, 2007), which incorporates uncertainties in both x- and y-directions. The LINMIX routine assumes a linear relationship of the form $\log(L_{\mathrm{TIR}}) = m \times \log(L_{\mathrm{dense}}) + \log(b)$, where m is the slope, and b is the y-intercept. The LINMIX code also allows us to incorporate upper limits into our fits; therefore, we also include upper limits of the molecular luminosities in the fits. We estimate the significance of each correlation by calculating the Spearman rank coefficients of the data sets for each fitted relationship. The one- and two-sigma uncertainties on the fits are estimated via Markov-Chain Monte-Carlo, and we take the median values of these iterations as our fit parameters. We compare our results with those of Gao and Solomon (2004a,b) and Liu, Gao, and Greve (2015), and also perform fits of the Antennae data combined with data sets from these studies. We also compare with measurements of L_{TIR} and L_{HCN} of the CMZ (Stephens et al., 2016), because we observe similarities between luminosity ratios of the CMZ and the two nuclei (see Section 2.5.2). The HCN luminosity for the CMZ is derived from the Mopra CMZ 3 mm survey, covering a $2.5° \times 0.5°$ area centered on $l = 0.5°$, $b = 0.0°$ (Jones et al., 2012), and the conversion to luminosity assumes a distance of $8.34 \pm 0.16\,\mathrm{kpc}$ (Reid et al., 2014). The infrared luminosity of the CMZ is estimated using a combination of 12, 25, 60, and 100 μm Infrared Astronomical Satellite fluxes and the calibration from Sanders and Mirabel (1996). We

[2]There are multiple clumps of dense-gas emission along most lines of sight, but in an aperture photometry analysis we sum up all this emission.

note that this region of the Milky Way is very crowded, and these luminosities are likely upper limits and may include emission from other sources along the line of sight. We assume uncertainties of $\sim$30% on $L_{\rm TIR}$ and $L_{\rm HCN}$ of the CMZ, because these are also the uncertainties prescribed by Liu, Gao, and Greve (2015) to the galaxies in their sample.

To determine upper limits of the Antennae luminosities, we first estimate the contribution of noise into each moment zero map. We approach this differently than applying a simple rms noise limit due to the large physical extent of the apertures (i.e., larger than the GMCs in our beam), and the large velocity range over which our moment maps are created. The moment zero maps are created with a two-sigma cutoff, such that no emission below two-sigma is allowed into the map. Because the noise follows a Gaussian distribution, only $\sim$2% of the noise should remain above this two-sigma cutoff; choosing a cutoff at two-sigma allows us to eliminate the majority of the noise from the moment zero map without sacrificing a significant amount of real emission. However, because $\sim$2% of the noise remains, each aperture will contain some signal from the noise proportional to the number of pixels per aperture ($n_{\rm pix} \approx 117$ for the hexagonal apertures, and varies for the elliptical apertures) and the total number of channels in the data cube ($n_{\rm chan} = 192$). Furthermore, the noise varies with position in the map according to the response of the primary beam ($\epsilon_{\rm pb}$). Optimally, the base rms noise is $\sigma = 1.2\,{\rm mJy\,beam^{-1}}$ ($5.5''$) or $\sigma = 1.4\,{\rm mJy\,beam^{-1}}$ ($6.8''$) at an efficiency of 100%, and larger as the response decreases toward the edges of the primary beam.

Therefore, the remaining Gaussian noise per aperture in the moment zero maps, $\sigma^{\rm ap}_{\rm Gauss}$, is

$$\sigma^{\rm ap}_{\rm Gauss} \approx 0.25 \times \frac{2\sigma}{\epsilon_{\rm pb}} \times \Delta v \times n_{\rm pix} \times n_{\rm chan} \div {\rm ppb} \tag{2.3}$$

where $\Delta v = 5.2\,{\rm km\,s^{-1}}$ and ppb is the number of pixels per beam (to give units of ${\rm Jy\,km\,s^{-1}}$). We require the aperture sums from the moment zero maps of the dense-gas tracers to be larger than this noise limit to be considered a detection. We set our upper limit to two times this noise limit:

$$\sigma^{\rm ap}_{\rm lim} = 2 \times \sigma^{\rm ap}_{\rm Gauss} \tag{2.4}$$

This requires at least $0.025 \times 192 = 5$ channels (per pixel per aperture) to have a signal of four-sigma to be considered a detection. Anything below $\sigma_{\rm lim}^{\rm ap}$ is considered an upper limit, and we set the values of these apertures to $\sigma_{\rm lim}^{\rm ap}$ and treat them as upper limits in our fitting routines. The upper limits are shown as the gray arrows in Figure 2.2. At the $6.8''$ resolution, the limit per hexagonal aperture is set to be $\sigma_{\rm lim}^{\rm ap} \approx 110\,{\rm mJy\,km\,s^{-1}}$ at maximum primary beam efficiency (which corresponds to $0.9\,{\rm mJy\,km\,s^{-1}}$ per pixel), and translates to luminosity limits of $\log(L_{\rm HCN}) = 5.46$, $\log(L_{\rm HCO^+}) = 5.46$, and $\log(L_{\rm HNC}) = 5.45$.

2.4 Results

Each approach to defining apertures has its own strengths: the hexagonal-grid approach allows us to optimally sample our data sets without introducing selection bias into our apertures, and the elliptical aperture analysis has the benefit of emphasizing individual source behavior. We therefore focus on the hexagonal aperture results when discussing fits, and then later focus on the results of the elliptical apertures when discussing variations in different regions of the Antennae.

In the tapered ALMA data set, we detect significant emission from HCN and HCO+ in both the nuclei (NGC 4038 and NGC 4039), the overlap region (containing SGMCs 1-5, C6 and C7 from Schirm et al. (2016), and newly detected sources 8 and 9), and the western arm (containing WArm 1-4). HNC is detected significantly in NGC 4038 and SGMCs in the overlap region, and upper limits are derived elsewhere. HCO+ is the overall brightest dense-gas tracer in this data set, and there are several regions where we detect HCO+ but not HCN; this includes the "bridge" region (Overlap-8) between SGMCs 3, 4, and 5 (hereafter referred to as one source, SGMC345) and NGC 4039 (the southern nucleus). HCO+ is also brightest in one of the regions we study in the western arm (WArm-2).

We plot the $L_{\rm TIR} - L_{\rm dense}$ Antennae data points of the hexagonal and elliptical apertures in Figures 2.2 and 2.3, respectively, and we list the luminosities measured within the elliptical apertures in Table 2.2. We overplot the LINMIX fits in grayscale (including upper limits) for both the hexagonal and elliptical aperture analyses; for comparison, we also plot fits to the hexagonal aperture luminosities without upper limits (salmon). The slopes and y-intercepts of the fits that includes upper

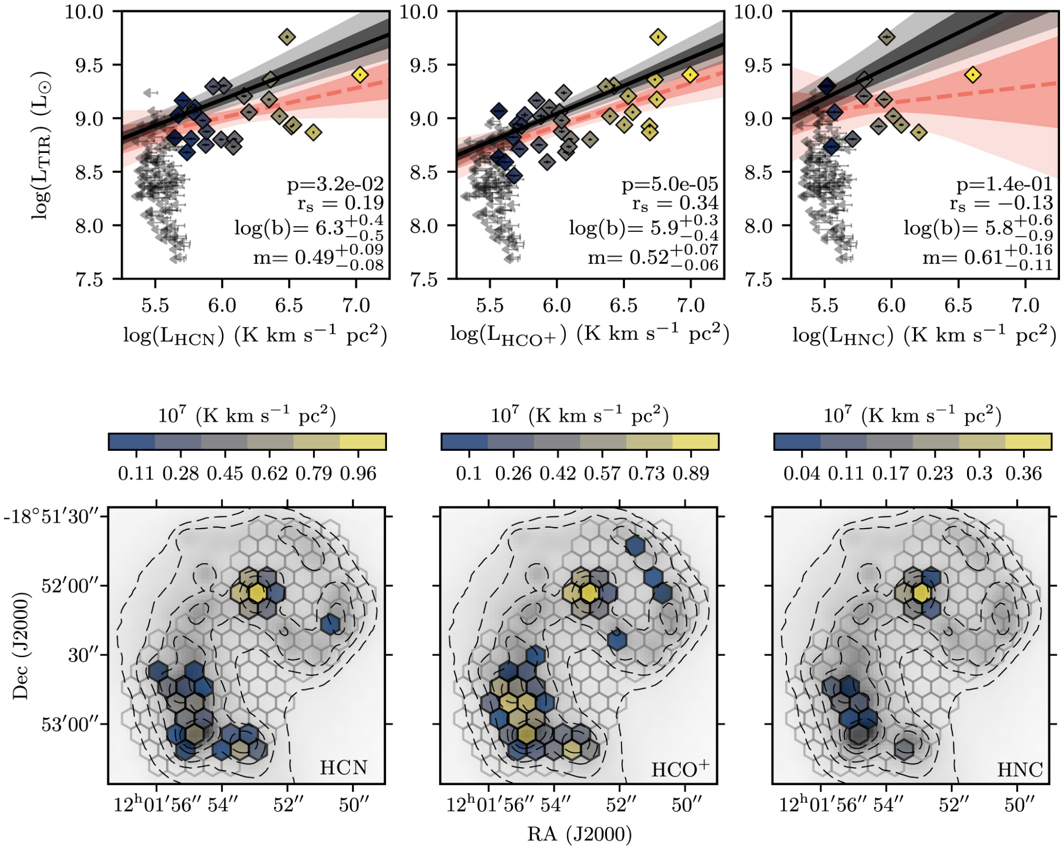

FIGURE 2.2: Top: from left to right, we show L_{TIR} vs. L_{HCN}, $L_{\mathrm{HCO^+}}$, and L_{HNC}. The data points are colorized according to the hexagonal apertures in the maps directly below; gray data points and open apertures are upper limits. The LINMIX fit including upper limits is shown as the solid black line. The fit without upper limits is shown for comparison as the salmon dashed line. The one-sigma (dark-shaded area) and two-sigma (light-shaded area) uncertainties resulting from the Monte Carlo Markov Chain (MCMC) iterations are also shown. The resulting fits assume a linear relationship of the form $\log(L_{\mathrm{TIR}}) = m \times \log(L_{\mathrm{dense}}) + \log(b)$, where m is the slope, and b is the y-intercept; we show the resulting slopes (m) and y-intercepts (b) for the fits including upper limits on the plots. The absolute uncertainties are plotted on each data point, which are generally small for $\log(L_{\mathrm{TIR}})$. The Spearman rank coefficients for each correlation are also shown. Bottom: from left to right, the hexagonal apertures are shown for HCN, HCO+, and HNC overlaid on top of the L_{TIR} map (dashed contours and grayscale, log stretch). The hexagons are colorized according to the luminosity of dense-gas emission corresponding to that aperture. The colorbar values are in units of $10^7\,\mathrm{K\,km\,s^{-1}\,pc^{-2}}$ (log stretch).

limits are shown in each plot. We list the fits from the hexagonal apertures below. The $L_{\mathrm{TIR}} - L_{\mathrm{dense}}$ fits present sublinear power-law indices (i.e., $m < 1.0$). The Spearman p-values indicate strong correlations ($p < 0.05$) between L_{TIR} and the dense-gas molecular luminosities, except for the HNC fits, which shows a weaker correlation ($p \sim 0.14$) likely due to the lower detection rate of this molecular line.

The fits from the hexagonal apertures shown in Figure 2.2 are as follows:

$$\log(L_{\mathrm{TIR}}) = 6.3^{+0.4}_{-0.5} + 0.49^{+0.09}_{-0.08} \log(L_{\mathrm{HCN}}) \tag{2.5}$$

$$\log(L_{\mathrm{TIR}}) = 5.9^{+0.3}_{-0.4} + 0.52^{+0.07}_{-0.06} \log(L_{\mathrm{HCO+}}) \tag{2.6}$$

$$\log(L_{\mathrm{TIR}}) = 5.8^{+0.6}_{-0.9} + 0.61^{+0.16}_{-0.11} \log(L_{\mathrm{HNC}}) \tag{2.7}$$

We also fit the L_{TIR} and L_{HCN} values from the Antennae hexagonal apertures with those of the sources in Liu, Gao, and Greve (2015), which includes the data from the Gao and Solomon (2004a,b) survey. This fit is presented in Figure 2.4. The power-law index on this fit is $m = 0.96 \pm 0.03$, which is slightly sublinear. The Antennae data extend the data points of Gao and Solomon (2004a,b) and Liu, Gao, and Greve (2015) to lower luminosities. This agrees with the findings of Bigiel et al. (2015), who performed a similar analysis on the Antennae using data from the Combined Array for Research in Millimeter-wave Astronomy. The median value of the $L_{\mathrm{TIR}}/L_{\mathrm{HCN}}$ ratio of the Antennae hexagonal apertures ($980\, L_\odot\, (\mathrm{K\, km\, s^{-1}\, pc^2})^{-1}$)) falls within the scatter of other studies (i.e. Gao and Solomon, 2004a,b; Liu, Gao, and Greve, 2015). The scatter of the Antennae data is also comparable (∼0.4 dex) to these other studies (Table 2.3). Fitting the surface densities of the Liu, Gao, and Greve (2015) and Antennae data also yields a slope $m = 1$ (Figure 2.5).

We convert the total infrared luminosity to estimates of the SFRs using the calibration initially published in Kennicutt (1998) and updated in Kennicutt and Evans (2012) with the more recent Kroupa initial mass function and Starburst99 model (Hao et al., 2011; Murphy et al., 2011):

$$\log \mathrm{SFR}\, (\mathrm{M_\odot\, yr^{-1}}) = \log \frac{L_{\mathrm{TIR}}}{(L_\odot)} - 9.83 \tag{2.8}$$

The uncertainty on the total infrared luminosities used for the SFR estimates is

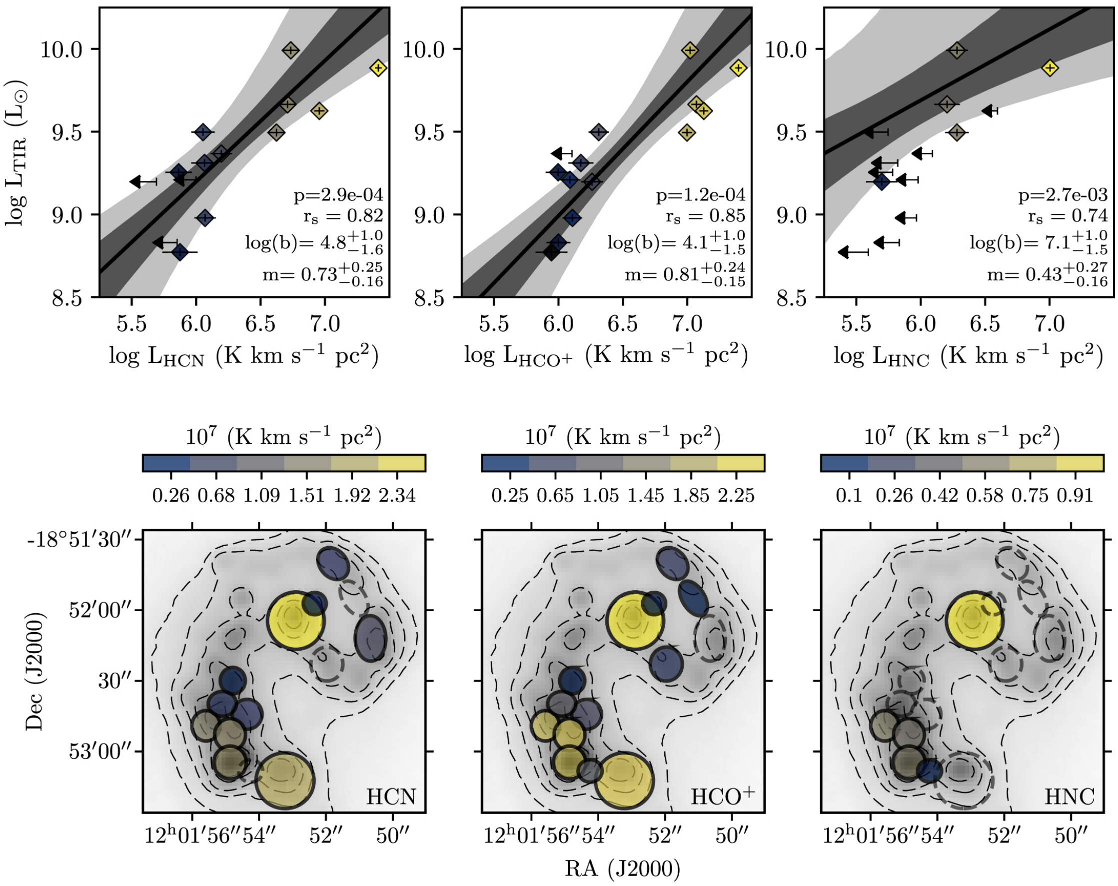

FIGURE 2.3: Top: from left to right, we show L_{TIR} vs. L_{HCN}, $L_{\mathrm{HCO^+}}$, and L_{HNC} resulting from the elliptical aperture analysis. The data points are colorized according to the elliptical apertures in the maps directly below; black data points and open apertures are upper limits. Bottom: from left to right, the elliptical apertures are shown for HCN, HCO+, and HNC overlaid on top of the L_{TIR} map (dashed contours and grayscale, log stretch). We do not plot fits without upper limits.

Table 2.2: Total Infrared and Molecular Luminosities

Source	$L^{a}_{\rm TIR}$ ($10^9\ L_\odot$)	$L_{\rm HCN}$	$L_{\rm HCO^+}$ (10^7 K km s^{-1} pc^2)	$L_{\rm HNC}$	$L_{\rm CO}$
NGC 4038	7.67 ± 0.39	2.60 ± 0.16	2.50 ± 0.15	1.008 ± 0.081	38.4 ± 7.9
NGC 4039	4.22 ± 0.21	0.905 ± 0.082	1.34 ± 0.11	< 0.039	18.0 ± 4.0
NGC 4038-2	0.592 ± 0.031	0.075 ± 0.024	0.088 ± 0.025	< 0.093	2.92 ± 0.91
WArm-1	0.953 ± 0.049	0.117 ± 0.023	0.128 ± 0.022	< 0.123	3.90 ± 0.97
WArm-2	0.676 ± 0.035	< 0.100	0.100 ± 0.021	< 0.095	4.2 ± 1.1
WArm-3	2.33 ± 0.12	0.16 ± 0.03	< 0.068	< 0.066	3.32 ± 0.83
WArm-4	1.619 ± 0.083	< 0.073	0.123 ± 0.023	< 0.070	2.01 ± 0.57
SGMC1	3.12 ± 0.16	0.420 ± 0.063	0.995 ± 0.087	0.19 ± 0.04	16.2 ± 3.6
SGMC2	4.62 ± 0.24	0.512 ± 0.079	1.18 ± 0.11	0.160 ± 0.037	22.7 ± 5.0
SGMC345	9.79 ± 0.51	0.543 ± 0.071	1.052 ± 0.094	0.191 ± 0.037	17.2 ± 3.8
Schirm-C6	2.05 ± 0.11	0.116 ± 0.028	0.149 ± 0.034	< 0.061	4.7 ± 1.3
Schirm-C7	3.14 ± 0.16	0.113 ± 0.024	0.205 ± 0.037	< 0.056	6.3 ± 1.6
Overlap-8	1.797 ± 0.093	0.073 ± 0.017	0.099 ± 0.022	< 0.068	4.6 ± 1.2
Overlap-9	1.575 ± 0.087	< 0.049	0.182 ± 0.036	0.050 ± 0.014	1.75 ± 0.55

Note. Luminosities measured from the elliptical apertures listed in Table 2.1. All values are measured at the 100 μm resolution ($6.8''$). The absolute uncertainties are shown next to each luminosity, except in the case of limits.
[a] This $L_{\rm TIR}$ is estimated using the Galametz et al. (2013) calibration that combines the Spitzer 24 and Herschel 70 and 100 μm maps. See Table 2.5 for a comparison with Galametz et al. (2013) monochromatic 70 μm $L_{\rm TIR}$ estimates.

$\sim$25% (Galametz et al., 2013), and thus we suggest this as a lower limit to the uncertainty on the SFRs derived via Equation 2.8 and listed in Table 2.4.

We estimate the dense molecular gas content, $M_{\rm dense}$, from the HCN luminosities using the conversion factor published by Gao and Solomon (2004a), $\alpha_{\rm HCN} \approx 10\,{\rm M_\odot}\,({\rm K\,km\,s^{-1}\,pc^2})^{-1}$. We discuss the possibility of variations in the HCN conversion factor in Section 2.5.5. To estimate the total molecular gas content, $M_{\rm H_2}$, we adopt a CO-to-H_2 conversion factor of $\alpha_{\rm CO} \approx 7\,{\rm M_\odot}\,({\rm K\,km\,s^{-1}\,pc^2})^{-1}$ from Schirm et al. (2014). Schirm et al. (2014) estimate the CO abundance and conversion factor in the Antennae by modeling a warm and cold gas component using RADEX (van der Tak et al., 2007) and Herschel Fourier transform spectrometer data of multiple CO transitions. Using an initial CO abundance of $x_{\rm CO} \sim 3 \times 10^{-4}$, they derive a warm H_2 gas mass that is 10 times lower than previous estimates from Brandl et al. (2009) based on direct H_2 observations; assuming CO is tracing the same gas as H_2, they adjust their CO abundance to $x \sim 5 \times 10^{-5}$. Using this

TABLE 2.3: Comparison of $L_{\mathrm{TIR}}/L_{\mathrm{HCN}}$ Statistics

	Non-Gaussian			Gaussian	
Data set	Median	Lower[a]	Upper[b]	Mean	1σ
GS04	850	440	620	950	550
L15 Normal	820	320	1100	1200	1100
L15 ULIRGs	1100	510	1200	1400	980
Antennae (Hex.)	980	610	990	1100	750
Antennae (Ell.)	900	270	1200	1300	780

Notes. We calculate both Gaussian (mean, standard deviation) and non-Gaussian statistics (median, 16th, and 84th percentiles), excluding upper limits. Quantities are in units of $L_{\odot}(\mathrm{K\,km\,s^{-1}\,pc^2})^{-1}$.
[a] Distance from the median to the 16th percentile.
[b] Distance from the median to the 84th percentile.

abundance, their cold gas mass estimate is $M_{\mathrm{cold}} \sim 1.5 \times 10^{10}\,\mathrm{M_{\odot}}$, resulting in the aforementioned CO $J = 1-0$ conversion factor. Wilson et al. (2003) derive a similar conversion factor, $\alpha_{\mathrm{CO}} \approx 6.5\,\mathrm{M_{\odot}}\,(\mathrm{K\,km\,s^{-1}\,pc^2})^{-1}$, by calculating the virial mass of resolved SGMCs using OVRO CO $J = 1-0$ data that we also use in this work.

Estimates of α_{CO} from Milky Way observations show a factor $\sim$5 spread, with the typical value of $X_{\mathrm{CO}} \sim 2 \times 10^{20}\,\mathrm{cm^{-2}}$ (see Bolatto, Wolfire, and Leroy 2013), which translates to $\alpha_{\mathrm{CO}} \sim 4\,\mathrm{M_{\odot}}\,(\mathrm{K\,km\,s^{-1}\,pc^2})^{-1}$. Measurements of α_{CO} in star-bursting galaxies show a spread of at least $\sim$3 (see Bolatto, Wolfire, and Leroy 2013), and are less studied and thus less well constrained than α_{CO} in more normal star-forming environments. Therefore, we suggest a factor $\sim$4 uncertainty on the mass estimates from α_{CO}. The HCN-to-dense H_2 conversion factor, α_{HCN}, is even less well constrained than α_{CO}, so we suggest a factor of $\sim$10 uncertainty on the dense-gas mass estimates.

We estimate the dense molecular gas fraction by taking the ratio of the dense molecular gas mass estimate from L_{HCN} to the total molecular mass from L_{CO}, $f_{\mathrm{dense}} = M_{\mathrm{dense}}/M_{\mathrm{H_2}}$. Similarly, we calculate the star formation efficiency of dense gas via $\mathrm{SFE_{dense}} = \mathrm{SFR}/M_{\mathrm{dense}}$ and the star formation efficiency of the total gas via $\mathrm{SFE} = \mathrm{SFR}/M_{\mathrm{H_2}}$. We calculate surface densities of the SFR, $M(\mathrm{H_2})_{\mathrm{dense}}$, and total

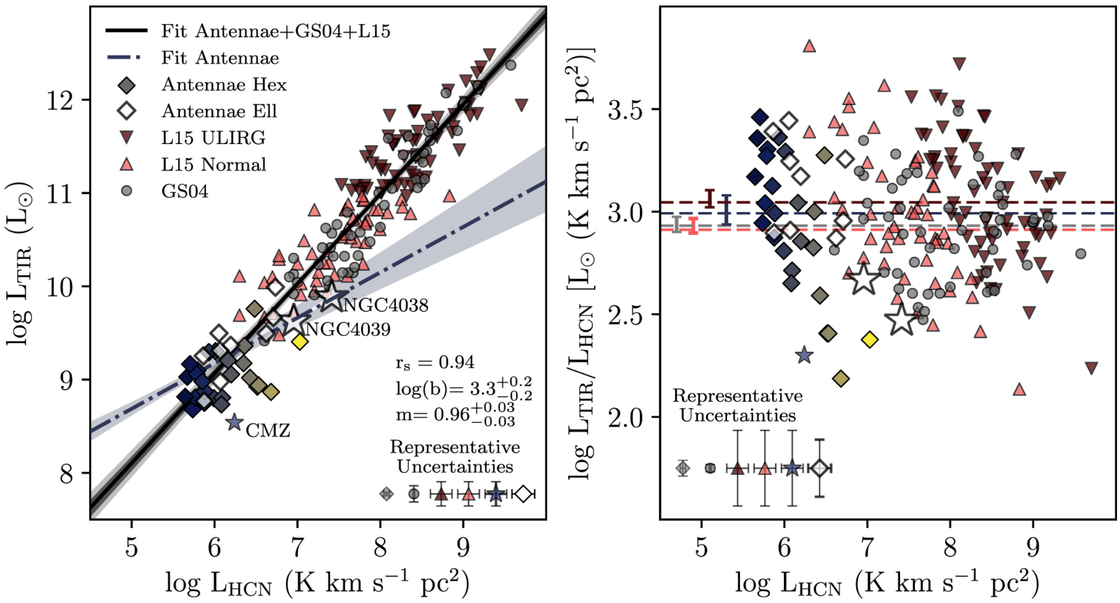

FIGURE 2.4: Left: L_{TIR} vs. L_{HCN} data points of the Gao and Solomon (2004a,b) sample (gray circles), the Liu, Gao, and Greve (2015) (U)LIRGs (maroon inverted triangles), the Liu, Gao, and Greve (2015) normal star-forming galaxies (salmon triangles), the Antennae hexagonal aperture luminosities (blue-yellow diamonds), and the Antennae elliptical aperture luminosities (white diamonds). We emphasize the data points of the two nuclei, NGC 4038 and NGC 4039, as white stars. The hexagonal data points are colorized according to HCN luminosity, as is done in Figure 2.2. We show measurements of the CMZ (as given in Stephens et al. 2016) for comparison as the blue star (see text for more information). We show the fit to the Liu, Gao, and Greve (2015) and Antennae hexagonal data points (black solid line), with the one- (light shade) and two-sigma (dark shade) uncertainties from the MCMC iterations. The resulting fit parameters are listed (assuming $\log(L_{TIR}) = m \times \log(L_{dense}) + \log(b)$, where m is the slope, and b is the y-intercept). The fit to the Antennae hexagonal apertures from Figure 2.2 is shown for comparison as the dashed–dotted line in blue. Right: L_{TIR}/L_{HCN} versus L_{HCN}. We show the median value (dashed line, see Table 2.3) of the L_{TIR}/L_{HCN} ratio for each data set, excluding the Antennae elliptical apertures. At the left end of the dashed lines, we show the statistical uncertainties on the median values. We show representative uncertainties in the lower-right corner (left plot) and lower-left corner (right plot). Upper limits are excluded. The two nuclei have the lowest L_{TIR}/L_{HCN} in the Antennae system, despite having the highest dense-gas fractions. The CMZ is also known to have a low star formation efficiency of dense gas and very high dense-gas fractions.

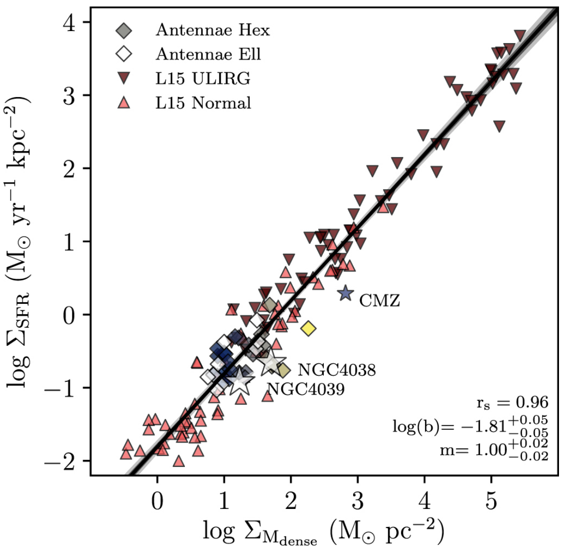

FIGURE 2.5: Σ_{SFR} vs. $\Sigma_{M_{dense}}$, excluding the data from Gao and Solomon (2004a,b). The symbols and colors are the same as in Figure 2.4. Liu, Gao, and Greve (2015) calculate source sizes using the radio continuum. Liu, Gao, and Greve (2015) calculate the dense molecular gas mass assuming an HCN conversion factor, $\alpha_{HCN} = 10\,M_\odot\,(K\,km\,s^{-1}\,pc^2)^{-1}$. We use the SFRs that Liu, Gao, and Greve (2015) calculate from IR luminosities. The two nuclei of the Antennae have surface densities comparable to those of other regions, and the locus of Antennae points falls in the overlapping regime of normal star-forming galaxies and (U)LIRGs from the Liu, Gao, and Greve (2015) sample. The fit to the Antennae hexagonal data points and Liu, Gao, and Greve (2015) data points yields a slope of $m = 1.00 \pm 0.02$. Upper limits are excluded.

$M(\mathrm{H_2})$ by dividing these quantities by their elliptical aperture area (Table 2.4). The dense-gas fraction should be uncertain by a factor of $\sim$10. The uncertainty on the star formation efficiencies is dominated by the mass uncertainties, and thus are also uncertain by a factor of $\sim$10 and $\sim$4 for $\mathrm{SFE_{dense}}$ and SFE, respectively.

TABLE 2.4: Physical Properties

Source	SFR ($M_\odot\,yr^{-1}$)	$M(H_2)_{dense}$ ($10^7\,M_\odot$)	$M(H_2)$ ($10^7\,M_\odot$)	f_{dense} (%)	SFE_{dense} ($10^{-8}\,yr^{-1}$)	SFE ($10^{-8}\,yr^{-1}$)	Σ_{SFR} ($M_\odot\,yr^{-1}\,kpc^{-2}$)	$\Sigma_{M_{dense}}$ ($M_\odot\,pc^{-2}$)	$\Sigma_M(H_2)$ ($M_\odot\,pc^{-2}$)
NGC 4038	1.1	26	270	9.7	0.44	0.043	0.22	50.0	510
NGC 4039	0.63	9.0	130	7.2	0.69	0.050	0.12	17.0	240
NGC 4038-2	0.088	0.75	20	3.7	1.2	0.043	0.11	9.0	240
WArm-1	0.14	1.2	27	4.3	1.2	0.052	0.093	7.7	180
WArm-2	0.10	<0.71	29	<2.4	>1.4	0.034	0.073	<5.1	210
WArm-3	0.35	1.6	23	6.8	2.2	0.15	0.15	6.9	100
WArm-4	0.24	<1.0	14	<7.1	>2.4	0.17	0.14	<5.7	80
SGMC1	0.46	4.2	110	3.7	1.1	0.041	0.34	30.0	820
SGMC2	0.69	5.1	160	3.2	1.3	0.043	0.43	32.0	990
SGMC345	1.5	5.4	120	4.5	2.7	0.12	0.84	31.0	700
Schirm-C6	0.30	1.2	33	3.5	2.6	0.092	0.21	8.1	230
Schirm-C7	0.47	1.1	44	2.5	4.1	0.11	0.42	10.0	400
Overlap-8	0.27	0.73	32	2.3	3.7	0.083	0.26	7.0	310
Overlap-9	0.23	<0.49	12	<4.0	>4.8	0.19	0.27	<5.7	140

Note. Estimates of physical properties from sources contained within the elliptical apertures (see Table 2.1). These properties are derived from the luminosities listed in Table 2.2. See Section 2.4 for further information about the conversion from luminosities to these values and the corresponding uncertainties.

2.5 Discussion

In this paper, we study four distinct gas-rich star-forming regions in the Antennae: (1) the nucleus of NGC 4038, (2) the nucleus of NGC 4039, (3) the overlap region, and (4) the western arm. Our primary goals are to constrain the subgalactic $L_{\rm TIR} - L_{\rm HCN}$ relation in the Antennae, study how it varies across different regions, and piece together what drives this variation by characterizing the environment and star formation using line ratios and other results from the literature. We include a list of luminosity ratios of regions in Table 2.6 in Appendix 2.C. In the following sections, we discuss the bulk properties of the Antennae observations and then discuss the ∼kpc-scale variations of different regions.

A note on SFRs from L_{TIR}: In a merging system such as the Antennae, we can expect to be tracing a variety of stellar populations and SFRs. Models of mergers suggest there will be multiple bursts of star formation over the evolution of the system, with these bursts being triggered within different regions of the system at different times (Mengel et al., 2001; Mihos and Hernquist, 1996). Recent simulations estimate the Antennae system to be 40 Myr after its second pass (Karl et al., 2010), placing it at a later stage in the Toomre sequence than previous estimates (e.g. Toomre, 1977). This provides a natural explanation for the different ages and distributions of stellar populations observed across the Antennae, from bursts <10 Myr old to ancient globular clusters born in the progenitor galaxies (∼10 Gyr, Whitmore et al. 1999). Therefore, using SFR tracers at subgalactic scales in this system requires caution, because the conversion from SFR-tracer luminosity to SFR may not be constant across the system.

The total infrared luminosity traces star formation over the past 100 Myr (Kennicutt and Evans, 2012) and so can be affected by the recent star formation history of a region. In particular, the $L_{\rm TIR}$ may underestimate the SFR in regions of young starbursts (≤10 Myr, Brandl et al. 2009; Kennicutt and Evans 2012), or overestimate it in systems with a large population of evolved stars ($\geq 100 - 200$ Myr) heating the dust. With a particularly violent episode of star formation ongoing in the overlap region, the first process could feasibly affect $L_{\rm TIR}$ SFR estimates in this region, while the second process may affect $L_{\rm TIR}$ SFR estimates in the nuclei and outer regions of the Antennae. However, these two effects would only act to enhance the discrepancy we see in $\mathrm{SFE_{dense}}$ between the nuclei and overlap region of the Antennae. Furthermore, many regions in the Antennae galaxies are highly obscured by dust, and so other SFR tracers such as ultraviolet and Hα are not reliable due to high extinction. L_{TIR} is commonly used as an SFR tracer in extragalactic studies and does not suffer from these extinction effects, making it a better SFR tracer in dusty environments. With these considerations, we use L_{TIR} as our main SFR tracer, but we compare our results with other studies from the literature that target different stages of star formation using observations from other wavebands: radio continuum from the Very Large Array (Neff and Ulvestad, 2000), X-ray from Chandra (Zezas et al., 2002), optical/infrared from the Hubble Space Telescope (Whitmore and Schweizer, 1995; Whitmore et al., 2010), and mm- and sub-mm observations from ALMA (Herrera and Boulanger, 2017; Johnson et al., 2015; Whitmore et al., 2014).

2.5.1 General Characteristics of the Dense Gas: Photon Dominated Regions (PDRs)

Leroy et al. (2017) show that (for a fixed T_{kin}) the total emissivity of a particular molecular transition is dependent on the width of the density PDF as well as the mean density at which it resides. This is such that even a molecule with a high critical density, like HCN, can emit brightly at low densities if the turbulence widens the density PDF sufficiently. They model emission from a number of molecular transitions, including HCN, HCO+, HNC, and ^{1}2CO $J = 1-0$, ratios using RADEX (van der Tak et al., 2007) for lognormal and lognormal+power-law density distributions. Throughout the majority of the Antennae, the integrated intensities of the dense-gas lines we observe rank HCO+ > HCN > HNC. When Leroy et al. (2017) vary only the mean density (and fix $T_{\mathrm{kin}} = 25\,\mathrm{K}$), interestingly, the line ratios are ranked HCO+ > HNC > HCN for low $n_0 < 10^3\,\mathrm{cm^{-3}}$, are ranked HCN > HNC > HCO+ for high $n_0 > 10^3\,\mathrm{cm^{-3}}$, or are all similar in strength at median densities $n_0 \sim 10^3\,\mathrm{cm^{-3}}$. This indicates that density variations alone cannot account for the difference in average lines strengths we observe, especially given that in all regions of the Antennae, HNC emission is weaker than both HCO+ and HCN.

By default, RADEX takes into account the effect[3] of chemical formation and destruction in the presence of cosmic-ray ionization plus cosmic-ray induced photodissociation on level populations. These rates are computed in a subroutine that can be modified to include a more complex treatment of chemical processes in molecular clouds. Loenen et al. (2008) present models of PDRs and X-ray dominated regions (XDRs) that incorporate mechanical heating in addition to the PDR and XDR chemistry models of previous work (i.e. Meijerink and Spaans, 2005; Meijerink, Spaans, and Israel, 2007). Loenen et al. (2008) compare observed HCN, HCO+, and HNC line ratios in nearby LIRGs to the results of the PDR and XDR modeling. Their results suggest that the HNC/HCN ratio is able to distinguish XDRs and PDRs, because this ratio never falls below unity for their X-ray dominated models. At higher temperatures (>100 K), HNC may be produced more efficiently than HCN in the HNC+H $\rightarrow$ HCN+H reaction (Schilke et al., 1992; Talbi, Ellinger, and Herbst, 1996). Thus, in the presence of mechanical heating the HNC/HCN ratio is expected to be suppressed. As HNC is consistently weaker than HCN across the Antennae, the chemistry of the HNC- and HCN-emitting gas is likely UV dominated (rather than X-ray dominated), with some amount of mechanical heating suppressing the HNC emission.

Loenen et al. (2008) also suggest that the HCO+/HCN and HCO+/HNC ratios can distinguish high-density ($n > 10^5\,\mathrm{cm}^{-3}$) PDRs from lower-density PDRs. They divide the mechanical heating into: (1) stellar UV-radiation dominated chemistry arising from denser ($n > 10^5\,\mathrm{cm}^{-3}$) PDR environments with young (<10 Myr) star formation, resulting in HNC/HCN ~ 1 and weak HCO+, and (2) mechanical/supernovae-shock dominated chemistry from more diffuse PDR environments and stellar populations with ages >10 Myr, with HNC/HCN < 1 and strong HCO+ possible. Loenen et al. (2008) attribute these differences in the HCO+/HCN ratio primarily to differences in the density of the gas, rather than abundance variations. Because HCO+ has a lower critical density than HCN and HNC, they argue that it is brighter than HCN and HNC in lower-density gas. For the majority of the Antennae, HCO+ is stronger than both HCN and HNC (except in NGC 4038 and WArm-3, where HCN is actually stronger). Thus, the average ratios across the Antennae are consistent with the lower-density PDRs

[3] These effects are included via source and sink terms in the statistical equilibrium calculations.

from Loenen et al. (2008), with some amount of shock heating from supernovae of >10 Myr stellar populations.

There is rough agreement between the lower-density models of Loenen et al. (2008) and Leroy et al. (2017) in the sense that HCO+ is expected to be brighter than HCN. However, there are still large differences in the actual densities of the models that produce this trend; the lower-density Loenen et al. (2008) models are at more moderate densities, $n \sim 10^{4.5}\,\mathrm{cm}^{-3}$, and the models of Leroy et al. (2017) that produce this trend are $n < 10^{3.5}\,\mathrm{cm}^{-3}$. The models of Loenen et al. (2008) (and Meijerink and Spaans 2005; Meijerink, Spaans, and Israel 2007) assume a single density for the gas, although there is mounting evidence that variations in the gas density PDF can also significantly alter molecular luminosities (e.g. Leroy et al., 2017). Alternatively, the Leroy et al. (2017) models do not expand upon the default treatment of chemistry in the RADEX code. Therefore, future modeling of line ratios should attempt to combine these treatments of gas density PDFs and chemistry for better constraints on the gas properties that these line ratios are tracing in extreme environments.

2.5.2 The Nuclei of NGC 4038 and NGC 4039

Low $L_{\mathrm{TIR}}/L_{\mathrm{dense}}$ and High $L_{\mathrm{HCN}}/L_{\mathrm{CO}}$

The two nuclei appear to have lower $L_{\mathrm{TIR}}/L_{\mathrm{dense}}$ ratios compared with the ratios of the remaining Antennae regions (see Tables 2.2, 2.4, and 2.6, and Figure 2.4). This ratio is taken as a proxy for the star formation efficiency of dense gas, $\mathrm{SFE}_{\mathrm{dense}}$, assuming $L_{\mathrm{TIR}} \propto \mathrm{SFR}$ and $L_{\mathrm{dense}} \propto M_{\mathrm{dense}}$. The estimated $\mathrm{SFE}_{\mathrm{dense}}$ for the nuclei are $0.44 \times 10^{-8}\,\mathrm{yr}^{-1}$ and $0.7 \times 10^{-8}\,\mathrm{yr}^{-1}$ for NGC 4038 and NGC 4039, respectively, compared with values of $(1.1 - 4.6) \times 10^{-8}$ for regions in the overlap and western arm. We compare the $L_{\mathrm{TIR}}/L_{\mathrm{HCN}}$ ratios of the Antennae sources (from elliptical apertures) to those of Gao and Solomon (2004a,b) and Liu, Gao, and Greve (2015) in Figure 2.4, which shows that the Antennae data, as a whole, span the majority of the range in $L_{\mathrm{TIR}}/L_{\mathrm{HCN}}$ ratios of these two samples of galaxies. This also emphasizes the difference between the two nuclei (white stars) and the overlap and western arm regions (orange diamonds). The nuclei appear on the lower end of the locus of points from Gao and Solomon (2004a,b)) and Liu, Gao, and Greve (2015), below the median of the Gao and Solomon (2004a,b) galaxies ($850\,L_\odot\,(\mathrm{K\,km\,s^{-1}\,pc^2})^{-1}$), while the overlap and western arm lie above this value in the typical starburst regime.

The two nuclei also show an enhancement in the $L_{\mathrm{HCN}}/L_{\mathrm{CO}}$ ratio relative to the overlap region (Schirm et al., 2016). This line ratio is often used as a proxy for f_{dense} ($L_{\mathrm{HCN}}/L_{\mathrm{CO}} \sim M_{\mathrm{dense}}/M_{\mathrm{H_2}}$), which would indicate that the nuclei have higher dense-gas fractions than other regions in the Antennae. Our calculated dense-gas fractions are listed in Table 2.4, and indeed show that the nuclei have the highest dense-gas fractions, with NGC 4038 at ∼9.7% and NGC 4039 at ∼7.1%, compared with 2.2%-4.5% for sources in the overlap region. Regions in the western arm exhibit higher dense-gas fractions up to 6.9% in WArm-3, although these regions also show higher $\mathrm{SFE_{dense}}$ (e.g., $\mathrm{SFE_{dense}} = 2.19 \times 10^{-8}\,\mathrm{yr^{-1}}$ in WArm-3), unlike the two nuclei.

This behavior in the nuclei (i.e., lower $\mathrm{SFE_{dense}}$ and higher f_{dense}) is similar to the inner regions of some disk galaxies (e.g. Bigiel et al., 2016; Usero et al., 2015), and could be attributed to an increase in interstellar medium (ISM) pressure. In some disk galaxies, f_{dense} has been observed to increase toward the center of the disk/bulge region (e.g., M51 in Bigiel et al. 2016 and the sample of galaxies in Usero et al. 2015), and the star formation efficiency of the dense gas appears to decrease toward the center, showing an inverse correlation with f_{dense}. This is also coincident with an increase in stellar density and gas fraction observed at the inner radii. If the gas is assumed to be in equilibrium with the hydrostatic pressure in the galaxy, then increased ISM pressures arise naturally from this situation (Bigiel et al., 2016; Helfer and Blitz, 1997; Hughes et al., 2013). Then, if the stellar potential were driving up the pressure in the nuclei, we might expect to see overall higher gas surface densities in these regions. Contrary to this, the nuclei appear to have moderate molecular gas surface densities (∼240 and $\sim 510\,\mathrm{M_\odot\,pc^{-2}}$) compared with the SGMCs in overlap region ($\sim 700 - 1000\,\mathrm{M_\odot\,pc^{-2}}$). However, the surface density of the dense gas is higher in the NGC 4038 ($\sim 50\,\mathrm{M_\odot\,pc^{-2}}$) than in the overlap region ($\sim 30\,\mathrm{M_\odot\,pc^{-2}}$, while NGC 4039 shows $\Sigma_{\mathrm{M_{dense}}} = 17\,\mathrm{M_\odot\,pc^{-2}}$. We also note that dynamical equilibrium may not be a valid assumption in a merger system. For example, Renaud, Bournaud, and Duc (2015) show that cloud–cloud collisions in the Antennae can increase pressure sufficiently through compressive turbulence to be able to produce massive cluster formation. Regardless of the source of increased pressure, it can potentially increase the dense-gas content, as well as the mean density of the gas. Loenen et al. (2008) model line ratios in extreme environments, such as (U)LIRGs (which are often merger systems), that are consistent with this.

Because the Antennae is a merger system, turbulent pressures are expected to be higher throughout this system (see Renaud, Bournaud, and Duc 2015). Furthermore, the gas in any merger system will be drawn to the higher gravitational potential wells of the nuclei, thus potentially creating an even higher turbulent pressure in these regions. Turbulent pressure may also act to suppress star formation, and is the strongest candidate for explaining the star formation suppression in the CMZ (Kruijssen et al., 2014). The CMZ is a region known to have high average gas densities ($n(\mathrm{H_2}) > 10^4\,\mathrm{cm^{-3}}$, Rathborne et al. (2014) despite a relative lack of star formation. Kruijssen et al. (2014) have suggested that the lower SFR is attributed to an overall slower evolution of the gas toward gravitational collapse in the presence of higher turbulence (because the gas density threshold required for star formation is higher). Turbulence is the strongest candidate of the potential star formation suppressors in the CMZ (compared with tidal disruption, gas heating, etc.), and is likely due to gas inflow along the molecular bar or other disk instabilities (Kruijssen et al., 2014). For this scenario to be true, the SFR in the CMZ must be episodic, suggesting that it is currently in a pre-starburst phase. Other evidence suggests that clouds in the CMZ are not strongly self-gravitating (Kauffmann et al., 2017c), but rather are being held together by the stellar potential. This also supports the idea that the SFR in the CMZ may increase in the future as gravitational collapse progresses in this region.

As mentioned previously, starburst episodes are natural in a merger system. If the nuclei are in a pre- (or post-) starburst phase, we may expect to measure higher ISM turbulent pressures from gas inflow (and/or stellar feedback). In the CMZ, pressures are $P/k_B \sim 10^9\,\mathrm{K\,cm^{-3}}$ (Rathborne et al., 2014). Previous estimates of the pressure of the warm and cold components of lower-density gas in the Antennae (as measured by CO) show little variation and are $P/k_B \sim 10^5\,\mathrm{K\,cm^{-3}}$ (Schirm et al., 2014). However, if mean gas densities are higher in the nuclei, then CO would not adequately trace the bulk properties of gas in these regions. Additionally, HCN/HCO+ and HNC/HCN integrated line ratios differ between these sources, indicating that there may be different mechanisms driving the lower $\mathrm{SFE_{dense}}$ and f_{dense} in each of the two nuclei (Schirm et al. 2016; NGC 4038 exhibits higher HNC/HCN and HCN/HCO+ luminosity ratios than NGC 4039). We investigate variation in the star formation between the two nuclei in Section 2.5.2.

Rathborne et al. (2014) argue that this lower SFR should be observed in the centers of other galaxies, and more evidence of this behavior is surfacing (e.g. Bigiel et al., 2016; Usero et al., 2015), with more work to come in the future. As discussed above, there are likely a number of sources of turbulence, including stellar feedback. In contrast, enhancements in the SFE of the total molecular gas content have been observed in the centers of some galaxies (Utomo et al., 2017). Chown et al. (2019) find enhancements in SFE and central gas concentrations in a number of barred and interacting galaxies, supporting the idea that mass transport can play a significant role in regulating star formation. However, the star formation history of these systems suggest that the enhancements have been sustained over long periods of time. More studies of the dense-gas content in these systems will help determine if there is a common relationship between SFE, $\mathrm{SFE_{dense}}$, and f_{dense} of the centers of barred and interacting galaxies. Overall, the parallels between the CMZ, the centers of disk galaxies, and the nuclei have interesting implications for star formation: processes affecting the SFR and gas PDFs of the CMZ and centers of disk galaxies may also be occurring in disturbed systems such as the Antennae. More work needs to be done to explore the mean density and density profile of the L_{HCN}-emitting gas in these environments.

Star Formation

The two nuclei have the second- and third-highest L_{TIR} measurements in the system, below the L_{TIR} from SGMC345. The SFRs we determine from our L_{TIR} measurements are 1.14 and 0.63 $\mathrm{M_{\odot}\,yr^{-1}}$, which are higher by a factor >2 than the estimates from Brandl et al. (2009). Brandl et al. (2009) use mid-IR fluxes (15 and 30 μm) to estimate L_{TIR}, where we use the 24, 70, and 100 μm fluxes; to compare our estimates with theirs, we apply a scaling factor of 0.86 from Kennicutt and Evans (2012) to their SFR estimates based on the older Kennicutt (1998) SFR calibration[4]. With the scaling factor applied, Brandl et al. (2009) find SFRs to be 0.52 and 0.27 $M_\odot\,yr^{-1}$ for NGC 4038 and NGC 4039, respectively, for $L_{\rm TIR} \sim 3.67$ and $1.86 \times 10^9\,L_\odot$. Using the 70 μm flux to estimate $L_{\rm TIR}$, Bigiel et al. (2015) find $L_{\rm TIR} \sim 8.8$ and $5.5 \times 10^9\,L_\odot$ for their apertures Nuc. N and Nuc. S, although they do not convert these to SFRs. Our estimates for $L_{\rm TIR}$ are similar to this, with $\sim$7.67 and $4.22 \times 10^9\,L_\odot$. It is likely our apertures are different from those used by Brandl et al. (2009), which may account for some of the differences. Regardless, NGC 4038 appears to have a SFR that is $\sim$2 times higher than NGC 4039.

NGC 4039 has the characteristics of a post-starburst nucleus with little star formation activity. It hosts an older stellar population ($\sim$65 Myr from IR spectroscopic results/CO absorption, Mengel et al. 2001) that is dominated by old giants and red supergiants (see photospheric absorptions line in the $\sim$2 μm stellar continuum, Gilbert et al. 2000). Gilbert et al. (2000) found no evidence of Brγ emission, which is expected to be present in the atmospheres of young stars. NGC 4039 also has a steep radio spectrum (Neff and Ulvestad, 2000) indicating that the radio emission is originating predominantly from SNe remnants of the $\sim$65 Myr-starburst. Chandra observations reveal a composite X-ray spectrum that supports this picture: it contains a thermal component (indicating a hot ISM) and steep power law with $\Gamma \sim 2$ (indicating X-ray binaries, Zezas et al. 2002). Furthermore, Brandl et al. (2009) find evidence that H_2 in NGC 4039 is shock-heated. The lower HNC/HCN ratio we find in NGC 4039 is consistent with these findings and suggests it is driven by the mechanical heating of previous starbust activity and supernovae shocks (Neff and Ulvestad, 2000).

Brandl et al. (2009) find high-excitation IR lines in the nucleus of NGC 4039, which is one potential indicator of an accreting stellar black hole binary. They measure a ratio [NIII]/[NII] $\sim$6 times higher in NGC 4039 than NGC 4038 and strong [S IV], which was not detected in NGC 4038 at all. To determine the source of these high-excitation lines in NGC 4039, Brandl et al. (2009) compare the mid-IR spectral continuum ($\sim 10-30\,\mu$m) with a starburst model template from Groves et al. (2008). They find it matches with a model representative of distributed star formation at solar metallicity, moderate pressures ($P/k_B \sim 10^5\,{\rm K\,cm^{-3}}$), and a

[4]Kennicutt and Evans (2012) recommend multiplying $L_{\rm TIR}$-based SFR estimates using the Kennicutt (1998) calibration by a factor of 0.86.

PDR fraction indicating star formation is still embedded. Brandl et al. (2009) therefore interpret their line ratios as being consistent with dust emission heated solely by star formation. The [S IV] emission in NGC 4039 may also trace young stars in a $\sim 4-6$ Myr starburst. It is possible an episode of star formation may be in the very early stages in this nucleus. This is again consistent with the picture painted above for the CMZ, because the gas may be in a pre-starburst phase that will eventually go on to form stars at a higher rate. Brγ emission is also detected in a circum-nuclear cluster (A1, Gilbert and Graham 2007), which is identified separately from and just north of NGC 4039; however, it falls within our aperture and is likely contributing to our SFR estimates in this region.

NGC 4038 also contains a post-starburst population aged at ∼65 Myr (Mengel et al., 2001). There is evidence of a younger ∼6 Myr population to the north of NGC 4038 (Mengel et al., 2001). NGC 4038 has a very soft X-ray spectrum likely due to thermal emission originating from winds from this region of young star formation (Zezas et al., 2002). Brγ emission is detected in the northern nucleus, which provides evidence for young star formation in this region. The X-ray luminosity of NGC 4038 is also lower than that of NGC 4039. Thus, the star formation in NGC 4038 is at a different stage than NGC 4039, and may be at the upswing of a starburst.

2.5.3 The Western Arm

Whitmore et al. (2010) show that the Antennae presents an interesting number of large- and small-scale patterns related to star formation. One of these regions with such patterns is the western arm. Whitmore et al. (2010) study the population of star clusters in the Antennae using HST images from Advanced Camera for Surveys and Near-Infrared Camera and Multi-Object Spectrometer (NICMOS). In the western arm, they designate five knots of clusters (originally discovered by Rubin, Ford, and D'Odorico 1970) that spatially coincide with dense-gas emission detected in our study; sources G, L, R, S, and T overlap with our apertures WArm-1 (G), WArm-3 (T, S, and R), and WArm-4 (L). In their study, they note linear spatial age gradients in several clusters, including knots S, T, and L in the western arm. The ages appear to increase toward the inner side of the spiral pattern in the direction of major dust lanes. The dense gas detected along the western arm also appears to be concentrated on the inner portion of the spiral pattern coincident with the dust lanes in this region, excluding WArm-1. (WArm-1 appears more centralized in the northern portion of the spiral pattern.) Whitmore et al. (2010) posit that this gradient may be due either to small-scale processes, such as sequential star formation, or larger-scale processes, such as density waves or gas cloud collisions. Either of these processes could also explain the position of the dense-gas emission toward the inner portion of the western arm.

The western arm hosts several bright HII regions, as evidenced in the Hα image from HST (Figure 2.1). The diameters of these hot bubbles are widest along the western arm, indicating slightly more evolved starbursts than the overlap region (Whitmore et al. 2010). The HCN/HCO+ ratio varies from $\sim$0.7 to 1.3 in this region, with the highest ratio exceeding unity in WArm-3.

WArm-3: The dense-gas emission associated with WArm-3 overlaps with the inner edge of the HII region associated with knot S, and likely originates from gas shock-heated by UV winds and SNe. This region also shows bright compact 4 cm and 6 cm emission with both shallow and steep spectral indices (Neff and Ulvestad, 2000), indicating a combination of thermal emission and synchrotron emission from SN remnants, which could potentially be from the exposed O-star remnants. This is one of the few regions in the Antennae where HCN emission exceeds HCO+ (HNC remains very weak/undetected), with HCN also appearing more spatially extended. The abundance of HCO+ can be significantly reduced in environments with a high ionization fraction, while the HCN abundance remains relatively unaffected (Papadopoulos, 2007). This could potentially account for the higher HCN/HCO+ ratio here, considering the proximity of this dense-gas emission to the HII regions of knots R, S, and T. Or, this region could simply be at an overall higher density, with mechanical heating continuing to drive down the HNC abundance. Brandl et al. (2009) also study this starbursting region in the western arm (their Peak 4). Age estimates place the stellar population here around $\sim$7 Myr (Brandl et al., 2009; Mengel et al., 2005; Whitmore and Zhang, 2002). Again, their SFR ($0.22\,\mathrm{M_\odot\,yr^{-1}}$) agrees with ours to within 50%.

WArm-2: The WArm-2 region, like WArm-3, is coincident with an obscuring dust lane (see Figure 2.1). This region does not appear to have compact cm-emission or optical knots associated with it (Neff and Ulvestad, 2000; Whitmore et al., 2010), and it also appears to have the lowest estimated SFR in our sample ($0.1\,\mathrm{M_\odot\,yr^{-1}}$). There are a few compact HII regions associated with this region (visible in Hα, Whitmore et al. 2010), indicative of younger, embedded star formation. There is HCO+ emission associated with this region, but no detected HCN or HNC. This is consistent with a lower mean density of gas, because both species have higher critical and effective densities than HCO+ (Shirley, 2015). It is interesting that HCN is not detected despite there being evidence of star formation in this region. This may indicate that HCN is not an efficient tracer of dense gas at this particular stage of star formation, or perhaps other mechanisms are suppressing the HCN emission that currently remain unclear. It is possible that one or more of these transitions are optically thick and subject to radiative trapping. For example, Jiménez-Donaire et al. (2017) show that radiative trapping can effectively reduce the critical density required to stimulate 12C-transitions, thus boosting the intensity of these lines relative to 13C-transitions. Something similar could potentially occur between HCO+, HCN, and HNC where one or more of these transitions is boosted relative to the other from optical depth variations. However, for optical depth variations to explain HCO+ being detected over HCN, HCO+ would need a higher optical depth and higher critical density than HCN, which we find unlikely.

Another possible explanation for the detection of HCO+ over HCN and HNC is that nitrogen is possibly depleted in WArm-2. A mechanism for this would be low-metallicity gas flowing into the western arm from the outskirts of the galaxy. However, this should affect all regions in the western arm equally, and HCN is detected in WArm-1 and WArm-3. In fact, HCN is brighter than HCO+ in WArm-3. Therefore, we find it more likely that the variations we observe are due to excitation effects, such as density variations.

WArm-1: North of WArm-2 is WArm-1, which has visible HCN and HCO+ emission. The line ratios for this source are consistent with the average line ratios of the entire system: HCO+ is brighter than HCN, and HNC is relatively weak/not detected. There also appear to be optical clusters associated with this region, in particular knot G from Whitmore et al. (2010). Neff and Ulvestad (2000) detect compact radio emission in the vicinity of WArm-1 (their region 13), of which five sources have detections at both 4 cm and 6 cm and allow for the estimation of their radio spectral indices. Three of these sources have indices >-0.4, indicating strong thermal sources, while two have steep nonthermal emission indicated by indices ~ -0.45 and ~ -1.64. Zezas et al. (2002) detect 18 ultraluminous X-ray (ULX) sources ($L_X > 10^39\,\mathrm{erg\,s^{-1}}$) in the Antennae, which they suggest are accreting black hole binaries. One of these sources, their X-ray source 16, is also coincident with the dense-gas emission in WArm-1. This is one of three variable ULX sources, which further supports the idea that these are black hole binaries.

WArm-4: The WArm-4 region appears at the southern tail of the spiral pattern. The ratios in this region also follow the average trend of the system. Again, optical clusters (knot L, Whitmore et al. 2010) and compact radio emission (region 8, Neff and Ulvestad 2000) are associated with this region. The region of compact radio emission associated with knot L has a spectral index that indicates thermal emission is the dominant source (~0.18, Neff and Ulvestad 2000). There appear to be no medium/hard X-ray sources associated with this region, although there is diffuse soft X-ray emission throughout the Antennae (Zezas et al., 2002).

2.5.4 The Overlap Region

We find our SFR estimates are systematically lower for the SGMCs in the overlap region than the estimates from Brandl et al. (2009), perhaps related to the different TIR calibrators used. For clouds in the overlap region, Brandl et al. (2009) estimate $0.61\,\mathrm{M_\odot\,yr^{-1}}$ for SGMC1 (their Peak 3, corrected) and $3.14\,\mathrm{M_\odot\,yr^{-1}}$ for SGMC345 (the addition of their measurements for their Peaks 1 and 2, corrected). Our estimate for SGMC2 (their Peak 5), $0.63\,\mathrm{M_\odot\,yr^{-1}}$, agrees well with their value of $0.55\,\mathrm{M_\odot\,yr^{-1}}$ (corrected). Brandl et al. (2009) suggest that L_{TIR} estimates may be high for regions with stellar populations <10 Myr; this in particular would affect measurements in the overlap region, which contains stellar populations as young as $\sim 2-5\,\mathrm{Myr}$ (Brandl et al., 2009; Gilbert and Graham, 2007; Mengel et al., 2005; Snijders, Kewley, and van der Werf, 2007; Whitmore and Zhang, 2002). Additionally, mid-IR fluxes are more sensitive to younger stellar populations (Kennicutt and Evans, 2012), and these wavelengths may be better tracers of star formation in the overlap region; this could explain the discrepancy between our measurements (from 24, 70, and 100 μm IR observations) and those from Brandl et al. (2009), implying our estimates may be low.

There are numerous studies on star formation in the overlap region, with recent high-resolution ALMA studies now revealing the formation of superstar clusters (SSCs) (Herrera and Boulanger, 2017; Johnson et al., 2015; Whitmore et al., 2010). At higher resolution, it is easier to distinguish the individual SGMCs, their associated clusters, and the conditions accompanying them. Theoretical studies of SSCs suggest that high pressures ($P/k_B \sim 10^7 - 10^8\,\mathrm{K\,cm^{-3}}$) are required for their formation (Herrera and Boulanger, 2017). As mentioned above, Schirm et al. (2014) found moderate pressures across the entire system, $P/k_B \sim 10^5\,\mathrm{K\,cm^{-3}}$ using an excitation analysis of multiple-J transitions of CO. However, these observations were using lower-resolution data ($\sim 43''$), which likely will not capture the conditions necessary to form SSCs, because these form on much smaller scales. The existence of SSCs in the overlap region strongly suggests that gas pressures are higher than these previous estimates.

Our apertures in the overlap region coincide with bright star-forming knots B (our aperture SGMC345), C, and D (Rubin, Ford, and D'Odorico 1970; Whitmore et al. 2010, our SGMC1), and a more extended star-forming region 2 (Whitmore and Schweizer 1995, our SGMC2, C6, C7, and C8*). Our C9* region is adjacent (west) to star-forming knot B and does not coincide with bright optical star-forming regions. The strongest thermal radio source in Neff and Ulvestad (2000) lies in the overlap region and falls within our aperture SGMC345. More specifically, this thermal source is overlapping with SGMCs 4 and 5, with SGMC 3 off further to the west. Neff and Ulvestad (2000) estimate that ~5000 O5 stars would be required to ionize this gas, resulting in an absolute magnitude of -15, or 500,000 B0, resulting in a magnitude of -18, bright enough to be detected with HST if the starlight is not obscured by foreground dust or gas. However, Whitmore and Schweizer (1995) do not detect bright cluster emission near this radio source. Therefore, Neff and Ulvestad (2000) suggest that star formation must be embedded in this particular complex, hidden by optical extinction that is at least 4 orders of magnitude. We measure the highest SFR in SGMC345, $1.46\,\mathrm{M_\odot\,yr^{-1}}$, which is consistent with this being the most vigorously star-forming complex in the Antennae.

2.5.5 Conversion Factors

We use the $L_{\mathrm{HCN}}/L_{\mathrm{CO}}$ ratio as an estimator of dense-gas fraction across the Antennae, assuming constant conversion factors, α_{HCN} and α_{CO}. However, if α_{HCN} and α_{CO} vary across the Antennae, the trends we see between L_{TIR}, L_{HCN}, and L_{CO} may not be a consequence of different dense-gas fractions. In particular, the CO conversion factor can vary with several gas properties, including metallicity, CO abundance, temperature, and gas density variations (see Bolatto, Wolfire, and Leroy 2013). Using computational models, Narayanan et al. (2011) study the effects of varying physical properties on α_{CO} in disks and merging systems, and they find α_{CO} is typically lower in regions of active star formation in merger-driven starbursts. This is primarily due to higher gas temperatures and larger gas velocity dispersions in these systems (from increased thermal dust-gas coupling). They also show that α_{CO} can either stay low or rebound after the starburst phase ends, depending on H_2 or CO abundances and the time required to revirialize gas. If we extrapolate these results to the ∼kpc scales studied in the Antennae, one would expect the overlap region to have a smaller α_{CO} than the two nuclei, because this is the most vigorously star-forming region in the merger.

However, Zhu, Seaquist, and Kuno (2003) find evidence that the CO conversion factor may be 2-3 times lower in NGC 4038 than in the overlap region using Large Velocity Gradient modeling of multiple ^{1}2CO and ^{1}3CO transitions. They find $X_{\mathrm{CO}} \sim (5.1 - 6.4) \times 10^{19} (10^{-4}/x_{\mathrm{CO}})\,\mathrm{cm^{-2}}\,(\mathrm{K\,km\,s^{-1}})^{-1}$ in the overlap region and $X_{\mathrm{CO}} \sim 2.3 \times 10^{19} (10^{-4}/x_{\mathrm{CO}})\,\mathrm{cm^{-2}}\,(\mathrm{K\,km\,s^{-1}})^{-1}$ for NGC 4038, where X_{CO} is the two-dimensional conversion factor, ΔV is the line width, and x_{CO} is the CO abundance relative to H_2 (the CO abundance is typically $x_{\mathrm{CO}} \sim 10^{-5} - 10^{-4}$ in starbursts, Booth and Aalto 1998; Mao et al. 2000). Zhu, Seaquist, and Kuno (2003) argue that the lower conversion factor in NGC 4038 is due to high-velocity dispersion, large filling fraction, and low optical depth of the CO-emitting gas. Sandstrom et al. (2013) show that the CO conversion factor is lower by a factor of ∼2 (on average) in the central 1 kpc of a sample of 26 star-forming disk galaxies, and they also find that it can be up to 10 times lower than the standard Milky Way value ($\alpha_{\mathrm{CO}} = 4.4\,\mathrm{M_\odot\,pc^{-2}}\,(\mathrm{K\,km\,s^{-1}})^{-1}$). Sandstrom et al. (2013) suggest several explanations for this discrepancy in α_{CO} in the central regions of these galaxies, including differences in ISM pressure, higher molecular gas temperatures, and/or more diffuse ISM molecular gas; optical depth variations can also alter the conversion factor of the gas and can act in accordance with any of the previous effects.

It is possible that the effects on α_{CO} in galaxy centers observed in the Sandstrom et al. (2013) sample could still apply to the two nuclei in the Antennae. If α_{CO} is indeed lower in NGC 4038, this would decrease the total molecular mass estimates in that nucleus and would increase the dense-gas fraction in NGC 4038, thus exacerbating the difference between this nucleus and the overlap region. Metallicities have been found for young and intermediate stellar clusters across the Antennae ranging from slightly subsolar to super-solar ($Z = 0.9 - 1.3\,Z_{\odot}$, Bastian et al. 2009), but there are no obvious differences between clusters near the two nuclei versus those in the overlap region. High-resolution observations resolving gas at ~kpc scales of multiple CO transitions have yet to be done in the Antennae, and therefore gas properties such as density, temperature, and abundance are not constrained at these scales.

The conversion between HCN luminosity and dense-gas mass is not as well studied as the CO conversion factor, but the HCN conversion factor is derived using the same principles assumed for α_{CO}. Thus, α_{HCN} may also change with metallicity, pressure, temperature, density, etc. Observations of HCN and HCO+ lines in (U)LIRGs suggest that HCN can experience a large range of excitation conditions (e.g. Papadopoulos, 2007; Papadopoulos et al., 2014), with some of these extreme galaxies showing subthermal HCN emission (i.e., Mrk 231, Papadopoulos 2007). Galactic observations of HCN in Orion A also show that HCN can be excited at more moderate densities, $n \sim 10^3\,\mathrm{cm}^{-3}$ (Kauffmann et al., 2017a), missing dense gas entirely in some star-forming environments. Shimajiri et al. (2017) directly compare HCN $J = 1-0$ emission and dust column density maps in three galactic star-forming clumps and find evidence that α_{HCN} may decrease with increasing local far-UV radiation field, G0. In an attempt to calibrate α_{HCN} numerically, Onus, Krumholz, and Federrath (2018) study the dependence of α_{HCN} on different physical conditions using simulations of star-forming gas at ~2 pc scales. They find that variations in HCN abundance (3.3×10^{-9} versus 3×10^{-8}) change α_{HCN} by a factor of ~2, and that moderate differences in temperature (10 versus 20 K) can also alter α_{HCN}, but less significantly. So far these observations and simulations have been limited to small spatial scales (on the order of ∼10 pc). At these smaller scales, there is some expected stochasticity of physical conditions within molecular clouds that may affect α_{HCN}. For applications to extragalactic observations, this work needs to be expanded to larger scales (kiloparsecs) to better estimate α_{HCN}.

2.5.6 Dense-gas Fractions

Traditionally, the dense-gas fraction is estimated as the direct ratio of total molecular mass (traced by CO) to dense-gas mass (traced by HCN). This works under the assumption that CO is tracing the mean density of gas, while HCN is tracing only the high-density gas that is more directly associated with star formation. However, recent work on the CMZ suggests that this may be an oversimplification; Kruijssen et al. (2014) show that the overall gas density PDF can be pushed to significantly higher densities via turbulence, while the gas densities more directly associated with star formation are even higher (Rathborne et al. 2014). In this regime, HCN is a better tracer of the mean density of gas. Therefore, our interpretation of the $L_{\mathrm{TIR}}/L_{\mathrm{dense}}$ and $L_{\mathrm{HCN}}/L_{\mathrm{CO}}$ ratios may vary depending on the regime of star formation we are in.

Current turbulent models of star formation predict lognormal gas density PDFs that evolve to have power-law tails once gravitational collapse begins in the process of star formation (e.g. Federrath and Klessen, 2012). Gravitational collapse will begin once the gas reaches a threshold density that is high enough to overcome pressure support in the cloud. If the source of pressure is turbulence, it can act to (1) widen the gas density PDF, and/or (2) push the overall mean density of the gas to higher values (Federrath and Klessen, 2012). In this case, we may expect to see an enhancement of luminosities of dense-gas tracers, such as HCN, relative to lower-density gas tracers such CO (see Leroy et al. 2017).

We suggested in Section 2.5.2 that similar effects of the gas and star formation in the CMZ may be affecting the two nuclei in the Antennae. If the gas density PDF is indeed shifted to higher densities in the nuclei, this may result in a smaller HCN conversion in these regions, which would decrease the dense-gas fraction in these regions. For example, turbulence in the CMZ has the effect of driving up the mean density of gas to $n(\mathrm{H_2}) \sim 10^4\,\mathrm{cm}^{-3}$, which is 100 times larger than the mean density of GMCs elsewhere in the Milky Way (Rathborne et al., 2014). Similarly, the threshold of gas required for star formation (also referred to as a critical density in some literature) in the CMZ is also higher, $n(\mathrm{H_2})_{\mathrm{thresh}} \sim 10^6\,\mathrm{cm^{-3}}$ (Rathborne et al., 2014). Therefore, an accurate measure of dense-gas fraction in this region is a comparison of the mass at densities $> 10^6\,\mathrm{cm^{-3}}$, $M(> 10^6\,\mathrm{cm^{-3}})$, to that of the total molecular gas content. In the CMZ, HCN can be well excited already at $n(\mathrm{H_2}) \sim 10^4\,\mathrm{cm^{-3}}$, the mean density of the gas. This makes HCN a better tracer of the mean density of gas in the CMZ, rather than CO. Similar effects likely affect the luminosity measurements in the nuclei of the Antennae.

2.6 Conclusions

We present a study of the dense-gas content and star formation in NGC 4038/9, with detections of HCN, HCO+, and HNC $J = 1-0$ emission in four distinct regions of the Antennae: the two nuclei (NGC 4038, NGC 4039), the overlap region, and the western arm. We consider the two nuclei separately as they exhibit differences in dense-gas line ratios and star formation activity.

1. The two nuclei show a suppression in the $L_{\mathrm{TIR}}/L_{\mathrm{HCN}}$ ratio, despite showing an enhanced $L_{\mathrm{HCN}}/L_{\mathrm{CO}}$ ratio, when compared with the overlap and western arm regions. Assuming constant conversion factors, α_{HCN} and α_{CO}, this suggests the two nuclei have a higher dense-gas fraction and lower star formation efficiency of dense gas compared with the rest of the Antennae. One potential explanation for this is an increase in overall turbulence in these regions that acts to suppress star formation while also increasing the overall gas density, similar to what appears to be happening in the CMZ in the Milky Way (Kruijssen et al., 2014). This behavior is expected in the pre-starburst phase of merger systems (Narayanan et al., 2011).

2. The Antennae data extend the L_{TIR} versus L_{HCN} relationship observed by Gao and Solomon (2004a,b) to lower luminosity, consistent with the results from Bigiel et al. (2015). The Antennae data points fit within the scatter of the Gao and Solomon (2004a,b) and Liu, Gao, and Greve (2015) data points.

A fit of the Antennae data with that of Liu et al. results in a power-law index of $m \sim 1$.

3. A fit to the Antennae $L_{\rm TIR}$ and $L_{\rm HCN}$ data shows a sublinear relationship with a power-law index $m \sim 0.5$ (hexagonal apertures). Fits with $L_{\rm HCO^+}$ and $L_{\rm HNC}$ similarly show sublinear power law indices of $m \sim 0.5$ and $m \sim 0.6$, respectively. Assuming $L_{\rm TIR} \sim$ SFR and $L_{\rm HCN} \sim M_{\rm dense}$, this indicates variations in the star formation efficiency of dense gas across this system, such that $\rm SFE_{dense}$ does not increase directly with $M_{\rm dense}$.

4. Except for NGC 4038 and WArm-3, the HCN/HCO+ ratio is less than unity for regions in the Antennae, and HNC is significantly weaker than HCN and HCO+. These average line ratios of HCN, HCO+, and HNC are consistent with a lower-density ($n < 10^5\,\rm cm^{-3}$) PDR dominated by mechanical heating from stellar UV- and SNe shock-driven chemistry (Loenen et al., 2008).

5. Schirm et al. (2016) revealed bright dense-gas emission in the overlap region and two nuclei. At the tapered resolution of this study, bright HCN and HCO+ $J = 1-0$ emission is also detected along the inner portion of the western arm of the Antennae, which also coincides with a dust lane. Stellar clusters show age gradients, increasing in age toward the inner portion of the arm. Because this coincides with bright dense-gas emission and dust, this supports the idea that the clusters formed via sequential star formation, or larger-scale processes such as density waves or gas cloud collisions (Whitmore et al., 2014).

We thank the referee for their comments, which have helped to improve the paper. This paper makes use of the following ALMA data: ADS/JAO.ALMA#2012.1.1.00185.S. ALMA is a partnership of ESO (representing its member states), NSF (USA), and NINS (Japan), together with NRC (Canada), MOST and ASIAA (Taiwan), and KASI (Republic of Korea), in cooperation with the Republic of Chile. The Joint ALMA Observatory is operated by ESO, AUI/NRAO, and NAOJ. The National Radio Astronomy Observatory is a facility of the National Science Foundation operated under cooperative agreement by Associated Universities, Inc. This work is based in part on observations made with the Spitzer Space Telescope, which is operated by the Jet Propulsion Laboratory, California Institute of Technology, under a contract with NASA. Part of this work is based on observations made with Herschel. Herschel is an ESA space observatory with science instruments provided by European-led Principal Investigator consortia and with important participation from NASA. AB wishes to acknowledge partial support from an Ontario Trillium Scholarship (OTS). CDW acknowledges financial support from the Canada Council for the Arts through a Killam Research Fellowship. The research of CDW is supported by grants from the Natural Sciences and Engineering Research Council of Canada and the Canada Research Chairs program. This research made use of Astropy, a community-developed core Python package for Astronomy (Astropy Collaboration et al., 2018). A significant amount of this research also made use of Matplotlib (Hunter, 2007), Photutils (Bradley et al., 2019), Numpy (Van Der Walt, Colbert, and Varoquaux, 2011), and Pandas (McKinney, 2010) Python packages. This research has made use of the NASA/IPAC Extragalactic Database (NED), which is operated by the Jet Propulsion Laboratory, California Institute of Technology, under contract with the National Aeronautics and Space Administration. This research has made use of NASA's Astrophysics Data System Bibliographic Services.

2.A Appendix: Uncertainties

2.A.1 Molecular Luminosities

There are three primary sources of uncertainty on the molecular luminosities that we consider: 1. the calibration uncertainty of the ALMA data (∼5% for Band 3, ALMA Technical Handbook for Cycle 1), 2. the rms uncertainty of the moment zero maps, and 3. the uncertainty on the luminosity distance from Schweizer et al. (2008) that we use. The rms uncertainty per aperture is discussed in Section 2.3 and given by Equation 2.2. There is a 5% flux calibration uncertainty on each pixel that adds with the distance and aperture rms uncertainties in quadrature:

$$\sigma_{L\prime} = L\prime\sqrt{\left(\frac{\sigma_{M_{0,ap}}}{M_{0,ap}}\right)^2 + (0.05)^2 + 2\left(\frac{\sigma_{D_L}}{D_L}\right)^2}$$

2.A.2 Infrared Measurements and Luminosities

Uncertainty maps of the Herschel and Spitzer data are included in each of the downloaded fits files (created by the relevant reduction software) and describe the instrumental uncertainty, such that each pixel has an associated value and uncertainty: $S_\nu(x, y) \pm \sigma_{\mathrm{inst},\nu}(x, y)$. Each of the instruments have a flux calibration uncertainty that also needs to be folded into the total uncertainty estimate of each pixel, σ_{cal}, which are 5%, 5%, and 4% for PACS (Poglitsch et al., 2010), SPIRE (Griffin et al., 2010), and MIPS (Bendo et al., 2012), respectively. For each of the IR maps, we estimate the background level using three separate apertures selected within the flat region of the background in each map. The average of this background level is subtracted from our measurements, and the corresponding background-subtraction uncertainty, $\sigma_{\mathrm{back},\nu}$, is also folded into our final measurement uncertainties. The absolute uncertainty on the flux in a single pixel, S_ν, can be written:

$$\sigma_{S_\nu}(x, y) = \sqrt{\sigma_{\mathrm{inst},\nu}(x, y)^2 + (\sigma_{\mathrm{cal}} \times S_\nu(x, y))^2 + \sigma^2_{\mathrm{back},\nu}}$$

We convert IR fluxes to single-band luminosities using Equation 2.2, so the absolute uncertainty on these luminosities at pixel (x, y) can be written (incorporating the distance uncertainty) as:

$$\sigma_{\nu L_\nu}(x,y) = \nu L_\nu(x,y)\sqrt{2\left(\frac{\sigma_{d_L}}{d_L}\right)^2 + \left(\frac{\sigma_{S_\nu}(x,y)}{S_\nu(x,y)}\right)^2}$$

The monochromatic $L_{\rm TIR}$ calibrations from Galametz et al. (2013) are given in the form $\log(L_{\rm TIR}) = a_i \, \log(\nu_i L_{\nu,i}) + b_i$, where $a_i \pm \sigma_{a_i}$ and $b_i \pm \sigma_{b_i}$ are fit parameters and their uncertainties for IR band i. To derive the uncertainty on $\log(L_{\rm TIR})$, we use standard error propagation:

$$\sigma_{\log(L_{\rm TIR})} = \sqrt{(\log(L_{\nu L_{\nu,i}})\sigma_{a,i})^2 + \sigma_{b,i}^2 + \left(\frac{a_i \sigma_{L_{\nu,i}}}{L_{\nu,i}\,\ln(10)}\right)^2}$$

where the absolute uncertainty on the total infrared luminosity is then:

$$\sigma_{L_{\rm TIR}} = L_{\rm TIR}\,\ln(10)\,\sigma_{\log L_{\rm TIR}}$$

The Galametz et al. (2013) calibrations combining more than one IR band are in the form $L_{\rm TIR} = \sum_i c_i \nu L_\nu(i)$ where $c_i \pm \sigma_{c_i}$ are the fit parameters and their uncertainties for band i. The uncertainties on $L_{\rm TIR}$ are then:

$$\sigma_{L_{\rm TIR}} = \sqrt{\sum_i (c_i \sigma_{\nu L_\nu(i)})^2 + (\nu L_\nu(i)\sigma_{c_i})^2}$$

Galametz et al. (2013) suggest an uncertainty of ∼50% on the monochromatic $L_{\rm TIR}$ estimates, and an uncertainty of ∼30% on those combining multiple bands. Therefore, we cite the uncertainties that are largest (i.e., the percentage uncertainty from Galametz et al. (2013) versus our absolute uncertainty derivations).

2.B Appendix: $L_{\rm TIR}$ Calibrations

We expect that the $L_{\rm TIR}(24 + 70 + 100 + 160 + 250)$ calibration from Galametz et al. (2013) puts the tightest constraints on the total infrared luminosity estimate

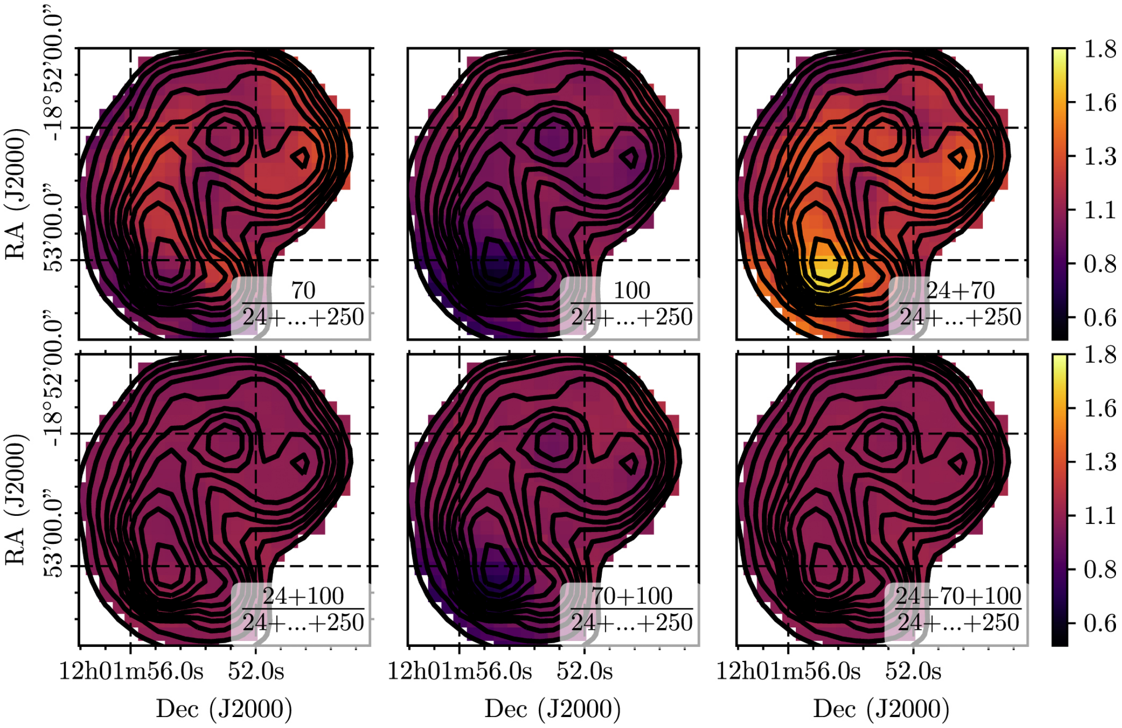

FIGURE 2.6: Ratio maps of Galametz et al. (2013) calibrations at the 250 μm resolution (18.1″) with 250 μm contours overlaid. The $L_{\mathrm{TIR}}(24+70+100+160+250)$ calibration puts the tightest constraints on the total infrared luminosity estimate; therefore, we compare combinations of calibrations with just the higher-resolution IR data (i.e., 24, 70, and 100 μm maps) to this calibration. Top, left to right: $L_{\mathrm{TIR}}(70)/L_{\mathrm{TIR}}(24+70+100+160+250)$, $L_{\mathrm{TIR}}(100)/L_{\mathrm{TIR}}(24+70+100+160+250)$, $L_{\mathrm{TIR}}(24+70)/L_{\mathrm{TIR}}(24+70+100+160+250)$. Bottom, left to right: $L_{\mathrm{TIR}}(70+100)/L_{\mathrm{TIR}}(24+70+100+160+250)$, $L_{\mathrm{TIR}}(24+100)/L_{\mathrm{TIR}}(24+70+100+160+250)$, $L_{\mathrm{TIR}}(24+70+100)/L_{\mathrm{TIR}}(24+70+100+160+250)$.

because it most precisely reproduces the modeled L_{TIR} estimates in Galametz et al. (2013) in comparison with the calibrations using fewer bands. Therefore, we compare other calibrations with just the higher-resolution IR data (i.e., 24, 70, and 100 μm maps) to this calibration to assess their spatial variation across the Antennae. We show ratios of these L_{TIR} calibrations to the $L_{\mathrm{TIR}}(24 + 70 + 100 + 160 + 250)$ at the 250 μm resolution in Figure 2.6. The $L_{\mathrm{TIR}}(24 + 100)$ and $L_{\mathrm{TIR}}(24 + 70 + 100)$ show the least spatial variation when compared with the $L_{\mathrm{TIR}}(24 + 70 + 100 + 160 + 250)$ calibration and agree well (ratio ≈ 1) with this estimate. The remaining calibrations tend to predict higher or lower values in the overlap, particularly near SGMC345.

The $L_{\mathrm{TIR}}(24 + 100)$ weights the 24 μm and 100 μm fluxes with coefficients of 2.453 ± 0.085 and 1.407 ± 0.013, while the $L_{\mathrm{TIR}}(24 + 70 + 100)$ calibration coefficients are 2.192 ± 0.114, 0.187 ± 0.035, and 1.314 ± 0.016 for the 24, 70, and 100 μm fluxes, respectively. The 24 μm and 100 μm fluxes appear to be similarly weighted across these two calibrations, with the 70 μm flux being weighted relatively low for $L_{\mathrm{TIR}}(24 + 70 + 100)$. In comparison with the other calibrations that use the 70 μm flux, this is the lowest 70 μm coefficient. Because of the low/non-dependence of these calibrations on the 70 μm flux, these appear to reduce the (potential) effect of dust heating in the strong-starbursting environment of SGMC345. See Section 2.2.2 for the remainder of our discussion on the variation of different Galametz et al. (2013) calibrations.

Galametz et al. (2013) find the Herschel 100 μm band to be the best monochromatic estimate for L_{TIR} for their sample of galaxies (it is within 30% of their SED-modeled L_{TIR} estimates). This calibration also shows little variation when compared with their modeled L_{TIR} (see Figure 7 in Galametz et al. (2013) as a function of the 70/100 color. The outliers of the 100 μm relationship were mainly strongly starbursting galaxies, NGC 1377 and NGC 5408, with SED peaks at lower IR wavelengths, ~60 and 70 μm, respectively. Galametz et al. (2013) find the 70 μm band tends to overestimate lower IR luminosity objects ($L_{\mathrm{TIR}} < 3 \times 10^8\, L_{\odot}$) and suggest using the 70 μm band as an estimator for starbursting objects. Similarly, Galametz et al. (2013) find the 160 μm calibration tends to underestimate L_{TIR} for hot objects, like starbursts or low-metallicity objects, and overestimate

Table 2.5: Total Infrared Luminosities from Different Calibrations

Source	$24+70+100/70$ Ratio (at 6.8″ res.)	$L_{\rm TIR}(70)$ ($10^9\,L_\odot$ at 6.8″ res.)	$L_{\rm TIR}(70)$ ($10^9\,L_\odot$ at 5.5″ res.)
NGC 4038	0.95	8.1 ± 0.4	8.3 ± 0.4
NGC 4039	0.85	4.9 ± 0.2	5.0 ± 0.3
NGC 4038-2	0.88	0.67 ± 0.03	0.66 ± 0.03
WArm-1	0.92	1.03 ± 0.05	1.08 ± 0.05
WArm-3	0.83	2.8 ± 0.1	2.9 ± 0.1
WArm-2	0.90	0.75 ± 0.04	0.75 ± 0.04
WArm-4	0.86	1.87 ± 0.09	2.0 ± 0.1
SGMC1	0.93	3.3 ± 0.2	3.5 ± 0.2
SGMC2	0.88	5.3 ± 0.3	5.3 ± 0.3
SGMC345	1.03	9.5 ± 0.5	10.1 ± 0.5
Schirm-C6	0.81	2.5 ± 0.1	2.5 ± 0.1
Schirm-C7	0.82	3.8 ± 0.2	4.0 ± 0.2
Overlap-8	0.87	2.1 ± 0.1	2.1 ± 0.1
Overlap-9	1.06	1.48 ± 0.08	1.41 ± 0.07

$L_{\rm TIR}$ for cooler objects. The 70 and 160 μm calibrations provide reasonable estimates of $L_{\rm TIR}$ to within <50%, but Galametz et al. (2013) suggest that the 70 and 160 μm calibrations are used with caution for hot or cold SEDs. Klaas et al. (2010) plot IR SEDs of several clumps that are identified in 24-160 μm maps of the Antennae and find that the SED shape agrees well for most regions across this wavelength range, with peaks at ∼100 μm. However, one clump in their study (which corresponds to the region in the overlap with SGMC345) shows a higher 24/70 ratio (∼0.15 versus $\sim 0.04 - 0.08$), with a hotter SED (peak at ∼70 μm). With this in mind, we compare $L_{\rm TIR}$ from several multiband $L_{\rm TIR}$ calibrations from Galametz et al. (2013) in Figure 2.6 and Table 2.5.

2.C Appendix: Luminosity Ratios

We include line luminosity ratios in Table 2.6 for the elliptical apertures. The table is divided into three sections: 1. The HCN and HCO+ luminosity relative to CO. 2. The total infrared luminosity relative to CO, HCN, and HCO+, and 3. Ratios of our three dense-gas tracers, HCN, HCO+, and HNC.

TABLE 2.6: Luminosity Ratios from Elliptical Apertures

Source	$L_{\mathrm{HCN}}/L_{\mathrm{CO}}$	$L_{\mathrm{HCO^+}}/L_{\mathrm{CO}}$	$L_{\mathrm{TIR}}/L_{\mathrm{CO}}$	$L_{\mathrm{TIR}}/L_{\mathrm{HCN}}$	$L_{\mathrm{TIR}}/L_{\mathrm{HCO^+}}$	$L_{\mathrm{HCN}}/L_{\mathrm{HCO^+}}$	$L_{\mathrm{HNC}}/L_{\mathrm{HCN}}$	$L_{\mathrm{HNC}}/L_{\mathrm{HCO^+}}$
				$L_\odot$ (K km s^{-1} pc^2)$^{-1}$				
NGC4038	0.068±0.015	0.065±0.014	0.200±0.043	2.95±0.24	3.07±0.24	1.04±0.09	0.388±0.039	0.404±0.041
NGC4039	0.050±0.012	0.075±0.017	0.234±0.053	4.67±0.48	3.14±0.29	0.673±0.081	<0.436	<0.293
NGC4038-2	0.026±0.011	0.030±0.013	0.202±0.064	7.9±2.5	6.7±1.9	0.85±0.36	<0.52	<0.4
WArm-1	0.0301±0.0094	<0.03	0.244±0.062	8.1±1.6	>7.4	>0.91	<0.79	–
WArm-2	<0.017	0.0237±0.0079	0.161±0.041	>9.5	6.8±1.5	<0.71	–	<0.68
WArm-3	0.047±0.015	0.038±0.012	0.70±0.18	14.9±2.9	18.3±3.5	1.23±0.33	<0.79	<0.63
WArm-4	0.050±0.017	0.061±0.021	0.80±0.23	16.2±3.5	13.2±2.5	0.81±0.23	0.85±0.26	0.78±0.22
SGMC1	0.026±0.007	0.062±0.015	0.193±0.044	7.4±1.2	3.14±0.32	0.422±0.073	0.45±0.12	0.192±0.044
SGMC2	0.0225±0.0061	0.052±0.012	0.204±0.046	9.0±1.5	3.93±0.42	0.435±0.078	0.312±0.086	0.136±0.034
SGMC345	0.0315±0.0081	0.061±0.015	0.57±0.13	18.0±2.6	9.31±0.96	0.516±0.082	<0.352	<0.182
Schirm-C6	0.025±0.009	0.031±0.011	0.43±0.12	17.6±4.3	13.7±3.2	0.78±0.25	<0.57	<0.44
Schirm-C7	0.0178±0.0057	0.0324±0.0098	0.50±0.12	27.8±6.0	15.3±2.9	0.55±0.15	<0.49	<0.271
Overlap-8	<0.0159	0.0216±0.0073	0.4±0.1	>24.6	18.1±4.1	<0.74	–	<0.61
Overlap-9	<0.028	0.104±0.039	0.90±0.29	>32.0	8.6±1.8	<0.270	>1.01	0.273±0.093

Note. Luminosities measured from the elliptical apertures listed in Table 2.1. All values are measured at the 100 μm resolution (6.8″). The absolute uncertainties are shown next to each ratio, except in the case of limits. We do not show ratios when both luminosity measurements are limits.

Bibliography

Aniano, G., B. T. Draine, K. D. Gordon, and K. Sandstrom (2011). *PASP* 123.908, p. 1218.

Astropy Collaboration et al. (2018). *AJ* 156.3, 123, p. 123.

Bastian, Nate, Gelys Trancho, Iraklis S. Konstantopoulos, and Bryan W. Miller (2009). *ApJ* 701.1, pp. 607–619.

Bendo, G. J., F. Galliano, and S. C. Madden (2012). *MNRAS* 423.1, pp. 197–212.

Bendo, G. J. et al. (2012). *MNRAS* 419.3, pp. 1833–1859.

Bigiel, F. et al. (2015). *ApJ* 815.2, 103, p. 103.

Bigiel, Frank et al. (2016). *ApJl* 822.2, L26, p. L26.

Bolatto, Alberto D., Mark Wolfire, and Adam K. Leroy (2013). *ARAA* 51.1, pp. 207–268.

Booth, R. S. and S. Aalto (1998). *The Molecular Astrophysics of Stars and Galaxies* 4, p. 437.

Bradley, Larry et al. (2019).

Brandl, B. R. et al. (2009). *ApJ* 699.2, pp. 1982–2001.

Briggs, Daniel (1995). PhD thesis. The New Mexico Institute of Mining and Technology.

Chen, Hao, Yu Gao, Jonathan Braine, and Qiusheng Gu (2015). *ApJ* 810.2, 140, p. 140.

Chown, Ryan et al. (2019). *MNRAS* 484.4, pp. 5192–5211.

Daddi, E. et al. (2010). *ApJl* 714.1, pp. L118–L122.

Federrath, C. and R. S. Klessen (2012). *ApJ* 761, 156, p. 156.

Galametz, M. et al. (2013). *MNRAS* 431.2, pp. 1956–1986.

Gallagher, Molly J. et al. (2018). *ApJ* 858.2, 90, p. 90.

Gao, Yu and Philip M. Solomon (2004a). *ApJS* 152.1, pp. 63–80.

— (2004b). *ApJ* 606.1, pp. 271–290.

Gilbert, Andrea M. and James R. Graham (2007). *ApJ* 668.1, pp. 168–181.
Gilbert, Andrea M. et al. (2000). *ApJl* 533.1, pp. L57–L60.
Graciá-Carpio, J., S. Garcá-Burillo, P. Planesas, A. Fuente, and A. Usero (2008). *A&A* 479.3, pp. 703–717.
Griffin, M. J. et al. (2010). *A&A* 518, L3, p. L3.
Groves, Brent et al. (2008). *ApJS* 176.2, pp. 438–456.
Hao, Cai-Na et al. (2011). *ApJ* 741.2, 124, p. 124.
Helfer, Tamara T. and Leo Blitz (1997). *ApJ* 478.1, pp. 162–171.
Herrera, C. N. and F. Boulanger (2017). *A&A* 600, A139, A139.
Hughes, Annie et al. (2013). *ApJ* 779.1, 46, p. 46.
Hunter, J. D. (2007). *Computing in Science & Engineering* 9.3, pp. 90–95.
Jiménez-Donaire, M. J. et al. (2017). *MNRAS* 466.1, pp. 49–62.
Johnson, K. E. et al. (2015). *ApJ* 806.1, 35, p. 35.
Jones, P. A. et al. (2012). *MNRAS* 419.4, pp. 2961–2986.
Karl, Simon J. et al. (2010). *ApJl* 715.2, pp. L88–L93.
Kauffmann, Jens et al. (2017a). *A&A* 605, L5, p. L5.
Kauffmann, Jens et al. (2017b). *A&A* 603, A89, A89.
Kauffmann, Jens et al. (2017c). *A&A* 603, A90, A90.
Kelly, Brandon C. (2007). *ApJ* 665.2, pp. 1489–1506.
Kennicutt Robert C., Jr. (1998). *ApJ* 498.2, pp. 541–552.
Kennicutt, Robert C. and Neal J. Evans (2012). *ARAA* 50, pp. 531–608.
Kepley, Amanda A. et al. (2014). *ApJl* 780.1, L13, p. L13.
Klaas, U., M. Nielbock, M. Haas, O. Krause, and J. Schreiber (2010). *A&A* 518, L44, p. L44.
Kruijssen, J. M. Diederik et al. (2014). *MNRAS* 440.4, pp. 3370–3391.
Krumholz, Mark R. and Christopher F. McKee (2005). *ApJ* 630.1, pp. 250–268.
Lada, Charles J., Jan Forbrich, Marco Lombardi, and João F. Alves (2012). *ApJ* 745.2, 190, p. 190.
Lada, Elizabeth A., John Bally, and Antony A. Stark (1991). *ApJ* 368, p. 432.
Lada, Elizabeth A., D. L. Depoy, II Evans Neal J., and Ian Gatley (1991). *ApJ* 371, p. 171.
Leroy, Adam K. et al. (2016). *ApJ* 831.1, 16, p. 16.
Leroy, Adam K. et al. (2017). *ApJ* 846.1, 71, p. 71.
Liu, L., Y. Gao, and T. R. Greve (2015). *ApJ* 805.1, 31, p. 31.

Loenen, A. F., M. Spaans, W. A. Baan, and R. Meijerink (2008). *A&A* 488.1, pp. L5–L8.

Mao, R. Q. et al. (2000). *A&A* 358, pp. 433–450.

McKinney, Wes (2010). *Proceedings of the 9th Python in Science Conference*. Ed. by Stéfan van der Walt and Jarrod Millman, pp. 56–61.

McMullin, J. P., B. Waters, D. Schiebel, W. Young, and K. Golap (2007). *Astronomical Data Analysis Software and Systems XVI*. Ed. by R. A. Shaw, F. Hill, and D. J. Bell. Vol. 376. Astronomical Society of the Pacific Conference Series, p. 127.

Meijerink, R. and M. Spaans (2005). *A&A* 436.2, pp. 397–409.

Meijerink, R., M. Spaans, and F. P. Israel (2007). *A&A* 461.3, pp. 793–811.

Mengel, S., M. D. Lehnert, N. Thatte, and R. Genzel (2005). *A&A* 443.1, pp. 41–60.

Mengel, Sabine, Matthew D. Lehnert, Niranjan Thatte, Lowell E. Tacconi-Garman, and Reinhard Genzel (2001). *ApJ* 550.1, pp. 280–286.

Mihos, J. Christopher and Lars Hernquist (1996). *ApJ* 464, p. 641.

Murphy, E. J. et al. (2011). *ApJ* 737.2, 67, p. 67.

Narayanan, Desika, Mark Krumholz, Eve C. Ostriker, and Lars Hernquist (2011). *MNRAS* 418.1, pp. 664–679.

Neff, Susan G. and James S. Ulvestad (2000). *AJ* 120.2, pp. 670–696.

Onus, Adam, Mark R. Krumholz, and Christoph Federrath (2018). *MNRAS* 479.2, pp. 1702–1710.

Padoan, Paolo and Åke Nordlund (2011). *ApJ* 730.1, 40, p. 40.

Papadopoulos, Padeli P. (2007). *ApJ* 656.2, pp. 792–797.

Papadopoulos, Padelis P. et al. (2014). *ApJ* 788.2, 153, p. 153.

Pilbratt, G. L. et al. (2010). *A&A* 518, L1, p. L1.

Poglitsch, A. et al. (2010). *A&A* 518, L2, p. L2.

Rathborne, J. M. et al. (2014). *ApJ* 795.2, L25, p. L25.

Reid, M. J. et al. (2014). *ApJ* 796.1, 2, p. 2.

Renaud, Florent, Frédéric Bournaud, and Pierre-Alain Duc (2015). *MNRAS* 446.2, pp. 2038–2054.

Rieke, G. H. et al. (2004). *ApJS* 154.1, pp. 25–29.

Rosolowsky, Erik and Adam Leroy (2006). *PASP* 118.842, pp. 590–610.

Rubin, Vera C., Jr. Ford W. Kent, and Sandro D'Odorico (1970). *ApJ* 160, p. 801.

Sanders, D. B. and I. F. Mirabel (1996). *ARAA* 34, p. 749.

Sandstrom, K. M. et al. (2013). *ApJ* 777.1, 5, p. 5.

Schilke, P. et al. (1992). *A&A* 256, pp. 595–612.

Schirm, Maximilien R. P., Christine D. Wilson, Suzanne C. Madden, and Dave L. Clements (2016). *ApJ* 823.2, 87, p. 87.

Schirm, Maximilien R. P. et al. (2014). *ApJ* 781.2, 101, p. 101.

Schweizer, François et al. (2008). *AJ* 136.4, pp. 1482–1489.

Shimajiri, Y. et al. (2017). *A&A* 604, A74, A74.

Shirley, Yancy L. (2015). *PASP* 127.949, p. 299.

Snijders, Leonie, Lisa J. Kewley, and Paul P. van der Werf (2007). *ApJ* 669.1, pp. 269–288.

Stephens, Ian W. et al. (2016). *ApJ* 824.1, 29, p. 29.

Tacconi, L. J. et al. (2018). *ApJ* 853.2, 179, p. 179.

Talbi, D., Y. Ellinger, and E. Herbst (1996). *A&A* 314, pp. 688–692.

Toomre, Alar (1977). *Evolution of Galaxies and Stellar Populations.* Ed. by Beatrice M. Tinsley and D. Campbell Larson Richard B. Gehret, p. 401.

Usero, Antonio et al. (2015). *AJ* 150.4, 115, p. 115.

Utomo, Dyas et al. (2017). *ApJ* 849.1, 26, p. 26.

van der Tak, F. F. S., J. H. Black, F. L. Schöier, D. J. Jansen, and E. F. van Dishoeck (2007). *A&A* 468.2, pp. 627–635.

Van Der Walt, Stefan, S Chris Colbert, and Gael Varoquaux (2011). *Computing in Science & Engineering* 13.2, p. 22.

Werner, M. W. et al. (2004). *ApJS* 154.1, pp. 1–9.

Whitmore, Bradley C. and Francois Schweizer (1995). *AJ* 109, p. 960.

Whitmore, Bradley C. and Qing Zhang (2002). *AJ* 124.3, pp. 1418–1434.

Whitmore, Bradley C. et al. (1999). *AJ* 118.4, pp. 1551–1576.

Whitmore, Bradley C. et al. (2010). *AJ* 140.1, pp. 75–109.

Whitmore, Bradley C. et al. (2014). *ApJ* 795.2, 156, p. 156.

Wilson, Christine D., Nicholas Scoville, Suzanne C. Madden, and Vassilis Charmandaris (2000). *ApJ* 542.1, pp. 120–127.

— (2003). *ApJ* 599.2, pp. 1049–1066.

Wilson, Christine D. et al. (2008). *ApJS* 178.2, pp. 189–224.

Wu, Jingwen et al. (2005). *ApJl* 635.2, pp. L173–L176.

Zezas, A., G. Fabbiano, A. H. Rots, and S. S. Murray (2002). *ApJ* 577.2, pp. 710–725.

Zhu, Ming, E. R. Seaquist, and Nario Kuno (2003). *ApJ* 588.1, pp. 243–263.

3 | Does the HCN/CO ratio trace the star-forming fraction of gas? I. A comparison to analytical models of star formation.

Bemis A.R., Wilson C.D., 2020, *in preparation*

Department of Physics & Astronomy, McMaster University, Hamilton ON L8S 4M1

Abstract

We use archival ALMA observations of the HCN and CO $J = 1-0$ transitions, in addition to the radio continuum at 93 GHz, to assess the relationship between dense gas, star formation, and gas dynamics in ten, nearby (U)LIRGs and late-type galaxy centers. We frame our results in the context of turbulent and gravoturbulent models of star formation to assess if the HCN/CO ratio is universally a tracer of the fraction of gravitationally-bound, star-forming gas in molecular clouds ($f_{\rm grav}$). We find that the HCN/CO ratio is a good tracer of gas above $n_{\rm thresh} \approx 10^{4.5}$ cm^{-3}, but that this ratio is not necessarily tracing $f_{\rm grav}$. We find strong evidence for the use of varying star formation density threshold models, which are able to reproduce trends observed in $t_{\rm dep}$ and $\epsilon_{\rm ff}$ that fixed threshold models cannot. Composite lognormal and power law models outperform pure lognormal models in reproducing the observed trends, even when using a fixed power law slope. The ability of the composite models to better reproduce star formation properties of the gas provides additional indirect evidence that star formation efficiency (per free-fall time) is proportional to the fraction of gravitationally bound gas.

3.1 Introduction

A current challenge for understanding star formation in molecular clouds is determining the fraction of gas that is converted into stars over a cloud's lifetime. Observations show that sites of star formation are primarily in regions of dense molecular gas in Milky Way clouds (Helfer and Blitz, 1997a,b; Lada, Bally, and Stark, 1991; Lada et al., 1991), and these regions are confined to ~ 0.1 pc scales within larger molecular structures in the form of clumps or filaments (André et al., 2016). Within these structures of gas, it is the gravitationally-bound gas that goes on to form stars. Analytical models of star formation rely on estimates of the self-gravitating gas fraction, $f_{\rm grav}$, to then predict the star formation rate (SFR, e.g. Burkhart and Mocz 2019; Federrath and Klessen 2012; Hennebelle and Chabrier 2011; Krumholz and McKee 2005; Padoan and Nordlund 2011), making $f_{\rm grav}$ an important parameter to constrain observationally.

Extragalactic observations rely on molecular transitions with high critical densities, $n_{\rm crit} \gtrsim 10^4$ cm^{-3} to gain information on the dense gas in other galaxies. The most commonly-used dense molecular gas tracer in extragalactic studies is the HCN $J = 1-0$ transition (Gao and Solomon, 2004a,b). Under the common assumption that the total emissivity of HCN traces the dense gas mass, $I_{\rm HCN} \propto \Sigma_{\rm dense}$, then the ratio of the HCN and CO emissivities, $I_{\rm HCN}/I_{\rm CO}$, is proportional to the fraction of molecular gas in the dense phase, $f_{\rm dense}$. If the dense gas mass traced by HCN is also self-gravitating, then this line ratio is then a simple, observational method for estimating $f_{\rm grav}$. However, the Interstellar Medium (ISM) of galaxies resides at a range of densities $\lesssim 1- \gg 10^8$ cm^{-3}, and molecular transitions are sensitive to a continuum of these densities, including some fraction below their critical density (Leroy et al., 2017b; Shirley, 2015). Recent studies within the Milky Way have also shown that HCN may predominantly trace moderate gas densities (Kauffmann et al., 2017), rather than denser gas associated with star formation.

The physics of ISM dynamics appears to be a combination of gravity, turbulence, and magnetic fields, and these processes act in unison to set the spatial distribution of gas densities and regulate star formation. Analytical models of star formation aim to capture this relationship by connecting the gas density Probability Distribution Function ($n-$PDF) to the star formation efficiency ($\epsilon_{\rm ff}$) over a free-fall time ($t_{\rm ff}$) in molecular clouds (Burkhart, 2018; Federrath and Klessen, 2012; Hennebelle and Chabrier, 2011; Krumholz and McKee, 2005; Padoan and Nordlund, 2011)[1]. Studies have found that the PDF of the diffuse ($n < 1$ cm^{-3}) component of gas in the Milky Way and M33 follows a lognormal PDF (cf. Berkhuijsen and Fletcher 2008; Hill et al. 2008; Tabatabaei et al. 2008. The seminal analytical work by Vazquez-Semadeni (1994) showed that if the turbulent ISM develops a series of isothermal and interacting supersonic shocks, the gas would naturally follow a lognormal PDF (cf. Nordlund and Padoan 1999; Padoan, Jones, and Nordlund 1997; Scalo et al. 1998; Vazquez-Semadeni 1994. In this picture, the shocks amplify each other via a turbulent cascade of energy, and this multiplicative process results in the gas density PDF taking on a lognormal shape (cf. Nordlund and Padoan 1999; Padoan, Jones, and Nordlund 1997; Scalo et al. 1998; Vazquez-Semadeni 1994.

Observations of molecular regions of the ISM reveal that the gas density PDF takes on a different form at high densities. The highest-density regions within more-evolved molecular clouds appear to contribute a power law tail to the gas density PDF (cf. Chen et al. 2018), with some cloud PDFs being almost entirely power law (e.g. Alves, Lombardi, and Lada, 2017; Kainulainen et al., 2009; Lombardi, Alves, and Lada, 2015; Schneider et al., 2013, 2015, 2016). This power law has also been observed in simulations that develop self-gravitating gas (cf. Ballesteros-Paredes et al. 2011; Burkhart, Stalpes, and Collins 2017; Collins et al. 2012; Padoan et al. 2017; Schneider et al. 2015. This strongly suggests that the gas density PDF in a star-forming molecular cloud is likely a combination of a lognormal and power law, and that the power law tail is potentially the result of gas becoming self-gravitating. The fraction of gas within this power law tail is then potentially the self-gravitating gas fraction, $f_{\rm grav}$. If the transition from lognormal to power law occurs at a threshold density, $n_{\rm thresh}$, then $f_{\rm grav}$ can be written as the fraction of mass above $n_{\rm thresh}$, relative to the total mass of a star-forming cloud:

$$f_{\rm grav} = \frac{M(n > n_{\rm thresh})}{M} \tag{3.1}$$

[1]Free-fall time is treated differently depending on the framework used, and in reality it must be a reflection of multiple free-fall times from the array of gas densities that span the $n-$PDF.

Many turbulent models of star formation have estimated $\epsilon_{\rm ff}$ by integrating over a purely lognormal gas density PDF, also above a gas threshold density (cf. Federrath and Klessen 2012; Hennebelle and Chabrier 2011; Krumholz and McKee 2005; Padoan and Nordlund 2011). This threshold density is also meant to capture when gas becomes self-gravitating in the ISM, so that the fraction of gas above this threshold is $f_{\rm grav}$ in these models. However, purely lognormal models fail to explain observed variations in $\epsilon_{\rm ff}$ and mach number, $\mathcal{M}$, seen in some galaxies, (e.g. Leroy et al., 2017a), in which GMCs in M51 show an anticorrelation between velocity dispersion (which is proportional to $\mathcal{M}$) and the star formation efficiency of gas per free-fall time, $\epsilon_{\rm ff}$. Leroy et al. (2017b) argue that this anti-correlation may reflect differences in the dynamical state of their clouds with galactocentric radius. Alternatively, gravoturbulent models of star formation predict an anti-correlation between $\epsilon_{\rm ff}$ and $\mathcal{M}$, without requiring variations in dynamical state (Burkhart and Mocz, 2019).

Burkhart and Mocz (2019) show that the inclusion of a power law tail to the gas density PDF reproduces the observed variations in $\epsilon_{\rm ff}$ in M51, without requiring changes in the dynamical state of the clouds and without explicitly setting $n_{\rm thresh}$, and they find a slight anticorrelation between $\epsilon_{\rm ff}$ and $\mathcal{M}$ for virialized clouds ($\alpha_{\rm vir} \approx 1$). This coincides with an increasing depletion time with $\mathcal{M}$, in agreement with the findings from PAWS (Leroy et al., 2017a). However, in the context of gravoturbulent models, $\epsilon_{\rm ff} \propto f_{\rm grav}$ implies $f_{\rm grav}$ anticorrelates with $\mathcal{M}$. If $I_{\rm HCN}/I_{\rm CO} \propto f_{\rm dense}$ and $f_{\rm dense} \propto f_{\rm grav}$, then this prediction appears contrary to what is observed in starbursts. Starbursts typically have enhanced HCN/CO ratios in addition to shorter depletion time, $t_{\rm dep}$. A potential explanation for these differences may be differences in the timescale for star formation, which may be set by the environment that a gas cloud is immersed in. In this context, the star formation law can be written as (Krumholz, Dekel, and McKee 2012):

$$t_{\rm ff}\Sigma_{\rm SFR} = \epsilon_{\rm ff}\Sigma_{\rm gas} \tag{3.2}$$

where $\Sigma_{\rm SFR}$ is the star formation rate surface density, and $t_{\rm ff}$ is the free-fall time and is set by the self-gravity of a cloud. $\epsilon_{\rm ff}$ is the mass fraction converted into stars over $t_{\rm ff}$, otherwise known as the efficiency per free-fall time. Krumholz, Dekel, and McKee (2012) argue that there are two regimes of star formation that can be separated as the Giant Molecular Cloud regime compared to the Toomre regime. The timescale of star formation of the former is then applicable to the Milky Way and other disk galaxies, while starbursts or mergers may fall into the Toomre regime.

An environmental dependence may be apparent in extragalactic observations. For example, Burkhart and Mocz (2019) demonstrate the connection between $f_{\rm grav}$ and the instantaneous efficiency of the gas, $\epsilon_{\rm inst} \approx \epsilon_0\, f_{\rm grav}$, which reflects both the local efficiency, ϵ_0 (set by e.g. stellar feedback), and $f_{\rm grav}$. This may correlate with its observational analog, the star formation efficiency per free-fall time, $\epsilon_{\rm ff}$ (Krumholz and McKee, 2005; Lee, Miville-Deschênes, and Murray, 2016). Furthermore, if turbulence plays a significant role in setting $n_{\rm thresh}$, then we may find a correlation between $\epsilon_{\rm ff}$ and observed velocity dispersions of gas, and turbulent pressure. Turbulent models of the ISM predict a dependence of $\sigma_{\rm n/n_0}$, the density variance of the volume density PDF ($n-$PDF) on the sonic mach number, $\mathcal{M} = \sigma_{v,3D}/c_s$[2]. Kainulainen and Tan (2013) find a correlation between measurements of the velocity dispersion from ^{12}CO and ^{13}CO and the density contrast (N/N_0) of column density PDFs ($n-$PDFs) derived from IR data in several Milky Way clouds, which shows potential in using the CO velocity dispersion to gain information on cloud $n-$PDFs. Before this, Lada et al. (1994) found a correlation between the magnitude of extinction, $A_{\rm V}$, in the Dark Cloud IC 5126 and the standard deviation of $A_{\rm V}$, with extinction increasing with dispersion (Goodman, Pineda, and Schnee, 2009). Combined, these correlations imply that the CO velocity dispersion may be sensitive to the density variance of the $N-$PDF, $\sigma_{\rm N/N_0}$, where $\sigma_{N/N_0} \propto \ln(N/N_0)$, and therefore a probe of the ISM physics.

In external galaxies where resolution is limited, molecular line ratios are an additional tool for assessing $n-$PDF shape. Shirley (2015) showed that molecular transitions have an emissivity[3] that extends over a range of gas densities, including a significant amount of emission at densities below the critical density

[2] The sound speed is given by $c_s = \sqrt{kT_{\rm kin}/\mu m_{\rm H}}$, $T_{\rm kin}$ is the gas kinetic temperature, $\mu = 2.33$ (Kauffmann et al., 2008) is the mean molecular weight, and $m_{\rm H}$ is the Hydrogen mass. $\sigma_{v,3D}$ is the three-dimensional velocity dispersion and is related to the one-dimensional velocity dispersion via $\sigma_{\rm 3D,v} = \sqrt{3}\sigma_{\rm v}$.

[3] Emissivity, which describes the emission per mass surface density, is effectively the inverse of a molecular line conversion factor.

associated with that transition[4]. To determine if molecular line ratios stay sensitive to $n-$PDF shape, Leroy et al. (2017b) model molecular line emissivities and explore a range of $n-$PDF shapes. They find that dense gas tracers (such as HCN and HCO^+) are more sensitive to changes in the shape of the $n-$PDF than lower-density tracers like CO. Combining molecular line ratios of dense gas tracers with information on kinematics therefore remains a promising tool for assessing $n-$PDF information of clouds in external galaxies.

To assess the relationship between the HCN/CO ratio and $f_{\rm grav}$, we look to more extreme star-forming environments in which turbulence is stronger (e.g. mergers, starbursts, (U)LIRGs, barred galaxies). We study a sample of 10 (U)LIRGs and disk galaxy centers that have archival CO, HCN, CN, and HCO^+ $J = 1 - 0$ data, in addition to the 93 GHz radio continuum. In this chapter, we focus on general trends of the HCN/CO ratio, the star formation rate surface density, and $\epsilon_{\rm ff}$, and we compare these modelled trends with the observed trends in our sample. We use the EMPIRE sample of galaxies (Jiménez-Donaire et al., 2019) as a comparison, which predominantly targets normal regions of star formation within galaxy disks.

3.2 Data and Sample

Our sample consists of ten nearby ($z < 0.03$) galaxies, including the dense centers of five disk galaxies and five mergers and (U)LIRGs. We list these galaxies and their basic properties in Tables 3.1 and 3.2. Four of the five disk galaxies in our sample are also barred (excluding Circinus). For each galaxy, we image archival ALMA data of the HCN, CN, CO, and HCO^+ $J = 1-0$ transitions, in addition to the radio continuum emission at 93 GHz. The data are $uv-$matched and tapered to a common beam for each individual galaxy. The sample selection and data reduction process are presented in Wilson, Bemis, and Kimli (2020) in detail, except for NGC 4038/9, NGC 1808, and NGC 3351, which have been reduced and imaged separately at higher velocity resolutions to be included in this analysis.

[4]Here the critical density is the density at which collisional interactions balance instantaneous de-excitation of a particular molecular transition (Draine, 2010)

TABLE 3.1: Spatial and spectral resolutions of the data for each galaxy. Distances and redshifts are also listed, which are used to determine the physical scale (in pc) per pixel, and to convert measured flux to luminosities. Redshifts are taken from the NASA/IPAC Extragalactic Database (NED). Inclination angles are taken from the papers listed below the table. Distances are the same as in Wilson, Bemis, and Kimli (2020), except for NGC 3627. We use the distance for NGC 3627 taken from Jiménez-Donaire et al. (2019) for consistency when comparing with the EMPIRE data.

Galaxy	Matched Beam ($''$)	Distance[a] (Mpc)	Physical Scale (pc)	δv (km s^{-1})	i^b ($^\circ$)	z
M83	2.10	4.7	48	10	24	0.00171
Circinus	3.00	4.2	61	20	66	0.00145
NGC 3351	3.45	9.3	156	10	45.1	0.00260
NGC 3627	4.15	9.4	189	20	56.5	0.00243
NGC 1808	3.75	7.8	142	10	57	0.00322
NGC 7469	0.95	66.4	306	20	45	0.01632
NGC 3256	2.20	44	469	27.5	–	0.00935
NGC 4038	5.00	22	110	5.2	–	0.00569
IRAS 13120-5453	1.10	134	715	20	–	0.02076
VV114	2.30	81	903	20	–	0.02007

[a] Distances from Wilson, Bemis, and Kimli (2020)
[b] M83: Tilanus and Allen (1993); Circinus: Jarrett et al. (2003); NGC 3351 & NGC 3627: Sun et al. (2020); NGC 1808: Salak et al. (2019)

3.2.1 Molecular Gas Surface Densities

One of the main goals of this study is to assess variations in the fraction of gas in the dense phase as traced by the HCN and CO molecular line luminosities. Our analysis allows us to estimate trends in the HCN and CO luminosity-to-mass conversion factors (cf. Bolatto, Wolfire, and Leroy 2013), which we define as follows:

$$\alpha_{\rm mol} = \frac{\Sigma_{\rm mol}}{I_{\rm mol}} \qquad [{\rm M}_\odot\,{\rm pc}^2\,({\rm K\ km\ s}^{-1})^{-1}] \tag{3.3}$$

where $\Sigma_{\rm mol}$ is the mass surface density of the molecular gas, including Helium, $I_{\rm mol} = L_{\rm mol}/A_{\rm pix}$ is the intensity in units of K km s^{-1}, and $L_{\rm mol}$ is total luminosity over the physical area of a pixel, $A_{\rm pix}$. To calculate the molecular gas mass surface density, $\Sigma_{\rm mol}$, we apply:

$$\Sigma_{\rm mol} = \alpha_{\rm mol}\ I_{\rm mol}\ \cos(i). \tag{3.4}$$

We apply inclination angles only to the disk galaxies in this sample. Inclination angles are typically uncertain in mergers and (U)LIRGs. With this in mind, the uncorrected measurements of galaxies with non-zero inclinations will result in overestimates of $\Sigma_{\rm mol}$ and other surface densities.

We compare our results using multiple prescriptions of $\alpha_{\rm CO}$, but for ease of comparison with other studies our fiducial value will be $\alpha_{\rm CO} = 1.1$ [M$_\odot$ (K km s^{-1} pc^2)$^{-1}$] for our sample of galaxies, the (U)LIRG value including Helium (Downes, Solomon, and Radford, 1993). This is $\sim$5 times lower than the Milky Way value. This lower value is motivated by evidence that gas in these systems is subject to more extreme excitation mechanisms, e.g. higher temperatures and densities (cf. Bolatto, Wolfire, and Leroy 2013; Downes, Solomon, and Radford 1993 and references therein). Additionally, the gas traced by CO in these systems often shows broad line widths, potentially reducing the opacity of the CO transition (Bolatto, Wolfire, and Leroy, 2013; Downes, Solomon, and Radford, 1993). Downes, Solomon, and Radford 1993 also suggest that CO may be subthermally excited ($T_{\rm ex} < T_{\rm kin}$) in starbursts and (U)LIRGs. We also choose a fixed value of $\alpha_{\rm CO} = 3$ [M$_\odot$ (K km s^{-1} pc^2)$^{-1}$] for the EMPIRE sample of galaxies, since these are mostly disk galaxies and are likely more similar to the Milky Way than to starbursts. In the case of NGC 3627, we use $\alpha_{\rm CO} = 1.1$ [M$_\odot$ (K km s^{-1} pc^2)$^{-1}$].

The HCN conversion factor is less certain. Historically, $\alpha_{\rm HCN} \approx 13.6$ [M$_\odot$ (K km s^{-1} pc^2)$^{-1}$] has been used (Gao and Solomon, 2004a,b), which is appropriate for a virialized cloud core with a mean density $n_{\rm H_2} \sim 3 \times 10^4$ cm^{-3} and brightness temperature $T_{\rm B} \sim 35$ K (e.g., Radford, Solomon, and Downes 1991, and has been corrected for Helium). This HCN conversion factor works under the same assumptions applied to Milky Way $\alpha_{\rm CO} = 4.35$ M$_\odot$ (K km s^{-1} pc^2)$^{-1}$: that this molecular transition is optically thick, and that the gas it traces is in local thermodynamic equilibrium (LTE). If all of the above assumptions are true, then the fraction of dense gas traced by HCN/CO is given by:

$$f_{\rm dense} = \frac{\alpha_{\rm HCN}}{\alpha_{\rm CO}}\frac{I_{\rm HCN}}{I_{\rm CO}}. \tag{3.5}$$

with $\alpha_{\rm HCN}/\alpha_{\rm CO} = 3.2$ implied from the above discussion. However, we distinguish this calculation of $f_{\rm dense}$ from analytical estimates of the fraction of dense, star-forming gas which is generally defined as the mass fraction above the density at which gas becomes self-gravitating, as described in the Introduction of this chapter. In a following chapter, we explore variations in the relative values of $\alpha_{\rm HCN}$ and $\alpha_{\rm CO}$ using a non-LTE radiative transfer analysis.

3.2.2 The Radio Continuum SFR

We detect radio continuum emission at 93 GHz in all of our sources and use this as our SFR tracer. The radio continuum is a combination of thermal (T) free-free emission and non-thermal (NT) synchrotron emission from regions with massive star formation, spanning $\sim 1 - 100$ GHz. At 93 GHz, we are in the regime where thermal free-free emission from young star-forming regions will likely dominate the radio continuum emission. Non-thermal emission is expected to contribute $\sim 25\%$ to the radio continuum luminosity at this frequency (see Murphy et al. 2011; Wilson et al. 2019), assuming an electron temperature $T_{\rm e} \sim 10^4$ K and non-thermal spectral index $\alpha_{\rm NT} \sim 0.84$. This fraction will change if there are variations in either $T_{\rm e}$ or $\alpha_{\rm NT}$. We adopt fixed values for $\alpha_{\rm NT} = 0.84$ and $T_{\rm e} = 10^4$ K, and we use the composite calibration from Murphy et al. (2011) which accounts for both thermal and non-thermal contributions to the SFR:

$$\left(\frac{\mathrm{SFR}_\nu}{M_\odot\ \mathrm{yr}^{-1}}\right) = 10^{-27}\Bigg[2.18\left(\frac{T_\mathrm{e}}{10^4\ \mathrm{K}}\right)^{0.45}\left(\frac{\nu}{\mathrm{GHz}}\right)^{-0.1} + 15.1\left(\frac{\nu}{\mathrm{GHz}}\right)^{-\alpha^{\mathrm{NT}}}\Bigg]^{-1} \times \left(\frac{L_\nu}{\mathrm{erg\ s^{-1}\ Hz^{-1}}}\right) \tag{3.6}$$

At 93 GHz, the radio continuum emission from star-forming regions may overlap with the lower-frequency tail of the dust SED. Wilson et al. (2019) estimate a $\sim 10\%$ contribution from dust at 93 GHz for IRAS 13120-5453, NGC 3256, and NGC 7469, the three most IR-luminous galaxies in our sample. This is done by comparing emission at ~ 230 GHz with that at 90 GHz, which is consistent with a dust emissivity index $\beta \sim 1.5 - 1.8$ (Wilson et al., 2019). The emissivity index is typically between $\beta \sim 1 - 2$ towards cold, dense cores in molecular clouds (cf. Sadavoy et al., 2013; Shirley et al., 2011), but other values cannot be ruled out in the presence of temperature variations. We adopt this correction factor of $\sim 10\%$ for all sources, but we acknowledge that the emissivity of dust at 93 GHz may vary between our sources. We further mask pixels that may be contaminated with AGN emission (cf. Table 3.2).

Variations in T_e and α_NT will impact our SFR estimates from the radio continuum at 93 GHz. Electron temperatures typical of HII regions are $T_\mathrm{e} \sim 5 \times 10^3 - 10^4$ K, which will produce a change of $\sim 30\%$ (Murphy et al., 2011). In contrast to this, α_NT has been observed as low as ~ 0.5, which would also give a change in luminosity $\sim 30\%$ at 93 GHz. Wilson et al. (2019) also find evidence of a significant fraction (up to 50%) of non-thermal emission in NGC 7469 at 93 GHz by comparing with an archival radio continuum map at 8 GHz.

Star Formation Timescales and Efficiency

We use estimates of the Star Formation Rate (SFR) and molecular gas surface densities to estimate the depletion time of the total (mol = CO) and dense (mol =

TABLE 3.2: Relevant characteristics of the galaxies in this sample, including the presence/absence of an AGN, bar, or interaction with another galaxy. These classifications are taken from NED.

Galaxy	AGN	Bar	Interacting	Classification
IRAS13120-5453	Sy 2	N	–	ULIRG
NGC3256	South Nucleus	N	Y	LIRG
VV114	East Nucleus	N	Y	LIRG
NGC7469	Sy 1	–	Y	LIRG
NGC4038	–	N	Y	SB
Circinus	Sy 2	–	–	SB
M83	–	Y	–	SB
NGC1808	Sy 2	Y	–	SB
NGC3351	–	Y	N	SB
NGC3627	LINER/Sy 2	Y	Y	Post-SB

HCN) molecular gas content:

$$t_{\rm dep} = \frac{\Sigma_{\rm mol}}{\Sigma_{\rm SFR}} \tag{3.7}$$

where $\Sigma_{\rm mol}$ is estimated using Eq. 3.4. To estimate the dimensionless star formation efficiency, we compare this depletion timescale with the free-fall timescale, which would be the minimum timescale for star formation if gravity alone regulated this process. A general definition of free-fall timescale can be written as:

$$t_{\rm ff} = \sqrt{\frac{3\pi}{32G\rho}} \tag{3.8}$$

where ρ is a characteristic density of the gas associated with star formation. In Krumholz, Dekel, and McKee (2012), there are multiple definitions of this timescale depending on the dominant physics of the gas, i.e. whether Giant Molecular Clouds (GMCs) are isolated objects with star formation mainly fueled by their own self-gravity, or whether the gas is in a denser, more-continuous environment and clouds are not distinguishable from the ISM. For an isolated GMC, Krumholz, Dekel, and

McKee (2012) estimate:

$$n_{\rm GMC} = \frac{3\sqrt{\pi}G}{4\,\mu m_{\rm H}}\frac{\sqrt{\Sigma^3_{\rm GMC}\Sigma_{\rm gal}}}{\sigma_{\rm v}} \tag{3.9}$$

In the case of an isolated GMC, observations of gas surface density might underestimate $\Sigma_{\rm GMC}$ if the resolution targets scales $> 10 - 100$ pc (Krumholz, Dekel, and McKee, 2012), which may instead trace the surface density of more diffuse gas in the galaxy, $\Sigma_{\rm gal}$. Krumholz, Dekel, and McKee (2012) argue for $t_{\rm ff}$ instead using the density Eq. 3.9 for disk galaxies with clumpy interstellar media. The disk galaxy centers in this analysis are at high resolution, and for simplicity the main results we present maintain a general definition of gas density assuming a fixed line of sight (LOS) depth via $\rho \approx \Sigma_{\rm mol}/R$, where R is equivalent to half of the 'cloud' or gas depth along the line of sight (LOS). We do not know R, so we take a fixed value of 100 pc, unless the resolution is higher than this, and then we take half of the FWHM.

The second Krumholz, Dekel, and McKee (2012) definition of $t_{\rm ff}$ is supposed to be applicable to denser systems where gas in the ISM is continuous, but it is likely not applicable to the (U)LIRGs in our sample, which are mostly disturbed systems not in a disk configuration. Thus, we maintain the definition of mean density assuming a fixed LOS depth. The efficiency of the star-formation process is then estimated by comparing the observed depletion timescales with estimates of the free-fall time:

$$\epsilon_{\rm ff} = \frac{t_{\rm ff}}{t_{\rm dep}} \tag{3.10}$$

which is just the star formation law presented in the Introduction re-written in terms of depletion time.

3.2.3 Velocity Dispersion

We measure the 1-dimensional velocity dispersion of the molecular gas in our sources, σ_v, using the CO $J = 1-0$ transition. The velocity dispersions, $\sigma_{\rm vmeas}$, are measured directly from moment 2 maps produces using the Astropy Spectral Cube package. We correct for broadening of the line due to the finite spectral resolution of our data using Rosolowsky and Leroy (2006):

$$\sigma_v = \sqrt{\sigma_{v\mathrm{meas}}^2 - \frac{\delta v^2}{2\pi}} \tag{3.11}$$

where δv is the channel resolution at which we image the data. This value is then converted to the 3-dimenional velocity dispersion via $\sigma_{v,3D} = \sqrt{3}\sigma_v$.

3.2.4 Uncertainties From a Multi-scale Sample

The spatial resolution of the data in our sample span $\sim 50 - 900$ pc. We consider how this range may impact our measurements from the context of a turbulent ISM, and how we can best interpret measured σ_v and line ratios in our sources. The beam filling fraction, $\phi_{ff,\mathrm{beam}}$ is less of an uncertainty in this study, since the sources with the lowest resolution are (U)LIRGs and likely have filling fractions approaching unity, and the spiral galaxy centers have resolutions approaching cloud scales. This reduces the issue of variations in beam filling fractions from galaxy-to-galaxy. A significant source of uncertainty instead comes from variations in the relative filling fractions of the HCN/CO transitions:

$$\Phi_{\mathrm{HCN/CO}} \approx \frac{r_{\mathrm{HCN}}^2}{r_{\mathrm{CO}}^2}, \tag{3.12}$$

where r_{HCN} and r_{CO} are the average radial extents of HCN and CO, respectively. We explore variations in the filling fraction in chapter 4 from a radiative transfer perspective.

In addition to the uncertainty in $\Phi_{\mathrm{HCN/CO}}$, the velocity dispersion in a turbulent medium is scale-dependent (ℓ) such that (Heyer et al., 2009; Larson, 1981):

$$\sigma_v(\ell) = \sigma_{v,L}\left(\frac{\ell}{L}\right)^p \tag{3.13}$$

where $p \sim 0.33 - 0.5$ depends on the type of turbulence, (e.g. $p \approx 0.33$ for Kolmogorov, Larson 1981), L can be defined as the cloud diameter (or turbulent injection scale) and $\sigma_{\mathrm{v,L}}$ is the cloud dispersion at that scale. A sample of galaxies at different physical scales will therefore be affected by this scale dependence, such that velocity dispersions will be smaller at smaller scales and vice versa. However, this relationship should saturate at the turbulent injection scale, which may mitigate some of this uncertainty. If larger-scale cloud-cloud motions do not affect the velocity dispersions of CO, then this saturation should be detected, although there is still uncertainty in L. This means that lower-resolution observations may still be useful for assessing $\sigma_{\rm v}$. We keep these points in mind as we assess the trends observed in our sample.

3.3 Theoretical Predictions of $f_{\rm grav}$

We consider several prescriptions of $f_{\rm grav}$ in the context of analytical models of star formation, and compare the predictions of these models to measurements of the $I_{\rm HCN}/I_{\rm CO}$ ratio and the star formation properties of our galaxies. We use Eq. 3.2, which is relevant to gravoturbulent models of star formation (KMD12):

$\epsilon_{\rm ff}$[5] is calculated by integrating over the star-forming portion of the density-weighted gas density Probability Distribution Function (PDF, e.g Federrath and Klessen 2012; Hennebelle and Chabrier 2011; Krumholz and McKee 2005; Padoan and Nordlund 2011):

$$\epsilon_{\rm ff} = \epsilon_0 \int_{n_{\rm thresh}}^{\infty} \frac{t_{\rm ff}(n_0)}{t_{\rm ff}(n)} \frac{n}{n_0} p(n) {\rm d}n \tag{3.14}$$

Here $p(n)$ is the cloud's volumetric density PDF, $n-$PDF, and n_0 is its mean density. The $n-$PDF characterizes the distribution of densities of *all* gas within the cloud, including the diffuse atomic and molecular components. We briefly review specific terms within this equation individually.

$p(n)$: Isothermal gas in the presence of supersonic turbulence naturally becomes distributed such that its $n-$PDF is roughly lognormal (Nordlund and Padoan, 1999; Vazquez-Semadeni, 1994; Wada and Norman, 2001), and is taken to be the basic shape of $p(n)$ of the diffuse gas component in analytical models of star formation. The $n-$PDF may then evolve to include a high-density power law tail

[5] $\epsilon_{\rm ff}$ has also been referred to as the star formation rate per free fall time, $\rm SFR_{ff}$ (Krumholz and McKee, 2005; Padoan and Nordlund, 2011), but we refer to this as an efficiency for the remainder of this chapter.

(Burkhart, 2018). In terms of the logarithmic volume density $s = \ln(n/n_0)$, the composite $n - PDF$ is given as:

$$\mathrm{p}_s = \begin{cases} N\frac{1}{\sqrt{2\pi\sigma_s^2}}\exp\left(-\frac{(s-s_0)^2}{2\sigma_s^2}\right), & s < s_t \\ NCe^{-\alpha s}, & s > s_t \end{cases} \tag{3.15}$$

where σ_s^2 is the logarithmic density variance, depends on the underlying physics of the gas, and sets the width of $p(n)$. The factors N and C are normalization constants given by Burkhart (2018), and $s_0 = -0.5\,\sigma_s^2$.

Numerical studies have shown that if the turbulence is super-Alfvénic, and the magnetic field (B) follows a power law relationship with gas density, $B \propto n^{1/2}$, then the logarithmic density variance is given by (Federrath and Klessen, 2012; Molina et al., 2012):

$$\sigma_s^2 = \ln\left(1 + b^2\mathcal{M}^2\frac{\beta}{\beta+1}\right) \tag{3.16}$$

where $\mathcal{M}$ is the mach number, $\beta = P_{\mathrm{th}}/P_{\mathrm{mag}}$ is the plasma beta (which characterizes the ratio of thermal pressure to magnetic pressure), and b is the turbulent forcing parameter (which characterizes the relative amount of solenoidal $b = 1$ or compressive $b = 0.33$ turbulence within the gas). Without a clear prescription for β and b in our sample, we simply take $\beta \to \infty$, which assumes that $B = 0$ G. We take an intermediate value $b = 0.4$, which assumes that turbulence is a mixture of compressive and solenoidal forcing.

Non-isothermal gas exists in reality and can add intermittency resulting in deviations from a lognormal shape of $p(n)$ (Federrath and Banerjee, 2015). For the purpose of this work, we assume an underlying lognormal exists in some $n-$PDFs and and remains a reasonable, intermediate approximation to part of the $n-$PDF (Federrath and Banerjee, 2015). Observations of clouds in the Milky Way are in support of some composite form of $p(n)$, where the power law tail is clearly present in addition to a more-diffuse component of gas. Over time, $p(n)$ may evolve to develop a power law tail at the high-density end which represents gas that is becoming gravitationally unstable to collapse.

n_{thresh}: Gravity overcomes supportive processes and begins the process of collapse above the density threshold, n_{thresh}. The processes competing with gravity may include some combination of magnetic support, internal turbulent motions, external ISM pressures, etc. Any gas with densities higher than $n_{\rm thresh}$ is then potentially gravitationally unstable and star-forming, so $n_{\rm thresh}$ serves as the lower limit of the integration that determines $\epsilon_{\rm ff}$.

$t_{\rm ff}(n_0)/t_{\rm ff}(n)$: Within this integral is a free-fall time factor, which converts the integrand into a dimensionless mass *rate* equivalent to the mass per free-fall time (Federrath and Klessen, 2012). This is treated differently depending on the analytical model being considered, e.g. single free-fall (SFF) time (Krumholz and McKee, 2005; Padoan and Nordlund, 2011) versus multi-free-fall (MFF) time models (Federrath and Klessen, 2012; Hennebelle and Chabrier, 2011), and these differences are summarized in Federrath and Klessen (2012) and Burkhart (2018). MFF models keep this factor in the integral, which predicts different rates of collapse for different densities, while SFF models take this factor out of the integral. Due to this, MFF models predict higher $\epsilon_{\rm ff}$.

ϵ_0: We also note that the prefactor in this equation, ϵ_0 is the *local* dimensionless efficiency of the star formation that depends on additional processes, such as the level of stellar feedback dispelling some of the gas that is already above $n_{\rm thresh}$ (Burkhart and Mocz, 2019). The mass that does get converted into stars is then $M_* = \epsilon_0 M(n > n_{\rm thresh})$.

Finally, we want to connect these theoretical estimates of $\epsilon_{\rm ff}$ to observations. We are actually measuring the local average of instantaneous efficiency, $\epsilon_{\rm inst} \approx \epsilon_0(t)\, f_{\rm grav}(t)$, through observations (Burkhart and Mocz, 2019). The fraction of gas above $n_{\rm thresh}$ is expected to evolve over time and approach a finite value, so that $f_{\rm grav}(t) \rightarrow f_{\rm max}$ and $\epsilon_{\rm inst} \rightarrow \epsilon_{\rm int}$, where $f_{\rm max}$ is the fraction of gas that becomes bound over the lifetime of a cloud and $\epsilon_{\rm int}$ is the integrated efficiency over the lifetime of a cloud (Burkhart and Mocz, 2019). This means that measurements of $\epsilon_{\rm inst} < \epsilon_{\rm ff}\, t_*/t_{\rm ff,0}$, and therefore $\epsilon_{\rm inst}$ likely underestimates $\epsilon_{\rm ff}$, and will be off by a factor proportional any additional mass that will go on to form stars in the future that is not yet gravitationally-bound. Since stars do not form instantaneously and do so over some finite timespan, $\epsilon_{\rm ff}$ also depends on the protostellar lifetime, t_*, relative to the mean free-fall time, $t_{\rm ff,0}$. This is given via Eq. (23) in Burkhart and

Mocz (2019) and is given in Lee, Miville-Deschênes, and Murray (2016):

$$\epsilon_{\rm ff} = \epsilon_{\rm int} \frac{t_{\rm ff,0}}{t_*}. \tag{3.17}$$

We note, however, that t_* may appear constant when averaging over a population of clouds in lower-resolution studies. To compare theory to observations, we actually need to calculate the following:

$$\epsilon_{\rm inst} \approx \epsilon_{\rm ff} \frac{t_*}{t_{\rm ff,0}} \times \frac{\epsilon_0 \, f_{\rm grav}}{\epsilon_0' \, f_{\rm max}}, \tag{3.18}$$

where we include $f_{\rm grav}/f_{\rm max}$, the current fraction of gravitationally-bound gas relative to the total fraction that gets converted into stars, and ϵ_0/ϵ_0', the ratio of the local efficiency now to the local efficiency at the end of the cloud lifetime. Lee, Miville-Deschênes, and Murray (2016) find $t_{\rm ff,0}/t_* \approx 1.1 - 2.3$. We are able to estimate $f_{\rm grav}$ by integrating over the model $n-$PDF above the threshold density. For simplicity, we assume $t_{\rm ff,0}/t_* = 1$ and $\epsilon_0' \, f_{\rm max} = 1$, so that we only multiply the model $\epsilon_{\rm ff}$ by ϵ_0 and $f_{\rm grav}$ to obtain $\epsilon_{\rm inst}$.

The observational efficiency is estimated via by taking the ratio of the free-fall time to the depletion time, $\epsilon_{\rm ff} = t_{\rm ff}/t_{\rm dep}$. Federrath and Klessen (2012) and Burkhart (2018) both provide analytical equations for estimating $\epsilon_{\rm ff}$ for different gravoturbulent formalisms which we adopt in this analysis. We use the Padoan and Nordlund (2011) formalism (cf. Burkhart and Mocz, 2019; Federrath and Klessen, 2012) to estimate $\epsilon_{\rm ff}$ from lognormal-only $n-$PDFs, which is given by:

$$\epsilon_{\rm ff,PN11} = \frac{\epsilon_0}{2} \left\{ 1 + {\rm erf}\left(\frac{\sigma_2^2 - 2\, s_{\rm thresh}}{\sqrt{8}\sigma_s} \right) \right\} \exp\left(s_{\rm thresh}/2 \right) \tag{3.19}$$

where $s_{\rm thresh} = \exp\left(n_{\rm thresh}/n_0 \right)$. This is almost identical to the Krumholz and McKee (2005) formalism for $\epsilon_{\rm ff}$ if we remove the exponential factor containing $s_{\rm thresh}$. The equation for $\epsilon_{\rm ff}$ using a composite LN+PL $n-$PDF is given by (Burkhart, 2018):

$$\epsilon_{\rm ff,BM18} = N \exp\left(s_{\rm thresh}/2\right) \frac{\epsilon_0}{2} \left\{ \mathrm{erf}\left(\frac{\sigma_2^2 - 2\, s_{\rm thresh}}{\sqrt{8}\sigma_s}\right) - \mathrm{erf}\left(\frac{\sigma_2^2 - 2\, s_{\rm t}}{\sqrt{8}\sigma_s}\right) + C\frac{\exp(\mathrm{s_t}(1-\alpha))}{\alpha - 1} \right\} \tag{3.20}$$

where s_t is the density at which the $n-$PDF transitions from a lognormal to power law shape, and N is a normalization factor.

3.3.1 Connecting Observations to Theory

In this section we outline how we connect theory with observation. We begin by providing a list of the analytical models we refer to in our analysis. These models are divided into two main subgroups based on their prescription for the density threshold. We mainly refer to analytical equations from Burkhart (2018) for brevity, but also refer the reader to Federrath and Klessen (2012) for another comprehensive summary of analytical models, as well as the original papers that have provided the basis of this work, e.g. Hennebelle and Chabrier (2011), Krumholz and McKee (2005), and Padoan and Nordlund (2011). The models we consider are as follows:

1. Models with a density threshold which varies according to $n_{\rm thresh} \propto \mathcal{M}^2$.
   (a) LN only $n-$PDF: We adopt the Padoan and Nordlund (2011) formalism to calculate $\epsilon_{\rm ff}$ and use their $n_{\rm thresh}$[6]. These quantities are given by Eqs. (13) and (11), respectively, in Burkhart (2018).
   (b) LN+PL $n-$PDF: We use Eq. (27) in Burkhart (2018) to calculate $\epsilon_{\rm ff}$. $\epsilon_{\rm ff}$ depends both on a physically-motivated threshold, (i.e. the Padoan and Nordlund 2011 formalism), and the density at which the $n-$PDF transitions from lognormal to a power law shape.
2. Fixed density threshold models for which the threshold density is universally $n_{\rm thresh} = 10^{4.5}$ cm^{-3}.

[6] $n_{\rm thresh}$ is referred to as $n_{\rm crit}$ in Padoan and Nordlund (2011) and Burkhart (2018), not to be confused with the critical density for a molecular transition.

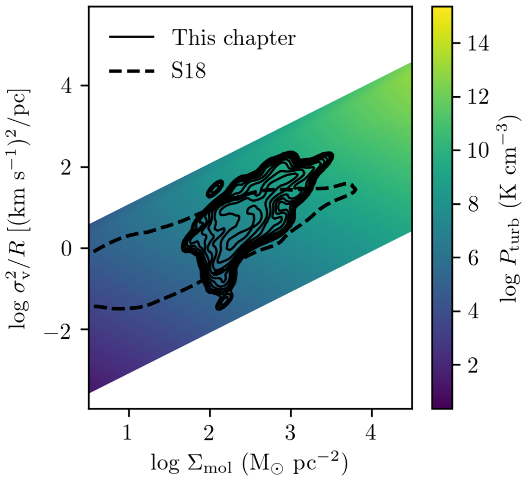

FIGURE 3.1: The grid of $\sigma_{\rm v}$ and $\Sigma_{\rm mol}$ used as inputs to the analytical models, colored by $P_{\rm turb}$. Velocity dispersion is also proportional to $\sigma_{\rm v} \propto \mathcal{M}$ and will follow the same trends as σ_v Similarly, the x-axis is proportional to model mean density. The data are shown as the contour density plots, with our sample as the solid black line, and an outline of the locus of Sun et al. (2018) cloud-scale measurements (dotted line).

(a) LN only $n-$PDF: We use Eq. (13) from Burkhart (2018) to calculate $\epsilon_{\rm ff}$, but instead use a fixed density threshold of $n_{\rm thresh} = 10^{4.5}$ cm^{-3}.

For the LN-only models, we perform a numerical integration of the $n-$PDF above $n_{\rm thresh}$ to calculate $f_{\rm grav}$. Otherwise, $f_{\rm grav}$ is given by Eq. (20) in Burkhart and Mocz (2019), which is referred to as $f_{\rm dense}$ in their work. We produce models over the $\sigma_{\rm v}^2/R - P_{\rm turb}$ parameter space that encompasses our data. We show this grid in Fig. 3.1. The region that we model over is colored by the corresponding $P_{\rm turb}$, which is tied to $n_{\rm thresh}$ in the varying-threshold models. For comparison, we also show the Sun et al. (2018) measurements of cloud-scale observations in nearby galaxies.

We summarize the observational measurements and the quantities that we estimate from them in Table 3.3. In the bottom panel of Table 3.3 we also list equations used to estimate the same quantities using model outputs. These model outputs are normalized by the measured molecular gas surface density, $\Sigma_{\rm mol}$. This normalization provides a side-by-side comparison of model and observational analogues and the underlying assumptions that go into these calculations.

TABLE 3.3: Observational quantities (top panel) compared to model inputs and outputs (bottom panel). We fix $T_{\mathrm{kin}} = 45$ K, $b = 0.4$, and $\beta \to \infty$ in this analysis, and we model over the observed ranges of Σ_{mol} and σ_{v}. Quantities with the subscript 'grid' are input from the grid shown in Fig. 3.1.

	Observational Estimate	Eqn.	Unit
	$\Sigma_{\mathrm{mol,obs}}$	$\alpha_{\mathrm{CO}}\,(I_{\mathrm{CO}}\,/\,\mathrm{K\ km\ s^{-1}})$	$M_\odot$ pc^{-2}
	$\Sigma_{\mathrm{mol,dense,obs}}$	$3.2\,\alpha_{\mathrm{CO}}\,(I_{\mathrm{HCN}}\,/\,\mathrm{K\ km\ s^{-1}})$	$M_\odot$ pc^{-2}
(1)	$\Sigma_{\mathrm{SFR,obs}}$	$1.14 \times 10^{-29}\,(L_{93\,\mathrm{GHz}}\,/\,\mathrm{erg\ s^{-1}\ Hz})$	$M_\odot$ yr^{-1} kpc^{-2}
(2)	$P_{\mathrm{turb,obs}}$	$(3/2)\,\Sigma_{\mathrm{mol}}\sigma_{\mathrm{v}}^2/R/k_{\mathrm{B}}$	K cm^{-3}
(3)	$t_{\mathrm{dep,obs}}$	$\Sigma_{\mathrm{mol}}/\Sigma_{\mathrm{SFR}}$	yr
	$n_{0,\mathrm{obs}}$	Σ_{mol}/R	kg cm^{-3}
	$t_{\mathrm{ff,obs}}$	$\sqrt{3\pi/32\,G\,n_{0,\mathrm{obs}}}$	yr
(4)	$\epsilon_{\mathrm{ff,obs}}$	$t_{\mathrm{ff,obs}}/t_{\mathrm{dep,obs}}$	–
(5)	f_{dense}	$3.2\,I_{\mathrm{HCN}}/I_{\mathrm{CO}}$	–
(6)	$t_{\mathrm{dep,dense,obs}}$	$\Sigma_{\mathrm{mol,dense}}/\Sigma_{\mathrm{SFR}}$	yr
	Model Estimates Normalized to Obs.	Eqn.	Unit
(2)	$P_{\mathrm{turb,model}}$	$(3/2)\,n_0\sigma_{\mathrm{v}}^2/k_{\mathrm{B}}$	K cm^{-3}
(5)	f_{grav}	Eq. 3.1, Eq. (20) in Burkhart and Mocz (2019)	–
(4)	$\epsilon_{\mathrm{ff,model}}$	Eq. (13) or (27) in Burkhart (2018)	–
(3)	$t_{\mathrm{dep,model}}$	$1/\epsilon_{\mathrm{ff,model}} \times t_{\mathrm{ff,grid}}$	yr
(6)	$t_{\mathrm{dep,grav}}$	$f_{\mathrm{grav}}/\epsilon_{\mathrm{ff,model}} \times t_{\mathrm{ff,grid}}$	yr
(6)	$t_{\mathrm{dep,dense,model}}$	$f_{n>10^{4.5}\,\mathrm{cm^{-3}}}/\epsilon_{\mathrm{ff,model}} \times t_{\mathrm{ff,grid}}$	yr
(1)	$\Sigma_{\mathrm{SFR,model}}$	$\epsilon_{\mathrm{ff,model}} \times \Sigma_{\mathrm{mol,grid}}/t_{\mathrm{ff,grid}}$	$M_\odot$ yr^{-1} kpc^{-2}

Velocity Dispersion as a Tracer of $\mathcal{M}$

As previous studies have done for Milky Way clouds (Kainulainen and Federrath, 2017), we use CO linewidths as an indicator of sonic mach number of the gas in our galaxies:

$$\mathcal{M} = \frac{\sqrt{3}\sigma_{\mathrm{v,1D}}}{c_s}, \tag{3.21}$$

where c_{s} is the thermal sound speed and $\sigma_{\mathrm{v,1D}}$ is the observed one-dimentional velocity dispersion. There are limits to this approach, and the ability of the CO line to trace cloud turbulence may be limited by its optical depth (Burkhart et al., 2013; Goodman, Pineda, and Schnee, 2009), but alternative measures of gas kinematics in extragalactic clouds are absent.

To estimate c_s, we consider an ideal gas equation of state ($P_{\mathrm{th}} = nk_{\mathrm{B}}T/\mu m_{\mathrm{H}}$), such that the sound speed is $c_s = \sqrt{k_{\mathrm{B}}T/\mu m_{\mathrm{H}}}$, where k_{B}, T, μ, and m_{H} are the Boltzmann constant, gas kinetic temperature, the mass of a hydrogen atom, and the mean particle weight. For a gas where hydrogen is primarily in molecular form $\mu = 2.33$ (assuming cosmic abundances, Kauffmann et al. 2008). For $\mu = 2.33$ and a temperature rage of $T = 10 - 100$ K, $c_s \approx 0.2 - 0.6$ km s^{-1}. The choice of c_s can have a significant impact on the estimate of $\mathcal{M}$. For $\sigma_v = 1 - 30$ km s^{-1}, this can be $\mathcal{M} = 5 - 150$ for $c_s = 0.2$ km s^{-1} or $\mathcal{M} = 1.7 - 50$ for $c_s = 0.6$ km s^{-1}. We choose the intermediate value $c_s = 0.4$ km s^{-1}, corresponding to $T \sim 45$ K as our fiducial value.

3.3.2 Power Law Slope

Ballesteros-Paredes et al. (2011) argue that variations in star formation may be due to evolution, and that the $n-$PDF evolves from a lognormal shape to a composite lognormal and power law over time. This is assumed to be from the continuous accumulation of gravitationally-bound gas over time, which contributed a power law to the $n-$PDF. Federrath and Klessen (2013) explore this connection using numerical simulations and find that decreases in power law slope indeed coincide with enhanced star formation efficiencies and vice versa (Burkhart and Mocz, 2019; Federrath and Klessen, 2013), and this is a reflection of the increased fraction of dense gas that coincides with shallow power law slopes. Federrath and Klessen

(2013) supply analytical calibrations for the instantaneous star formation efficiency and the slope of the density power spectrum, γ. Due to the range of velocity dispersions that we are considering, there is no single calibration from Federrath and Klessen (2013) that is appropriate for our data, so we adopt a fixed value of $\alpha = 1.4$.

3.3.3 Two Prescriptions for Density Thresholds

The simplest prescription for f_{grav} is that of fixed density-threshold models, which predict that $n_{\mathrm{thresh}} \approx 10^{4.5}$ cm^{-3}. In this context, the fraction of star-forming gas is any gas above this density. For purely lognormal $n-$PDFs, increases in σ_n and mean density will both contribute to higher f_{grav} and subsequently higher ϵ_{ff}.

A fixed density threshold then has several testable predictions:

- Higher $\mathcal{M}$ contribute to *higher* f_{grav}, higher star formation efficiencies, and ultimately higher Σ_{SFR}. It is then increases in Σ_{mol} that contribute directly to higher Σ_{SFR}, i.e. only the increase in mass is important for increasing Σ_{SFR} for a given $\mathcal{M}$.

- Higher mean densities correlate with *higher* f_{grav}, higher star formation efficiencies, and ultimately higher Σ_{SFR}.

A second, general prescription for n_{thresh} is that this threshold varies temporally and with local environment within galaxies. There are a number of prescriptions for varying n_{thresh}, and each predicts some dependence on the level of virialization of the gas and the level of turbulence affecting the gas, which is characterized via either $\mathcal{M}$ or turbulent pressure, P_{turb} (Walker et al., 2018).

We adopt the Padoan and Nordlund (2011) equation for n_{thresh} which simplifies to:

$$n_{\mathrm{thresh}} \approx 0.54\, n_0\, \alpha_{\mathrm{vir}}\, \mathcal{M}^2 \tag{3.22}$$

when we have taken the prefactor in their original equation to be $\phi = 0.35$ and have neglected magnetic fields. The remaining dependence is then only with mean density, virial parameter (α_{vir}), and $\mathcal{M}$. This equation is nearly identical to the Krumholz and McKee (2005) formalism, which has a prefactor $\pi/15$ (assuming

$\phi_t = 1$). We can also re-frame this equation in terms of the turbulent pressure, which we are able to estimate directly from our data (cf. Walker et al., 2018):

$$n_{\rm thresh} \approx 0.36\, \alpha_{\rm vir} \frac{P_{\rm turb}}{k_B\, T_{\rm kin}} \tag{3.23}$$

where $P_{\rm turb} \approx (3/2)\Sigma_{\rm mol}\sigma_v^2/R$ or $P_{\rm turb} \approx (3/2)n_0\sigma_v^2$ for the data and models, respectively. The direct scaling $n_{\rm thresh} \propto \mathcal{M}^2$ and $n_{\rm thresh} \propto P_{\rm turb}$ assumes that turbulence acts as a supportive process to the gas.

The virial parameter, $\alpha_{\rm vir}$, is given by:

$$\alpha_{\rm vir} \approx \frac{5\sigma_v^2 R}{G\Sigma} \tag{3.24}$$

and is the ratio of internal kinetic to gravitational energy in a cloud, $E_{\rm kin}$ and $E_{\rm grav}$. $\alpha_{\rm vir}$ must also be divided by a factor, $f_{\rm corr}$, to correct for the spatial gas density distribution. We treat the *radial* distribution as a double power law, but its integral is indefinite, so an approximation can be made if the two power laws are treated separately:

$$f_{\rm corr} \approx \left(\frac{1}{3-k_0}\right)\left(1-\frac{r_t}{r_{\rm norm}}\right)^{3-k_0} + \left(\frac{1}{3-\kappa}\right)\left(\frac{n_t}{n_{\rm norm}}\right)^{1-k/3} \tag{3.25}$$

where $r_{\rm norm}$ is the radius corresponding to the density $n_{\rm norm}$. $n_{\rm norm}$ is the mean density for LN-only models, and is a combination of mean density and transition density in the LN+PL models, such that $r_{\rm norm}$ falls between r_0 and r_t, the radii corresponding to mean density and transition density, respectively[7]. It then follows that a higher $n_{\rm thresh}$ would be required for gas to collapse in the case that $E_{\rm kin} > 2 \times E_{\rm grav}$. For the range of scales we target with our observations, estimates of $\alpha_{\rm vir}$ may not be accurate. It is also impossible to distinguish higher $\alpha_{\rm vir}$ from increases in $\sigma_{\rm v}$ due to pressure-confinement. We simply take $\alpha_{\rm vir} = 1$. This assumption then implies that increases in $n_{\rm thresh}$ are primarily due to increases in measurements of turbulence / turbulent pressure of the gas in our galaxies.

A varying density threshold then also has several testable predictions:

[7]For a single power law, the correction factor is instead given by $f_{\rm corr} = (1-k/3)/(1-2k/5)$, where k is the power law slope (Bertoldi and McKee, 1992).

- Clouds with higher $\mathcal{M}$ (higher $P_{\rm turb}$) will have a broader $n-$PDF and higher $n_{\rm thresh}$, *lower* $f_{\rm grav}$, *lower* star formation efficiencies, and ultimately smaller $\Sigma_{\rm SFR}$.

- Higher temperatures may *decrease* $n_{\rm thresh}$ and potentially *increase* $f_{\rm grav}$ and *enhance* star formation efficiencies. This effect will likely be much smaller than changes in $P_{\rm turb}$, which can span > 5 orders of magnitude, compared to $T_{\rm kin}$ which only can span ~ 2 orders of magnitude.

- For the LN+PL models, smaller values of α (i.e. shallower slopes) will result in more mass in the PL tail and higher $f_{\rm grav}$, which will ultimately *enhance* $\epsilon_{\rm ff}$.

The major difference between the predictions for a fixed $n_{\rm thresh}$ and one that varies as $n_{\rm thresh} \propto \mathcal{M}^2$ is whether $\mathcal{M}$ directly enhances or suppresses star formation. We consider this difference when we are comparing the predictions of these analytical models with our data in the following section.

3.4 Results

In this section we review general trends between observation-based quantities and the predictions of those from analytical models of star formation. We focus on variations in star formation timescales (depletion time and free-fall time), star formation efficiency, and the dense gas fraction. We do not directly assess variations in emissivity in this chapter, and defer an analysis of emissivity (and therefore conversion factors) to chapter 4, where we present modelling of the HCN and CO emissivities for our sample of galaxies on a pixel-by-pixel basis.

We convert continuum measurements to SFRs, and we adopt an uncertainty of 30% for SFR estimates derived from the radio continuum. We compare the results of our sample with that of the EMPIRE survey (Jiménez-Donaire et al., 2019), for which there are publicly-available single-dish (IRAM 30m) observations of HCN and CO. We estimate $\Sigma_{\rm SFR}$ in EMPIRE galaxies using 24 μm IR maps from the *Spitzer* Space Telescope. These IR data are convolved to a 15″ Gaussian beam utilizing Aniano et al. (2011) Gaussian kernels and further smoothed to a 33″

Gaussian beam with CASA. Backgrounds are subtracted and SFRs are derived using the Rieke et al. 2009 calibration.

The results from analytical models are binned using equal-frequency binning, and are compared to the data in Figures 3.2-3.10. We show separate plots with only the data and their measurement uncertainties, and we refer to Spearman rank coefficients as a measure of the strength and direction of correlations between two parameters. For reference, a coefficient of $r_s = 0$ indicates that there is no monotonic relationship between the two parameters, negative values indicate negative monotonic relationships, and positive values indicate positive monotonic relationships. In the following discussion, we use the following definitions: $0.1 \leq |r_s| < 0.4$ is considered a weak correlation, $0.4 \leq |r_s| < 0.7$ is considered a moderate correlation, and $|r_s| \geq 0.7$ is considered a strong correlation.

3.4.1 The Kennicutt-Schmidt Relationship

We begin by presenting the Kennicutt-Schmidt (KS) relationship of our data in Fig. 3.2. In the right-hand panel of this figure we compare the data to model predictions of Σ_{SFR}, which are determined using the relevant equation in Table 3.3. We must adopt a local efficiency of $\epsilon_0 = 2\%$ for the LN-only models, or they both over-predict Σ_{SFR} by ~ 2 orders of magnitude. This is consistent with estimates of ϵ_{ff} from observations and simulations imply low efficiencies, which range from $0.01 - \lesssim 20\%$ (Evans et al., 2009; Grudić et al., 2018; Krumholz, 2014; Lada, Lombardi, and Alves, 2010; Lee, Miville-Deschênes, and Murray, 2016; Ostriker and Shetty, 2011; Semenov, Kravtsov, and Gnedin, 2017; Zamora-Avilés and Vázquez-Semadeni, 2014). ϵ_0 is also applied to the LN+PL models, which the imposes a shallower PL slope, $\alpha \sim 1.4$, to remain consistent with the measured Kennicutt-Schmidt relationship (Fig. 3.2).

3.4.2 Does HCN/CO trace f_{grav}?

We compare observational and model estimates of dense gas fraction ($f_{\mathrm{dense}} = \alpha_{\mathrm{HCN}}/\alpha_{\mathrm{CO}}\, I_{\mathrm{HCN}}/I_{\mathrm{CO}}$ and f_{grav} from the models) with estimates of turbulent pressure, P_{turb} in Figs. 3.3 and 3.4. The model comparison to f_{grav} is shown in Fig. 3.4. In the right panel we instead plot the fraction of gas above $n = 10^{4.5}$ cm^{-3}, which

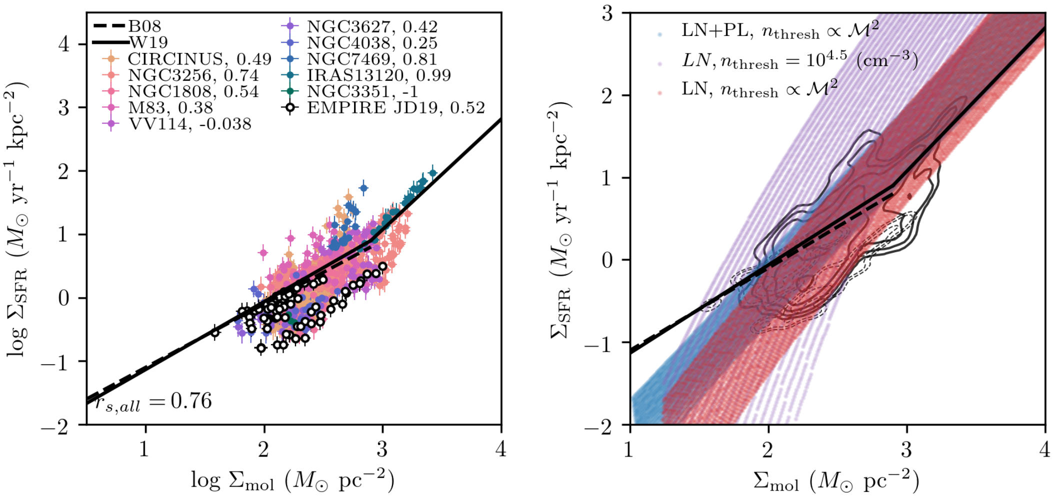

FIGURE 3.2: The Kennicutt-Schmidt relationship for our galaxies and the EMPIRE sample, compared to the model predictions. We also include fits to this relationship from previous studies (e.g. nearby disk galaxies from Bigiel et al. 2008, B08, and (U)LIRGs from Wilson et al. (2019), W19). *Left:* Data is shown for our sample (colorized by galaxy) and the EMPIRE galaxies (white points). Spearman rank coefficients are shown for individual galaxies next to their name in the legend, and the coefficient for the combined sample is shown in the lower left corner. *Right:* We compare the KS relationship of our data to that predicted by the three models we consider in this analysis: the LN+PL model with varying $n_{\rm thresh}$ (blue), the LN-only model with varying $n_{\rm thresh}$ (red), and the LN-only model with a fixed $n_{\rm thresh}$ (purple). We show a contour density plot of our data (solid black contours), and of the EMPIRE data (dashed black contours).

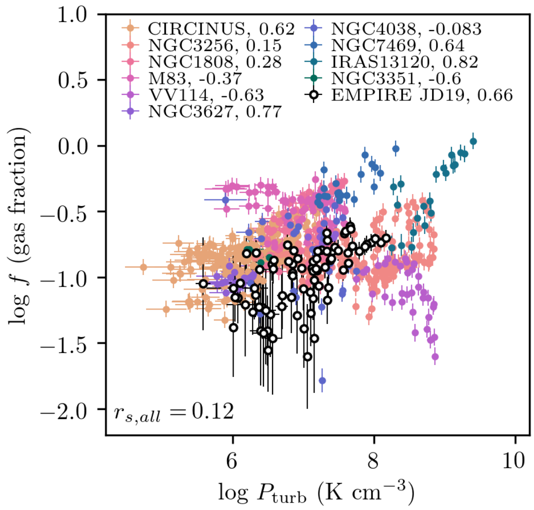

FIGURE 3.3: Gas fraction as a function of turbulent pressure, where $f = \alpha_{\rm HCN}/\alpha_{\rm CO}\, I_{\rm HCN}/I_{\rm CO}$. Data is colorized by galaxy, similar to the formatting in Fig. 3.2.

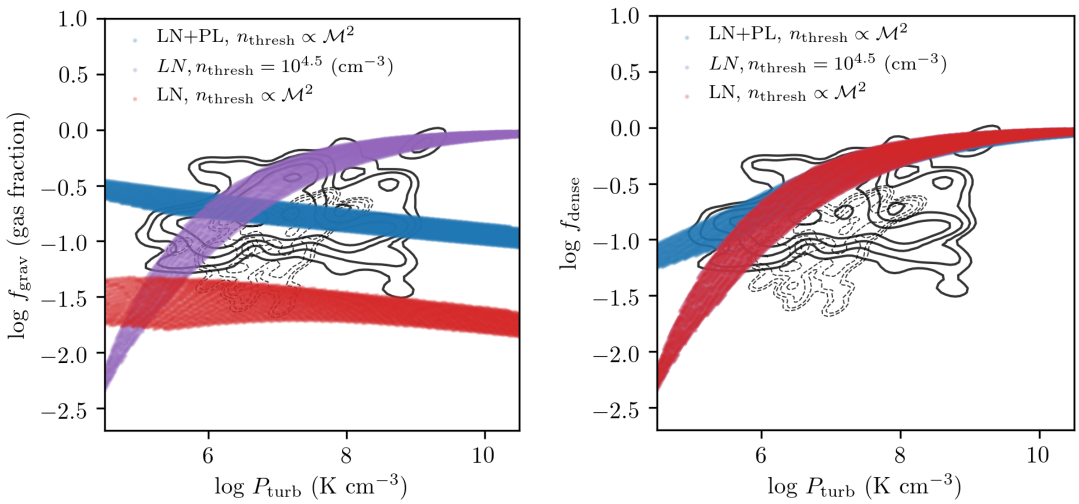

FIGURE 3.4: Gas fractions are shown as a function of $P_{\rm turb}$. *Left:* Model predictions of $f_{\rm grav}$ in addition to the fraction estimated from $I_{\rm HCN}/I_{\rm CO}$ ($f = \alpha_{\rm HCN}/\alpha_{\rm CO}\, I_{\rm HCN}/I_{\rm CO}$ and $f_{\rm grav}$ from the models).*Right:* Predictions of $f_{\rm dense}$ from the three models. Formatting is the same as in Fig.3.2. Note: $f_{\rm grav} = f_{\rm dense}$ for models with $n_{\rm thresh} = 10^{4.5}$ cm^{-3}.

is estimated from the model $n-$PDFs. The LN+PL models show the best fit to the data when comparing $f_{\rm grav}$ and $P_{\rm turb}$. $f_{\rm grav}$ estimates from the LN-only varying $n_{\rm thresh}$ models are consistently smaller than the data predicts from $I_{\rm HCN}/I_{\rm CO}$. The predictions of $f_{\rm grav}$ from the varying threshold models both show negative trends, in contrast to the trend observed with $f_{\rm dense}$, which is positive for all models. This is primarily from differences in $n_{\rm thresh}$, since higher turbulent pressures will push $n_{\rm thresh}$ to higher densities. We find that all models perform similarly when using $f(n > 10^{4.5}\ {\rm cm}^{-3})$ in place of $f_{\rm dense}$. From these results, $I_{\rm HCN}/I_{\rm CO}$ appears to be a decent tracer of $f_{\rm grav}$ when compared to the LN+PL model results, although it has large scatter.

A Comparison of Observational and Model Estimates of $\epsilon_{\rm ff}$

As a check to the results above, we also consider $\epsilon_{\rm ff}$. As discussed in §3.3, fixed vs. varying density-threshold models of star formation have different predictions for the behavior of $\epsilon_{\rm ff}$ with $\mathcal{M} \sim \sigma_{\rm v}$ and $P_{\rm turb}$. In Figs. 3.5 and 3.6, we plot $\epsilon_{\rm ff}$ as a function of $P_{\rm turb}$ and $f_{\rm dense} \propto I_{\rm HCN}/I_{\rm CO}$, and we compare the predictions of $\epsilon_{\rm ff}$ from models with estimates of $\epsilon_{\rm ff}$ from our data.

In our data, $\epsilon_{\rm ff}$ appears to scale negatively with $P_{\rm turb}$, and scales positively with $f_{\rm dense}$ (cf. Fig. 3.5). However, both correlations are weak. The negative trend between $\epsilon_{\rm ff}$ and $P_{\rm turb}$ is not reproduced by the varying threshold models (cf. Fig 3.6), however they pass through the locus of datapoints. Instead, the varying threshold models predict an increase in $\epsilon_{\rm ff}$ with $P_{\rm turb}$. This is partially a result of the decrease in $f_{\rm grav}$ towards higher $P_{\rm turb}$ in these models. Points at higher $P_{\rm turb}$ are also generally at higher $\Sigma_{\rm mol}$ and higher $\Sigma_{\rm SFR}$, and star formation is still increasing relative to the $f_{\rm grav}$. The fixed threshold models consistently overpredict $f_{\rm grav}$.

The varying threshold models are offset from the data in the plot comparing $\epsilon_{\rm ff}$ with $f_{\rm grav}$, and their trends appear perpendicular to the data. The varying threshold models are able to better match the data when comparing against $f(n > 10^{4.5}\,{\rm cm}^{-3})$. $\epsilon_{\rm ff}$ itself is still calculated with $f_{\rm grav}$.

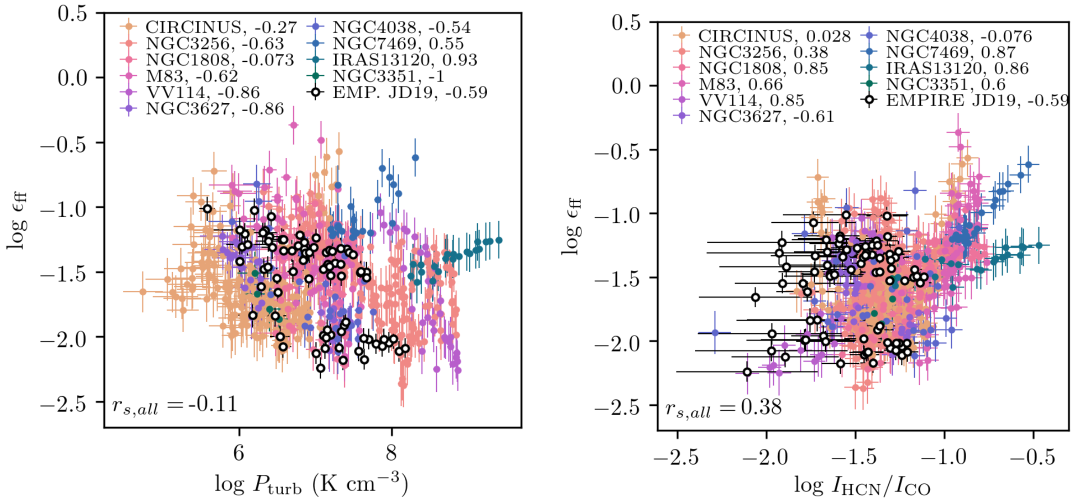

FIGURE 3.5: Efficiency per free-fall time as a function of $P_{\rm turb}$ (left) and $I_{\rm HCN}/I_{\rm CO}$ (right). Data is formatted as it is in Fig. 3.2.

A Comparison of Observational and Model Estimates of Depletion Times

Finally, we consider if estimates of depletion time may give insight into the discrepancy between $f_{\rm grav}$ and observational estimates of $f_{\rm dense}$. We plot $t_{\rm dep}$ as a function of $P_{\rm turb}$ and gas fraction (i.e. $f_{\rm dense}$ and $f_{\rm grav}$) in Figs. 3.7 and 3.8. We find moderate negative correlations between $t_{\rm dep}$ and the gas fraction traced by $I_{\rm HCN}/I_{\rm CO}$. $t_{\rm dep}$ estimated from the data appears relatively constant with $P_{\rm turb}$, but the Spearman rank coefficient of the combined data indicates a weak, negative correlation (cf. Fig. 3.7). The varying-threshold models best reproduce the observed trend between $t_{\rm dep}$ and $P_{\rm turb}$. The varying-threshold models also perform better than the fixed-threshold at reproducing the observed trend between $t_{\rm dep}$ and $f_{\rm dense}$.

If $f_{\rm grav} \propto f_{\rm dense}$ (as traced by $I_{\rm HCN}/I_{\rm CO}$), and if Eq. 3.2 is an appropriate star formation law, we should also see that $t_{\rm dep}$ decreases (or is relatively constant) with increasing $f_{\rm dense}$. This can be seen when we consider $\epsilon_{\rm ff} = \epsilon_0 f_{\rm grav} \approx t_{\rm ff}/t_{\rm dep}$, which implies that $f_{\rm grav} \propto 1/t_{\rm dep}$. We do see that $t_{\rm dep}$ decreases with $f_{\rm dense}$ in Fig. 3.7, but this is only reproduced by the models when plotting against $f(n > 10^{4.5}\,{\rm cm}^{-3}$. The model depletion times also appear to decrease with increasing $P_{\rm turb}$, while the data only show a weak, negative correlation. The decrease in both $\epsilon_{\rm ff}$ and

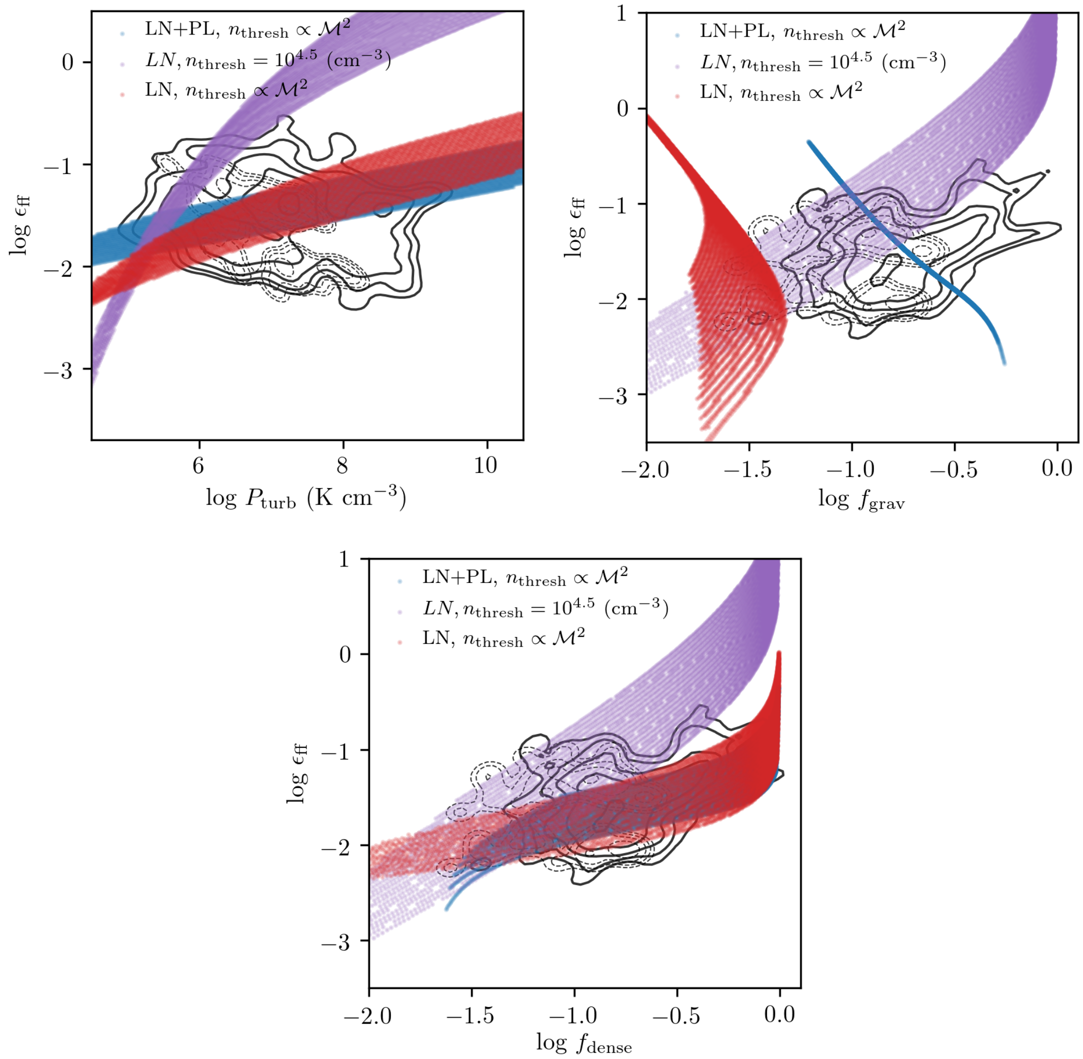

FIGURE 3.6: The efficiency of star formation per free-fall time as a function of $P_{\rm turb}$ (top left), model predictions of $f_{\rm grav}$ (top right), model predictions of $f_{\rm dense}$ (bottom). Formatting and colors are the same as in Fig. 3.2.

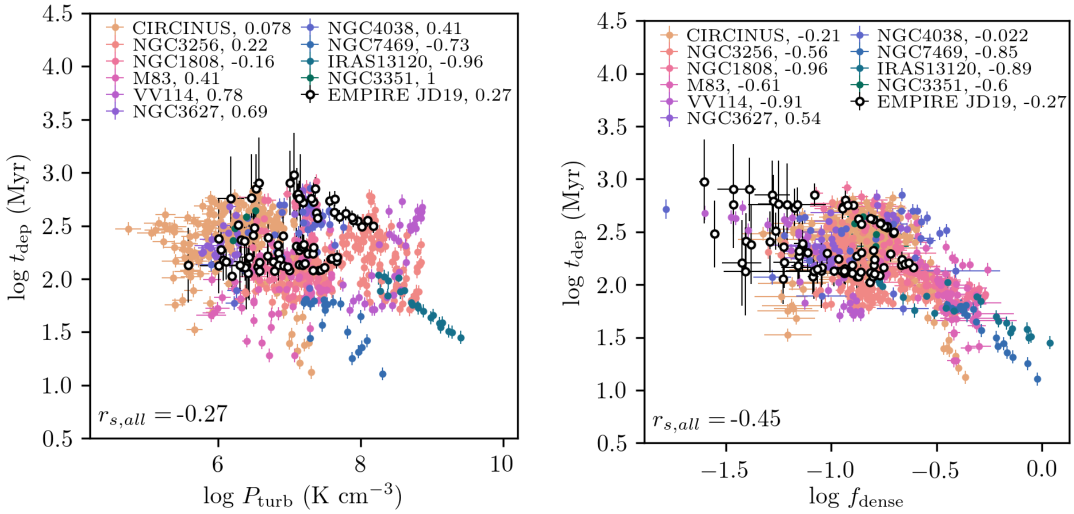

FIGURE 3.7: Depletion time of the total molecular gas content as a function of $P_{\rm turb}$ (left) and $f_{\rm dense}$ (right). Data is formatted as it is in Fig 3.2.

$t_{\rm dep}$ with $P_{\rm turb}$ implies that $t_{\rm ff}$ is decreasing faster than than $t_{\rm dep}$ when compared against $P_{\rm turb}$. This two trends imply that there are processes suppressing star formation relative to the increase in gas, and this suppression scales with $P_{\rm turb}$.

We also look at the depletion time of the dense gas, and compare against predictions of $t_{\rm dep,grav} = f_{\rm grav}\Sigma_{\rm mol}/\Sigma_{\rm SFR,mod}$, which is normalized to the observational estimates of $\Sigma_{\rm mol}$ in our sample. We plot the depletion time of the dense gas as traced by HCN, $t_{\rm dep,dense}$, as a function of $P_{\rm turb}$ and gas fraction in Figs. 3.9 and 3.10. We see a moderate positive correlation between $t_{\rm dep,dense}$ and $f_{\rm dense}$ in $\sim$ half of our sources and the EMPIRE galaxies. The Spearman rank coefficient is positive for the combined dataset. At first this appears counter to the expectation of star formation models, but all models are able to roughly reproduce this increase in $t_{\rm dep,dense}$ with gas fraction. The varying-threshold models predict a turnover in $t_{\rm dep,dense}$ around $P_{\rm turb} \sim 10^6$ K cm^{-3}. By eye, the data appear to peak around $P_{\rm turb} \sim 10^7$ K cm^{-3}. It is also worth noting the differences in the $t_{\rm dep} - P_{\rm turb}$ and $t_{\rm dep,dense} - P_{\rm turb}$ relationships, which indicate that the star formation from dense gas (traced by $I_{\rm HCN}/I_{\rm CO}$) is less efficient.

The above results again provide support against the interpretation of the $I_{\rm HCN}/I_{\rm CO}$ ratio as a a tracer of $f_{\rm grav}$.

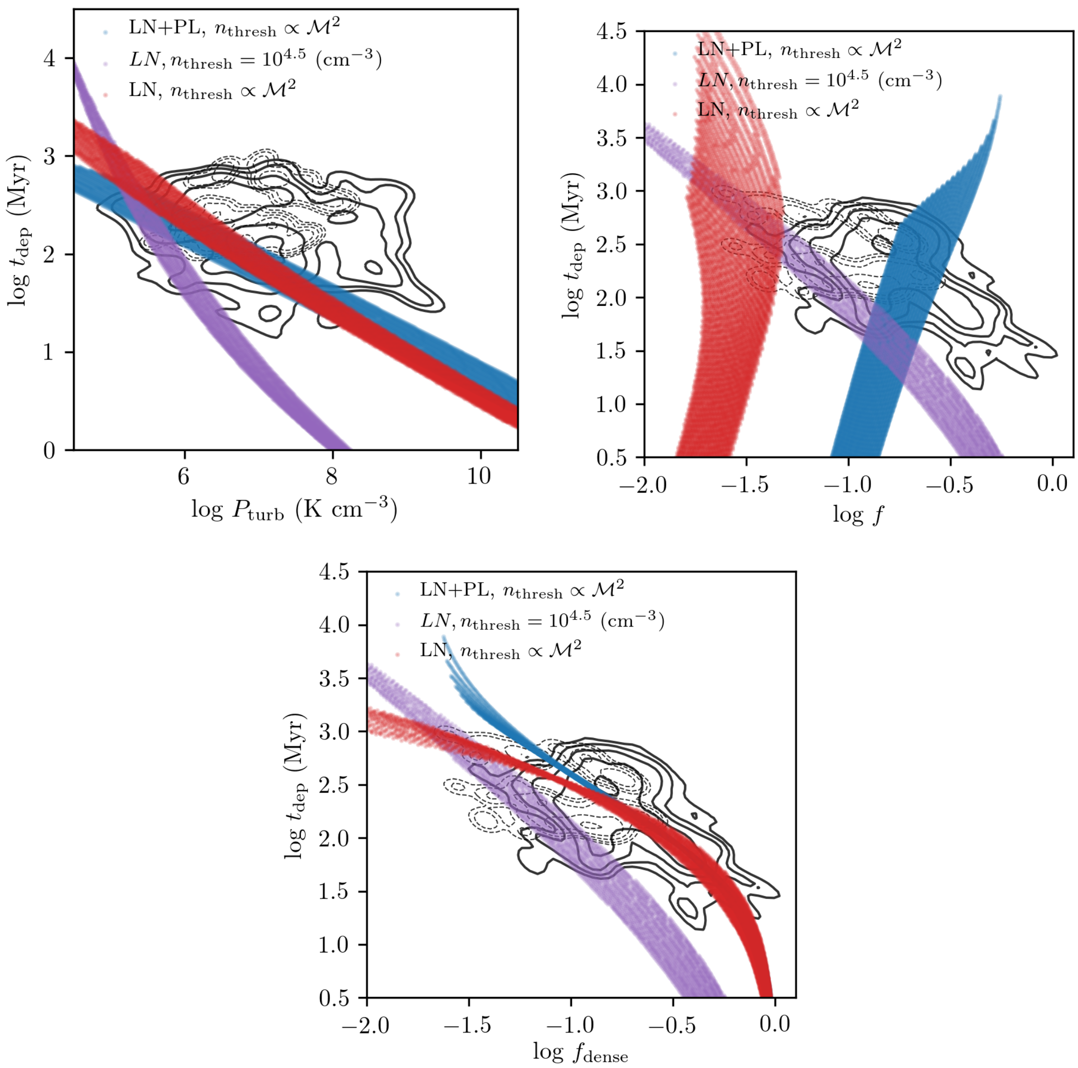

FIGURE 3.8: The the depletion time of the total molecular gas content as a function of $P_{\rm turb}$ (top left), gas fraction including the model predictions of $f_{\rm grav}$ (top right), and gas fraction including the model predictions of $f_{\rm dense}$ (bottom). Formatting and colors are the same as in Fig. 3.2.

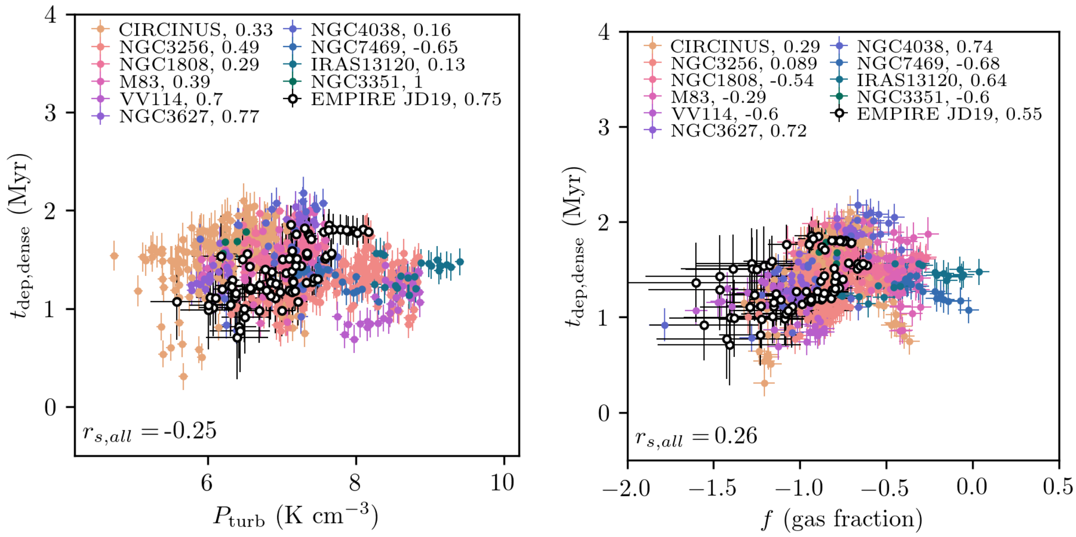

FIGURE 3.9: Depletion time of the dense molecular gas content as a function of $P_{\rm turb}$ (left) and $f_{\rm dense}$ (right). Data is formatted as it is in Fig 3.2.

3.5 Discussion

The above results show that each model is able to reproduce many observed trends, but there is a clear discrepancy between the fixed and varying density threshold models and their predictions for $f_{\rm grav}$. The fixed density threshold models do relatively well at reproducing the observed trends when comparing against $f(n > 10^{4.5})$ cm^{-3}. We find that plotting trends against $f(n > 10^{4.5}\,{\rm cm}^{-3})$ in place of $f_{\rm grav}$ generally improves agreement between the models and the data. However, the agreement between the $\epsilon_{\rm ff}$, $t_{\rm dep}$, and $t_{\rm dep,dense}$ with $f_{\rm dense}$ does not necessarily imply that $f_{\rm grav} \sim f_{\rm dense}$, since we still use $f_{\rm grav}$ when calculating $\epsilon_{\rm ff}$ from the models. Instead, we take this as an indication that the $I_{\rm HCN}/I_{\rm CO}$ ratio is consistently tracing gas above a relatively constant density that may be close to $n \sim 10^{4.5}\,{\rm cm}^{-3}$.

3.6 Conclusions

We find the following conclusions from our comparison between observation and the predictions of analytical models of star formation:

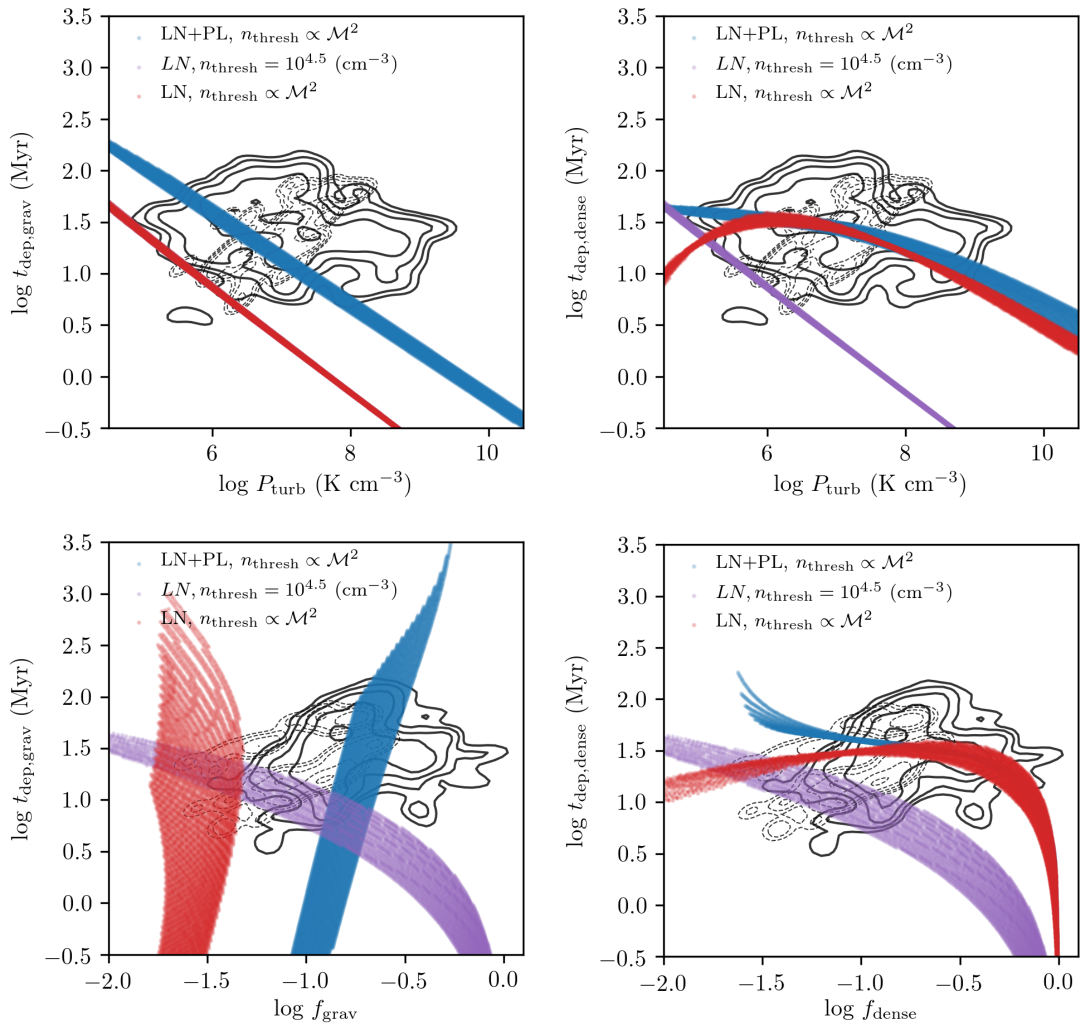

FIGURE 3.10: The the depletion time of the dense molecular gas content as a function of $P_{\rm turb}$ (top two plots), and gas fraction (bottom two plots). We plot the dense gas depletion time against $f_{\rm grav}$ (bottom left), $f_{\rm dense}$ (bottom right), and $P_{\rm turb}$ (top two panels). In the left column, model $f_{\rm grav}$ is applied to the model total gas depletion time, and in the right hand column we instead use $f(n > 10^{4.5})$ cm^{-3}. Formatting is the same as in Fig. 3.2.

1. The observed HCN/CO ratio does not track f_{grav} if $n_{\text{thresh}} \propto P_{\text{turb}}$.

2. The HCN/CO may track gas above a $\sim$constant mean density.

3. HCN/CO does not track f_{grav} if $\epsilon_{\text{inst}} \propto f_{\text{grav}}$, which varying threshold models predict.

4. Models predict a turnover in $t_{\text{dep,dense}}$ with P_{turb}, which appears to coincide with a peak or turnover in our data. This indicates that the consumption time of dense gas is not consistently decreasing with P_{turb}, in contrast to t_{dep}. This either requires that either the efficiency of star formation from the dense gas is varying, such that it peaks and turns over at high P_{turb}, or that there are systemics in how I_{HCN} scales with the mass of star-forming gas.

In summary, the HCN/CO ratio is likely a reliable tracer of gas above a constant density, such as $n_{\text{thresh}} \approx 10^{4.5}$ cm^{-3}, but not necessarily f_{grav}. If varying thresholds exist in nature, then the HCN/CO ratio is a poor tracer of f_{grav}. The discrepancy between the fixed threshold model predictions of f_{grav} and measurements of ϵ_{ff} in our galaxies could indicate a failure of these models to characterize f_{grav}, particularly if our assumption that $\epsilon_{\text{ff}} \propto f_{\text{grav}}$ holds, on average.

3.A Appendix: Moment Maps and Uncertainties

We use the following expressions to calculate moments and their corresponding uncertainties.

$$\textsc{Moment 0}: \quad I = \Sigma_i T_i \Delta v \tag{3.26}$$

$$\delta I = \delta \bar{T} \Delta v \sqrt{N_{\mathrm{chan}}} \tag{3.27}$$

$$\textsc{Moment 1}: \quad \bar{v} = \frac{\Sigma_i T_i v_i}{\Sigma_i T_i} \tag{3.28}$$

$$\delta \bar{v} = \frac{N_{\mathrm{chan}} \Delta v}{2\sqrt{3}} \frac{\delta I}{I} \tag{3.29}$$

$$\textsc{Moment 2}: \quad \sigma_v = \sqrt{\frac{\Sigma_i T_i (v_i - \bar{v})^2}{\Sigma_i T_i}} \tag{3.30}$$

$$\delta \sigma_v = \frac{(N_{\mathrm{chan}} \Delta v)^2}{8\sqrt{5}} \frac{1}{\sigma_v} \tag{3.31}$$

A full derivation of the uncertainties on Eqs. 3.29 and 3.31 will be given in Wilson et al. (2020, in prep.).

Bibliography

Alves, João, Marco Lombardi, and Charles J. Lada (2017). *A&A* 606, L2, p. L2.

André, Ph. et al. (2016). *A&A* 592, A54, A54.

Aniano, G., B. T. Draine, K. D. Gordon, and K. Sandstrom (2011). *PASP* 123.908, p. 1218.

Ballesteros-Paredes, Javier et al. (2011). *MNRAS* 416.2, pp. 1436–1442.

Berkhuijsen, E. M. and A. Fletcher (2008). *MNRAS* 390.1, pp. L19–L23.

Bertoldi, Frank and Christopher F. McKee (1992). *ApJ* 395, p. 140.

Bigiel, F. et al. (2008). *AJ* 136.6, pp. 2846–2871.

Bolatto, Alberto D., Mark Wolfire, and Adam K. Leroy (2013). *ARAA* 51.1, pp. 207–268.

Burkhart, B. (2018). *ApJ* 863, 118, p. 118.

Burkhart, Blakesley and Philip Mocz (2019). *ApJ* 879.2, 129, p. 129.

Burkhart, Blakesley, V. Ossenkopf, A. Lazarian, and J. Stutzki (2013). *ApJ* 771.2, 122, p. 122.

Burkhart, Blakesley, Kye Stalpes, and David C. Collins (2017). *ApJl* 834.1, L1, p. L1.

Collins, D. C. et al. (2012). *ApJ* 750, 13, p. 13.

Downes, D., P. M. Solomon, and S. J. E. Radford (1993). *ApJl* 414, p. L13.

Draine, B.T. (2010). Princeton Series in Astrophysics. Princeton University Press.

Evans Neal J., II et al. (2009). *ApJS* 181.2, pp. 321–350.

Federrath, C. and R. S. Klessen (2012). *ApJ* 761, 156, p. 156.

Federrath, Christoph and Supratik Banerjee (2015). *MNRAS* 448.4, pp. 3297–3313.

Federrath, Christoph and Ralf S. Klessen (2013). *ApJ* 763.1, 51, p. 51.

Gao, Yu and Philip M. Solomon (2004a). *ApJS* 152.1, pp. 63–80.

— (2004b). *ApJ* 606.1, pp. 271–290.

Goodman, Alyssa A., Jaime E. Pineda, and Scott L. Schnee (2009). *ApJ* 692.1, pp. 91–103.

Grudić, Michael Y. et al. (2018). *MNRAS* 475.3, pp. 3511–3528.

Helfer, Tamara T. and Leo Blitz (1997a). *ApJ* 478.1, pp. 233–245.

— (1997b). *ApJ* 478.1, pp. 162–171.

Hennebelle, Patrick and Gilles Chabrier (2011). *ApJl* 743.2, L29, p. L29.

Heyer, Mark, Coleman Krawczyk, Julia Duval, and James M. Jackson (2009). *ApJ* 699.2, pp. 1092–1103.

Hill, Alex S. et al. (2008). *ApJ* 686.1, pp. 363–378.

Jarrett, T. H., T. Chester, R. Cutri, S. E. Schneider, and J. P. Huchra (2003). *AJ* 125.2, pp. 525–554.

Jiménez-Donaire, Marıa J. et al. (2019). *ApJ* 880.2, 127, p. 127.

Kainulainen, J., H. Beuther, T. Henning, and R. Plume (2009). *A&A* 508.3, pp. L35–L38.

Kainulainen, J. and C. Federrath (2017). *A&A* 608, L3, p. L3.

Kainulainen, J. and J. C. Tan (2013). *A&A* 549, A53, A53.

Kauffmann, J., F. Bertoldi, T. L. Bourke, II Evans N. J., and C. W. Lee (2008). *A&A* 487.3, pp. 993–1017.

Kauffmann, Jens et al. (2017). *A&A* 605, L5, p. L5.

Krumholz, Mark R. (2014). *Phys. Rep.* 539, pp. 49–134.

Krumholz, Mark R., Avishai Dekel, and Christopher F. McKee (2012). *ApJ* 745.1, 69, p. 69.

Krumholz, Mark R. and Christopher F. McKee (2005). *ApJ* 630.1, pp. 250–268.

Lada, Charles J., Elizabeth A. Lada, Dan P. Clemens, and John Bally (1994). *ApJ* 429, p. 694.

Lada, Charles J., Marco Lombardi, and João F. Alves (2010). *ApJ* 724.1, pp. 687–693.

Lada, Elizabeth A., John Bally, and Antony A. Stark (1991). *ApJ* 368, p. 432.

Lada, Elizabeth A., D. L. Depoy, II Evans Neal J., and Ian Gatley (1991). *ApJ* 371, p. 171.

Larson, R. B. (1981). *MNRAS* 194, pp. 809–826.

Lee, Eve J., Marc-Antoine Miville-Deschênes, and Norman W. Murray (2016). *ApJ* 833.2, 229, p. 229.

Leroy, Adam K. et al. (2017a). *ApJ* 846.1, 71, p. 71.

Leroy, Adam K. et al. (2017b). *ApJ* 835.2, 217, p. 217.

Lombardi, Marco, João Alves, and Charles J. Lada (2015). *A&A* 576, L1, p. L1.

Molina, F. Z., S. C. O. Glover, C. Federrath, and R. S. Klessen (2012). *MNRAS* 423, pp. 2680–2689.

Murphy, E. J. et al. (2011). *ApJ* 737.2, 67, p. 67.

Nordlund, Å. Ke and Paolo Padoan (1999). *Interstellar Turbulence*. Ed. by Jose Franco and Alberto Carraminana, p. 218.

Ostriker, Eve C. and Rahul Shetty (2011). *ApJ* 731.1, 41, p. 41.

Padoan, Paolo, Troels Haugbølle, Åke Nordlund, and Søren Frimann (2017). *ApJ* 840.1, 48, p. 48.

Padoan, Paolo, Bernard J. T. Jones, and Åke P. Nordlund (1997). *ApJ* 474.2, pp. 730–734.

Padoan, Paolo and Åke Nordlund (2011). *ApJ* 730.1, 40, p. 40.

Radford, Simon J. E., P. M. Solomon, and D. Downes (1991). *ApJl* 368, p. L15.

Rieke, G. H. et al. (2009). *ApJ* 692.1, pp. 556–573.

Rosolowsky, Erik and Adam Leroy (2006). *PASP* 118.842, pp. 590–610.

Sadavoy, S. I. et al. (2013). *ApJ* 767.2, 126, p. 126.

Salak, Dragan, Naomasa Nakai, Masumichi Seta, and Yusuke Miyamoto (2019). *ApJ* 887.2, 143, p. 143.

Scalo, John, Enrique Vázquez-Semadeni, David Chappell, and Thierry Passot (1998). *ApJ* 504.2, pp. 835–853.

Schneider, N. et al. (2013). *ApJl* 766.2, L17, p. L17.

Schneider, N. et al. (2015). *A&A* 578, A29, A29.

Schneider, N. et al. (2016). *A&A* 587, A74, A74.

Semenov, Vadim A., Andrey V. Kravtsov, and Nickolay Y. Gnedin (2017). *ApJ* 845.2, 133, p. 133.

Shirley, Yancy L. (2015). *PASP* 127.949, p. 299.

Shirley, Yancy L. et al. (2011). *ApJ* 728.2, 143, p. 143.

Sun, Jiayi et al. (2018). *ApJ* 860.2, 172, p. 172.

Sun, Jiayi et al. (2020). *ApJ* 892.2, 148, p. 148.

Tabatabaei, F. S., M. Krause, A. Fletcher, and R. Beck (2008). *A&A* 490.3, pp. 1005–1017.

Tilanus, R. P. J. and R. J. Allen (1993). *A&A* 274, p. 707.

Vazquez-Semadeni, Enrique (1994). *ApJ* 423, p. 681.

Wada, Keiichi and Colin A. Norman (2001). *ApJ* 547.1, pp. 172–186.

Walker, D. L. et al. (2018). *MNRAS* 474.2, pp. 2373–2388.

Wilson, Christine D., Ashley R. Bemis, and Osvald Kimli (2020). *in prep.*

Wilson, Christine D., Bruce G. Elmegreen, Ashley Bemis, and Nathan Brunetti (2019). *ApJ* 882.1, 5, p. 5.

Zamora-Avilés, Manuel and Enrique Vázquez-Semadeni (2014). *ApJ* 793.2, 84, p. 84.

4 | Does the HCN/CO ratio trace the fraction of gravitationally-bound gas? II. A radiative transfer perspective.

Bemis A.R., Wilson C.D., 2020, *in preparation*
Department of Physics & Astronomy, McMaster University, Hamilton ON L8S 4M1

Abstract

We model emissivities of the HCN and CO transitions using the non-LTE radiative transfer code RADEX. These models are compared with archival observations of the HCN and CO $J = 1 - 0$ transitions (presented in Chapter 3), in addition to the radio continuum at 93 GHz for 10 nearby galaxies. We combine these model emissivities with predictions of turbulent and gravoturbulent models of star formation presented in Chapter 3. In particular, we assess if the HCN/CO ratio tracks the fraction of gravitationally-bound gas, $f_{\rm grav}$, in molecular clouds. We find our modelled HCN/CO ratios are consistent with the measurements within our sample. The model results reveal an anticorrelation between HCN/CO and $f_{\rm grav}$ in the case of increasing velocity dispersion. In this case, the HCN/CO ratio is not a good tracer of $f_{\rm grav}$. The modelled HCN/CO ratio is instead strongly correlated with mean gas density, n_0, and velocity dispersion, σ_v. We use the model results to calibrate a relationship between n_0, HCN/CO, and $\sigma_{\rm v}$ that we then apply to our sample. We do the same with filling fraction, CO conversion factor, $\alpha_{\rm CO}$, and HCN conversion factor, $\alpha_{\rm HCN}$. We find that our estimates of $\alpha_{\rm CO}$ agree well with the predictions of the Narayanan and Krumholz, 2014 calibration for $\alpha_{\rm CO}$.

4.1 Introduction

The HCN/CO ratio is commonly used to assess the fraction of dense gas ($> 10^4$ cm^{-1}) in external galaxies that may be associated with star formation. The seminal work by Gao and Solomon 2004a,b found a nearly linear scaling between the HCN luminosity and the star formation rate as traced by the infrared (IR), suggesting that HCN is a useful tracer of star-forming gas for a range of galaxies. The nearly linear scaling between $L_{\rm IR}$ and $L_{\rm HCN}$ also implies that the critical density for HCN $J = 1-0$ emission, $n_{\rm crit,HCN}$, is close to a common, mean threshold density, $n_{\rm thresh}$, that is important for star formation. Although individual galaxies have scatter in the $L_{\rm IR}$ and $L_{\rm HCN}$ relationship, a linear scaling implies that the average $L_{\rm IR}/L_{\rm HCN}$ ratio is relatively constant over many orders of magnitude. Systematic deviations from linearity have been found in (U)LIRGs (Garcıa-Burillo et al., 2012; Graciá-Carpio et al., 2008), at sub-kpc scales in disk galaxies (Chen et al., 2015; Gallagher et al., 2018; Usero et al., 2015), and at sub-kpc scales in a merger (Bemis and Wilson, 2019; Bigiel et al., 2015). Most of these non-linearities are not associated with any obvious mechanism that may significantly alter HCN emissivity, such as the presence of an AGN. In the absence of an active galactic nucleus (AGN), these variations in emissivity can be interpreted as a fundamental difference in the depletion time of dense gas within different systems, which may signal a connection between star formation and environment.

Saintonge et al. (2012) also find for a sample of nearby massive galaxies that decreases in $t_{\rm dep}$ of the total gas are connected to real increases in the underlying star formation efficiency of some galaxies. They ultimately predict this to occur in response to an enhanced dense gas fraction. The opposite is true in some of the clouds in the Central Molecular Zone (CMZ) of the Milky Way. Gas in the CMZ is dense ($n \sim 10^4$ cm^{-3}) and warm ($T \sim 65$ K) compared to gas in the disk ($n_0 \sim 10^2$ cm^{-3}, $T \sim 10$ K, Ginsburg et al. 2016; Rathborne et al. 2014). Some clouds in the CMZ display a lack of star formation (Kruijssen et al., 2014; Walker et al., 2018) despite their abundance of dense gas (cf Mills, 2017) that appears to be connected to a suppression of the onset of star formation (Walker et al., 2018). This suppression of star formation is also apparent in the centers of nearby disk galaxies as shown by Gallagher et al. (2018).

A significant impediment to these results is the uncertainty of the *relative* emissivities of HCN and CO. The CO conversion factor, $\alpha_{\rm CO}$, is estimated to vary with excitation and metallicity (Narayanan and Krumholz, 2014), can be nearly five times lower in (U)LIRGs (Downes, Solomon, and Radford, 1993), and is lower in the centers of disk galaxies (Sandstrom et al., 2013). To further complicate this relationship, the HCN conversion factor, $\alpha_{\rm HCN}$, is also likely to vary across different systems (Usero et al., 2015), but may not necessarily track $\alpha_{\rm CO}$. Observations of HCN and $\rm H^{13}CN$ in galaxy centers suggest that HCN is only moderately optically thick (Jiménez-Donaire et al., 2017), unlike CO which typically has $\tau_{\rm CO} > 10$. The currently assumed value for $\alpha_{\rm HCN}$ may overestimate the mass traced by HCN if $\tau_{\rm HCN} < 10$, and underestimate the mass if $\tau_{\rm HCN} > 10$. *Thus, the HCN/CO ratio may not scale linearly with the fraction of gas* $\gtrsim 10^4\,{\rm cm}^{-3}$ *due to variations in excitation and optical depth.* As we refine our understanding of star formation in galaxies, it is clear we must also adopt a more complex approach to estimating masses using molecular line emission, and we must develop a better understanding of the information they can provide on star formation.

In Chapter 3, we assessed the ability of the $I_{\rm HCN}/I_{\rm CO}$ ratio to determine the fraction of gravitationally bound gas by comparing the observed star formation properties and HCN/CO ratios in 10 galaxies to the predictions of analytical models of star formation (Burkhart, 2018; Federrath and Klessen, 2012; Hennebelle and Chabrier, 2011; Krumholz and McKee, 2005). In this chapter, we model emissivities of HCN and CO using the non-LTE radiative transfer code RADEX, (Leroy et al., 2017a; van der Tak et al., 2007) to compare with the results of Chapter 3. We use the archival ALMA data from Chapter 3 of the HCN and CO $J = 1 \rightarrow 0$ transitions, in addition to the radio continuum at 93 GHz, to assess the relationship between dense gas and star formation. This sample includes the dense centers of five disk galaxies and five (U)LIRGs, (see Table 1 of Chapter 3). In §4.2, we describe the model framework, emissivity (§4.2.1), and the underlying gas density Probability Distribution Function, $n-$PDF, models that we adopt. In §4.2.1, we present how we connect volume and column density, which allows us to incorporate radiative transfer into our analysis. The model results are compared with observations in §4.4, and conclusions are presented in §4.5.

4.2 Model Framework

We model molecular line emissivities using the radiative transfer code, RADEX (van der Tak et al., 2007), and we connect these emissivities to gravoturbulent models of star formation. We present several gravoturbulent models of star formation in chapter 3, which are either purely lognormal (cf. Federrath and Klessen 2012; Krumholz and McKee 2005; Padoan and Nordlund 2011) or a composite lognormal and power law distribution (cf. Burkhart, Stalpes, and Collins 2017). We focus on the results of the composite LN+PL models in this analysis .

4.2.1 Emissivity

We adopt the following definition of the emissivity of a molecular transition (Leroy et al., 2017a):

$$\epsilon = \frac{I_{\rm mol}}{N_{\rm H_2}} = \frac{I_{\rm mol}}{N_{\rm mol}/x_{\rm mol}} \tag{4.1}$$

where $I_{\rm mol}$ is the total line intensity of a molecular transition (in units of K km s^{-1}), $N_{\rm H_2}$ is the column density of gas that emits I, $N_{\rm mol}$ is the molecular column density of an observed molecule (in units of cm^{-2}), and $x_{\rm mol}$ is the fractional abundance of the molecule relative to the molecular hydrogen, H_2. Emissivity is analogous to the inverse of molecular conversion factors ($X_{\rm mol}$ and $\alpha_{\rm mol}$, Leroy et al. 2017a), which are commonly used to estimate the mass traced by a molecular transition, $N_{\rm H_2} = X_{\rm mol} I_{\rm mol}$ ($\alpha_{\rm mol} = X_{\rm mol}/(6.3 \times 10^{19})$, Leroy et al. 2017b). In practice, the relationship between the total emissivity of an observed molecular cloud and an appropriate conversion factor is also dependent on the beam filling fraction and the uniformity of gas properties within the beam.

To build our models, we use the analytical models of the column and volume density PDFs (p_s and p_η) from Burkhart, Stalpes, and Collins (2017) and Burkhart (2018), respectively, and we use the density variance relationship from Burkhart and Lazarian (2012). Burkhart and Lazarian (2012) show that the variances of lognormal column and volume density PDFs are recoverable from one another via a scale factor, $A \approx 0.11$, and are given by:

$$\sigma_s^2 = \ln\left(1 + b^2\mathcal{M}^2\right) \tag{4.2}$$

$$\sigma_\eta^2 = A\,\sigma_s^2, \tag{4.3}$$

respectively, where b is the turbulent forcing parameter which describes the dominant mode(s) of turbulence (i.e. compressive, mixed, or solenoidal, which spans $b = 1/3 - 1$), and we have neglected magnetic fields. This provides an analytical connection between the 2D and 3D gas density PDFs that we use in our models. Equations 4.2 and 4.3 are the variances of the $n-$PDF in terms of logarithmic density, $s = \ln\left(n/n_0\right)$, where n_0 is the mean volume density. Likewise, $\eta = \ln\left(N/N_0\right)$. In terms of the logarithmic volume density, the volumetric density PDF p_s, which is a composite of a lognormal and a power law distribution, is given as:

$$\mathrm{p}_s = \begin{cases} N_s \frac{1}{\sqrt{2\pi\sigma_s^2}} \exp\left(-\frac{(s-s_0)^2}{2\sigma_s^2}\right), & s < s_t \\ N_s C_s e^{-\alpha_s s}, & s > s_t \end{cases} \tag{4.4}$$

where s_t is the density at which the PDF transitions from lognormal to power law, α is the slope of the power law component, $s_0 = -0.5\ \ln\sigma_s^2$ is the mean logarithmic density, and σ_s is the standard deviation. These expressions are normalized by constants N_s and C_s, which are given in Burkhart, Stalpes, and Collins, 2017 and Burkhart, 2018. The equivalent density distribution in terms of the logarithmic column density is then given as (Burkhart, Stalpes, and Collins, 2017):

$$\mathrm{p}_\eta = \begin{cases} N_\eta \frac{1}{\sqrt{2\pi\sigma_\eta^2}} \exp\left(-\frac{(\eta-\eta_0)^2}{2\sigma_\eta^2}\right), & \eta < \eta_t \\ N_\eta C_\eta e^{-\alpha_\eta \eta}, & \eta > \eta_t \end{cases} \tag{4.5}$$

where η_t is the logarithmic column density at which the PDF transitions from lognormal to power law, α_N is the slope of the column density power law component, $\eta_0 = -0.5\ \ln\sigma_s = \eta^2$ is the mean logarithmic density, and σ_η is the standard deviation. These distributions are converted to their linear forms via $p_s = n\,p_n$ and $p_\eta = N\,p_N$. We demonstrate the connection between the two PDFs in Fig. 4.1. We also compare with the results of a purely lognormal model in the absence of a power law tail. The addition of the power law tail adds mass to the high-density end of the $n-$PDF that is not available in the lognormal only model.

Incorporating Radiative Transfer

To calculate PDF-weighted emissivities using RADEX, we adopt a simple spherical geometry assuming a double power law radial density distribution. Federrath and Klessen (2013) show that the slope of the gradient in a radially-symmetric density distribution will be related to the slope of the corresponding $n-$PDF if they both follow power law scalings[1]. The high-density slopes of the logarithmic forms of the $n-$PDF and $N-$PDF (α_s and α_η) are then related to the radial slope of the clump density profile, k, via:

$$k = \begin{cases} 3/\alpha_s, & \text{for p}(s) \\ (\alpha_\eta - 2)/\alpha_\eta, & \text{for p}(N) \end{cases} \tag{4.6}$$

The slope of the spatial density gradient, k, is also related to the slopes of the linear PDFs via $k = 3/(\alpha_n - 1)$ and $k = (\alpha_N - 1)/(\alpha_N + 1)$. Assuming abundances of $x_{\mathrm{HCN}} \sim 10^{-8}$ and $x_{\mathrm{CO}} \sim 10^{-4}$ relative to H_2, we can use this analytical relationship to set the appropriate molecular column density input into RADEX. For comparison, a power law with $k = 2$ is consistent with the expectation for isothermal cores (Shu, 1977), and results in an $n-$PDF slope of $\alpha = 1.5$. Shallower $n-$PDF slopes then correspond to steeper spatial density gradients and vice versa.

The radially-symmetric approximation assumed above is only analytically exact for the gravitationally-bound gas in the power law tail of the $n-$PDF. The gas outside of the power law tail is primarily governed by turbulence, which produces fractal, self-similar structure (Elmegreen and Falgarone, 1996; Schneider et al., 2011). Self-similarity implies there is no characteristic scale of the gas, but this is not inconsistent with the existence of density gradients in turbulent gas. In the interest of simplicity we also adopt a power law density gradient for the gas that

[1] One zone models bypass this requirement by assuming a fixed optical depth, which indirectly determines the $n-N$ relationship, but can underestimate molecular abundance at high densities, and overestimate it at low densities.

we attribute to the lognormal component of the $n-$PDF. This gives us a double power law distribution, in terms of the linear density:

$$n(r) = \tilde{n}\left(\frac{r}{\tilde{r}}\right)^{-k_t}\left(1+\frac{r}{\tilde{r}}\right)^{k_t-k_e} \tag{4.7}$$

where k_e is the slope of the gas in the turbulent envelope, and k_t is the slope of the gas in the tail of the PDF, and $\tilde{r}$ and $\tilde{n}$ are scale factors dependent on the two power law slopes, the mean radius and density of the model, r_0 and n_0, and the density at which the $n-$PDF transitions from lognormal to power law, n_t. These factors are set such that $n(r_t) = n_t$ and $n(r_0) = n_0$. The equivalent radial column density profile is then also given by:

$$N(r) = \tilde{N}\left(\frac{r}{\tilde{r}}\right)^{-k_t+1}\left(1+\frac{r}{\tilde{r}}\right)^{k_t-k_e} \tag{4.8}$$

and similarly, $N(r_t) = N_t$. We then estimate the *spatial* slope (density gradient) of the turbulent component of gas based on parameters of the $n-$PDF. The spatial density gradient likely scales with the width of the $n-$PDF, which is characterized by the standard deviation, σ_n. Combining this with the width of the $N-$PDF, we can then derive an estimate of the density gradient of the turbulent gas. This method assumes that the $1-\sigma$ upper and lower column ($N_{+\sigma}$ and $N_{-\sigma}$) and volume ($n_{+\sigma}$ and $n_{-\sigma}$) densities spatially coincide with one another. We take the average slope of the radial distribution of n of the diffuse, turbulent component of gas to be:

$$k_{\mathrm{e}} \approx \theta\frac{\ln(\sigma_n)}{\ln(\sigma_N)+\ln(\sigma_n)} \tag{4.9}$$

where θ is a scale factor that accounts for the asymmetry of the lognormal PDF and additional uncertainties. This results in wider $N-$PDFs having shallower density gradients and vice versa. From observations we also know that column density decreases, on average, towards larger scales in molecular clouds, which implies that $k_e > 1$. We take $\theta = 2$, which then gives values of $1 \lesssim k_e \lesssim 2$. We show example volume and column density PDFs in the left two panels of Fig 4.1.

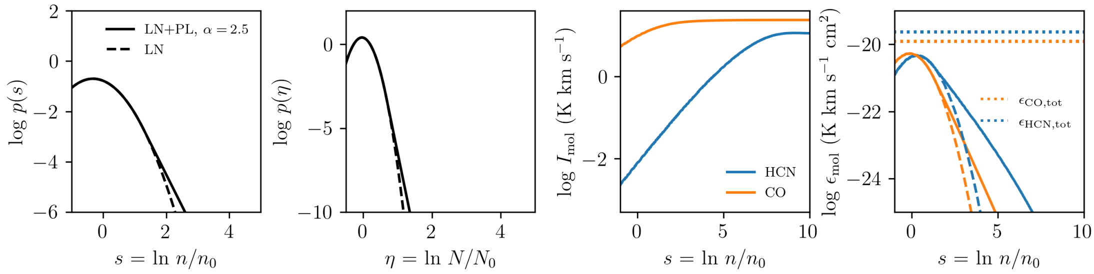

FIGURE 4.1: *Left*: An example volumetric gas density PDF in its logarithmic form. The lognormal-only PDF is shown as the dashed curve, and the LN+PL PDF is shown as the solid lines. *Left center:* The two-dimensionsional PDFs are shown in the same formatting. *Right center:* HCN and CO intensity as a function of the logarithmic density. This is the uncorrected output from RADEX. *Right:* The emissivity of HCN and CO prior to integration. This is the $n-$PDF multiplied by molecular intensity, and divided by the corresponding column density. The integrated emissivities are shown as the horizontal lines.

Producing PDF-weighted Quantities

With the framework to estimate n and N in place, we can numerically solve for the intensity of the transitions of interest, $I_{\rm mol}$, using RADEX (cf. Eq. 4.1). We weight the unintegrated emissivities (Eq. 4.1) by p_s and integrate to determine the PDF-weighted emissivity,

$$\langle \epsilon \rangle = \frac{\int_0^\infty \ \epsilon(s) \ \exp(s) \ \mathrm{p}_s \ \mathrm{d}s}{\int_0^\infty \ \exp(s) \ \mathrm{p}_s \ \mathrm{d}s} \tag{4.10}$$

where we have re-written Eq. 4.1 in terms of s. We numerically integrate the PDF over densities that are relevant to molecular gas, roughly $\sim 10 - 10^8$ cm^{-3}.

RADEX also returns optical depth and excitation temperature, and we calculate the expectation values of these quantities weighted by emissivity:

$$\langle X \rangle = \frac{\int_{s_{\rm edge}}^\infty \ X(s) \, \epsilon(s) \exp(s) \, \mathrm{p}_s \ \mathrm{d}s}{\int_{s_{\rm edge}}^\infty \epsilon(s) \exp(s) \, \mathrm{p}_s \ \mathrm{d}s}. \tag{4.11}$$

This produces estimates of $\tau_{\rm mol}$ and $T_{\rm ex,mol}$ that are relevant to observations.

Filling Fractions

We estimate absolute filling fractions of individual transitions by setting $X = r$ in Eq. 4.11. This returns a scale that is most appropriate for a particular molecular transition's emissivity, $r_{\rm mol} = \langle r_{\rm mol} \rangle$. We similarly estimate the mass-weighted radius, $r_{\rm M}$, of the cloud by removing $\epsilon(s)$ from Eq. 4.11 when integrating. The absolute filling fraction of a molecular transition over a model cloud is then given by:

$$\Phi_{\rm mol} \equiv \frac{r_{\rm mol}^2}{r_{\rm M}^2}. \tag{4.12}$$

The application of $\Phi_{\rm mol}$ corrects the emissivity for the reduced mass associated with the smaller scale of the transition of interest. It can therefore also be treated as a volume filling fraction. Since $\Phi_{\rm mol}$ is dependent on both the mass distribution and the emissivity, values greater than unity are possible in the case that molecular emission extends to lower-density gas beyond $r_{\rm M}$. This arises in our models that have high molecular emissivity, but in general it does not affect our results.

In the case that the observations completely resolve a source, and if the source properties are relatively uniform, then the filling fraction correction of an individual transition is simply the absolute filling fraction of that transition. The HCN-to-CO filling fraction is given by $\Phi_{\rm HCN/CO} = r_{\rm HCN}^2/r_{\rm CO}^2$. We use $\Phi_{\rm mol}$ when estimating conversion factors in section 4.4.2.

Gas Fractions

To determine the fraction of gas above an arbitrary threshold density, we can integrate across the $n-$PDF above that threshold, $s_{\rm thresh}$:

$$f(s > s_{\rm thresh}) = \frac{\int_{s_{\rm thresh}}^{\infty} \exp(s)\, {\rm p}_s\, {\rm d}s}{\int_0^{\infty} \exp(s)\, {\rm p}_s\, {\rm d}s}. \tag{4.13}$$

Gas fractions are calculated using the $n-$PDF gas fractions above densities $\log{(n)} =$ 2.5, 3.5, 4.5, 5.5 cm^{-3}, and denoted by $f_{2.5}$, $f_{3.5}$, $f_{4.5}$, and $f_{5.5}$. By construction, the estimated molecular emissivities are with respect to the *total* H_2 and He column density. To convert the HCN emissivity of the total gas to one relevant to dense gas, we must normalize the emissivity by the gas fraction of interest:

$$\epsilon_{\mathrm{HCN,dense}} = \epsilon_{\mathrm{HCN}} \times \frac{1}{f_{4.5}}. \tag{4.14}$$

When we refer to the HCN emissivity, we are referring to $\epsilon_{\mathrm{HCN,dense}}$.

4.2.2 The Model Parameter Space

We construct a model parameter space that aims to capture observed trends associated with star-forming gas clouds. For example, we choose velocity dispersion so that the median $\sigma_{\mathrm{v}} - \Sigma_{\mathrm{mol}}$ trend generally follows the $\Sigma - \sigma_{\mathrm{v}}$ fit to PHANGs data in Sun et al. (2018) and other cloud-scale studies (Field, Blackman, and Keto, 2011; Heyer et al., 2009). This is consistent with the $\sigma_{\mathrm{v}}^2 - \Sigma_{\mathrm{mol}}$ relationship observed within our sample. This also results in the velocity dispersion of each individual model scaling with α_{vir}, n_0, and r_0:

$$\sigma_{\mathrm{v}} \approx \sqrt{\frac{4\pi G\, \mu m_{\mathrm{H}}}{15}} \left(\alpha_{\mathrm{vir}}\, n_0\, r_0^2\right)^{1/2} \mathrm{~km~s^{-1}}. \tag{4.15}$$

which is the expression for α_{vir} of a homogeneous, spherical cloud rearranged (μm_{H} is the mean molecular mass). Using a Monte Carlo approach, we pseudo-randomly sample >10000 points on a grid of five variables: mean density, n_0, molecular gas surface density, Σ_{mol}, kinetic temperature, T_{kin}, virial parameter, α_{vir}, and the power law slope, α. We reduce the range we randomly sample by restricting the parameters to:

$$T_{\mathrm{kin}} \in [10, 300]\,\mathrm{K} \tag{4.16}$$

$$\Sigma_{\mathrm{mol}} \in [10, 10^5]\,\mathrm{M_\odot\,pc^{-2}} \tag{4.17}$$

$$r_0 \in [1, 150]\,\mathrm{pc} \tag{4.18}$$

$$\alpha \in [1.3, 2.9] \tag{4.19}$$

$$\alpha_{\mathrm{vir}} \in [0.1, 10] \tag{4.20}$$

$$\mathcal{M} \in [2, 300] \tag{4.21}$$

To optimize our grid sampling, we narrow our range of densities and temperatures to those that will roughly produce HCN excitation and optical depths of $T_{\rm ex,HCN}/T_{\rm kin} \in [0.1, 1]$ and $\tau_{\rm HCN} \in [0.1, 50]$. This is done using a rough, analytical estimate of $n_{\rm HCN,crit}$:

$$n_{\rm crit}({\rm HCN}_{1-0}) \approx 3.2 \times 10^5 \frac{\langle\beta\rangle}{T_{\rm ex}^{-1/2}} \exp\left(\frac{4.25356~{\rm K}}{T_{\rm ex}}\right) \tag{4.22}$$

where $\langle\beta\rangle$ is the photon escape probability and is a function of optical depth, τ. We assume the expression for a spherically symmetric and homogeneous medium from van der Tak et al. (2007). Assuming random values for $T_{\rm ex}$ and τ, we can estimate $n_{\rm crit}({\rm HCN}_{1-0})$. We then randomly sample around the range of densities and temperatures consistent with the two-level approximation (Tielens, 2005):

$$T_{\rm kin} = \frac{T_{\rm ex}}{1 - \frac{k\,T_{\rm ex}}{E_{ul}} \ln\left(1 + \frac{\beta\, n_{\rm crit}}{n}\right)} \tag{4.23}$$

where E_{ul} is the energy of the rotational transition from $J = u \rightarrow l$. This considerably reduces the time that the random search takes to find a model fitting the above requirements, and still incorporates random sampling.

Since our main motivation is to produce realistic emissivities, we further require that the resulting emissivities produce:

$$\alpha_{\rm CO} \in (0.1, 10) \tag{4.24}$$

$$\tau_{\rm CO} \in (5, 200) \tag{4.25}$$

$$\Phi_{\rm CO} \in (0.01, \infty). \tag{4.26}$$

We show the extent of the grid in the $\sigma_v^2/R - \Sigma_{\rm mol}$ space in Fig. 4.2, which encompasses all of our data and part of the PHANGs sample. Although abundance variations are possible within our sources, they still remain uncertain and we assume fixed molecular abundances $x_{\rm HCN} = 10^{-8}$ and $x_{\rm CO} = 10^{-4}$ relative to H_2. We also fix $b = 0.4$, which represents stochastic mixing between the two turbulent forcing modes (Federrath et al., 2010), and we neglect magnetic fields and take $\beta \rightarrow \infty$.

To demonstrate how different parameters impact the emissivity of the HCN

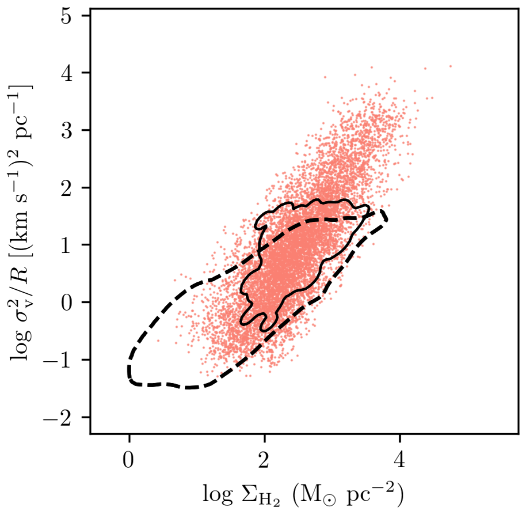

FIGURE 4.2: The model points are plotted as the salmon points in the $\sigma_v^2/R - \Sigma_{mol}$ parameter space (cf. Field, Blackman, and Keto, 2011; Heyer and Dame, 2015). The data from our sample are outlined by the black solid line, and the Sun et al., 2018 sample is outlined by the black, dotted line.

and CO transitions, we present plots of example PDF-weighted emissivity curves in Fig. 4.3 (second row from top) that compares $n-$PDFs for variations in n_0, k, σ_v, and $T_{\rm kin}$. Additionally, we show the corresponding $n-$PDFs (top), optical depths (third row from the top), and excitation temperatures (bottom). Fiducial quantities for the plotted set of models are $\Sigma = 5\times10^2$ M$_\odot$ pc^{-2}, $k = 1.5$, $\sigma_v = 14$ km s^{-1}, and $T_{\rm kin} = 45$ K. This gives a $\mathcal{M} = 60$, which may be appropriate for the galaxies in our sample.

4.3 Model Results

We present the model results in a set of pairwise Kernel Density Estimation (KDE) plots in Figs. 4.4 to 4.9. Spearman rank coefficients are shown and are colorized to indicate the strength of a correlation. Red indicates strong correlations ($r \gtrsim 0.7$), green indicates moderate correlations ($0.4 \gtrsim r < 0.7$), and black indicates a weak correlation ($r < 0.4$). The first set of KDE plots (Figs. 4.4, 4.5, 4.6, and 4.7) focus on the results of the radiative transfer analaysis, and the second set (Figs. 4.8 and

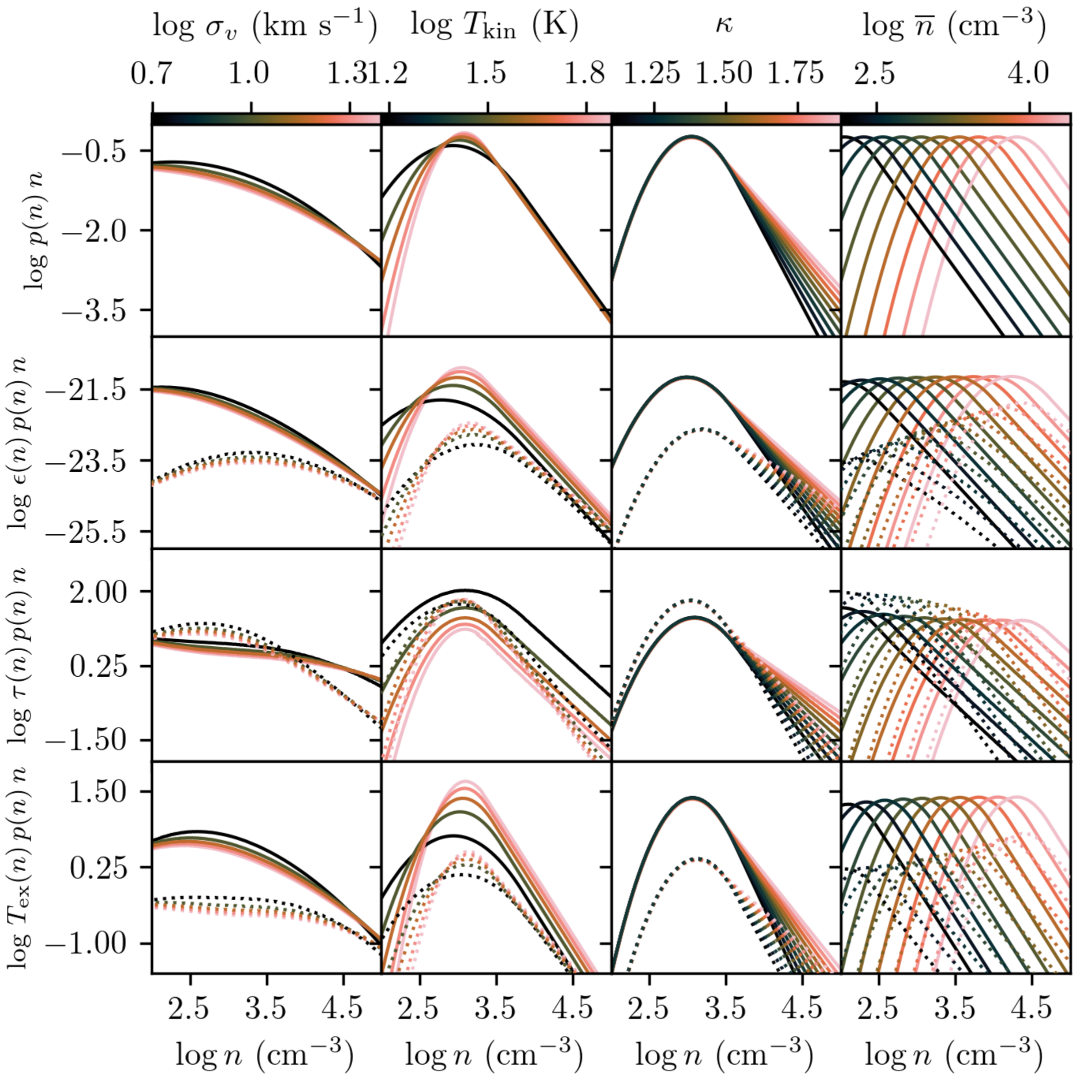

FIGURE 4.3: Representative n–PDFs (top row), emissivity weighted by the PDF (second row from top), optical depth weighted by the PDF (third row from top), and excitation temperature weighted by PDF (bottom row). From left to right, we consider variations in $\sigma_{\rm v}$ (left), $T_{\rm kin}$ (center left), power law slope (center right), and n_0 (right). These curves are colorized by the quantity that is varied. In the bottom three rows, CO results are plotted as solid lines, and HCN results are the dashed lines. Fiducial parameters of these model sets are $\Sigma = 5 \times 10^2$ M$_\odot$ pc^{-2}, $k = 1.5$, $\sigma_v = 14$ km s^{-1}, and $T_{\rm kin} = 45$ K.

4.9) incorporate the predictions of analytical models of star formation. We take the correlation coefficients to be indicative of trends that may also exist in nature, but the strength of these correlations will likely vary.

4.3.1 Excitation and Optical Depth

Figure 4.4 presents the model HCN/CO emissivity ratio in addition to the excitation and optical depth of the CO and HCN $J = 1 - 0$ transitions. The most notable correlations with the modelled emissivity ratio are as follows:

1. The CO optical depth shows no trend with the $\epsilon_{\rm HCN}/\epsilon_{\rm CO}$ ratio and is relatively constant around $\tau_{\rm CO} \sim 10$.

2. The HCN optical depth turns over around $\epsilon_{\rm HCN}/\epsilon_{\rm CO} \gtrsim 0.01$, such that it decreases with increasing $\epsilon_{\rm HCN}/\epsilon_{\rm CO}$ ratio.

3. The CO and HCN optical depths are moderately, positively correlated with each other, and CO and HCN excitation temperatures are moderately positively correlated.

4. HCN experiences a broader range of excitation temperature than CO, and HCN excitation appears moderately correlated with $\epsilon_{\rm HCN}/\epsilon_{\rm CO}$.

In Fig. 4.5, we compare the HCN/CO emissivity ratio to mean density, velocity dispersion, kinetic temperature, and the relative HCN-to-CO filling fraction. We note that this filling fraction is not applied to the models in these plots. We find the following from Fig. 4.5:

1. $\epsilon_{\rm HCN}/\epsilon_{\rm CO}$ has a moderate to strong, positive correlation with n_0.

2. $\epsilon_{\rm HCN}/\epsilon_{\rm CO}$ has a moderate to strong, positive correlation with $\sigma_{\rm v}$.

3. $\epsilon_{\rm HCN}/\epsilon_{\rm CO}$ has a strong, negative correlation with $\Phi_{\rm HCN/CO}$.

It is interesting that the relative filling fraction of HCN and CO, $\Phi_{\rm HCN/CO}$ decreases with increasing $\epsilon_{\rm HCN}/\epsilon_{\rm CO}$. Our models predict that the extent of emission should increase for both HCN and CO at higher HCN/CO ratios. However, the excitation of HCN also increases with $\epsilon_{\rm HCN}/\epsilon_{\rm CO}$, which coincides with an increase

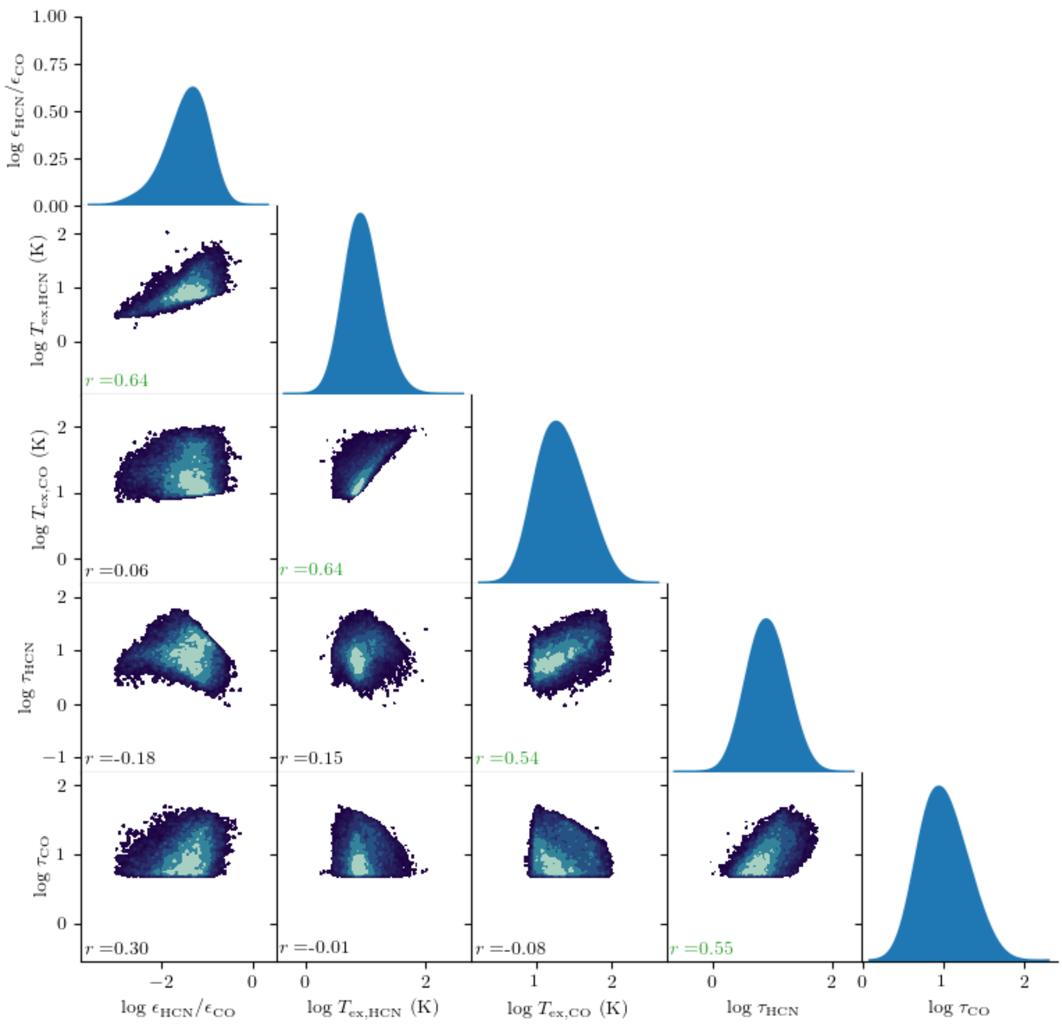

FIGURE 4.4: Results of the radiative transfer analysis and resulting correlations between (left to right, and top to bottom) HCN/CO emissivity ratio, HCN and CO excitation temperatures, and HCN and CO optical depths. The 1D KDE distributions of these parameters are shown at the top of each row. Spearman rank coefficients are printed in the lower left corner. Red indicates a strong correlation, green indicates a moderate correlation, and black indicates a weak correlation.

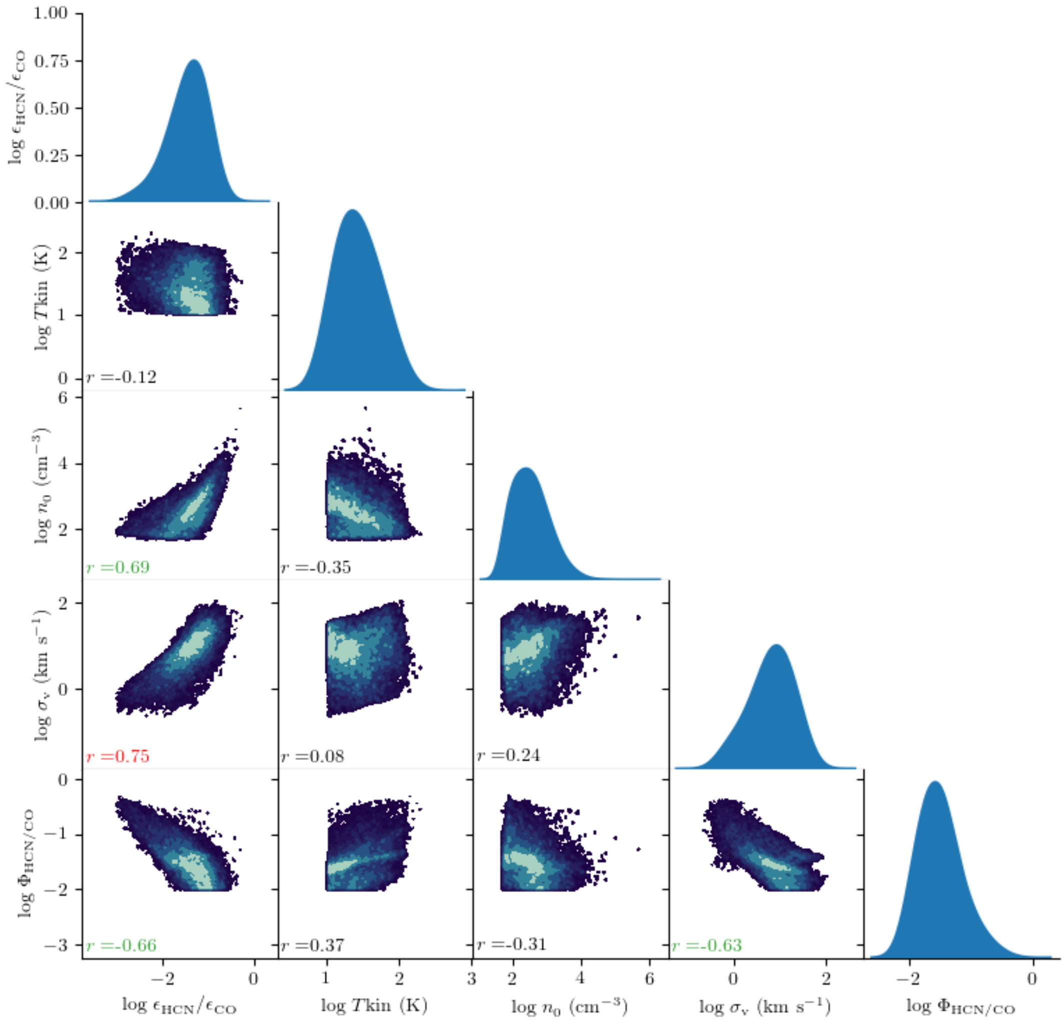

FIGURE 4.5: *Left to right, top to bottom:* The HCN/CO emissivity ratio, kinetic temperature, mean density, velocity dispersion, and the relative HCN-to-CO filling fractions. Formatting is the same as in Fig. 4.4.

in the HCN emissivity towards higher $\epsilon_{\rm HCN}/\epsilon_{\rm CO}$. The HCN emissivity increases more than two orders of magnitude with $\epsilon_{\rm HCN}/\epsilon_{\rm CO}$, while CO instead appears to increase by roughly one order of magnitude.

We look at the dependence of optical depth on other physical quantities in Fig. 4.6. From this plot we can see that most quantities are weakly correlated with the molecular optical depths, except kinetic temperature, which has a moderate, positive correlation with $\tau_{\rm HCN}$. Mean density appears uncorrelated with CO optical depth, but shows a modest anti-correlation with $\tau_{\rm HCN}$. Fig. 4.7 replaces optical depths with excitation temperatures. HCN excitation only has a moderate correlation with $T_{\rm kin}$ and with $\sigma_{\rm v}$. CO excitation appears to be set by kinetic temperature in our models. Mean density has little effect on $T_{\rm ex,CO}$ or $T_{\rm ex,HCN}$.

The results above imply the following for our models:

1. The HCN/CO ratio is strongly, positively correlated with mean density and $\sigma_{\rm v}$. This indicates that the HCN/CO ratio may be a reliable diagnostic of mean density, but studies that aim to constrain n_0 with the HCN/CO ratio should also incorporate velocity dispersion into their analysis.

2. CO is more strongly excited by kinetic temperature than mean density, while HCN excitation has a moderate correlation with $T_{\rm kin}$.

3. HCN optical depth shows more variability than CO optical depth. Changes in HCN optical depth imply that mass estimates using HCN should correct for this systematic bias. We produce a calibration for $\alpha_{\rm HCN}$ with $I_{\rm HCN}$ from our models that can be applied to observations in section 4.4.

4.3.2 The HCN/CO Ratio and $f_{\rm grav}$

For convenience, we produce a summary of the most relevant equations in Table 4.1, similar to that in chapter 3. In this section we combine predictions of the LN+PL analytical models of star formation (Burkhart, 2018) with the modelled emissivities from RADEX. We take two approaches to this comparison: 1. we derive mass-related quantities from the model CO and HCN intensities and use

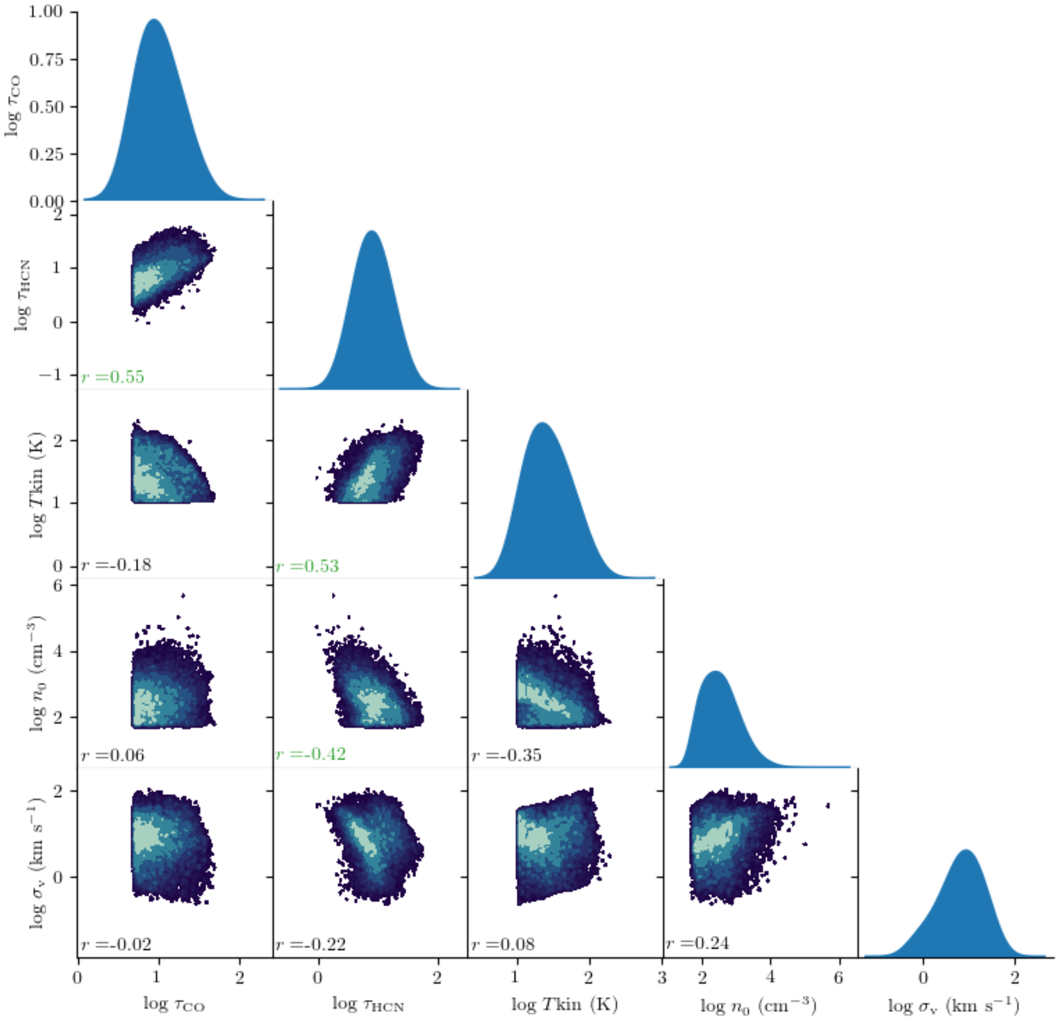

FIGURE 4.6: *Left to right, top to bottom:* Optical depths of CO and HCN, kinetic temperature, mean density, and velocity dispersion. Formatting is the same as in Fig. 4.4.

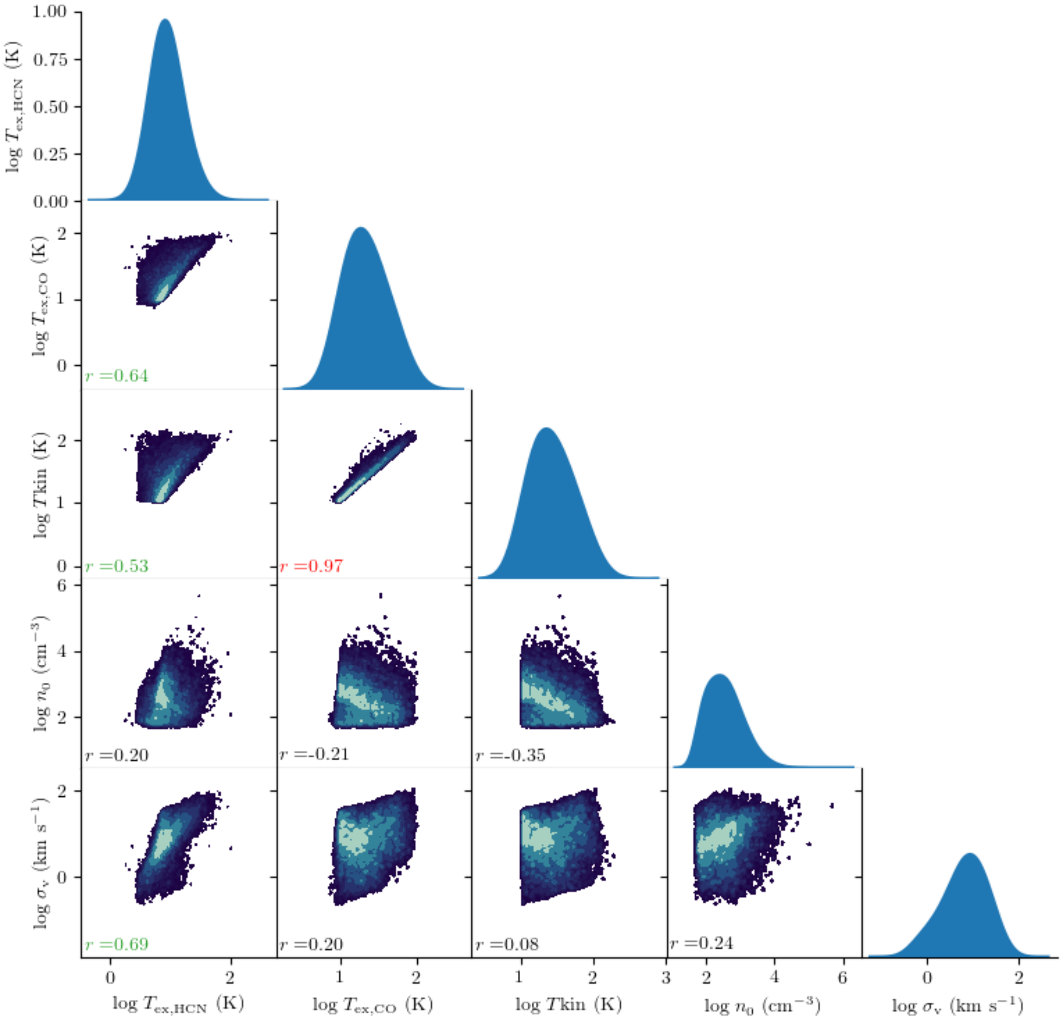

FIGURE 4.7: *Left to right, top to bottom:* Excitation temperatures of CO and HCN relative to $T_{\rm kin}$, kinetic temperature, mean density, and velocity dispersion. Formatting is the same as in Fig. 4.4.

TABLE 4.1: Observational quantities (top panel) compared to model inputs and outputs (bottom panel). We fix $b = 0.4$, and $\beta \to \infty$ in this analysis, and we model over the observed ranges of $\Sigma_{\rm mol}$ and $\sigma_{\rm v}$.

	Observational Estimate	Eqn.	Unit
	$\Sigma_{\rm mol,obs}$	$\alpha_{\rm CO}\,(I_{\rm CO}\,/\,\rm K\ km\ s^{-1})$	$M_\odot$ pc^{-2}
	$\Sigma_{\rm mol,dense,obs}$	$3.2\,\alpha_{\rm CO}\,(I_{\rm HCN}\,/\,\rm K\ km\ s^{-1})$	$M_\odot$ pc^{-2}
(1)	$\Sigma_{\rm SFR,obs}$	$1.14\times10^{-29}\,(L_{\rm 93\,GHz}\,/\,\rm erg\ s^{-1}\ Hz)$	$M_\odot$ yr^{-1} kpc^{-2}
(2)	$P_{\rm turb,obs}$	$(3/2)\,\Sigma_{\rm mol}\sigma_{\rm v}^2/R/k_{\rm B}$	K cm^{-3}
(3)	$t_{\rm dep,obs}$	$\Sigma_{\rm mol}/\Sigma_{\rm SFR}$	yr
	$n_{\rm 0,obs}$	$\Sigma_{\rm mol}/R$	kg cm^{-3}
	$t_{\rm ff,obs}$	$\sqrt{3\pi/32\,G\,n_{\rm 0,obs}}$	yr
(4)	$\epsilon_{\rm ff,obs}$	$t_{\rm ff,obs}/t_{\rm dep,obs}$	–
(5)	$f_{\rm dense}$	$3.2\,I_{\rm HCN}/I_{\rm CO}$	–
(6)	$t_{\rm dep,dense,obs}$	$\Sigma_{\rm mol,dense}/\Sigma_{\rm SFR}$	yr
	Model Estimates Normalized to Obs.	Eqn.	Unit
(2)	$P_{\rm turb,model}$	$(3/2)\,n_{\rm 0grid}\sigma_{\rm v,grid}^2/k_{\rm B}$	K cm^{-3}
(5)	$f_{\rm grav}$	Eq. (20) in Burkhart and Mocz (2019)	–
(4)	$\epsilon_{\rm ff,model}$	Eq. (13) or (27) in Burkhart (2018)	–
(3)	$t_{\rm dep,model}$	$1/\epsilon_{\rm ff,model}\times t_{\rm ff,grid}$	yr
(6)	$t_{\rm dep,grav}$	$f_{\rm grav}/\epsilon_{\rm ff,model}\times t_{\rm ff,grid}$	yr
(6)	$t_{\rm dep,dense,model}$	$f_{n>10^{4.5}\,\rm cm^{-3}}/\epsilon_{\rm ff,model}\times t_{\rm ff,grid}$	yr
(1)	$\Sigma_{\rm SFR,model}$	$\epsilon_{\rm ff,model}\times\Sigma_{\rm mol,grid}/t_{\rm ff,grid}$	$M_\odot$ yr^{-1} kpc^{-2}

these in place of the true model gas surface densities, and 2. we use the model mass-related quantities. The relevant equations are listed in the bottom of Table 4.1. Method 1. is presented in the Appendix.

Intensity is recovered from the models by multiplying the modelled emissivity by the mean model column density, e.g:

$$I_{\rm CO} = \epsilon_{\rm CO}\, N_{\rm H_2+He}. \tag{4.27}$$

For method 1, molecular intensity is then multiplied by constant conversion factors, and we choose an intermediate value for $\alpha_{\rm CO}$: $\alpha_{\rm CO} = 3\,[{\rm M}_\odot\,({\rm K\,km\,s^{-1}\,pc^2})^{-1}]$ and $\alpha_{\rm HCN} = 3.2\,\alpha_{\rm CO}$ to produce estimates of gas mass surface densities. The results of method (1) are presented in the Appendix in Figs. 4.14 and 4.15.

In Fig. 4.8 we compare the modelled HCN/CO emissivity ratio to $\epsilon_{\rm ff}$ and $f_{\rm grav}$ predicted by the LN+PL analytical models of star formation. The dense gas fraction, $f_{\rm dense}$, is that above a density of $n = 10^{4.5}$ cm^{-3}. We find that the HCN/CO emissivity ratio has a strong, positive correlation with $f_{\rm dense}$ but appears to have a weak, negative correlation with $f_{\rm grav}$ with significant scatter. This is consistent with the results of Chapter 3, where we made a similar conclusion by comparing the analytical star formation model predictions to observed HCN/CO ratios. We also find that the HCN/CO emissivity shows almost no correlation with $\epsilon_{\rm ff,obs}$ or $\epsilon_{\rm ff}$. This implies that we should exercise caution in our interpretation of results reliant upon molecular line emissivities. From these results, it appears that the HCN/CO emissivity ratio is not a reliable tracer of $f_{\rm grav}$. Instead, $\epsilon_{\rm ff,obs}$ is strongly, positively correlated with $f_{\rm grav}$ and is a better tracer of this quantity, assuming that there are varying thresholds of star formation that scale with $P_{\rm turb}$ (see chapter 3).

The above results also have important implications for the interpretation of dense gas depletion times. We show the model results including dense gas depletion times in Fig. 4.9. As shown in Chapter 3, the depletion time of the dense gas is anticorrelated with the depletion time of the gravitationally-bound gas, and a moderate anti-correlation is also seen in Fig. 4.9. Our models indicate that longer $t_{\rm dep,dense}$ do not necessarily imply lower star formation efficiencies of the directly star-forming gas, but rather that a smaller fraction of the dense gas is unstable

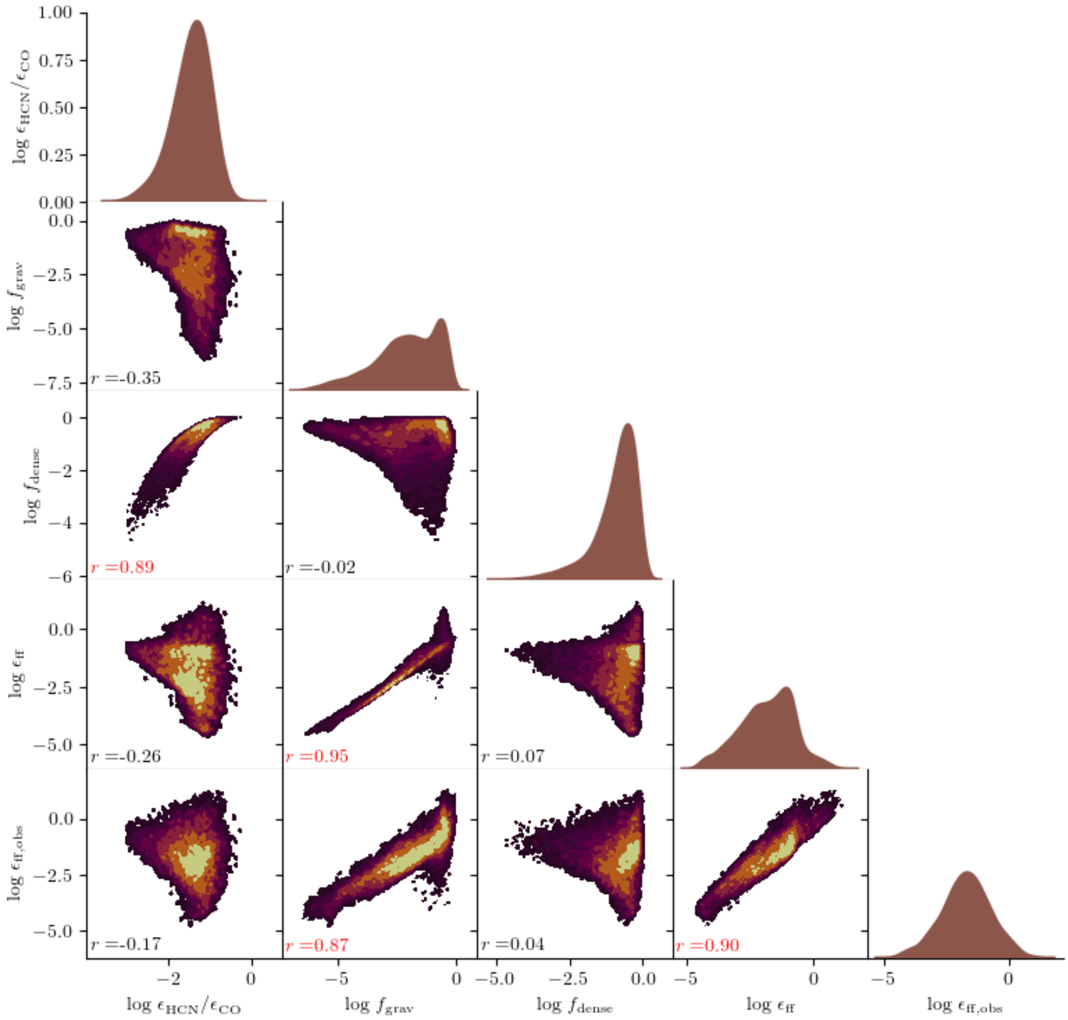

FIGURE 4.8: *Left to right, top to bottom:* The HCN/CO emissivity ratio, f_{grav}, f_{dense}, ϵ_{ff}, and $\epsilon_{\mathrm{ff,obs}}$. See text for more information on $\epsilon_{\mathrm{ff,obs}}$. Formatting is the same as in Fig. 4.4, except warm colors are used to distinguish these plots from those that focus mainly on the results of the radiative transfer analysis.

to collapse in these systems. This is primarily due to the increase in $P_{\rm turb}$ since $n_{\rm thresh} \propto P_{\rm turb}$ in our models.

4.4 The Applicability of the HCN/CO Ratio

The results above imply that the HCN/CO emissivity ratio does track the fraction of gas above $n \sim 10^{4.5}$ cm^{-3}, and that the HCN/CO ratio traces gas above a ∼constant gas density. However, so far we have only considered $n > 10^{4.5}$ cm^{-3} since this is the assumed threshold density for some clouds in the Milky Way disk. Other studies have shown that HCN is tracing gas primarily at moderate densities, $n \sim 10^{3}$ cm^{-3} (Kauffmann et al., 2017), such that it may be more sensitive to fractions including densities below $n \sim 10^{4.5}$.

We compare the modelled HCN/CO ratio to several gas fractions derived from the model $n-$PDFs in Fig. 4.10, including gas fractions above $n \sim 10^{2.5}$, $10^{3.5}$, $10^{4.5}$ and $10^{5.5}$ cm^{-3}. It appears that the HCN/CO is strongly correlated with all of the gas fractions we consider, but is most strongly correlated with gas above $n \sim 10^{3.5}$ cm^{-3} and below $n \sim 10^{5.5}$ cm^{-3} out of the densities that we consider.

4.4.1 Dense Gas Fraction

For application to observations, we derive calibrations between the HCN/CO ratio and $f_{\rm dense}$ from our models. Although these are relatively simple models, we show in section 4.4.2 that they reproduce the $\alpha_{\rm CO}$ calibration from Narayanan and Krumholz (2014). We derive calibrations for $\alpha_{\rm HCN}$ and $\alpha_{\rm CO}$ in section 4.4.2, but first we fit the models to return $f_{\rm dense}$ directly. The relationship between $f(n > 10^{4.5}\,{\rm cm^{-3}})$ and $I_{\rm HCN}/I_{\rm CO}$ resembles a logistic curve, which reflects that $f(n > 10^{4.5}\,{\rm cm^{-3}}) \rightarrow 1$ for models with high HCN/CO ratios. The inclusion of velocity dispersion improves the fit, but it has a power law scaling with $f(n > 10^{4.5}\,{\rm cm^{-3}})$. We therefore combine these functions when fitting $f(n > 10^{4.5}\,{\rm cm^{-3}})$ as a function of HCN/CO ratio. This gives the form:

$$\log_{10} f_{4.5} = \frac{a\ (\sigma_{\rm v}) + b}{\exp\left(c\, I_{\rm HCN}/I_{\rm CO}\right) - d} \tag{4.28}$$

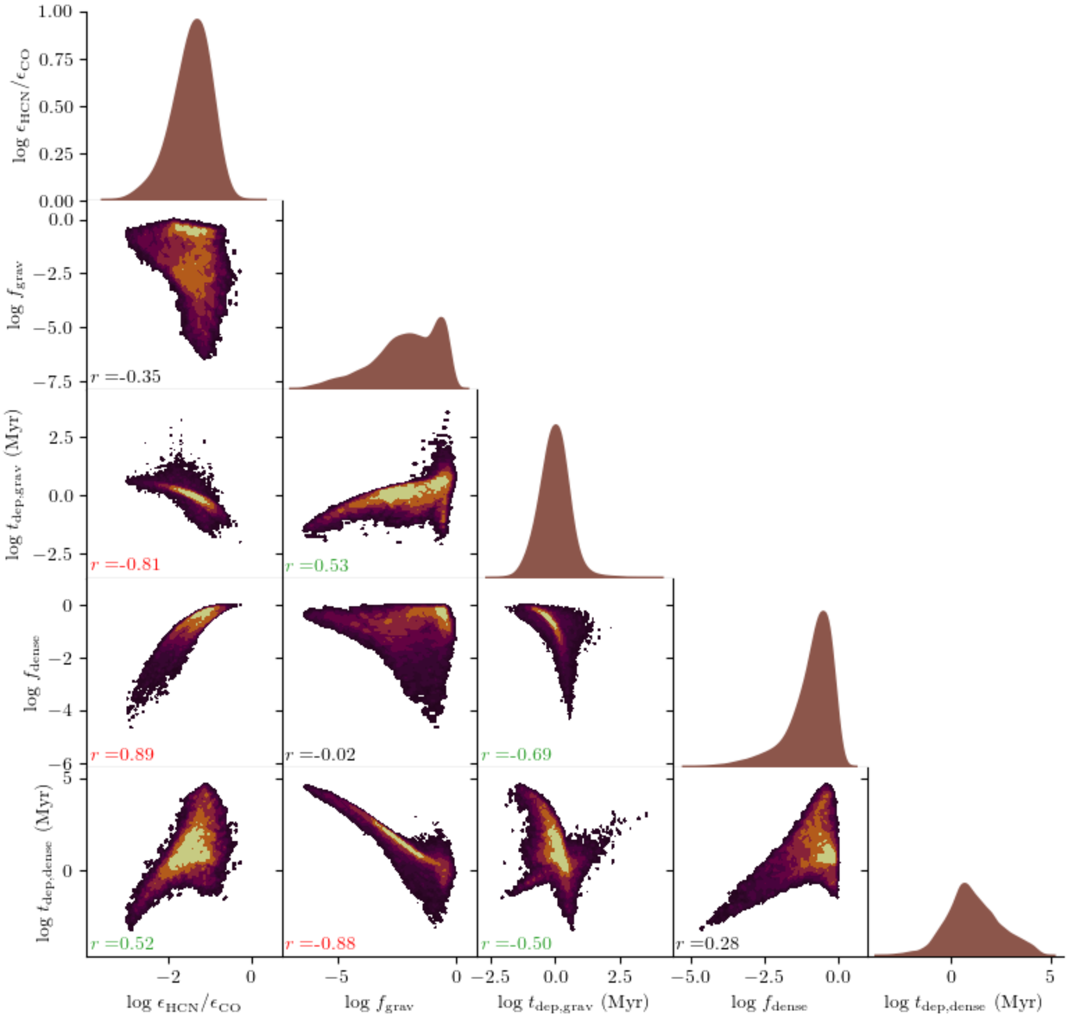

FIGURE 4.9: *Left to right, top to bottom:* The HCN/CO emissivity ratio, $f_{\rm grav}$, $t_{\rm dep,grav}$, $f_{\rm dense}$, and $t_{\rm dep,dense}$. Formatting is the same as in Fig. 4.4.

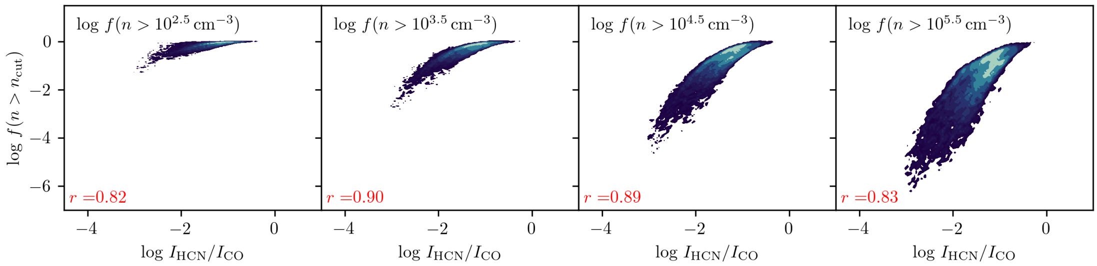

FIGURE 4.10: $n-$PDF Gas fractions as a function of the HCN/CO emissivity ratio. These include fractions above $n_{\text{cut}} = 10^{2.5}$, $10^{3.5}$, $10^{4.5}$ and $10^{5.5}$ cm^{-3}.

and the following fit results:

$$\log_{10} f_{4.5} = \frac{-1.9 \times 10^{-4}\ (\sigma_{\rm v}) + 0.1}{\exp\left(-3.2\, I_{\rm HCN}/I_{\rm CO}\right) - 1}. \tag{4.29}$$

The fit coefficients and their uncertainties are presented in Table 4.2. If filling fractions are known, then this calibration can be used to estimate $f(n > 10^{4.5}\,\mathrm{cm}^{-3})$ directly from molecular line observations. We derive filling fractions in following section. Model $f(n > 10^{4.5}\,\mathrm{cm}^{-3})$ is shown as a function of HCN/CO ratio in Fig. 4.11, and estimates of $f(n > 10^{4.5}\,\mathrm{cm}^{-3})$ in our sources from this calibration are plotted for comparison. The resulting $1-\sigma$ confidence intervals of our source estimates span $f(n > 10^{4.5}\,\mathrm{cm}^{-3}) \approx 0.16 \sim 0.44$.

Equation	Fit Coefficients and Uncertainties				
	a	b	c	d	e
4.29	$(-1.9 \pm 2.0) \times 10^{-4}$	0.1 ± 0.1	-3.2 ± 3.1	-1.04 ± 0.02	–
4.33	5.56 ± 0.05	-0.250 ± 0.002	-0.18 ± 0.02	0.548 ± 0.005	0.68 ± 0.02
4.34	475 ± 4	-0.433 ± 0.002	-0.41 ± 0.03	0.09 ± 0.01	0.52 ± 0.03
4.35	48 ± 48	-0.433 ± 0.002	-3.2 ± 3.1	-1.04 ± 0.02	–

TABLE 4.2: Fit coefficients and $1 - \sigma$ confidence intervals. They are ordered from their appearance in each equation from left to right.

4.4.2 Conversion Factors

An estimate of $f(n > 10^{4.5}\,\mathrm{cm}^{-3})$ can also be achieved using the appropriate conversion factors, and has the advantage of also giving information on the absolute masses associated with HCN and CO emission. We derive calibrations for α_{HCN} and α_{CO} applicable to a range of HCN and CO intensities. An intensity analogous to observed intensities is derived from the models via:

$$I_{\mathrm{mol}} = \Phi_{\mathrm{mol}}\,\epsilon_{\mathrm{mol}}\,N_{\mathrm{tot}} \tag{4.30}$$

where N_{tot} is the total molecular hydrogen and helium column density, Φ_{mol} is from Eq. 4.12, and ϵ_{mol} is from Eq. 4.10. The conversion factor is then larger by the factor Φ_{mol}, so we fit to $\alpha_{\mathrm{mol}}/\Phi_{\mathrm{mol}}$. Finally, the molecular conversion factor is derived from emissivity through:

$$\alpha_{\mathrm{mol}} = 1.6 \times 10^{20} \left(\frac{\epsilon_{\mathrm{mol}}}{\mathrm{K\ km\ s^{-2}\ cm^{2}}}\right)^{-1}. \tag{4.31}$$

Including T_{kin}, τ_{CO}, and $T_{\mathrm{ex,CO}}$ returns a tighter fit. These terms can be ignored in the case any of these are unknown. We fit the following form:

$$\alpha_{\mathrm{mol}} = a \left(\frac{I_{\mathrm{mol}}}{\mathrm{K\ km\ s^{-1}}}\right)^{b} \left(\frac{T_{\mathrm{kin}}}{26\,\mathrm{K}}\right)^{c} \left(\frac{\tau_{\mathrm{mol}}}{8}\right)^{d} \left(\frac{T_{\mathrm{ex}}}{8\,\mathrm{K}}\right)^{e}. \tag{4.32}$$

The resulting calibration for α_{CO} is:

$$\alpha_{\mathrm{CO}} = 5.6 \left(\frac{I_{\mathrm{CO}}}{\mathrm{K\ km\ s^{-1}}}\right)^{-0.25} \left(\frac{T_{\mathrm{kin}}}{26\,\mathrm{K}}\right)^{-0.18} \left(\frac{\tau_{\mathrm{mol}}}{8}\right)^{0.55} \left(\frac{T_{\mathrm{ex}}}{8\,\mathrm{K}}\right)^{0.68} \tag{4.33}$$

We find that our calibration for α_{CO} agrees well with the calibration from Narayanan and Krumholz (2014), which is shown in Fig. 4.12 along with our fit. Fits to α_{HCN} are shown in the right panel of Fig. 4.12. Our calibration results in $\alpha_{\mathrm{CO}} \sim 0.8 - 2\,\mathrm{M_{\odot}}\,(\mathrm{K\,km\,s^{-1}\,pc^{2}})^{-1}$ in our sample, whereas the Narayanan and Krumholz (2014) calibration results in $\alpha_{\mathrm{CO}} \sim 0.6 - 2\,\mathrm{M_{\odot}}\,(\mathrm{K\,km\,s^{-1}\,pc^{2}})^{-1}$.

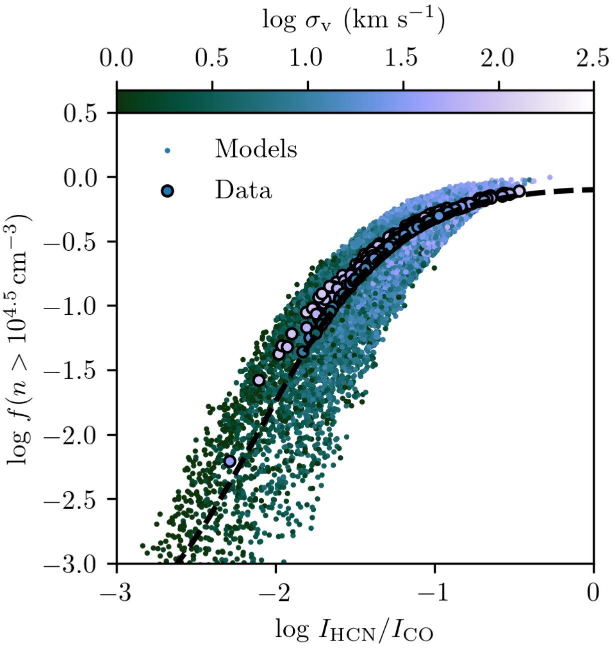

FIGURE 4.11: The fraction of gas above $n \sim 10^{4.5}$ cm^{-3} as a function of $I_{\mathrm{HCN}}/I_{\mathrm{CO}}$. The model output is shown as the small, color points with no outline. The data with Eq. 4.29 applied are the color points with a black outline. Points are on the same color scale and show velocity dispersion. The median trend to the model fit is shown as the black dashed line.

Without correcting for $f_{4.5}$, we get the following expression for $\alpha_{\rm HCN}$:

$$\alpha_{\rm HCN}(N_{\rm tot}) = 470 \left(\frac{I_{\rm HCN}}{\rm K\ km\ s^{-1}}\right)^{-0.43} \left(\frac{T_{\rm kin}}{26\,{\rm K}}\right)^{-0.41} \left(\frac{\tau_{\rm HCN}}{8}\right)^{0.09} \left(\frac{T_{\rm ex,HCN}}{8\,{\rm K}}\right)^{0.52} \tag{4.34}$$

The HCN conversion factor of the dense gas is then just $\alpha_{\rm HCN}(N_{\rm tot})$ multiplied by the fraction of dense gas. If we input the median velocity dispersion of our models ($\sigma_{\rm v} = 7$ km s^{-1}) into Eq. 4.29 and only keep terms with $I_{\rm HCN}$ and $I_{\rm CO}$ we get:

$$\alpha_{\rm HCN}(N_{\rm dense}) \approx \frac{48\ (I_{\rm HCN})^{-0.43}}{\exp\left(-3.2\, I_{\rm HCN}/I_{\rm CO}\right) - 1} \tag{4.35}$$

Our calibration for the HCN conversion factor results in a median value of $\alpha_{\rm HCN,dense} \sim 32\,{\rm M_\odot}\,({\rm K\,km\,s^{-1}\,pc^2})^{-1}$ in our sample. The calibrations for $\alpha_{\rm HCN}$ that we have presented implicitly incorporates the relative HCN-to-CO filling fractions. Without these corrections, $\alpha_{\rm HCN} \sim 3.8\,{\rm M_\odot}\,({\rm K\,km\,s^{-1}\,pc^2})^{-1}$. If one wants to remove the assumption of filling fraction, they can multiply $\alpha_{\rm mol}$ by the filling fraction in either Eq. 4.36 or 4.37.

4.4.3 Filling Fractions

So far we have implicitly included filling fraction into the fits for conversion factors. We now also produce calibrations from our models of both the absolute and relative filling fractions of HCN and CO. These filling fractions are designed such that they can be applied to uncorrected intensities. The absolute filling fractions are fitted against their respective intensities, and we include additional fit parameters from the models to produce tighter correlations (i.e. mean density, kinetic temperature, velocity dispersion). Filling fraction is particularly important for estimates of $f_{\rm dense}$ since the relationship between $\alpha_{\rm HCN}$ and dense gas mass is dependent upon $f_{\rm dense}$. It is important to note that our model $\Phi_{\rm mol}$ estimates are weighted by the emissivity, and this means models with high-emissivity low-density gas can have larger filling fractions that exceed the mass-weighted cloud radius.

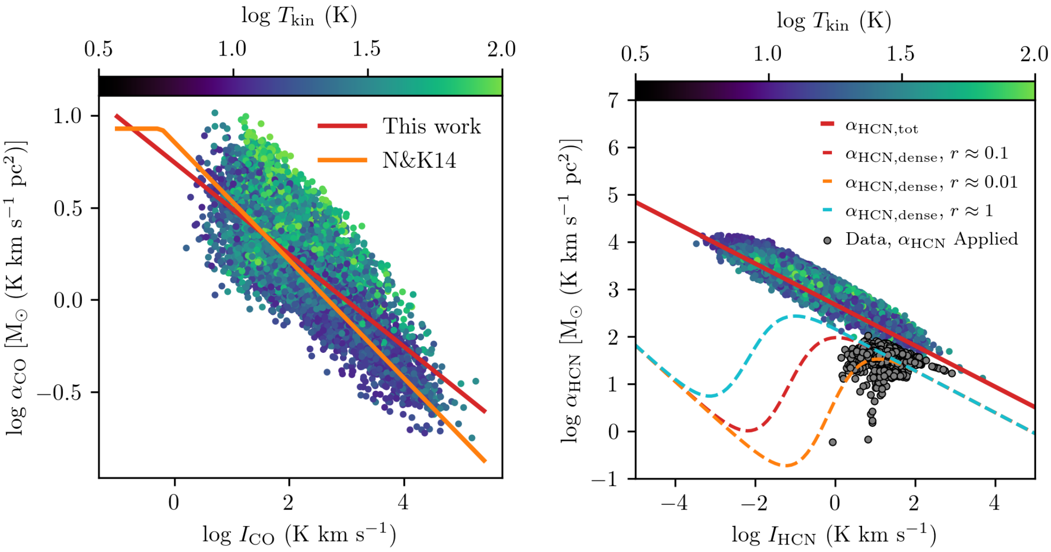

FIGURE 4.12: (*Left:*) The CO conversion factor as a function of CO intensity. The model CO conversion factors are the small, color points in the background. The fit to our models is shown as the the red, solid line. For comparison, we also show the Narayanan and Krumholz (2014) calibration as the orange, solid line. Points are colored by kinetic temperature. The HCN conversion factor as a function of HCN intensity. (*Right:*) The model HCN conversion factors are the small points in the background and are colored by kinetic temperature. The data with the $\alpha_{\rm HCN}$ calibration applied are shown as the gray points with black edges (right panel). The red solid and dashed lines in the right panel are estimates of $\alpha_{\rm HCN}$ without and with $f_{4.5}$ applied, respectively, assuming a constant $I_{\rm HCN}/I_{\rm CO} = 0.1$ and $\Phi_{\rm HCN} \approx 0.1$. r denotes $I_{\rm HCN}/I_{\rm CO}$.

We fit using an equation of the same form as in Eq. 4.32, replacing α_{mol} with Φ_{mol}. We first fit for the CO filling fraction, which is given via:

$$\Phi_{\mathrm{CO}} = 1.3 \left(\frac{I_{\mathrm{CO}}}{\mathrm{K\ km\ s^{-1}}}\right)^{-0.044} \left(\frac{\sigma_{\mathrm{v}}}{\mathrm{km\ s^{-1}}}\right)^{0.31} \left(\frac{T_{\mathrm{kin}}}{26\ \mathrm{K}}\right)^{0.32} \left(\frac{n_0}{310\,\mathrm{cm^{-3}}}\right)^{-0.20} \tag{4.36}$$

where we have again included mean density and temperature to improve the fit. Uncertainties on this fit are listed in Table 4.3. The corresponding filling fraction for HCN is then given by:

$$\Phi_{\mathrm{HCN}} = 0.3 \left(\frac{I_{\mathrm{HCN}}}{\mathrm{K\ km\ s^{-1}}}\right)^{0.31} \left(\frac{\sigma_{\mathrm{v}}}{\mathrm{km\ s^{-1}}}\right)^{-0.55} \left(\frac{T_{\mathrm{kin}}}{30\ \mathrm{K}}\right)^{-0.086} \left(\frac{n_0}{10^2\,\mathrm{cm^{-3}}}\right)^{0.39}. \tag{4.37}$$

These fits highlight how important filling fraction can be to how we interpret line ratios and mass estimates. Where the CO filling fraction from our models has a positive relationship with both σ_{v} and T_{kin}, the HCN filling fraction has negative relationships with these parameters. Furthermore, the CO filling fraction appears almost independent of its own intensity, which is a surprising result since it clearly has a positive correlation with I_{CO} (see Fig. 4.5). However, it is also correlated with velocity dispersion, which may dominate variations in Φ_{CO} over I_{CO}.

Equation	Fit Coefficients and Uncertainties				
	a	b	c	d	e
4.36	1.27 ± 0.02	-0.044 ± 0.003	0.314 ± 0.005	0.316 ± 0.003	-0.200 ± 0.005
4.37	0.258 ± 0.007	0.310 ± 0.007	-0.553 ± 0.009	-0.086 ± 0.009	0.390 ± 0.009

TABLE 4.3: Fit coefficients and $1-\sigma$ confidence intervals.. They are ordered from their appearance in each equation from left to right.

As a conclusion to this section, we apply the derived calibrations to our data and present the results in Table 4.4.

4.5 Conclusions

The general results of the model grid runs can be summarized as follows:

1. Simple spherical models of clouds that incorporate the $n-$PDF into radiative transfer are successful at reproducing observed HCN/CO ratios and star formation trends.

2. The modelled HCN/CO emissivity ratios are negatively correlated with $f_{\rm grav}$, assuming varying star formation thresholds. It is instead a better tracer of the fraction of gas above $n \sim 10^{4.5}$ cm^{-3}. Using our models, we derive a calibration between HCN/CO ratio, velocity dispersion, and the fraction of gas above $n \sim 10^{4.5}$ cm^{-3}.

3. In a gravoturbulent interstellar medium, the velocity dispersion or $\epsilon_{\rm ff}$ (cf. Paper II) is a better measure of $f_{\rm grav}$ than the HCN/CO luminosity ratio.

4. We estimate $\alpha_{\rm HCN}$ from our models, and derive a relationship between $\alpha_{\rm HCN}$ and observables. We also do this for $\alpha_{\rm CO}$ and find that our models produce similar results to those obtained in Narayanan and Krumholz (2014).

5. We provide calibrations for filling fractions of HCN and CO that can also be used to improve estimates of $f(n > 10^{4.5}$ cm$^{-3})$ in the case of unresolved observations of CO and/or HCN.

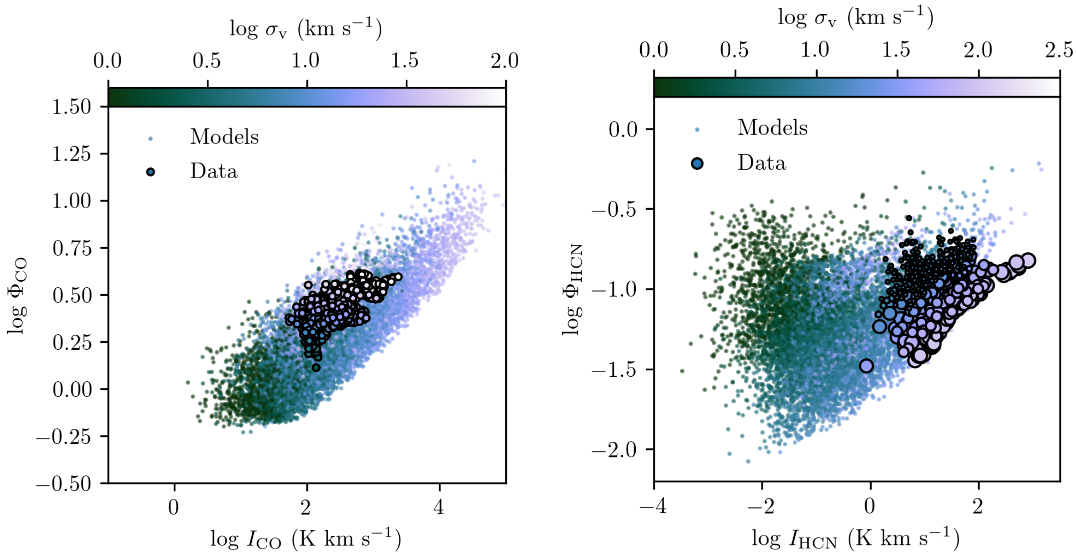

FIGURE 4.13: (*Left:*) The CO filling fraction as a function of CO intensity. The model CO filling fractions are the small, color points in the background. The data with the Φ_{CO} calibration applied are shown as the color points with black edges. Points are colored by velocity dispersion. See text about filling fractions greater than unity. (*Right:*) The HCN filling fraction as a function of HCN intensity. The model HCN filling fractions are the small, color points in the background. The data with the Φ_{HCN} calibration applied are shown as the color points with black edges. Points are colored by velocity dispersion.

TABLE 4.4: The results of the calibrations applied to the data. Average values are shown for each galaxy. Units of conversion factors are $M_\odot\,(\mathrm{K\,km\,s^{-1}\,pc^2})^{-1}$

Galaxy	$\alpha_{\mathrm{CO,fit}}$	$\alpha_{\mathrm{CO,N14}}$	$\alpha_{\mathrm{HCN,dense,fit}}$	$\alpha_{\mathrm{HCN,fit}}$	$f(n > 10^{4.5\,\mathrm{cm^{-3}}})$	$\Phi_{\mathrm{HCN/CO}}$	Φ_{HCN}	Φ_{CO}
Circinus	1.55	1.38	35.09	193.21	0.18	0.07	0.16	2.27
IRAS13120	0.97	0.76	24.29	55.22	0.54	0.04	0.14	3.88
M83	1.31	1.12	43.21	98.93	0.46	0.07	0.19	2.58
NGC1808	1.44	1.26	44.97	130.84	0.32	0.04	0.13	2.86
NGC3256	1.24	1.04	21.27	135.84	0.15	0.03	0.10	3.29
NGC3351	1.61	1.45	37.16	207.22	0.19	0.05	0.12	2.42
NGC3627	1.64	1.48	21.12	251.72	0.09	0.04	0.10	2.37
NGC4038	1.56	1.40	42.31	197.30	0.27	0.03	0.08	3.12
NGC7469	1.23	1.03	41.58	81.98	0.51	0.05	0.16	2.98
VV114	1.12	0.92	6.03	152.72	0.04	0.02	0.06	3.95

4.A Star Formation Trends with Observational Analogs

We present star formation relations from our models with mass-related quantities replaced by their observational analogues in this section. Fig. 4.14 shows star formation timescales, $\epsilon_{\rm ff}$, $\Sigma_{\rm SFR}$, and HCN/CO ratio. Fig. 4.15 shows dense gas depletion time and dense gas fraction compared with turbulent pressure and $\Sigma_{\rm SFR}$. We find good correspondence between the trends in these figures and those in Figs. 4.8 and 4.9.

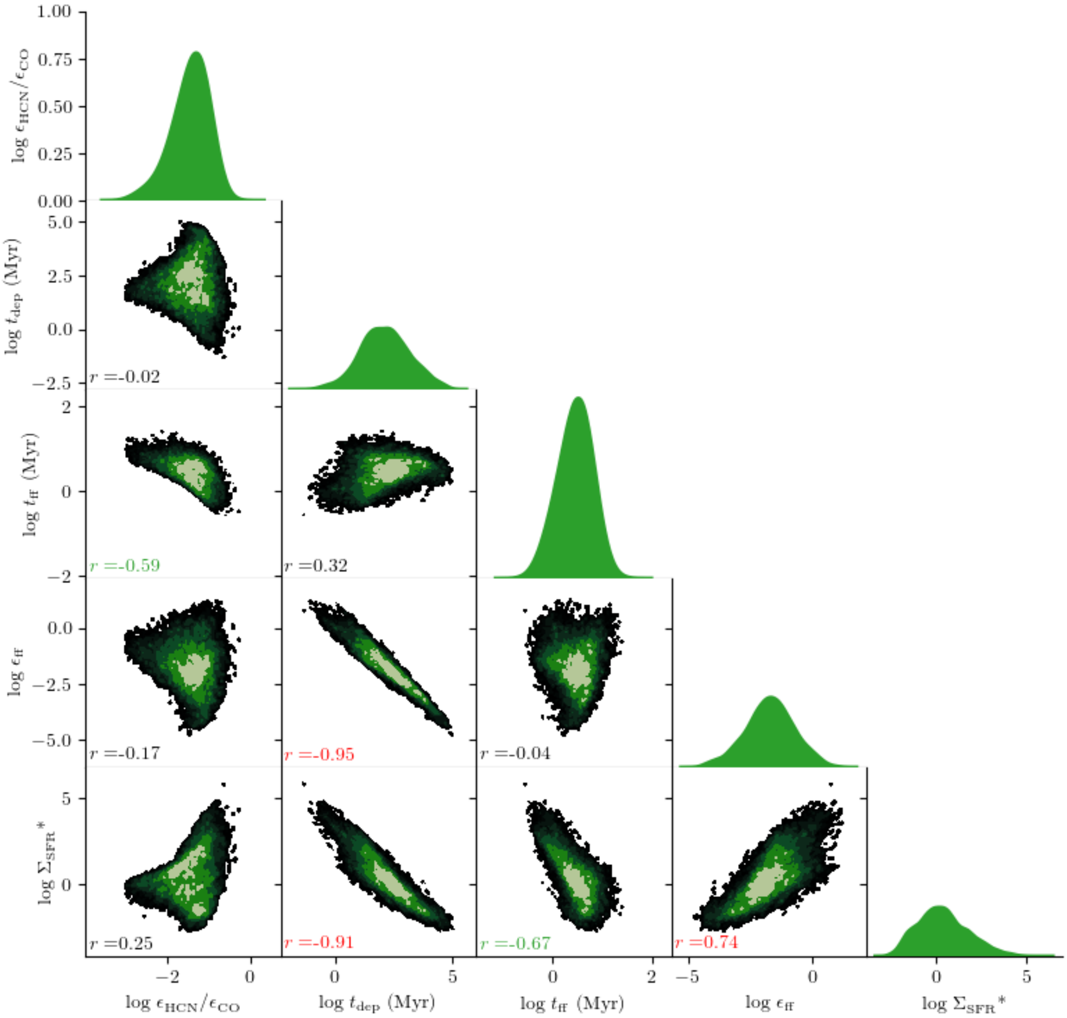

FIGURE 4.14: *Left to right, top to bottom:* The HCN/CO emissivity ratio, t_{dep}, t_{ff}, ϵ_{ff}, and Σ_{SFR}. Formatting is the same as in Fig. 4.4.

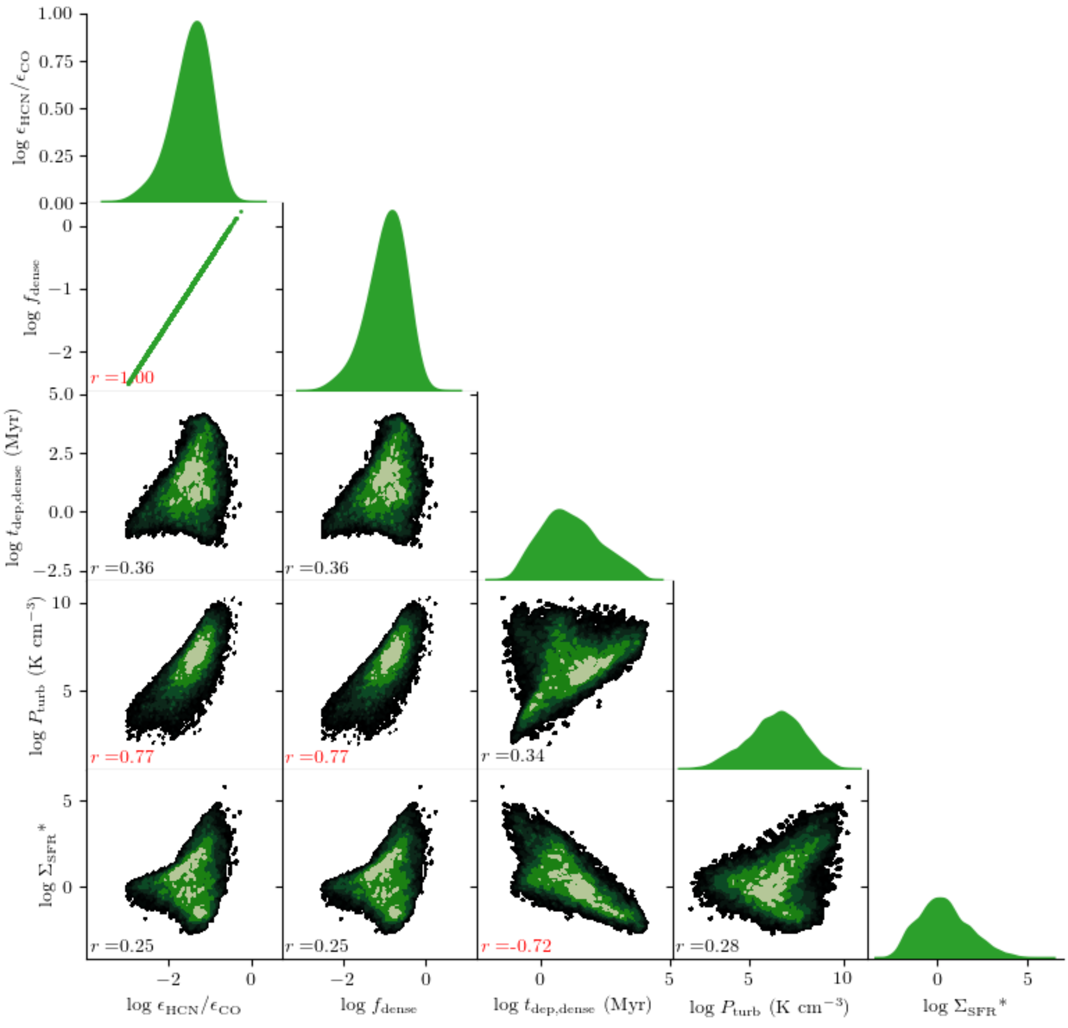

FIGURE 4.15: *Left to right, top to bottom:* The HCN/CO emissivity ratio, $t_{\rm dep}$, $f_{\rm dense}$, $t_{\rm dep,dense}$, $P_{\rm turb}$, and $\Sigma_{\rm SFR}$. Formatting is the same as in Fig. 4.4.

Bibliography

Bemis, Ashley and Christine D. Wilson (2019). *AJ* 157.3, 131, p. 131.

Bigiel, F. et al. (2015). *ApJ* 815.2, 103, p. 103.

Burkhart, B. (2018). *ApJ* 863, 118, p. 118.

Burkhart, Blakesley and A. Lazarian (2012). *ApJl* 755.1, L19, p. L19.

Burkhart, Blakesley and Philip Mocz (2019). *ApJ* 879.2, 129, p. 129.

Burkhart, Blakesley, Kye Stalpes, and David C. Collins (2017). *ApJl* 834.1, L1, p. L1.

Chen, Hao, Yu Gao, Jonathan Braine, and Qiusheng Gu (2015). *ApJ* 810.2, 140, p. 140.

Downes, D., P. M. Solomon, and S. J. E. Radford (1993). *ApJl* 414, p. L13.

Elmegreen, Bruce G. and Edith Falgarone (1996). *ApJ* 471, p. 816.

Federrath, C. and R. S. Klessen (2012). *ApJ* 761, 156, p. 156.

Federrath, C., J. Roman-Duval, R. S. Klessen, W. Schmidt, and M. -M. Mac Low (2010). *A&A* 512, A81, A81.

Federrath, Christoph and Ralf S. Klessen (2013). *ApJ* 763.1, 51, p. 51.

Field, George B., Eric G. Blackman, and Eric R. Keto (2011). *MNRAS* 416.1, pp. 710–714.

Gallagher, Molly J. et al. (2018). *ApJ* 858.2, 90, p. 90.

Gao, Yu and Philip M. Solomon (2004a). *ApJS* 152.1, pp. 63–80.

— (2004b). *ApJ* 606.1, pp. 271–290.

Garcıa-Burillo, S. et al. (2012). *A&A* 539, A8, A8.

Ginsburg, Adam et al. (2016). *A&A* 586, A50, A50.

Graciá-Carpio, J., S. Garcá-Burillo, P. Planesas, A. Fuente, and A. Usero (2008). *A&A* 479.3, pp. 703–717.

Hennebelle, Patrick and Gilles Chabrier (2011). *ApJl* 743.2, L29, p. L29.

Heyer, Mark and T. M. Dame (2015). *ARAA* 53, pp. 583–629.

Heyer, Mark, Coleman Krawczyk, Julia Duval, and James M. Jackson (2009). *ApJ* 699.2, pp. 1092–1103.

Jiménez-Donaire, M. J. et al. (2017). *MNRAS* 466.1, pp. 49–62.

Kauffmann, Jens et al. (2017). *A&A* 605, L5, p. L5.

Kruijssen, J. M. Diederik et al. (2014). *MNRAS* 440.4, pp. 3370–3391.

Krumholz, Mark R. and Christopher F. McKee (2005). *ApJ* 630.1, pp. 250–268.

Leroy, Adam K. et al. (2017a). *ApJ* 846.1, 71, p. 71.

Leroy, Adam K. et al. (2017b). *ApJ* 835.2, 217, p. 217.

Mills, E. A. C. (2017). *arXiv e-prints*, arXiv:1705.05332, arXiv:1705.05332.

Narayanan, Desika and Mark R. Krumholz (2014). *MNRAS* 442.2, pp. 1411–1428.

Padoan, Paolo and Åke Nordlund (2011). *ApJ* 730.1, 40, p. 40.

Rathborne, J. M. et al. (2014). *ApJ* 795.2, L25, p. L25.

Saintonge, Amélie et al. (2012). *ApJ* 758.2, 73, p. 73.

Sandstrom, K. M. et al. (2013). *ApJ* 777.1, 5, p. 5.

Schneider, N. et al. (2011). *A&A* 529, A1, A1.

Shu, F. H. (1977). *ApJ* 214, pp. 488–497.

Sun, Jiayi et al. (2018). *ApJ* 860.2, 172, p. 172.

Tielens, A. G. G. M. (2005).

Usero, Antonio et al. (2015). *AJ* 150.4, 115, p. 115.

van der Tak, F. F. S., J. H. Black, F. L. Schöier, D. J. Jansen, and E. F. van Dishoeck (2007). *A&A* 468.2, pp. 627–635.

Walker, D. L. et al. (2018). *MNRAS* 474.2, pp. 2373–2388.

5 | Discussion and Conclusions

5.1 Summary of this Thesis

Much of this work has been focused on dense gas and star formation in the extreme environments of starbursts, (U)LIRGs, and galaxy centers. These galaxies provide insight into the impact of a range of environments on the connection between dense gas and star formation. I use this sample to test gravoturbulent models of star formation in different galaxy environments, and to put important constraints on current models of star formation.

I began this work in Chapter 2 with a case study of the Antennae Galaxies using high resolution ALMA data. In this Chapter I compared emission from dense gas tracers HCN, HNC, and HCO^+ with the total infrared luminosity at sub-kpc scales in this system. I found that the two nuclei appear to have lower star formation efficiencies of dense gas relative to the overlap region, an intense off-nuclear starburst. This result suggests that there is either a mechanism suppressing star formation from dense gas in the nuclei, or that there is some bias in our observational tracers. A potential physical explanation for suppressed star formation is enhanced pressure in the local environment of the nuclei. This is likely coming from the large potential well of the stellar component in the nuclei in addition to the vast amount of gas in these regions. Furthermore, the two nuclei are likely past the peak of a recent starburst, which indicates that temporal evolution may play a role in the observed efficiency of star formation. I also detect dense gas emission in the Western Arm which is physically offset from HII regions visible across the Western Arm. This implies that there may be some motion of the Western Arm producing an appearance of gas trailing star-forming regions, a phenomenon seen in nearby spiral galaxies.

In Chapter 3 I extend the study of dense gas and star formation to a larger sample of ten galaxies, which includes the centers of disk galaxies and mergers at various stages. I focus primarily on the ratio of HCN to CO emission and its connection to star formation in these systems. In addition to analyzing the observational data I incorporate analytical models of star formation from the literature (Burkhart, 2018; Federrath and Klessen, 2012; Krumholz and McKee, 2005; Padoan and Nordlund, 2011). Specifically, I compare estimates of the fraction of gravitationally bound gas from these models to the dense gas fraction estimated from the HCN/CO ratio. This work aims to address outstanding questions from Chapter 2, namely, whether there is a bias in the HCN/CO ratio as a tracer of dense gas. The data are compared to several different density threshold models of star formation. Two of these models incorporate varying density thresholds, which depend on local pressure and virialization of the gas (Walker et al., 2018). One of these varying threshold models includes a power law tail in the gas density PDF (Burkhart, 2018), while the other is purely lognormal (Krumholz and McKee, 2005; Padoan and Nordlund, 2011). The third adopts a fixed threshold of $n = 10^{4.5}\,\mathrm{cm}^{-3}$ (Lada, Lombardi, and Alves, 2010), which is the apparent threshold for star formation in Milky Way clouds within the disk. I find that all models are able to reproduce some observed star formation properties of the total and dense gas. However, the varying threshold models perform the best compared to observations. The primary conclusion from this work is that the HCN/CO ratio appears to be tracing gas above a roughly fixed density, but not necessarily the fraction of gas which is gravitationally bound within clouds. The strong, apparent correlation between dense gas as traced by HCN and star formation in galaxies (e.g. Gao and Solomon, 2004a,b) still holds on average, but the scatter within this relationship is partially from optical depth effects and variations in excitation at sub-kpc scales, and these biases may become more pronounced in more extreme environments, such as in galaxy nuclei. Furthermore, if varying threshold models accurately characterize the fraction of gravitationally bound gas, then the HCN/CO ratio is not a good tracer of this quantity.

To confirm the conclusions of Chapter 4 I perform a radiative transfer analysis to model HCN and CO emissivities. I am able to directly connect the model emissivities to predictions for star formation through the gas density PDF. I model emissivities over a grid spanning the observed range of gas surface densities and velocity dispersions, as measured from CO. My models are able to reproduce the observed range of HCN/CO ratios. The results of the radiative transfer analysis confirm the conclusions from Chapter 3: that the HCN/CO ratio is tracing gas above a roughly constant density, and that the HCN/CO ratio is anti-correlated with the fraction of gravitationally bound gas from varying threshold models. I consider what information can be obtained from the HCN/CO ratio and determine that it is still a reliable tracer of gas above $10^{4.5}\,\mathrm{cm}^{-3}$, but is slightly more sensitive to moderate density gas ($\sim 10^{3.5}\,\mathrm{cm}^{-3}$). I provide several calibrations from our models which can be applied to data to improve observational estimates of the dense gas fraction. These calibrations include estimates of conversion factors for molecular gas masses, and I find good agreement between our CO calibration and that found by Narayanan and Krumholz (2014).

The results of these three studies show that there are variations in the efficiency of star formation from dense gas across galaxies. These variations may be a result of varying gas density thresholds for star formation, in addition to temporal evolution of star-forming molecular clouds. As a result of this, the HCN/CO ratio may not reliably track the fraction of gravitationally bound gas. As I continue probing smaller scales in nearby galaxies, I must develop better calibrations for our molecular gas tracers and be careful in how I interpret them. Furthermore, varying threshold models are better at characterizing the star formation properties of the total and dense molecular gas content, relative to fixed density threshold models.

5.2 Future Work and Open Questions

The results of this thesis show that these simple models are able to reproduce both observed molecular emissivities and star formation properties in nearby galaxies. Furthermore, these models show that specific molecular line ratios are sensitive to specific ranges of gas densities. By incorporating multiple line ratios, such as HCN/HCO^{+}, with sensitivities to various densities, I can put better constraints on the shapes of gas density PDFs in external galaxies. Incorporating higher-J molecular transitions will also put better constraints on excitation. Excitation and optical depth both impact molecular line emissivities and constraining excitation is an important aspect of interpreting molecular line observations.

I have targeted high-J lines of HCN and HCO^+ in the Antennae Galaxies to assess the relative excitation of these dense gas tracers between the nuclei and the overlap region. This will provide further context for the results presented in Chapter 2. The results in Chapter 2 imply that either HCN is more emissive in the two nuclei, or there is a true suppression of star formation relative to the amount of dense gas. The results from Chapter 4 indicate that HCN in the two nuclei of the Antennae is more emissive relative to other regions across the system. The longer dense gas depletion times observed in the nuclei in Chapter 2 become consistent with the rest of the Antennae when updated conversion factors from Chapter 4 are applied. Therefore it may be variations of the HCN conversion factor which are driving the trends in Chapter 2 as opposed to a true decrease in the star formation efficiency of dense gas.

I have already completed substantial work to compare emissivities of HCN and HCO^+, in addition to CO, across the sample of galaxies studied in this thesis. One of the main goals of this ongoing work is to search for variations in emissivity associated with different morphological features within these galaxies. For example, I look at how nuclei in these galaxies compare with bars, merger tidal features, and circumnuclear disks. The addition of HCO^+ helps indicate when there are potential abundance variations of HCN, which is an important underlying uncertainty to constrain when studying emissivity. I find evidence that there are varying abundances, particularly in the case where the HCN/HCO^+ ratio is greater than unity, indicating that either HCN is more abundant or more emissive relative to HCO^+. The next steps will be to check whether these potential abundance variations are preferentially associated with specific morphological regions within these galaxies. As an extension of this project I will incorporate HCO^+ and apply the models from Chapter 4 on a pixel-by-pixel basis to these galaxies. This will put constraints on the emissivity of HCO^+ relative to HCN.

Since the work in this thesis has been focused on external galaxies, we are not able resolve the gas density PDF for molecular clouds in these systems. To further test the analytical models and their emissivities we need to turn to Milky Way clouds, which can be decomposed into their individual gas density PDFs. I have already begun building a sample to do this, with HCN, CO, and dust continuum observations of multiple Milky Way molecular clouds. This work specifically targets clouds with high quality maps of H_2 column density from the Herschel Gould Belt Survey (André et al., 2010). This work incorporates data from a number of observatories including the James Clerk Maxwell Telescope, the Mopra Telescope, and the Nobeyama 45m Telescope. The goal of this work is to use observations of Milky Way clouds to determine the true emissivity HCN, CO, and HCO^+ relative to each other. This project uses a measure of molecular gas column density that is independent from molecular line emission to derive emissivities directly. This work also incorporates higher-J lines to examine how a traditional molecular line excitation analysis performs relative to the direct comparison between molecular gas mass estimates to molecular line intensities. This work will assess how effective multi-J line analyses are at constraining gas properties and emissivities, which are typically applied to extragalactic observations.

This thesis has made extensive use of observations from ALMA. Moving forward, increasing the number of galaxies with high resolution observations of dense gas tracers with ALMA will be essential to better constrain the connection between dense gas and star formation. Due to its large bandwidth, observations with the Submillimeter Array can target multiple molecular transitions simultaneously, which is ideal for efficiently building up a larger molecular line sample. I plan to incorporate more galaxies into this study in order to probe a wider range of star formation environments. This will take advantage of more archival data available from ALMA and the SMA, as well as proposing for new data for galaxies which have not yet been observed. Expanding the sample of galaxies and including multiple molecular lines will not only increase the statistical significance of these conclusions, but it will help separate environmental effects on star formation from variations in radiative transfer or excitation of the observed molecular transitions.

Bibliography

André, Ph. et al. (2010). *A&A* 518, L102, p. L102.

Burkhart, B. (2018). *ApJ* 863, 118, p. 118.

Federrath, C. and R. S. Klessen (2012). *ApJ* 761, 156, p. 156.

Gao, Yu and Philip M. Solomon (2004a). *ApJS* 152.1, pp. 63–80.

— (2004b). *ApJ* 606.1, pp. 271–290.

Krumholz, Mark R. and Christopher F. McKee (2005). *ApJ* 630.1, pp. 250–268.

Lada, Charles J., Marco Lombardi, and João F. Alves (2010). *ApJ* 724.1, pp. 687–693.

Narayanan, Desika and Mark R. Krumholz (2014). *MNRAS* 442.2, pp. 1411–1428.

Padoan, Paolo and Åke Nordlund (2011). *ApJ* 730.1, 40, p. 40.

Walker, D. L. et al. (2018). *MNRAS* 474.2, pp. 2373–2388.